Soft-template directed functional composite nanomaterials

Xuefeng Pan

Univ.-Diss. (cumulative)

zur Erlangung des akademischen Grades
"doctor rerum naturalium"
(Dr. rer. nat.)
in der Wissenschaftsdisziplin "Materialwissenschaft"

eingereicht an der
Mathematisch-Naturwissenschaftlichen Fakultät
Institut für Chemie
der Universität Potsdam

Ort und Tag der Disputation: Potsdam, 2023

Hauptbetreuerin: Prof. Dr. Yan Lu
Betreuer*innen: Prof. Dr. Helmut Schlaad
Gutachter*innen: Prof. Dr. Guosong Chen
Dr. Axel Neffe

Published online on the
Publication Server of the University of Potsdam:
https://doi.org/10.25932/publishup-61270
https://nbn-resolving.org/urn:nbn:de:kobv:517-opus4-612709

To My Family & Friends

Abstract

Soft-template strategy enables the fabrication of composite nanomaterials with desired functionalities and structures. In this thesis, soft templates, including poly(ionic liquid) nanovesicles (PIL NVs), self-assembled polystyrene-*b*-poly(2-vinylpyridine) (PS-*b*-P2VP) particles, and glycopeptide (GP) biomolecules have been applied for the synthesis of versatile composite particles of PILs/Cu, molybdenum disulfide/carbon (MoS_2/C), and GP- carbon nanotubes-metal (GP-CNTs-metal) composites, respectively. Subsequently, their possible applications as efficient catalysts in two representative reactions, *i.e.* CO_2 electroreduction (CO_2ER) and reduction of 4-nitrophenol (4-NP), have been studied, respectively.

In the first work, PIL NVs with a tunable particle size of 50 to 120 nm and a shell thickness of 15 to 60 nm have been prepared *via* one-step free radical polymerization. By increasing monomer concentration for polymerization, their nanoscopic morphology can evolve from hollow NVs to dense spheres, and finally to directional worms, in which a multi-lamellar packing of PIL chains occurred in all samples. The obtained PIL NVs with varied shell thickness have been *in situ* functionalized with ultra-small Cu nanoparticles (Cu NPs, 1-3 nm) and subsequently employed as the electrocatalysts for CO_2ER. The hollow PILs/Cu composite catalysts exhibit a 2.5-fold enhancement in selectivity towards C_1 products compared to the pristine Cu NPs. This enhancement is primarily attributed to the strong electronic interactions between the Cu NPs and the surface functionalities of PIL NVs. This study casts new aspects on using nanostructured PILs as novel electrocatalyst supports in efficient CO_2 conversion.

In the second work, a novel approach towards fast degradation of 4-NP has been developed using porous MoS_2/C particles as catalysts, which integrate the intrinsically catalytic property of MoS_2 with its photothermal conversion capability. Various MoS_2/C composite particles have been prepared using assembled PS-*b*-P2VP block copolymer particles as sacrificed soft templates. Intriguingly, the MoS_2/C particles exhibit tailored morphologies including pomegranate-like, hollow, and open porous structures. Subsequently, the photothermal conversion performance of these featured particles has been compared under near infrared (NIR) light irradiation. When employing the open porous MoS_2/C particles as the catalyst for the reduction of 4-NP, the reaction rate constant has increased by 1.5-fold under light illumination. This catalytic enhancement mainly results from the open porous architecture and photothermal conversion performance of the MoS_2 particles. This proposed strategy

offers new opportunities for efficient photothermal-assisted catalysis.

In the third work, a facile and green approach towards the fabrication of GP-CNTs-metal composites has been proposed, which utilizes a versatile GP biomolecule both as a stabilizer for CNTs in water and as a reducing agent for noble metal ions. The abundant hydrogen bonds in GP molecules bestow the formed GP-CNTs with excellent plasticity, enabling the availability of polymorphic CNTs species ranging from dispersion to viscous paste, gel, and even dough by increasing their concentration. The GP molecules can reduce metal precursors at room temperature without additional reducing agents, enabling the *in situ* immobilization of metal NPs (*e.g.* Au, Ag, and Pd) on the CNTs surface. The combination of excellent catalytic property of Pd NPs with photothermal conversion capability of CNTs makes the GP-CNTs-Pd composite a promising catalyst for the efficient degradation of 4-NP. The obtained composite displays a 1.6-fold increase in conversion under NIR light illumination in the reduction of 4-NP, mainly owing to the strong light-to- heat conversion effect of CNTs. Overall, the proposed method opens a new avenue for the synthesis of CNTs composite as a sustainable and versatile catalyst platform.

The results presented in the current thesis demonstrate the significance of using soft templates for the synthesis of versatile composites with tailored nanostructure and functionalities. The investigation of these composite nanomaterials in the catalytic reactions reveals their potential in the development of desired catalysts for emerging catalytic processes, *e.g.* photothermal- assisted catalysis and electrocatalysis.

Keywords: nanocomposite, soft template, block copolymer, poly(ionic liquid), glycopeptide, catalyst

Zusammenfassung

Die Weiche-Vorlagen-Strategie ermöglicht die Herstellung von zusammengesetzten Nanomaterialien mit gewünschten Funktionalitäten und Strukturen. In dieser Arbeit wurden weiche Vorlagen, darunter Poly(ionische Flüssigkeit) -Nanovesikeln (PIL-NVs), selbstorganisierte Polystyrol-*b*-Poly(2-Vinylpyridin)-Partikeln (PS-*b*-P2VP) und Glykopeptid (GP)-Biomoleküle verwendet, um vielseitige Kompositen aus PILs/Cu, Molybdändisulfid/Kohlenstoff (MoS_2/C) bzw. GP-Kohlenstoffnanoröhren -Metall (GP-CNTs- Metall) zu synthetisieren. Anschließend wurden ihre möglichen Anwendungen als effiziente Katalysatoren in zwei repräsentativen Reaktionen, d. h. CO_2-Elektroreduktion (CO_2ER) und Reduktion von 4-Nitrophenol (4-NP), untersucht.

Im ersten Abschnitt wurden PIL-NVs mit einer einstellbaren Partikelgröße von 50 bis 120 nm und einer Schalendicke von 15 bis 60 nm durch einstufige radikalische Polymerisation hergestellt. Durch Erhöhung der Monomerkonzentration für die Polymerisation kann sich ihre nanoskopische Morphologie von hohlen NVs zu dichten Kugeln und schließlich zu gerichteten Schnecken entwickeln, wobei in allen Proben eine multilamellare Packung von PIL-Ketten auftritt. Die erhaltenen PIL-NVs mit unterschiedlicher Schalendicke wurden durch ultrakleinen Cu-Nanopartikeln (Cu-NPs, 1-3 nm) funktionalisiert und anschließend als Elektrokatalysatoren für CO_2ER eingesetzt. Die PILs/Cu-Komposit-Elektrokatalysatoren zeigen eine 2,5-fache Steigerung der Selektivität gegenüber C_1-Produkten im Vergleich zu den unbehandelten Cu-NPs. Diese Verbesserung wird in erster Linie auf die starken elektronischen Wechselwirkungen zwischen den Cu-NPs und den Oberflächenfunktionalitäten der PIL -NVs zurückgeführt. Diese Studie wirft neue Aspekte auf die Verwendung nanostrukturierter PILs als neuartige Elektrokatalysatorträger für eine effiziente CO_2-Umwandlung.

Im zweiten Abschnitt wurde ein neuartiger Ansatz für den schnellen Abbau von 4 -NP entwickelt, bei dem poröse MoS_2/C-Partikeln als Katalysatoren verwendet werden, die die intrinsische katalytische Eigenschaft von MoS_2 mit seiner photothermischen Umwandlungsfähigkeit verbinden. Verschiedene MoS_2/C-Verbundpartikeln wurden unter Verwendung von zusammengesetzten PS-*b*-P2VP Blockcopolymerpartikeln als geopferte weiche Vorlagen hergestellt. Erstaunlicherweise weisen die MoS_2/C-Partikeln maßgeschneiderte Morphologien auf, darunter eine granatapfe lartige, hohle und offenporige Struktur. Anschließend wurde die photothermische Umwandlungsleistung dieser Partikeln unter Bestrahlung von Nahinfrarotlicht (NIR) verglichen. Bei der

Verwendung der offenporigen MoS_2-Teilchen als Katalysator für die Reduktion von 4 -NP hat sich die Reaktionsgeschwindigkeitskonstante unter Lichtbeleuchtung um das 1,5-fache erhöht. Diese katalytische Verbesserung ist hauptsächlich auf die offenporige Architektur und die photothermische Umwandlungsleistung der MoS_2-Partikeln zurückzuführen. Diese vorgeschlagene Strategie bietet neue Möglichkeiten für eine effiziente photothermisch unterstützte Katalyse.

Im dritten Abschnitt wird ein einfacher und umweltfreundlicher Ansatz für die Herstellung von GP-CNTs-Metall-Verbundwerkstoffen vorgeschlagen, bei dem ein vielseitiges GP-Biomolekül sowohl als Stabilisator für CNTs in Wasser auch als Reduktionsmittel für Edelmetallionen eingesetzt wird. Die zahlreichen Wasserstoffbrüc kenbindungen in den GP-Moleküle verleihen den gebildeten GP-CNTs eine ausgezeichnete Plastizität, die es ermöglicht, polymorphe CNT - Spezies zu erhalten, die von einer Dispersion über eine visko se Paste und ein Gel bis hin zu einem Teig reichen, wenn man ihre Konzentration erhöht. Die GP -Moleküle können Metallvorläufer bei Raumtemperatur ohne zusätzliche Reduktionsmittel reduzieren und ermöglichen so die In -situ- Immobilisierung von Metall-NPs (z. B. Au, Ag und Pd) auf der Oberfläche der CNTs. Die Kombination der hervorragenden katalytischen Eigenschaften von Pd-NPs mit der photothermischen Umwandlungsfähigkeit von CNTs macht den GP -CNTs-Pd- Verbundstoff zu einem vielversprechenden Katalysator für d en effizienten Abbau von 4- NP. Das erhaltene Komposit zeigt eine 1,6-fache Steigerung der Umwandlung unter NIR- Licht- Beleuchtung, wenn es als Katalysator bei der Reduktion von 4-NP verwendet wird, was hauptsächlich auf den starken Licht -Wärme -Umwandlungseffekt der CNTs zurückzuführen ist. Insgesamt eröffnet die vorgeschlagene Methode einen neuen Weg für die Synthese von CNT-Verbundwerkstoffen als nachhaltige und vielseitige Katalysatorplattform.

Die in dieser Arbeit vorgestellten Ergebnisse zeigen, wie wichtig die Verwendung weicher Templates für die Synthese vielseitiger Verbundwerkstoffe mit maßgeschneiderter Nanostruktur und Funktionalitäten ist. Die Untersuchung dieser Komposit -Nanomaterialien in katalytischen Reaktionen zeigt ihr Potenzial für die Entwicklung gewünschter Katalysatoren für neue katalytische Prozesse, z. B. für die Elektrokatalyse und die photothermisch unterstützte Katalyse.

Stichworte: Nanokomposit, weiche Vorlage, Blockcopolymer, Poly(ionische Flüssigkeit), Glykopeptid, Katalysator

Table of Contents

1 Introduction

Templating synthesis has been demonstrated to be one of the most effective approaches towards the fabrication of multi-functional composites with desired nanostructures.[1, 2] Desired active components can grow or self-replicate in the inner space or on the surface of the template. Templating synthesis is primarily classified into two categories: soft-template and hard-template methods. Hard templates often involve a group of inorganic materials such as metal particles, silica spheres, and alumna oxide, which have been widely employed to prepare functional composites with unique nanostructures.[3-5] Hard templates are, however, limited by the choice of obtained morphologies (*e.g.* simply hollow structure) and challenges in template removal. The latter is often implemented under extreme conditions, *e.g.* strong acid or base etching. On the contrary, soft templates made up of surfactant micelles, organic molecules, and homo/co- polymer assemblies have been demonstrated as outstanding candidates for the construction of novel composite materials.[6, 7] Such soft assembles can be easily altered to form various complex ordered nanostructures (*e.g.* hierarchical porous structure), thus providing large space for the control over desired architectures as well as functionalities. Another advantage of the soft template over the hard template is the ease of template removal *via* simple solvent extraction or calcination. Thus, rational design and synthesis of composite nanomaterials with controllable architectures as well as versatile functionalities *via* soft template is in great demand.

Among the considerable candidates, poly(ionic liquid) (PIL) particles have been an intriguing alternative due to their unique nanostructures based on intra-/inter- molecular assembly.[8] Moieties with different properties (*e.g.* polarity and solvophilicity) can be directly integrated into the same repeating unit of PIL chains.[9] PILs typically carry hydrophilic cationic backbones with hydrophobic alkyl side chains and counter anions.[10, 11] The amphiphilicity of PILs can be easily modulated by tuning either the length/type of side chains or type of counter ions. Driven by micro-phase separation, PILs are capable of forming various well-ordered nanostructures including spheres, vesicles, and worms.[12] Their simple and controllable synthesis permits the large-scale production of nanostructured PIL nano-/micro- objects. Taking these into consideration, PILs can be employed as the soft template for the scalable production of advanced composite materials.

Apart from PILs, block copolymers (BCPs) composed of two or more different moieties have been intensively applied as the soft template for the formation of both organic and inorganic functional

nanomaterials.[13] BCPs open new opportunities in the development of novel ordered nanostructures due to their tunable microphase-separation.[14] Concerning functionalization, abundant active binding sites in selected blocks can incorporate with other metal and organic/inorganic components, thus creating innovative hybrid materials. Therefore, using BCP as a soft template could be a promising alternative for the production of nanostructured composite materials.

Alternatively, the structural diversity and complexity of nature-inspired biomaterials have presented substantial potential in self-assembly and hybridization with other components.[15, 16] At a molecular level, hydrophilic carbohydrates are often conjugated with hydrophobic peptides or nucleobases, which could form versatile assembled nanostructures ranging from spherical micelles, and nanofibers, to cubic structures. Besides, the electron donor groups (*e.g.* oxygen or nitrogen-rich segments) of peptides or DNA may enhance the binding capacity to a variety of metals or metal ions. Therefore, green and controllable synthesis of metal or inorganic materials can be realized with the assistance of these amphiphilic biomolecules.[17, 18] Thus, multi-functional biomaterials could also serve as promising templates for the sustainable synthesis of functional composite materials.

This cumulative thesis aims at exploring novel functional nanocomposites based on the above-mentioned soft templates including BCPs, PILs, and amphiphilic biomolecules. Three systems have been investigated including the synthesis of PILs/copper (PILs/Cu) vesicles, molybdenum disulfide/carbon (MoS_2/C) particles, and glycopeptide-carbon naontubes-metal (GP-CNTs-metal) composites using PILs, BCPs, and amphiphilic GP biomolecules as the soft template, respectively. Their possible applications as heterogeneous catalysts in different reactions have been studied and will be discussed in the following chapters.

1.1 PIL particles as carriers for catalytic metal particles

Owing to the unique asymmetric ionic structure, ILs typically refer to organic salts with a low melting point (below 100 °C). [19] ILs have received extensive research interest in many fields including catalysis, sensing, energy conversion and storage, and many more.[20] Their polymerized ILs (PILs) are composed of covalently linked IL monomers, where the charged backbones can be integrated either in the side chains or main chains of the polymer structure. The incorporation of charged backbones with surrounding counter ions yields a huge variety of PILs including anionic,

cationic, or even zwitter-ionic PILs (**Figure 1.1.1a**). By varying the composition and structure of the IL monomers, the resulting PILs can exhibit tunable physical or chemical properties such as solubility and ion conductivity. [10, 21] Therefore, the rational design and synthesis of PILs determine their fundamental properties, nanostructures, and final functionalities. So far, various polymerization methods have been developed for the fabrication of PIL particles and PIL-based functional composite materials, such as emulsion polymerization, suspension polymerization, and dispersion polymerization.[22, 23] Among them, one-pot dispersion polymerization has emerged as a simple and scalable method for the synthesis of nanostructured PIL particles for decades. Notably, both internal and surface nanostructures of PIL particles can be controllably designed through this method due to the intrinsic electrostatic repulsion generated by charged PIL chains. Nevertheless, current reports primarily focus on the design of their molecular architecture that significantly affects the final morphologies of the resulting particles. The key to determine the self-assembly behavior of PILs through dispersion polymerization remains elusive.

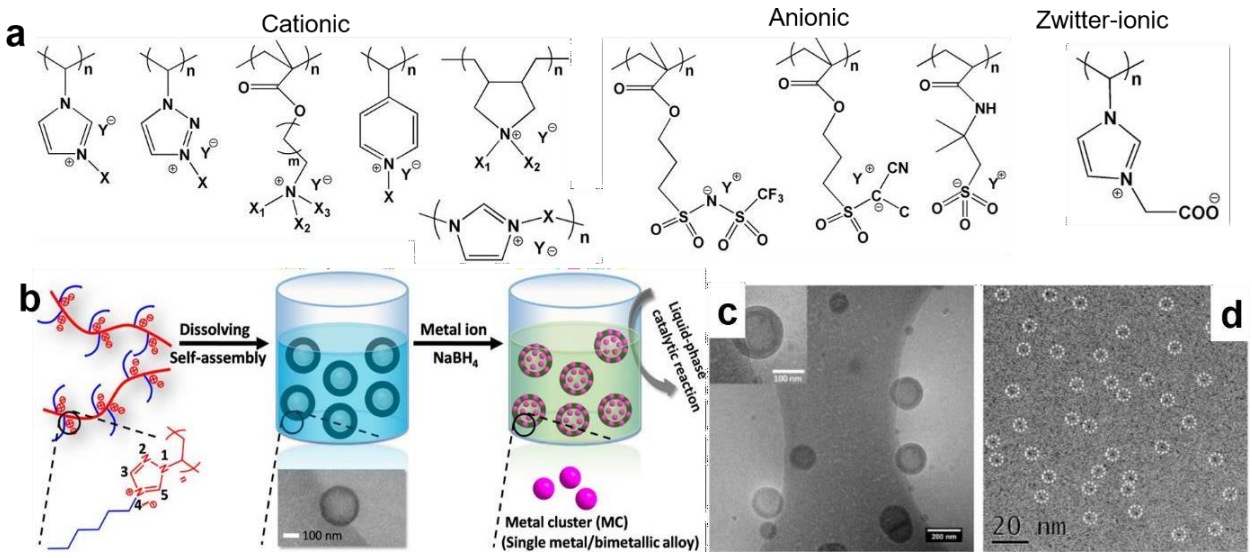

Figure 1.1.1. (a) Chemical structure of several typical PILs. X: functional groups. Y: counter ions. (b) Synthetic scheme of vesicular metal/PIL composites. (c) Cryo-TEM image and (d) bright-field TEM image of Pd clusters in the PIL vesicle. Reproduced with permission. Copyright 2017, American Chemical Society.[24]

Metal nanoparticles have gained significant attention owing to their potential applications in diverse fields such as catalysis, photonics, and magnetic devices.[25, 26] No doubt that the small size of metal particles could significantly enhance the reaction efficiency due to the abundant specific surface area. However, when the size of metal particles goes down to several nanometers, *e.g.* 2

nm, direct synthesis and application of metal nanoparticles (NPs) is rather challenging as metal NPs with the ultra-small size is prone to irreversibly aggregate, driven by high surface energy.[27] The most frequently reported strategy is to use amphiphilic molecules or surfactants as a capping agent to stabilize the metal particles as well as a mediator to tune the catalytic activity. Amphiphilic PILs have been demonstrated to attach to the surface of various materials such as carbon, inorganic materials, and metal NPs. For instance, copper NPs (Cu NPs) coated with a thin layer of PILs have been recently reported to adjust the reaction selectivity towards hydrocarbons in the conversion of CO_2.[28] However, the surface modification by capping agents may lead to the partial loss of accessible active sites, which are paramount for the possible catalytic reactions.

By contrast, loading metal particles on polymer templates is another promising approach to simultaneously dispersing and stabilizing the catalytically active centers. Increasing the number and/or decreasing the size of metal NPs on desired polymer templates is capable of enriching the total surface-active sites involved in the catalytic reactions. In principle, a high specific surface area of the polymer templates could enable high loading amount of metal particles. From the structural perspective, a hollow or porous interior possesses a relatively higher specific surface area than that of a solid counterpart of the same size. PIL particles have been reported to work both as carriers and stabilizers to support metal particles on their surface, thus ensuring sufficient amounts of surface-active sites of metal NPs. For instance, Sun *et al.* developed triazolium-based PIL vesicles in mixed solvents (dichloromethane and methanol) for the support of ultra-small size of palladium (Pd) clusters (below 1 nm) with a high loading amount of 14.5 wt.% (**Figure 1.1.1b-d**).[24] However, the formation of such PIL hollow particles is driven by sequential three-step methods, namely, polymerization from IL monomers, self-assembly of obtained PILs, and final functionalization with metal NPs. In addition, the sophisticated synthesis and inevitable involvement with organic solvents could impede the sustainable fabrication of PIL composite particles. Therefore, it is essential to develop a novel strategy that could efficiently functionalize metal NPs with PIL assembles for the fabrication of versatile PIL-based nanocomposites *via* a scalable and green approach.

1.2 BCP-templated synthesis of functional metal sulfides

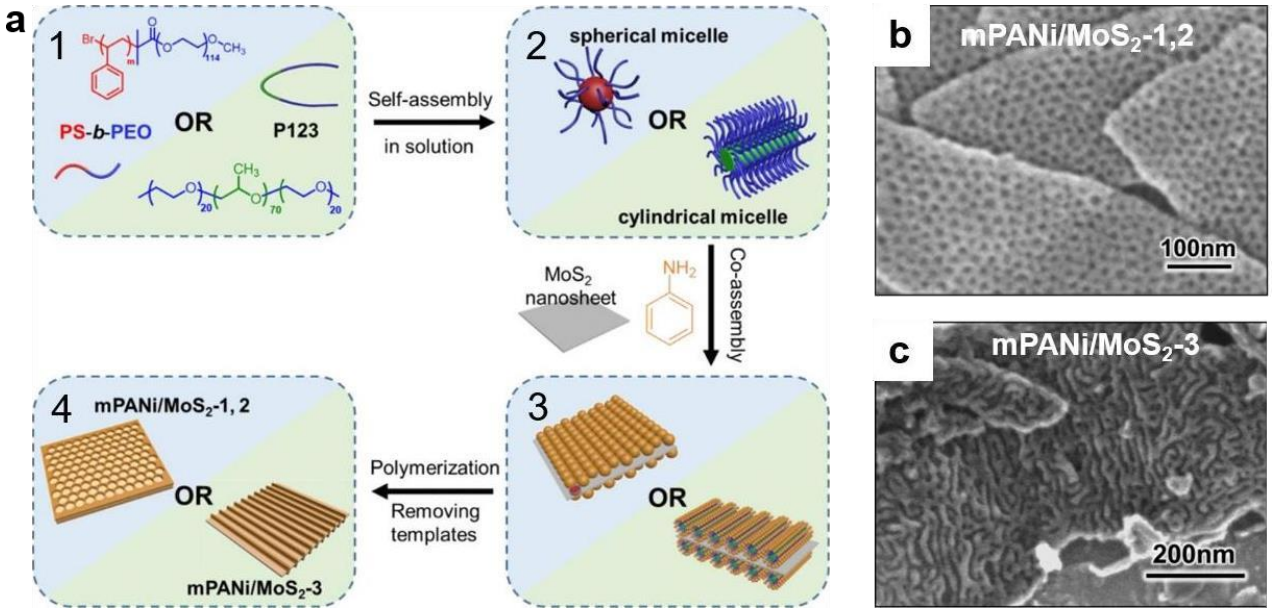

Figure 1.2.1. (a) Synthetic scheme of the mesoporous PANi/MoS_2 composites. SEM images of the PANi/MoS_2 composites with (b) spherical and (c) cylindrical pore structure. Reproduced with permission. Copyright 2017, American Chemical Society.[29]

Assembled BCPs in bulk or other medium has been attractive owing to their astonishing diversity in morphological control and capability in creating hybrid materials with tailored functionalities. Using nanostructured BCPs assemblies as a sacrificed soft template makes it possible for the controllable fabrication of multi-functional composite materials. Typically, BCPs can co-assemble with inorganic salts or direct self-assemble into featured nanomaterials. The co-assembly process strongly relies on the weak non-covalent interactions (*e.g.* hydrogen bonding, electrostatic interactions, or coordination interactions) between BCPs with the inorganic materials or ion precursors (*e.g.* metal alkoxides or nitrates). For instance, Mai *et al.* reported a co-assembly approach for the synthesis of polyaniline/molybdenum disulfide (PANi/MoS_2) composites with tunable pore structures and sizes using polystyrene-block-poly(ethylene oxide) (PS-*b*-PEO) and commercial triblock copolymer poly(ethylene oxide)-block-poly(propylene glycol)-block-poly(ethylene oxide) (PEO-*b*-PPO-*b*-PEO, P123) as the structure-directing agents (**Figure 1.2.1**).[29] However, such strategy requires a highly precise control over synthetic conditions, including ionic strength and solvent quality for the assembly process, as well as annealing or aging treatment for the formation of targeted inorganic components. By contrast, the direct assembly

method appears to be relatively easier to manipulate the resulting structure of the targeted composites due to its sequential synthesis. Driven by the minimization of free energy, the micro/nanoscopic morphologies of given BCP particles can be simply tuned by varying synthetic conditions such as solvent composition, temperature, or additives. Even subtle changes in temperature or solvent of the dispersion could trigger the partial movement of selective blocks of the primary BCP chains. This could lead to the formation of novel hierarchical architecture or morphologic transformation. Subsequently, the featured BCP particles can be employed as a robust scaffold for the deposition of active inorganic components. The targeted functional composites can be thereby achieved after removing the organic polymer framework through subsequent calcination or solvent dissolution, leaving a highly ordered and porous structure. Therefore, BCP particles fabricated through direct self-assembly could be a promising soft template for the controllable synthesis of multi-functional composite particles.

In recent years, metal sulfides such as MoS_2 and tungsten disulfide (WS_2) have emerged as a prominent field of research due to their widespread application in energy conversion and storage, catalysis, and photothermal conversion.[30-32] Of particular interest is the enormous availability of metal sulfides in various geometries, crystal sizes, crystalline phases, and chemical compositions. The edge sites of their crystal sheets are inherently active centers for the catalytic reaction. Metal sulfides also exhibit good stability under various reaction conditions, which is vital for maintaining their catalytic activity over time. In addition, metal sulfides are a class of semiconductor materials with distinctive electronic band gaps and band positions as well as remarkable light response, rendering them capable of harnessing the most/entire spectrum of solar light and converting the solar energy to thermal energy through photothermal conversion.[33] Upon light irradiation, excited electrons and holes are generated with exceptional mobilities. Their recombination will lead to the generation of additional heat, which transports from the bulk surface of metal sulfides to the surrounding regions. The resulting light-induced heat can facilitate the chemical reaction rates in return. However, the lack of active catalytic sites and low efficiency of light capture/conversion remain significant challenges for pristine metal sulfides.

Several protocols have been developed to improve the photothermal conversion efficiency including band gap engineering, defects design, and structural heterojunction *via* hybridization with other active chemical components such as titanium oxide (TiO_x), nickel oxide (NiO_x), or

tungsten oxide (WO_x). However, these modification approaches often involve complex fabricating techniques including hydrothermal or acid etching treatments, which are either energy-demanding, time-consuming, or unsustainable. Alternatively, structural engineering is another promising method for simultaneously boosting their light-to-heat conversion and catalytic performance. Specifically, the fabrication of hollow or porous nanostructures has been reported to increase the interaction between incident light and the metal sulfide framework. The resulting hollow architecture enables multiple light reflections and extended residence time within the metal sulfide channels, thus promoting the efficient utilization of light. In addition to the advantages in light harvest, nanoporous engineering approaches also maximize the curvature of particle templates, providing abundant exposed active sites of metal sulfide nanosheets for possible catalytic reactions.[34-36] Therefore, there is a great demand for the development of nanostructured metal sulfide materials for light harvest/conversion as well as efficient catalysis.

1.3 Carbohydrate as stabilizer and reducer for the synthesis of metal nanoparticles

Carbohydrate-containing biomolecules such as glycoproteins, proteoglycans, and glycolipids are extremely diverse due to a large family of natural building blocks in biological systems.[37, 38] Functionalization with synthetic polymers, metal, or inorganic materials greatly broadens their application fields such as in catalysis, sensing, and energy conversion and storage.[39-41] The driving force for the formation of those specific nanostructures at the molecular level involves hydrogen bonding interactions, hydrophobic interactions, electrostatic interactions, or coordination interactions with metal ions. The interplay of those multiple interactions in biomolecules collectively determines their assembled morphologies, binding affinity, and final multi-functionalization. Naturally, carbohydrates are highly hydrophilic, which are often conjugated to hydrophobic lipids, aromatic nitrogenous bases, or peptides to form glycolipids, nucleosides (nucleotides), and glycopeptides (GP), respectively (**Figure 1.3.1a**). Such combination confers the carbohydrates with amphiphilic properties and thus provides their diversity in both self-assembly and functionalization.

Specifically, glycolipids comprise a hydrophilic carbohydrate head with fatty chains (long hydrophobic alkyl tail). The hydrophobic interactions of the alkyl chains in glycolipids result in the formation of microphase separation, which in turn gives rise to the creation of various

morphologies, including micelles, vesicles, and nanotubes. Tailoring the chain length of the alkyl tail, the corresponding packing parameter would be changed thus affecting the final morphology of glycolipid assemblies.[42] For glycolipids tethered with given carbohydrate units, however, the nonpolar nature of alkyl tails provides them weak interactions with other polar active components (*e.g.* organic molecules or metal ions), thus restricting their widespread functionalization.

By contrast, nucleosides and nucleotides typically possess a monosaccharide covalently linked with a highly polar nucleobase (*i.e.* aromatic nitrogenous base), thus enabling the incorporation with other inorganic materials.[43] From the perspective of self-assembly, aside from hydrogen bonding interaction and π-π stacking, electrostatic interactions resulting from the phosphate groups make it possible for nucleotides to complex with various metal or metal ions.[44] Nevertheless, the limited type of nucleobases (only five) in nature leads to the lack of molecular structural diversity. This limitation could hinder the capability to meet the increasing demand for self-assembly and functionalization of nucleobases.

Therefore, intensive attention has focused on synthetic GP molecules due to their massive availability in structural composition and potential for multi-functionalization. In terms of chemical components, mono- or di- saccharide (*e.g*. mannose and glucosamine) is often conjugated with several amino acid parts with known physiochemical properties.[45] One of the most popular strategies is to insert additional aromatic segments either as a part of the linker or at the peptide end of the amphiphiles. Thus, additional π-π stacking interactions could further enhance the self-assembly of these obtained amphiphiles (**Figure 1.3.1b-c**). The complex multiple interactions normally result in the formation of core-shell nanofibers with peptides in the core and carbohydrates on the shell.[46]

In addition to the possibilities in self-assembly, functional carbohydrate amphiphiles have been also utilized for the stabilization of metal or metal-based nanoparticles.[47, 48] Chemical modification or co-assembly with metal particles is an effective approach towards the fabrication of ordered functional metal/carbohydrate composites.[16, 49, 50] In most of the current studies, however, the synthesis of metal nanoparticles has been conducted in the presence of strong toxic reducing agents, such as sodium borohydride, hydrogen, or hydrazine, which are undesirable for scalable production and unsustainable. Considering the presence of reducing hydroxyl groups in common carbohydrate units, metal ions could be directly reduced and stabilized by carbohydrate-based

molecules under mild conditions, which is yet rarely reported for GP-based assembly.[51] Thus, it is worth attempting to develop a novel hybrid material using reducible GP without the use of additional reducing agents for the synthesis of hybrid functional metal/carbohydrate composites and facilitate their catalytic applications.

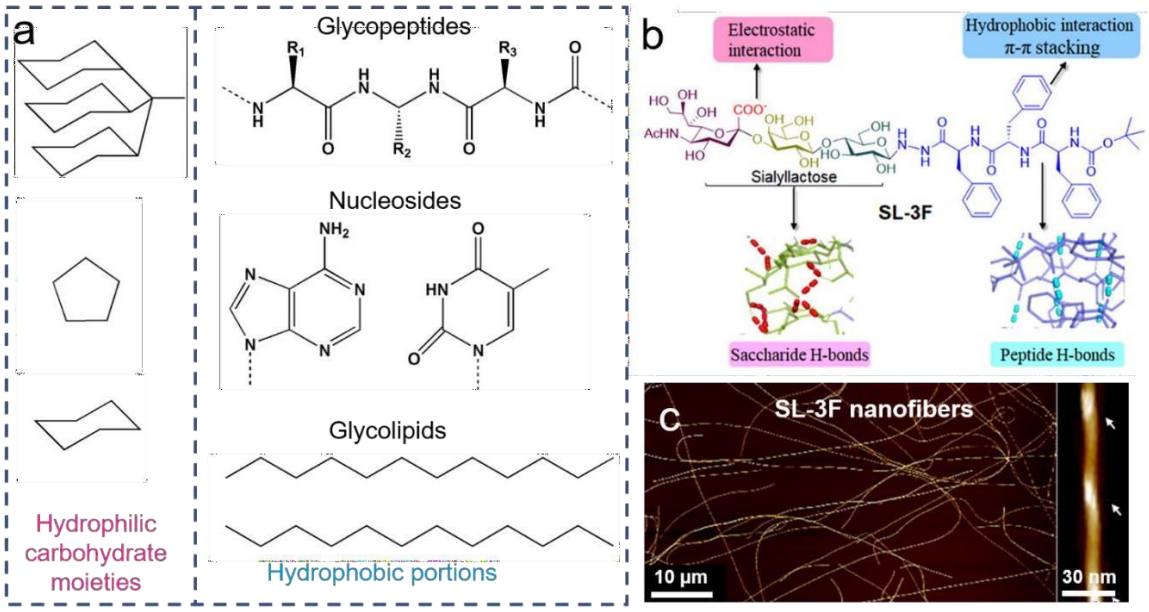

Figure 1.3.1. (a) Chemical structure of three typical carbohydrate amphiphiles. Copyright 2021, Elsevier.[37] (b) Chemical structure of sialyllactose-triphenylalanine and (c) AFM images of the corresponding nanofibers assembled in water. Reproduced with permission. Copyright 2021, American Chemical Society.[46]

1.4 Application of nanostructured functional composites

Environment pollution and energy crisis are long-standing issues that threaten human's health and future civilization development.[52] Catalytic chemical reactions (*e.g.* reduction, oxidation, or coupling reaction) using suitable catalysts are effective means to thoroughly degrade/harvest the dissolved gases or organic compounds, and subsequently, convert them into other valuable chemical products. Indeed, catalytic reactions often demand catalysts with specific properties for the desired reaction. Efficient catalyst systems can be constructed through the optimization of their nanostructures and chemical components. For instance, tuning the size and morphology of the catalyst particle can endow the desired catalysts with abundant accessible active sites. In addition, the incorporation of photo-responsive materials such as plasmonic metal NP, metal sulfides, or

carbon materials (*e.g.* CNTs) could lead to a substantial temperature increase in the reaction interface when illuminated with appropriate wavelengths. This localized heat at the nanoscale in return accelerates the catalytic reaction progress. However, from the perspective of material synthesis, these strategies are commonly realized based on different templates. Hence, the screening and design of suitable templates is essential for the synthesis of catalysts with desired properties, thus optimizing the corresponding catalytic performance.

1.4.1 CO_2 electroreduction

Another attractive catalytic reaction is CO_2 conversion. Considering the surging CO_2 emissions and energy shortage, attention has been attracted to the strategies for capturing and converting CO_2 into more valuable products. No doubt that plants or other phototrophs are consuming and utilizing a large amount of CO_2 every moment *via* natural photosynthesis. The converted biomass as a carbon source could be a promising alternative for carbon recycling. However, this method is often limited by the huge land requirement for the planting and transporting of biomass-based products. The traditional chemical industry provides several significant solutions for CO_2 fixation and transformation, which includes methanation, Fischer-Tropsch transformation, and methanol synthesis. However, extreme working conditions such as at high pressures and temperatures are usually involved, thus hampering the efficient conversion of CO_2.[53]

The CO_2 electrochemical reduction (CO_2ER), typically under mild liquid/gas-phase conditions, enables the efficient production of various valuable adducts [54-56]. A primary technological challenge is the design of selective catalysts that are capable of reducing CO_2 electrochemically at low overpotentials with high selectivity and current densities. Unsurprisingly, the parasitic, thermodynamically favorable hydrogen evolution reaction (HER) is another crucial issue that needs to be tackled [57, 58]. Metal-based catalysts have been intensively reported for decades in reducing CO_2 to various products *via* different electron routes, ranging from $2e^-$ process for the formation of CO and formic acid to $18e^-$ process for propanol. [53, 59, 60] The final products are often determined by the binding energy of specific intermediates on the catalyst surface. Generally, most metal catalysts only produce limited kinds of products such as CO and formic acid, and lack availability in the production of high calorific valued hydrocarbons (*e.g.* CH_4 and C_2H_4). Cu is the only reported metal catalyst that can convert CO_2 to various adducts *via* CO_2ER, particularly multi-

carbon products, with considerable production rates *i.e.* current density. Another distinct advantage of Cu metal is its low price and massive availability in nature compared to other metal catalysts such as Ag and Au. However, its poor selectivity towards specific products is an apparent bottleneck for practical applications.[61-63] To circumvent such issue, many efforts have been devoted to tailoring the crystal structure, particle size and shape, and even surface oxidation state.[53, 64] Among them, size manipulation has been frequently reported to effectively alter the catalytic activity of CO_2ER. A decrease in the size of Cu particles, particularly below 5 nm, has been reported to result in an appreciable increase in the catalytic activity and selectivity for H_2 and CO.[65] Therefore, the synthetic advance in the Cu-based catalyst with small particle size for the modulation of the CO_2ER activity is in great demand.

1.4.2 Catalytic reduction of 4-nitrophenol

4-Nitropheol (4-NP) is a typical organic pollutant in water, while its reduced product 4-aminophenol (4-AMP) is an important intermediate for the production of other valuable chemicals including paracetamol, antipyretic, and phenacetin. Its reduction reaction has been intensively studied by researchers predominantly due to distinctive merits such as reduction under mild conditions and few side reactions or byproduct generation. A large number of materials have been reported to catalyze the reduction reaction of 4-NP. These materials generally include metallic NPs such as silver (Ag) and gold (Au), and metal-based compounds (metal sulfides or oxides). Among them, metal particles are the most frequently reported catalysts owing to their highly catalytic reactivity.[26] However, metal NPs face challenges in limited availability in nature, production cost, as well as catalytic and structural instability during reaction recycling as mentioned above.

As a typical heterogeneous catalytic reaction, the reduction of 4-NP is a surface reaction as well as a temperature-dependent reaction. Enriching the accessible surface area by creating hierarchical hollow or porous architectures is the most common approach to increasing the catalytically active sites. Moreover, increasing the operating reaction temperature, particularly the surface temperature of the catalysts, is also of great significance in accelerating the conversion reaction rate.[66] Although conventional heating methods through water or oil bath are commonly used to elevate the operating temperature of catalytic reactions, novel approaches such as photothermal heating under light irradiation have been explored to increase the temperature more efficiently. However, it is

important to note that the heat induced by light irradiation can transport from the surface of photothermal absorbers to the surrounding environment. In this regard, the surface temperature of the absorbers, particularly those that act as thermo-insulators (*e.g*. metal sulfides), might be considerably higher than that of the reaction solution, which could remarkably accelerate the reduction rate of 4-NP on the catalyst surface.

Therefore, two possible strategies can be applied to address the abovementioned issues. One is to downsize the catalytic metal NPs, thus reducing the catalyst amount and maximizing the active centers for the reaction. Meanwhile, the reaction rate can be further accelerated by combining with other photothermal converting materials such as conjugating polymers and carbon materials. To address the high production cost of metal catalysts, an alternative strategy is to explore low-cost multi-functional metal sulfides. These materials display excellent catalytic performance and stability in reactions, as well as exceptional photothermal conversion performance when exposed to light irradiation. These characteristics have led to great interest in the design of multi-functional metal sulfides that can integrate with superior catalytic properties and photothermal conversion capabilities for the fast degradation of 4-NP.

Overall, this thesis focuses on these two catalytic reactions using well-designed composite nanomaterials. Briefly, porous MoS_2/C composite particles derived from BCP templates and GP-CNTs-metal composites have been used for the reduction of 4-NP with the assistance of light irradiation. In addition, PILs/Cu composite particles based on PIL assembles have been employed as the electrocatalyst for CO_2ER.

1.5 Objectives

The main objective of this cumulative thesis is to synthesize novel functional composite materials with desired complex structures and functionalities using three kinds of organic molecules, *i. e.* PILs, polystyrene-*b*-poly(2-vinylpyridine) (PS-*b*-P2VP) block copolymers, and versatile glycopeptide (GP) biomolecules as soft templates. Their possible applications as efficient catalysts in two representative reactions, *i.e.* reduction of 4-NP and CO_2ER, will be investigated respectively. Concretely, the investigation of these novel functional composite materials has been carried out as follows:

Article I: The design of polymer nanovesicles (NVs) with controllable shell thickness and overall size remains challenging. Herein, a straightforward, scalable synthetic route towards PIL homopolymer NVs have been proposed. Taking advantage of their hollow architectures as well as functional backbones, desired metal Cu NPs have been functionalized as the electrocatalysts for the CO_2ER.

1) To tune their particle size and shell thickness, PIL NVs have been synthesized at various monomer concentrations *via* one-step free radical polymerization induced self-assembly. The morphologic transformation has been discussed in detailed

2) To explore their potential applications, PIL NVs with varied shell thickness have been *in situ* functionalized with ultra-small Cu NPs. The obtained PIL/Cu composite particles have been subsequently employed as the electrocatalysts for CO_2ER.

Article Ⅱ: Porous MoS_2/carbon particles can be employed as catalysts as well as photothermal conversion agents. The main interest of this section is to realize the integration of their catalytic properties and photothermal heating capability for the efficient reduction of 4-NP.

1) To synthesize nanostructured MoS_2/carbon particles, assembled PS-*b*-P2VP particles have been applied as sacrificed soft templates. Various MoS_2/carbon particles have been thus prepared, exhibiting a variety of tailored morphologies.

2) To evaluate their catalytic reduction activity with the assistance of near infrared (NIR) light irradiation, their photothermal conversion performance has been first compared under the light irradiation. The dispersion temperature variation has been tracked by a digital thermometer as well as an IR camera. Finally, their catalytic reduction in the absence/presence of NIR light irradiation have been conducted.

Article Ⅲ: A straightforward strategy for the synthesis of GP-CNTs-metal composites have been presented. A versatile GP biomolecule has been used not only as a reducing agent for the *in situ* generation of metal NPs but also as a stabilizer for both CNTs and metal NPs in aqueous solution. The GP-CNTs-metal composites have been ultimately utilized for the degradation of 4-NP.

1) To prepare a homogenous dispersion of CNTs in water, GP has been used as a green amphiphilic dispersant. In addition to the diluted dispersion, GP-CNTs in various states

can be consecutively achieved by simply increasing their concentrations in water. In the absence of any additional reducing agents, a variety of noble metal ions could be directly reduced to metallic NPs (*e.g.* Au, Ag, Pt, and Pd) by GP molecules at room temperature, and subsequently *in situ* immobilized on the surface of CNTs.

2) To study their catalytic performance, the GP-CNTs loaded with metal NPs have been subsequently used as catalysts for the fast catalytic degradation of 4-NP with the help of NIR light irradiation.

2 Theory

2.1 Self-assembly of PIL particles

2.1.1 Synthetic strategy of PILs

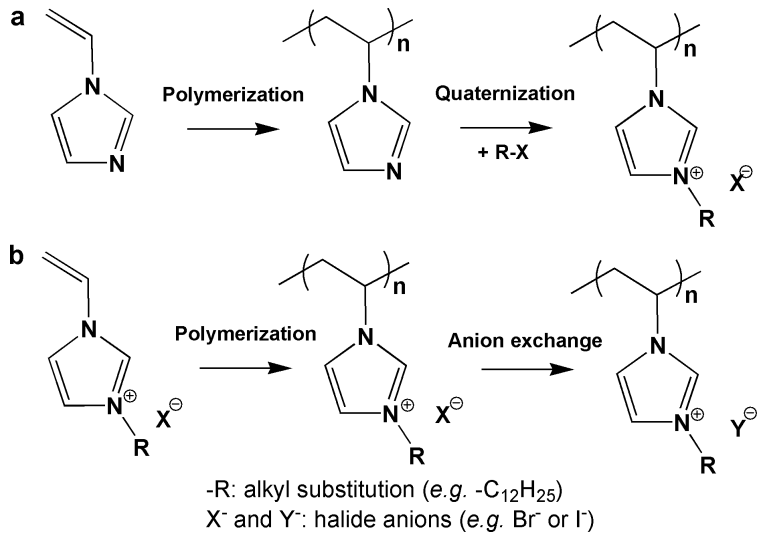

Figure 2.1.1. Typical synthetic routes for imidazolium-based PILs: (a) polymerization of non-ionic monomers followed by quaternization and (b) direct polymerization of IL monomers with subsequent anion exchange to obtain the desired PILs.

The synthetic strategy towards PILs from their IL monomers can be classified into two approaches (**Figure 2.1.1**): polymerization of existing non-ionic monomers followed by post-modification of the obtained polymers (*Route a*) and direct polymerization of IL monomers (*Route b*). *Route a* allows a huge diversity in the molecular design of PILs through various polymerization techniques. The ionization of neutral polymers is further realized by quaternization reaction. Taking imidazole-based PILs as an example, the neutral poly(1-vinylimidazole) is first polymerized from its 1-vinylimidazole monomer or even received as purchased. Afterwards, alkyl substitution reactants attack the N3-site in the imidazole rings, thus forming the charged PIL products. However, the quaternization yield is hard to reach 100 %, thus leading to the original uncharged block remaining in the ultimate polymer chains.

Alternatively, direct polymerization of IL monomers shows much higher purity of targeted PILs (*Route b*). The vinylimidazolium specie is first converted to the IL monomers, followed by polymerization under appropriate conditions. The counter ions in PILs can be replaced *via* anion exchange. Similar to the post-modification method, the impurity issue still exists if a different

counter ion is required. Therefore, it is significant to design the targeted counter ion in the initial step of monomer synthesis. In terms of polymerization technique, direct polymerization of IL monomers can be conducted *via* radical polymerization. This involves conventional free radical polymerization and controlled radial polymerizations including reversible addition-fragmentation chain transfer polymerization (RAFT) and atom transfer radical polymerization (ATRP).[67, 68] Despite the latter two methods having been demonstrated effective to control the molecular weight distribution of the obtained polymers, their relatively tedious synthesis could impede the scalable production of PILs. Alternatively, free radical polymerization has been demonstrated to be a straightforward and robust method for the synthesis of various PILs.

2.1.2 Self-assembly of PILs *via* dispersion polymerization

To construct a stable colloidal system, additional repulsive interaction such as steric or electrostatic interaction among colloidal particles is needed to compromise Van der Waals attraction.[69] The Derjaguin-Landau-Verway-Overbeck (DLVO) theory is commonly used to quantitatively analyze the aggregation behavior of colloidal particles. The DLVO theory describes the sum of Van der Waals attraction (G_A) and electrostatic repulsion (G_R) as a function of the distance (h) between two particles.[70, 71] For two ideal spherical particles with an identical diameter (R) at a certain h, the G_A and G_R can be described as below:

$$G_A = -\frac{A_H R}{12h} \tag{2.1.1}$$

$$G_R = -\frac{RkT\kappa}{12} e^{-\kappa h} \tag{2.1.2}$$

where A_H, k, T, and κ are the Hamaker constant, Boltzmann constant, system temperature, and Debye-Hückel parameter, respectively. Therefore, the total potential energy (G) can be given by:

$$G = G_A + G_R = \frac{A_H R\kappa}{12}\left(\frac{bkT}{A_H} e^{-\kappa h} - \frac{1}{\kappa h}\right) \tag{2.1.3}$$

$$b = -\frac{384\pi\gamma^2 n}{\kappa^3} \tag{2.1.4}$$

where γ and n are reduced surface potential and the total number of charge density, respectively. The plot of G as a function of h is depicted in **Figure 2.1.2**. When two particles initially approach

each other from an infinite distance, the attraction interaction dominates during this period until reaching a reverse aggregation point (second minimum well). At distances closer than this reverse point, the Van der Waal attraction force becomes more intense than the repulsion force. Once the energy barrier is overcome, typically through thermal energy or external forces, the particles come into close contact and irreversibly aggregate, leading to particle growth and potentially even macroscopic sedimentation. Therefore, the colloidal stability of dispersed polymer particles mainly depends on the concentration of the particle dispersion, nature of dispersed particles (size, shape, and charge amount), solvent quality (ionic strength and polarity), and so on. These factors can collectively affect the balance between attractive and repulsive forces, ultimately determining the kinetics of particle aggregation.

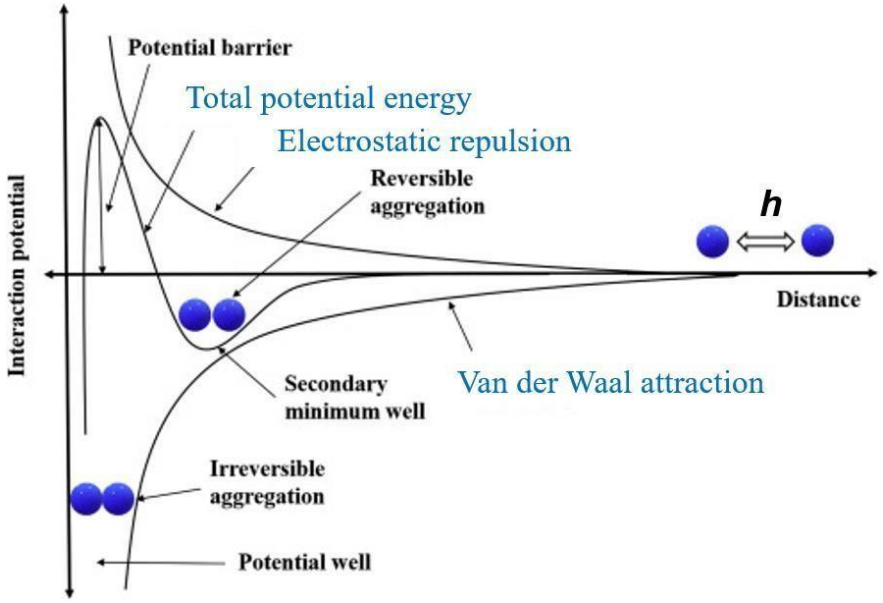

Figure 2.1.2. DLVO theory described by a sum of the attractive and repulsive forces as a function of the distance. Reproduced with permission. Copyright 2022, Elsevier.[70]

To prevent the particle aggregation, additional amphiphilic molecules have been introduced as the stabilizer in the dispersion to provide essential repulsive forces for the formation of stable colloids. The physical adsorption or chemical grafting of amphiphilic molecules onto the particle surface leads to the formation of a protective layer, known as a steric or electrostatic barrier. In case of PIL dispersions, charged PILs usually exhibit inherently electrostatic repulsion and thus require no external stabilizer for the preparation of colloidal particles. From the perspective of the driving force for the self-assembly, the electrostatic interaction from their charged backbone also endows

them with richness and distinction in the self-organization activity. Crucial factors include the chemical nature of PILs, polymerization conditions, and external additives, *e.g*. crosslinking or salting-in effects.

2.1.2.1 Charged backbones

Charged backbone, as the most fundamental component of PILs, highly influence the solubility of PILs in water or organic medium. A subtle difference in hydrophilicity of charged backbones could alter the surface preference or energy of the entire PIL particles, thus determining the surface as well as internal structure. For example, replacing the imidazolium with the more hydrophilic triazolium backbone in PILs could give rise to the formation of "wasp-like" PIL particles (**Figure 2.1.3a-b**). Compared with imidazolium cations, the triazolium counterparts are demonstrated to show higher affinity with water medium *via* proton exchange. More exposure of the internal hydrophobic part thus enables the elongation of PIL particles.[72]

2.1.2.2 Side chain

Considering the highly hydrophilic feature of centered backbones, a hydrophobic side chain is thus needed for driving the self-aggregation process of polymeric IL chains. A practical approach towards the formation of PIL assembles is to modulate the type or length of their side chains, as shown in **Figure 2.1.3a** and **c**. When it comes to the vinylimidazolium-type PILs with hydrophobic side chains, PIL chains can segregate into assembly nanoparticles *via* simple free-radical polymerization in water. When the side chain length increases above a critical value, the side chain could also undergo crystallization during the assembly process, which further induces the formation of an anisotropic PIL particle instead of a standard spherical geometry. Although a long alkyl or aromatic tail is beneficial for the microphase separation, excessively long hydrophobic side chain could also lead to the low solubility of IL monomers in water, thus preventing the subsequent polymerization process. In addition, high hydrophobicity of the propagating PIL chains could result in a fast particle nucleation and thus a relatively small size of final PIL particles.[73, 74]

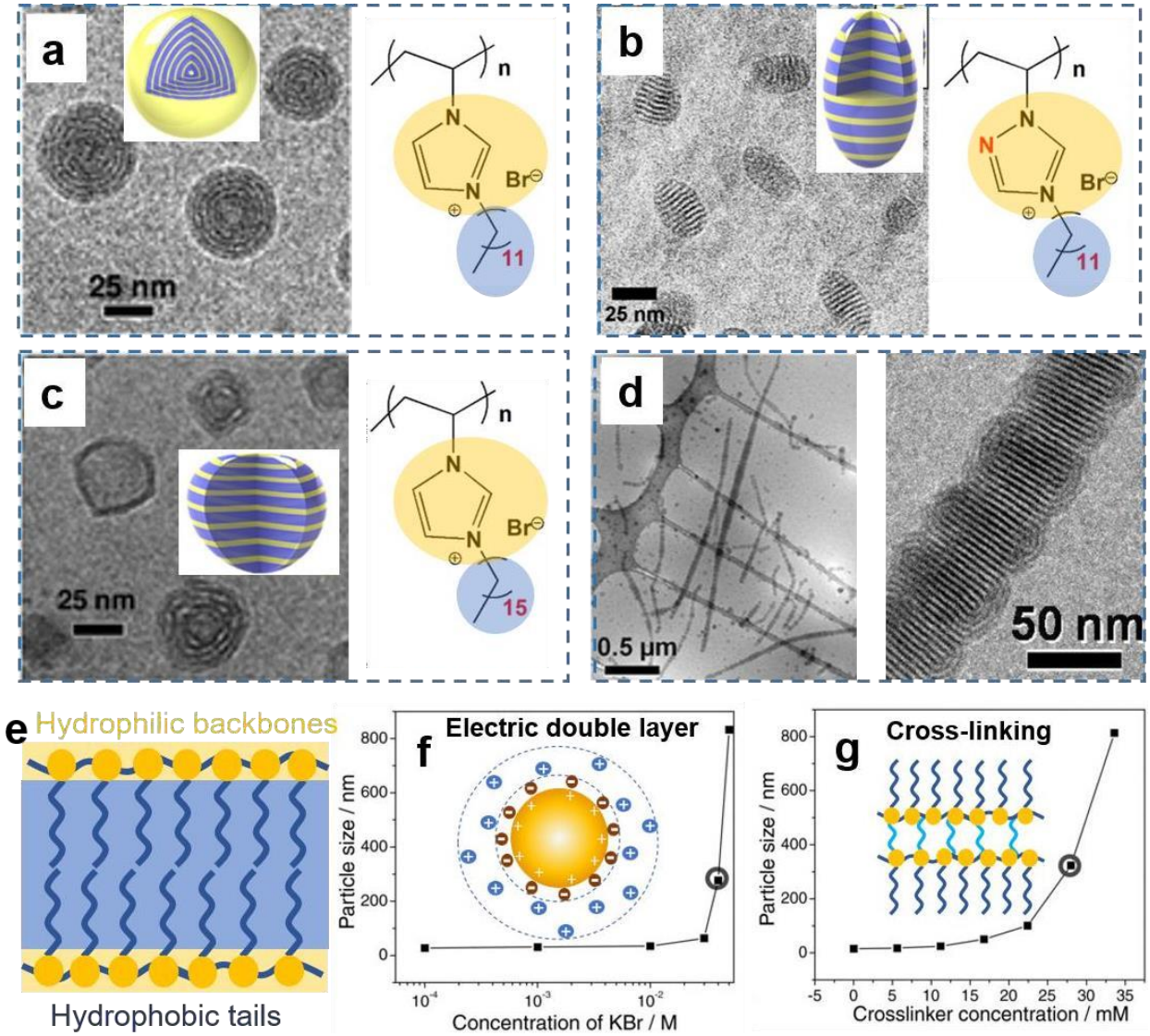

Figure 2.1.3. Featured PIL particles prepared under various conditions: (a) Imidazolium-based and (b) triazolium-based PILs with a *n*-dodecyl side chain (C12). Reproduced with permission. Copyright 2011 and 2016, American Chemical Society.[12, 72] (c) Imidazolium-based PILs with a *n*-hexydecyl chain (C16).[12] (d) Imidazolium-based PILs were prepared at an extremely high monomer concentration of 50 mg/mL. [12] (e) Scheme of the possible packing mechanism of the PIL molecular bilayer. (f) The particle size of PILs as a function of the concentration of additional KBr salts. The inset is a scheme of the compressed electric double layer. (g) Particle size as a function of the cross-linker concentration. The inset is a scheme of the cross-linked molecular bilayer.[74] Reproduced with permission. Copyright 2012, WILEY-VCH.

2.1.2.3 Polymerization conditions

Polymer assembly is usually sensitive to the polymerization kinetics that can be correlated by the type and amount of used initiator, polymerization temperature, and initial monomer concentration. Nevertheless, the former two have been reported to exert little influence on the assembly behavior of PILs. On the contrary, monomer concentration has been reported to strongly impart the assembly behavior of PIL particles. The transformation from a zero-dimensional sphere to a one-dimensional rod of PILs has been realized by polymerizing IL monomers at a high concentration. When polymerizing at extremely high monomer concentrations, both the size and number of PIL particles drastically increase. When the charged particles come closer and the distance between each other becomes narrow until a critical value, the strong Van der Waal force induced by charge polarization would facilitate the alignment organization of the neighboring PIL particles owing to the liquid feature of their internal space (**Figure 2.1.3d**).[73] For these PILs with hydrophobic side chains (*e.g.* long alkyl chains), a typical bilayer packing model often occurs as a general molecular organization of the polymer chains (**Figure 2.1.3e**). This ordered lamellar architecture can be identified by small-angle X-ray scattering (SAXS) or cryogenic transmission electron microscopy (cryo-TEM). In the cryo-TEM images, the lighter lamellae domain comes from the hydrophobic alkyl substituent, while the darker rings result from the polymer backbones that commonly exhibit higher electron density of ion pairs.

2.1.2.4 Additives

Adding external salt and cross-linker has been proven to impact the assembly of PIL particles. Different from the conventional neutral polymer candidates, additional electrostatic interaction with other metal or inorganic ions enriches the self-assembly behavior of PILs (or polyelectrolytes) owing to their highly charged backbones and surrounding counter ions. Upon introducing a slight amount of external electrolyte during PIL polymerization, the PIL particles could drastically expand in size due to the weakened electrostatic double layers (decreasing the amount of surface charge), as shown in **Figure 2.1.3f**. Another approach toward tuning the particle size of PILs is to add a cross-linker in the polymerization. Chemical cross-linking is often adopted in the assembly of PIL particles using dual-functional vinyl-based monomers for copolymerization (**Figure 2.1.3g**). Limited chain mobility gives rise to the fast self-organization process as well as an obvious increase in final particle size.[74]

Hence, the use of PILs in one-pot polymerization processes offers a wide range of possibilities for the customization of assembled polymer particles. Desired structures and properties can be realized by tuning the molecular structure of IL monomers or polymerization conditions. This allows for precise control over the size, shape, and composition of the resulting particles, making PILs a promising candidate as the soft template for various applications.

2.2 Self-assembly of BCPs

BCPs stand out as a prominent example of self-assembly due to their adjustable phase behavior, especially when incorporating different moieties with distinctive interactions with other medium.[75, 76] The methodology for building up a unique molecular architecture of BCP for hierarchical interaction has become another emerging topic and raised widespread interest in polymer assembly. The phase behavior of a given BCP molecule strongly relies on the thermodynamic of the entire system. Herein, we take diblock copolymer (A-*b*-B) as an example and assume A is the selective minority block (*e.g.* solvophobic). The relative mass/volume fraction (f), the polymerization degree (N), and the Flory-Huggins interaction parameter (χ_{AB}) are the key parameters that direct their self-assembly process. Among them, χ_{AB} can be given by the following equation:

$$\chi_{AB} = \frac{z}{k_B T}\left[\varepsilon_{AB} - \frac{1}{2}(\varepsilon_{AA} + \varepsilon_{BB})\right] \quad (2.2.1)$$

where T, z, and k_B are the system temperature, Boltzman constant, and coordination number, respectively. ε_{AB}, ε_{AA}, ε_{BB} are the interaction energies of each block, respectively. The value of $\chi_{AB}N$ describes the incompatibility degree of the block A and B, thus determining the microphase separation behavior.[14] Based on self-consistent field theory (SCFT), its phase diagram ($\chi_{AB}N$ as a function of f_A) can be depicted, as shown in **Figure 2.2.1a**.[77] As f_A increases, the morphology of BCP correspondingly evolves from spheres (SPH), to cylinders (CYL), gyroids (GYR), and finally to lamellae (LAM). Specifically, when the BCP molecules are exposed to a selected solvent at a low f_A, the solvopholic block A are confined within the center of segregated domains. While, the solvophilic block B (higher fraction in the entire BCP chain) tends to actively interact with the surrounding medium, leading to the formation of SPH. Increasing f_A of BCP results in a closely packing of solvophobic block A, inducing the formation of CYL. When f_A further rises up to ~ 0.5, a highly ordered lamellar organization forms. The block A presents in most aggregated state in

this stage. On the contrary, the solvophilic block B interacts least with solvent and transfers into a least energetically favorable state. In addition to the segregated structure, the size of the segregated domains (a) can be expressed by:

$$a \approx l\,\chi_{AB}^{1/6}\,N^{2/3} \tag{2.2.2}$$

where l is the statistical segment length.[78] Therefore, the formation of segregated domains with a relatively small size is favored when using a BCP with a high χ value but low N. By carefully selecting the appropriate BCP composition and controlling the synthetic conditions, a desired nanostructure with suitable segregated size could be achieved in the BCP self-assembly system.

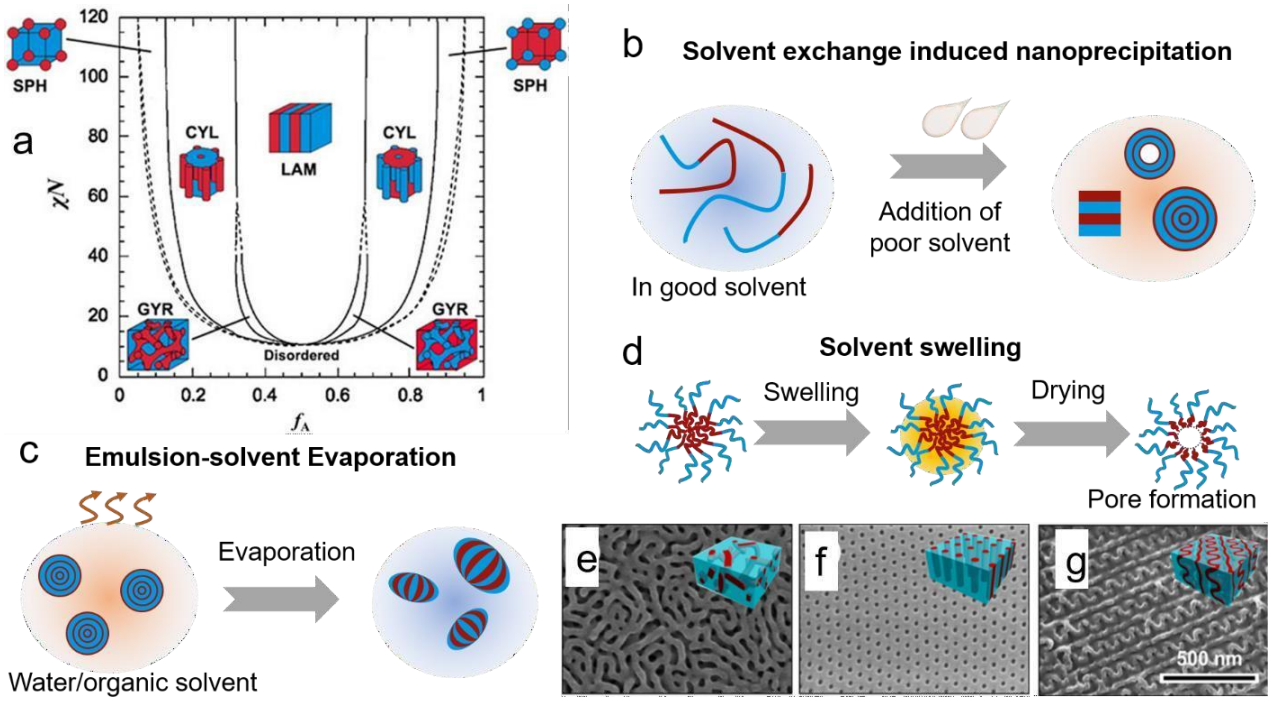

Figure 2.2.1. (a) Phase diagram of the self-assembly morphology of BCP. Reproduced with permission. Copyright 2022, Frontiers Media S.A.[77] Scheme of the solvent variation methods: (b) solvent exchange induced nanoprecipitation, (c) emulsion-solvent evaporation, and (d) solvent swelling. Porous PS-*b*-P2VP films prepared by selective swelling in ethanol: (e) bicontinuous pores, (f) standing pores, and (g) gyroidal pores. The inset are corresponding models before swelling. P2VP and PS block are highlighted in red and blue, respectively. Reproduced with permission. Copyright 2019, American Chemical Society.

From the perspective of experimental conditions, featured BCP assemblies are directly related to synthetic methods, which are generally determined by factors including their component, surface chemistry, space size, and geometric conformation.[79] These factors have been intensively

investigated by studying the dispersions of polymer colloids. To date, several significant synthetic strategies of nanostructured BCP particles have been proposed, which can be mainly divided into the following strategies: solvent variation, template-assisted method, and polymerization-induced assembly.

2.2.1 Solvent variation

As discussed above, solvent quality plays a pivotal role in the morphology formation or transformation of BCPs. The corresponding phase behavior of BCPs relies on the interaction between polymer and polymer chains or polymer and solvent, which can be altered through removing the original solvent or tuning the solvent component by introducing additional solvents. The Hansen solubility parameter (δ_i) of a selected block can be calculated from the sum of dispersion force (δ_d), dipolar force (δ_p), and hydrogen bonding (δ_h) as below:

$$\delta_i = (\delta_d + \delta_p + \delta_h)^{1/2} \tag{2.2.3}$$

Next, the total solubility parameter (δ_t) of BCPs can be estimated by:

$$\delta_t = x_A\delta_A + x_B\delta_B \tag{2.2.4}$$

where x_A and x_B are the corresponding molar ratio of block A and B, respectively.[80, 81] To maximize the dissolution of a given BCP in a selected solvent, their solubility values needs to be well-matched. Also, the deviation between a specific block of BCPs and solvent could trigger the reorganization of BCP chains. In terms of experimental synthesis, several significant strategies have been developed typically including emulsion-solvent evaporation, solvent exchange induced nanoprecipitation, and solvent swelling method.

In solvent-exchange induced nanoprecipitation method, the selected BCP has to be first dissolved in a good solvent to form a homogenous polymer solution (**Figure 2.1.1b**). Afterwards, a relatively poor solvent is introduced, thus leading to a rapid solution exchange. This solvent variation could trigger the phase separation and the polymer chains gradually precipitate out as dispersed particles in the mixture solvent. During the solvent exchange from a good to poor solvent, the interaction between polymer chains and solvent medium becomes slightly weakened and enhances the incompatibility between polymer chains and surrounding medium[5]. Especially, different blocks of

BCPs show different affinity to the good or poor solvent. Therefore, the final morphology of polymer particles relies on the nature of the used polymers, ratio of poor/good solvent, and so on.[82]

Emulsion-solvent evaporation is another widely used strategy for the preparation of nanostructured BCP assemblies (**Figure 2.2.1c**).[83-85] Desired components such as polymer blends or BCPs are first dissolved in a suitable (organic) solvent that is usually immiscible with water. Afterwards, the mixture solution is emulsified into colloidal particle or droplets (with primary nanostructures) with the assistant of additional surfactants. Then, nanostructured polymer particles can be obtained after removing the organic solvent at specific temperature. During vaporing process, the diffusion rate of the organic solvent in each domain of BCPs directly determines the chain movement of selective blocks including stretching, mobility, or orientation.[86, 87] Therefore, the formation or transformation of (secondary) nanostructure of BCPs collectively depends on solvent composition and evaporation rate.

Similar to emulsion-solvent evaporation method, solvent swelling requires BCP to be in the form of thin film or colloidal particles in a medium (**Figure 2.2.1d**). Afterwards, the solvent composition is changed by adding or replacing to a good solvent, thus inducing the morphology change. Taking polystyrene-*b*-poly(2-vinylpyridine) (PS-*b*-P2VP) as example, good solvents such as ethanol or chloroform are often used to swell PVP block. Cylindrical PVP blocks are randomly distributed in PS matrix before swelling. Slight swelling in ethanol results in the formation of bicontinuous nanopores after evaporating ethanol (**Figure 2.2.1e**). While, replacing ethanol with 1, 1, 2-trichloroethane could induce the perpendicular orientation of PVP block along the film plane, finally leading to the formation of well-ordered cylindrical hollow channels (**Figure 2.2.1f**). Moreover, a unique gyroid phase of PS-*b*-P2VP was first obtained owing to the intense hydrogen interactions between the solvent and PVP block. Thus, an ordered gyroidal pore was preserved after swelling (**Figure 2.2.1g**). Considering that the Flory-Huggins interaction parameter is also strongly affected by the environment temperature according to the equation (2.2.1), further elevating the environment temperature could promote the uptake of good solvent molecules into selected PVP blocks. In addition, the chain movement of the selected blocks leads to a partial plastic deformation of BCP, driven by the local osmotic pressure. Compared with the abovementioned two means, selective swelling method is relatively easier to control without

precise control over solvent kinetics. Particularly, porous or hollow nanostructures can be obtained using this swelling strategy after finally removing the solvent.

2.2.2 Template-assisted engineering

An interesting strategy towards nanostructured BCP particles is to induce microphase separation of a multicomponent system within a confined space.[88] Template synthesis is especially promising because various unique structures can be directly synthesized by simple processes of materials growth and replication in the inner space or surface of the template. Moreover, the surface/internal structure of BCPs can be further tuned by solvent composition, addictive, and the chemical nature of polymers.

Anodic aluminum oxide (AAO) membrane owing to its well-defined geometry, is considered as an ideal template for the formation of versatile internally nanostructured BCP particles.[89-91] Normally, AAO template presents a strong attraction for BCP solution filtration due to the high surface energy of the hydroxylated wall (**Figure 2.2.2a**). The interfacial interaction between AAO nanochannels and a given BCP is strongly influenced by the BCP concentration, solvent quality, and volume faction of a selected polymer block. In addition, the physical confinement effect could lead to the entropy loss of the entire BCP system, thus inducing the assembly of polymer chains to a segregated microdomains. Therefore, the ratio of its diameter (D_0) and length (L_0) is another key parameter to direct the self-assembly behavior of BCPs inside the confined hollow channels. Based on Monte Carlo simulation (**Figure 2.2.2b**), the morphology of a given diblock polymer (the volume fraction of the minority block is 0.25) was found to vary with the ratio of D_0/L_0 from 0.5 to 4.5, showing a transformation from a string of spheres to a continuous cylinder or discs, and even a single or double helix.[92] At a low ratio of D_0/L_0 (below 1), the polymer chains are strongly compressed due to the confinement effect from the surround AAO wall. While at relatively high ratio of D_0/L_0 (above 1), the sufficient free space of AAO facilitates the fully stretching of BCP chains along the lateral direction, enriching the possibility of molecular organization. Furthermore, the inert surface and wide temperature window (above 500 °C) of AAO allow the investigation of the thermal behavior.[93] For instance, PS-*b*-P2VP nanospheres with a tunable size can form within AAO with a D_0/L_0 ratio above 5 (**Figure 2.2.2c-e**).[94] Upon thermal annealing, nanorods containing regular encapsulated holes were first generated due to Rayleigh instability. Because of the

susceptibility to sonication, these nanorods could be further cut into short rod-like blocks with a uniform size. With an appropriate surfactant and a good solvent to minimize the surface energy, the swollen PS-*b*-P2VP chains deformed and spontaneously transformed into nanospheres.

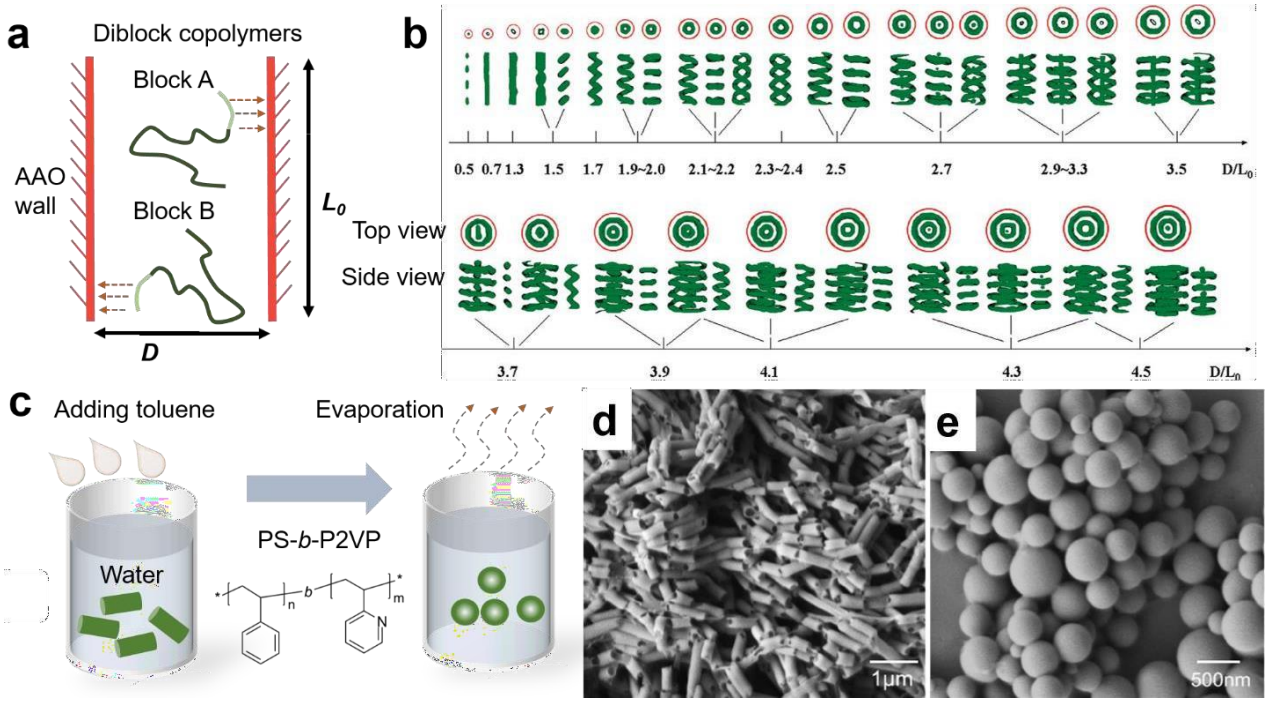

Figure 2.2.2. (a) Scheme of the self-assembly of BCPs inside AAO channels. (b) Assembled morphologies of diblock copolymer within AAO at various ratios of D/L_0 using Monte Carlo simulation. Reproduced with permission. Copyright 2006, American Chemical Society.[92] (c) Scheme of the swelling process for the preparation of PS-*b*-P2VP particles. The corresponding SEM images of structural transformation from (d) nanotubes to (e) nanospheres. Reproduced with permission. Copyright 2011, American Chemical Society.[94]

2.2.3 Polymerization-induced self-assembly

Polymerization-induced self-assembly (PISA) become prevailing due to the combination of polymerization and self-assembly process in one step. Chemical polymerization triggers the physical transformation, thus leading to the formation of versatile nanostructure of BCPs. Many amphiphilic BCPs have been explored to produce colloidal nanoparticles in water or a water-based dispersant.[95] As the polymerization of BCP proceeds, the growing polymer chains become insoluble in water once their polymerization degree (N) is beyond a critical value. The insoluble chains are subsequently swollen by the surrounding monomers and fed by monomer diffusion from

large monomer droplets through the water phase, the growing particles can continue to consume monomers and incorporate the formed polymer chains, leading to the formation of final nanoparticles. From the perspective of polymerization method, there are mainly two groups that are often used for the generation of featured polymer particles. The first group is reversible chain transfer reaction such as RAFT. PISA *via* the RAFT polymerization technique combined the favorable tolerance of the radical process with a controlled chain growth in polymerization.[96, 97] The second one is reversible termination reaction including nitroxide-mediated polymerization (NMP) and ATRP.[98-101] Additional source of macromolecular radicals is not necessarily in NMP or ATRP.[102, 103] The radicals can be produced through the thermal activation of an alkoxylamine or halogen-carbon bond with a metallic complex. In both cases, BCPs with desired chain structure can be controllably synthesized using specific macromolecular radicals, enabling the controllable design and synthesis of BCPs. Various morphologies could be obtained by adjusting the molar masses of both the hydrophilic and hydrophobic blocks, degree of polymerization, solvent composition, and monomer concentration.

In short, solvent composition/kinetics, polymer composition, and environmental responses (pH, temperature, and ionic strength) could influence both the thermodynamics and kinetics of the assembly process. A suitable technique for the microphase separation of BCP chains is paramount for the formation of robust BCP templates with desired nanostructures.

2.3 CO_2 electrochemical reduction using metal particles as catalyst

CO_2 is a typical nonpolar molecule that exhibits chemically inert and stable under normal conditions. As the carbon atom in the CO_2 molecule is at the highest formal oxidation state, and its conversion to reduced products with high energy densities requires the transfer from additional electrons to the carbon atom.[104] A mixture of gaseous and or liquid products instead of a single product tends to be generated *via* CO_2ER. To assess the selectivity of a specific product (*e.g.* H_2, CO, CH_4, and C_2H_4) during CO_2ER, Faradaic efficiency (FE) is an important parameter that can be explained by:

$$FE\ (\%) = \frac{m \cdot x \cdot F \cdot f}{i} \cdot \times\ 100\% \qquad (2.3.1)$$

where *x* is the mole fraction of the product, *m* is the electron transfer number that is required to generate a given product from CO_2, *f* is the gas flow rate, *i* is the total current, and *F* is the Faradaic constant (96485 C/mol).

Combining with Henry's Law, all the standard potentials (*E*) of the resulted products can be calculated through the Gibbs free energy of each reaction. The commonly reported products and corresponding equilibrium potentials are shown in **Table 2.3.1**. As a typical electrochemical reaction, reduced products are produced at the cathode, while the oxygen generation reaction proceeds at the anode (**Figure 2.3.1a**).

Table 2.3.1. Various products and the corresponding potentials *via* electrochemical reactions. Reproduced with permission. Copyright 2017, WILEY-VCH.

Reaction	**E/(V *vs.* RHE)**	**Product**
$2H^+ + 2e^- \rightarrow H_2$ (g)	0	Hydrogen (H_2)
$2H_2O \rightarrow O_2 + 4H^+ + 4e^-$	1.23	Oxygen (O_2)
$CO_2 + 2H^+ + 2e^- \rightarrow$ HCOOH (aq)	-0.12	Formic acid (HCOOH)
$CO_2 + 2H^+ + 2e^- \rightarrow$ CO (g) + H_2O	-0.10	Carbon monoxide (CO)
$CO_2 + 6H^+ + 6e^- \rightarrow CH_3OH$ (aq) + H_2O	0.03	Methanol (MeOH)
$CO_2 + 8H^+ + 8e^- \rightarrow CH_4$ (g) + $2H_2O$	0.17	Methane (CH_4)
$CO_2 + 12H^+ + 12e^- \rightarrow C_2H_4$ (g) + $4H_2O$	0.08	Ethylene (C_2H_4)
$CO_2 + 14H^+ + 12e^- \rightarrow C_2H_6$(g) + $4H_2O$	0.14	Ethane (C_2H_6)
$2CO_2 + 12H^+ + 12e^- \rightarrow C_2H_5OH$ (aq) + $3H_2O$	0.09	Ethanol (EtOH)
$3CO_2 + 18H^+ + 18e^- \rightarrow C_3H_7OH$ (aq) + $5H_2O$	0.10	Propanol (PrOH)

The reaction mechanism of the product can be affected by many parameters, such as the reaction condition (*e.g.* local pH, temperature, and gas pressure), electrolyte, and electrocatalyst (*e.g.* geometry, crystal face, and size), thus determined the reaction pathways.[53] The selectivity of specific products mainly depends on the binding energies of the corresponding reaction intermediates on the active sites of the metal catalysts. For example, metallic Tin (Sn) and Lead (Pb) mainly produce formic acid ($HCOO^-$) in aqueous solution due to the weak binding between the $CO_2^{\bullet-}$ intermediates with their surface. On the contrary, the CO is the main product of Ag, Pd, and Au metals since their tight binding capability with the formed *COOH intermediates but weak adsorption with the *CO species. The CO formation mainly proceeds through the following steps:

$$CO_2(g) + H^+(aq) + e^- \rightarrow COOH \quad (2.3.2)$$

$$COOH + H^+(aq) + e^- \rightarrow * CO + H_2O(l) \quad (2.3.3)$$

$$* CO \rightarrow CO(g) \quad (2.3.4)$$

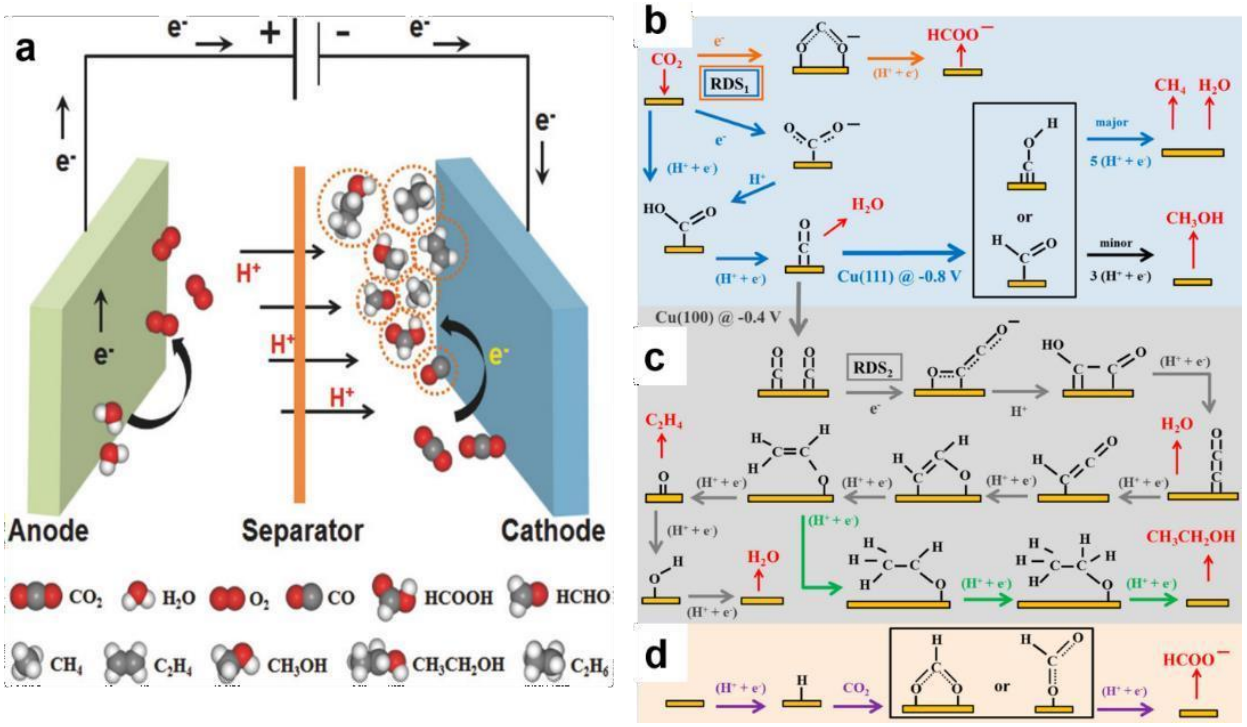

Figure 2.3.1. (a) Scheme of a typical CO_2ER with various generated products. Reproduced with permission. Copyright 2017, WILEY-VCH.[104] Possible reaction routes for the formation of various products in CO_2ER using Cu as catalysts: (b) methane and methanol, ethylene and ethanol, and (d) formic acid. Reproduced with permission. Copyright 2015, American Chemical Society.[105]

Particularly, Cu metal is capable of generating various products including alcohols, CO, even other long-chain hydrocarbons. This is predominantly because the *CO intermediates can tightly bind on the Cu surface and subsequently dimerize with *COH or *CHO intermediates, thus ultimately generating other products. Concretely, the adsorbed CO_2 molecules will form into $CO_2^{\bullet-}$ intermediate that is quickly desorbed into $HCOO^-$ in the aqueous solution, as revealed in **Figure** 2.3.1**b-d**. In this process, the formation of $CO_2^{\bullet-}$ is a rate-determined step (RDS). When it comes to the multiple electrons transfer reaction, such as methane (CH_4) or ethylene (C_2H_4) generation, the reaction steps become more complicated and could run in various reaction routes. For CH_4 generation, $*COO^-$ or *COOH intermediate is generated and transformed into the most important CO intermediate. Afterwards, the CO intermediate will be reduced to a *CHO or *COH specie

and finally reduced to methane. For C_2 product (*e.g.* C_2H_4) formation, the C-C coupling reaction for the multi-carbon product formation is realized by CO dimerization. This dimerization is the key RDS for the subsequent generation of $*C_2O_2^-$ intermediate as well as the reduction of CO.

Thus, the development of an efficient catalyst system with high catalytic activity is crucial to improve the current density and selectivities towards valuable hydrocarbon products, particularly valuable CH_4 and C_2H_4 in CO_2ER.

2.4 Reduction reaction of 4-nitrophenol

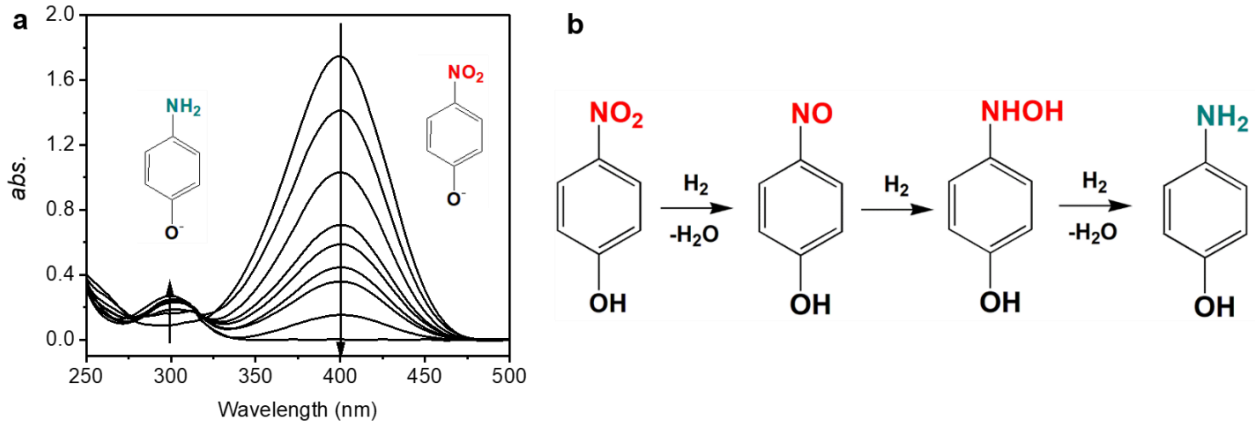

Figure 2.4.1. (a) A set of typical UV-Vis absorption spectra of the reduction of 4-nitrophenol. (b) Possible reaction routes for the reduction of 4-nitrophenol using an excess amount of $NaBH_4$ as reducing agent.

In the reduction reaction of 4-NP, a suitable catalyst and reducing agent are needed. The most common reducing agent for the reduction of 4-NP is $NaBH_4$. The reaction process in an aqueous solution can be recorded by UV-Vis absorption spectroscopy. In **Figure 2.4.1a**, a set of typical UV-Vis absorption spectra of the 4-NP reduction shows the adsorption intensity as a function of reaction time. When the reaction takes place under alkaline conditions, the reactant 4-NP will be first deprotonated into nitrophenolate ions, which exhibit a distinct absorption peak at 400 nm. After reduced by $NaBH_4$, nitrophenolate ions are progressively converted to 4-aminophenol (4-AMP), which shows an absorption peak located at *ca.* 300 nm. Eventually, a disappearing intensity of the absorption peak at 400 nm demonstrates the completion of the reduction of 4-NP. In addition to the two distinctive peaks resulting from reactant and product, the presence of isosbestic points

at *ca.* 280 and 310 nm in the UV-Vis spectra point out that no side reactions take place or possible byproducts are generated.

It should be noted that due to the electrostatic strong repulsion between negative nitrophenolate and BH_4^- ions, direct reduction without the catalyst is a kinetically unfavorable process. It has been demonstrated that the reduction of 4-NP mainly proceeds on the surface of the catalyst, which is supported by the classical Langmuir - Hinshelwood (LH) model. According to the LH model, an ideal catalyst needs to provide a sufficient reaction surface for the adsorption of nitrophenolate ions. Meanwhile, BH_4^- ions will transfer surface-hydrogen species onto the surface of catalyst particles. Subsequently, the adsorbed nitrophenolate ions are reduced by the surrounding hydrogen species. During the reduction, two reaction intermediates, 4-nitrosophenol and 4-hydroxylamine (H_x) will be generated, as shown in **Figure 2.4.1b**. H_x is relatively stable compared to 4-nitrosophenol. The formed H_x is ultimately reduced to the stable product 4-AMP, which subsequently desorbs and diffuses from the catalyst surface to the bulk solution.

The overall reaction process can be summarized into two steps. Step A: reduction of 4-NP to H_x. Step B: reduction of H_x to 4-AMP. To establish an overall kinetic model for this reduction reaction, two significant assumptions are often made. Firstly, reactant molecules adsorbed on the catalyst surface are assumed to be negligible compared to those in the bulk solution, implying that the adsorption process hardly affects the total concentration of 4-NP. Secondly, it is assumed that the adsorption/desorption equilibrium between the bulk solution and catalyst surface can be rapidly achieved. Therefore, the reduction kinetics for step A can be expressed by:

$$-\frac{dc_{NP}}{d_t} = k_{app}c_{NP} = k_A S\theta_{NP}\theta_{BH_4} = \frac{dc_{Hx}}{dt} \quad (2.4.1)$$

$$-\frac{dc_{NP}}{d_t} = k_A S \frac{(K_{NP}c_{NP})^n K_{BH_4}c_{BH_4}}{(1+(K_{NP}c_{NP})^n + K_{H_x}c_{H_x} + K_{BH_4}c_{BH_4})^2} \quad (2.4.2)$$

where c_{Hx}, c_{BH4} and c_{NP} are the concentration of H_x, BH_4^-, and 4-NP, respectively. θ_{NP} and θ_{BH4} refer to the actual coverage fraction of the catalyst surface by 4-NP and BH_4^-, respectively. S represents the specific surface area of the catalyst normalized by the total volume of reaction dispersion. k_{app} and k_A are the apparent rate constant and the overall reaction rate of step A normalized by S, respectively. K_{NP}, K_{Hx}, and K_{BH4} is the corresponding Langmuir adsorption

constant, respectively. *n* stands for the LH exponent, which normally is assigned to be 0.6 for simplification. Likewise, the reduction kinetics of step B can be also described by:

$$-\frac{dc_{Hx}}{d_t} = k_B S \frac{K_{H_x} c_{H_x} K_{BH_4} c_{BH_4}}{(1+(K_{NP} c_{NP})^n + K_{H_x} c_{H_x} + K_{BH_4} c_{BH_4})^2} \quad (2.4.3)$$

where k_B is the overall reaction rate of step B normalized by *S*. Therefore, the overall rate equation for the generation of H_x can be written as below:

$$\frac{dc_{Hx}}{dt} = k_A S \frac{(K_{NP} c_{NP})^n K_{BH_4} c_{BH_4}}{(1+(K_{NP} c_{NP})^n + K_{H_x} c_{H_x} + K_{BH_4} c_{BH_4})^2} - k_B S \frac{K_{H_x} c_{H_x} K_{BH_4} c_{BH_4}}{(1+(K_{NP} c_{NP})^n + K_{H_x} c_{H_x} + K_{BH_4} c_{BH_4})^2} \quad (2.4.4)$$

It has been reported that step B (*i.e.* conversion of H_x to 4-AMP) is the rate-determining step of the overall reduction reaction. Therefore, k_A is usually much larger than k_B. Also, these kinetics models directly correlate the concentration of the reactant and reducing agent, which can be used for the comprehensive study of reaction kinetics from the standpoint of both simulation and experiment.

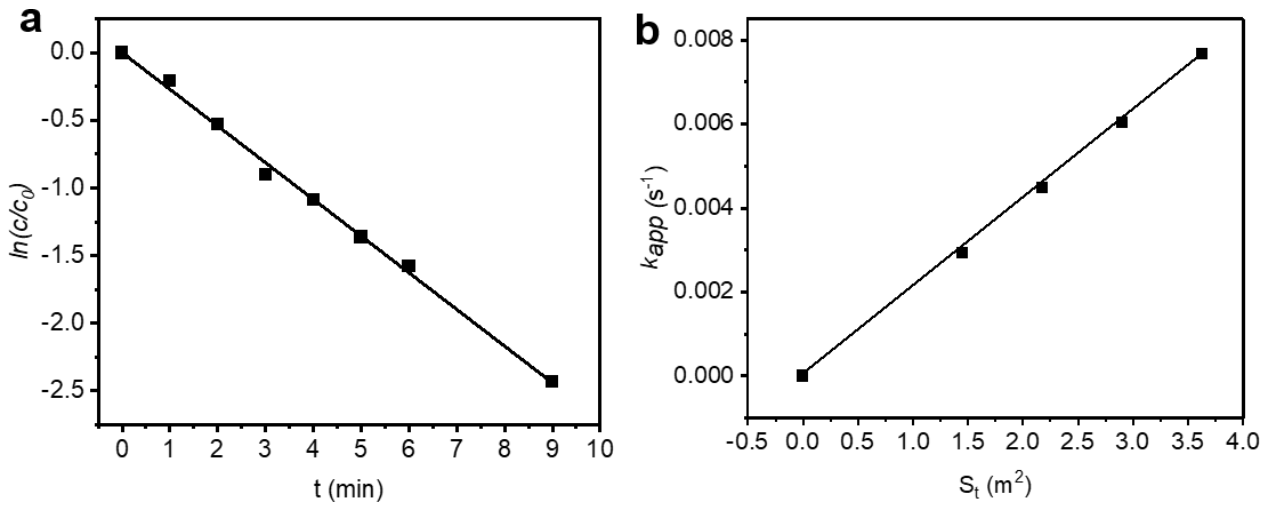

Figure 2.4.2. (a) The linear relationship between $ln(c/c_0)$ and *t* obtained from the reduction reaction when using an excess amount of $NaBH_4$ as the reducing agent. (b) k_{app} as a function of the total surface area S_t of the catalyst particles.

Two kinetic constants, the apparent rate constant (k_{app}) and surface area-normalized rate constant (k_1), are essential for the quantitative evaluation of the catalytic activity of various catalysts.[106] The reactant concentration is correlated with reaction time. According to Beer-Lambert law, the reactant concentration is proportional to the absorption intensity in UV-Vis spectroscopy. Besides,

when introducing an excess amount of the $NaBH_4$ (**Figure 2.4.2a**), the reduction of 4-NP follows a pseudo first-order law, as shown in the equation (2.4.5):

$$ln\frac{c}{c_0} = ln\frac{I}{I_0} = -k_{app}\,t \qquad (2.4.5)$$

where c and c_0 are the 4-NP concentration, I and I_0 are the absorption intensity at 400 nm at a given reaction time t, and the corresponding initial intensity, respectively. k_{app} can be directly calculated from the linear relationship between $ln(I/I_0)$ or $ln(c/c_0)$ and t.

Considering that the reduction of 4-NP is mainly conducted on the surface of the catalyst particles. The k_{app} is thereby proportional to the total active surface area (S_t) of the catalyst particles used in the reaction, as shown in **Figure 2.4.2b**. The surface area-normalized k_1 can be given by:

$$k_{app} = k_1 S_t \qquad (2.4.6)$$

If we assume the catalyst particles used in the reduction reaction are ideally spheres, S_t can be calculated according to the total mass of catalyst particles estimated from TGA measurement and their average diameter calculated from HRTEM analysis.

3 List of Articles

This cumulative thesis is mainly composed of the following three articles. They have been drafted, revised, and completed during my doctoral time at Helmholtz-Zentrum Berlin and the University of Potsdam. My contribution to each work has been specified in detail in the following sections.

I. **X. Pan**, Z. Kochovski, Y. Wang, R. M. Sarhan, E. Härk, S. Gupta, S. Stojkovikj, G. A. El - Nagar, M. T. Mayer, R. Schürmann, J. Deumer, C. Gollwitzer, J. Yuan, and Y Lu, Poly(ionic liquid) nanovesicles via polymerization induced self-assembly and their stabilization of Cu nanoparticles for tailored CO_2 electroreduction, *J. Colloid Interface Sci*. **2023**, 637, 408-420.

II. **X. Pan**, R. M. Sarhan, Z. Kochovski, G. Chen, A. Taubert, S. Mei, and Y. Lu, Template synthesis of dual-functional porous MoS_2 nanoparticles with photothermal conversion and catalytic properties, *Nanoscale* **2022**, 14, 6888.

III. **X. Pan**, R. Liu, Z. Yu, B. Haas, Z. Kochovski, S. Cao, R. M. Sarhan, G. Chen, and Y. Lu, Multi-functionalized carbon nanotubes towards green fabrication of heterogeneous catalyst platforms with enhanced catalytic properties under NIR light irradiation, submitted to *Nanoscale*, accepted (DOI: 10.1039/D3NR02607H).

3.1 Poly(ionic liquid) nanovesicles *via* polymerization induced self-assembly and their stabilization of Cu nanoparticles for tailored CO_2 electroreduction

Xuefeng Pan[a,g], Zdravko Kochovski[a], Yong-Lei Wang[a], Radwan M. Sarhan[a], Eneli Härk [a], Siddharth Gupta[b,c], Sasho Stojkovikj[b,c], Gumaa A. El-Nagar[b,d*], Matthew T. Mayer[b], Robin Schürmann [e], Jérôme Deumer [e], Christian Gollwitzer[e], Jiayin Yuan[f*] and Yan Lu[a,g*]

[a] *Department for Electrochemical Energy Storage, Helmholtz-Zentrum Berlin für Materialien und Energie, Hahn-Meitner-Platz 1, 14109 Berlin, Germany.*
[b] *Helmholtz Young Investigator Group: Electrochemical Conversion, Helmholtz-Zentrum Berlin für Materialien und Energie, Hahn-Meitner-Platz 1, 14109 Berlin, Germany.*
[c] *Institut für Chemie und Biochemie, Freie Universität Berlin, Arnimallee 22, D -14195 Berlin, Germany.*
[d] *Chemistry department, Faculty of Science, Cairo University, Egypt.*
[e] *Physikalisch-Technische Bundesanstalt (PTB), Abbestr. 2-12, 10587 Berlin, Germany.*
[f] *Department of Materials and Environmental Chemistry (MMK), Stockholm University, Svante Arrhenius väg 16C, 10691 Stockholm, Sweden.*
[g] *Institute of Chemistry, University of Potsdam, Karl-Liebknecht-Str. 24-25, 14476 Potsdam, Germany.*

This work (**Article I)** has been published in:

J. Colloid Interface Sci. ***2023****, 637, 408-420. (DOI: 10.1016/j.jcis.2023.01.097)*

Contribution to this Article Literature research

Literature research

1. Self-assembly of PILs: the principle of PILs assembly, polymerization methods, and self-assembly behavior of PILs, essential factors for the structural transformation of PIL assembles.

2. Functionalization of PILs with metal particles: synthesis of metal particles, incorporation of metal particles with PILs templates; challenges in size and morphology control.
3. Application in CO_2ER: advancement in CO_2ER; catalyst screen, comparison analysis of Cu-based catalysts the role of PILs in CO_2ER.

Experimental and characterization

1. Self-assembly of PILs: synthesizing IL monomers and corresponding PILs *via* dispersion polymerization; determining their chemical structures by analyzing the NMR results; studying their thermal properties by analyzing the DSC and TGA results; studying the influence of monomer concentration on the final morphology through SEM and TEM; exploring the original structure by analyzing the cryo-TEM results; determining the particle size by DLS; proposing a possible evolution mechanism.
2. Synthesis of the PILs/Cu composites: preparing metallic particles on PILs template by using hydrazine as the reducing agent; optimizing the PILs/Cu synthesis using various PILs templates; analyzing their nanostructures by SEM and TEM; determining the crystal structure of Cu NPs in the PILs/Cu composites by XRD; studying the interaction between Cu and PILs by UV-Vis spectroscopy.
3. Optimization of PILs/Cu for CO_2ER: enhancing the CO_2ER efficiency and current density through PILs/Cu optimization: tuning the synthetic conditions such as PILs/Cu dispersion concentration and using different templates, optimizing the Cu loading in the PILs/Cu composites.

Manuscript writing: result analysis, schemes and figures plotting, manuscript drafting, collaborative revising, and finalizing with co-authors.

Detailed manuscript can be found in **Appendix**.

3.2 Template synthesis of dual-functional porous MoS_2 nanoparticles with photothermal conversion and catalytic properties

Xuefeng Pan[a,c], Radwan M. Sarhan[a], Zdravko Kochovski[a], Guosong Chen[b], Andreas Taubert[c], Shilin Mei[a*] and Yan Lu[a,c*]

[a] *Department for Electrochemical Energy Storage, Helmholtz-Zentrum Berlin für Materialien und Energie, Hahn-Meitner-Platz 1, Berlin 14109, Germany*

[b] *The State Key Laboratory of Molecular Engineering of Polymers and Department of Macromolecular Science, Fudan University, Shanghai 200433, China*

[c] *Institute of Chemistry, University of Potsdam, Potsdam 14476, Germany*

This work (**Article II)** has been published in:

*Nanoscale **2022**, 14, 6888. (DOI: 10.1039/D2NR01040B)*

Contribution to this Article Literature research

Literature research

1. Assembled BCP: the principle of BCP assembly, weakness and strength of BCP assemblies for the formation of nanostructured inorganic particles; essential factors for the transformation of organic to inorganic materials.
2. Functional metal sulfides: basis of metal sulfides, synthetic methods and application of metal sulfides; feasibility of using soft assemblies as templates for the preparation of desired metal sulfides.

3. Photothermal conversion and catalytic reduction: photothermal conversion of nanostructured MoS_2, reduction of 4-NP, and catalytic kinetics.

Experimental and characterization

1. Assembled BCP particles: preparing the colloidal BCP particles using commercial PS-*b*-PVP; studying the influence of block components and swelling temperature on their final structures; analyzing their morphologies by SEM and TEM.
2. Nanostructured MoS_2/C composites: preparing the MoS_2 particles using BCP particles as the soft templates; optimizing the shell thickness by varying the precursor concentration; analyzing their nanostructures by SEM and TEM; determining the crystal structure of the obtained MoS_2 by XRD, determining the mass fraction of MoS_2 and carbon by analyzing the TGA results.
3. Photothermal conversion-assisted reduction of 4-NP: recording the temperature change of photothermal conversion by IR camera and digital thermometer; studying the catalytic reduction behavior of 4-NP by UV-Vis spectroscopy; investigating the influence of various reaction conditions (catalyst concentration, reaction temperature, with/without NIR light irradiation) on the catalytic performance; exploring their catalytic stability; studying the reaction mechanism by comparing the activation energy with/without light irradiation.

Manuscript writing: result interpretation, graphic content creation, manuscript writing, revising, and finalizing.

Detailed manuscript can be found in **Appendix**.

3.3 Multi-functionalized carbon nanotubes towards green fabrication of heterogeneous catalyst platforms with enhanced catalytic properties under NIR light irradiation

Xuefeng Pan[a,d], Rongying Liu[b], Zhilong Yu[a], Benedikt Haas[c], Zdravko Kochovski[a], Sijia Cao[a,d], Radwan M. Sarhan[a], Guosong Chen[b], and Yan Lu[a,d]**

[a] *Department for Electrochemical Energy Storage, Helmholtz-Zentrum Berlin für Materialien und Energie, Hahn-Meitner-Platz 1, 14109 Berlin, Germany*

[b] *The State Key Laboratory of Molecular Engineering of Polymers and Department of Macromolecular Science, Fudan University, Shanghai 200433, China*

[c] *Department of Physics & IRIS Adlershof, Humboldt-Universität zu Berlin, Newtonstr. 15, 12489 Berlin, Germany*

[d] *Institute of Chemistry, University of Potsdam, Karl-Liebknecht-Str. 24-25, 14476 Potsdam, Germany*

This work (**Article III)** has been published in:

Nanoscale, accepted. (DOI: 10.1039/D3NR02607H)

Contribution to this Article Literature research

Literature research

1. Aqueous dispersants for CNTs: synthesis and application of CNTs; dispersion of CNTs in various liquid phases; existing candidates for CNTs dispersing in water, interaction between CNTs and dispersants; green methods for dispersing CNTs, bio-based dispersants.

2. Metal/CNTs: strategy of loading metal particles on CNTs; reduction mechanism of metal particles by various reducing agents; existing methods for the simple synthesis of metal/CNTs composites; possible application in catalytic reaction in aqueous solution; comparison of metal-based catalyst in the reduction of 4-NP.
3. Photothermal conversion-assisted reduction of 4-NP: photothermal heating mechanism of composite materials; comparison of photothermal conversion of various materials; specific role in the catalytic reaction; catalytic activity of various catalysts in the reduction of 4-NP.

Experimental and characterization

1. Water-dispersible GP-CNTs: preparing the CNTs dispersions using glycopeptide (GP) molecules as the multi-functional dispersant; analyzing their dispersion state by SEM and TEM; investigating the interaction between GP and CNTs through UV-Vis spectroscopy measurements and analyzing the Raman spectroscopy results.
2. Synthesis of metal/CNTs composites: synthesizing various metallic particles by directly mixing GP-CNTs dispersion with the corresponding metal precursors; tuning the size of Au particles by varying the Au precursor, GP concentration, and reaction temperature; determining the morphology by SEM and TEM; exploring the spatial distribution of Au NPs on CNTs by analyzing the STEM results; determining the metal loading by analyzing the TGA results.
3. Photothermal assisted reduction of 4-NP: studying the photothermal heating effects by tracking the solution temperature recorded by digital thermometer and IR camera; comparing the reduction activities using various metal/CNTs composites as the catalysts; comparing the reduction with/without NIR light irradiation; analyzing the reduction rate constant and conversion determined by UV-Vis spectroscopy.

Manuscript writing: Result analysis, scheme creation, manuscript writing, revising, and finalizing.

Detailed manuscript can be found in **Appendix**.

4 Discussion

Templating methods have been attractive for decades due to their potential in fabricating versatile composite materials. To realize specific functionalities or architectures of the final composites, it is critical to design and synthesize suitable templates with special superficial/internal structures and physiochemical properties. Correspondingly, the synthetic methods for these templates also vary. Soft templates allow effective control over their size or morphologies through self-assembly. In this thesis, three distinct soft templates have been used for the synthesis of versatile composite materials, which have been applied in two different catalytic reactions. **Article I** focuses on CO_2ER using homopolymer templated composites as the catalysts. **Articles II** and **III** explore the photothermal conversion-assisted reduction of 4-nitrophenol (4-NP) using block copolymer and biomolecule templated composites as the catalysts, respectively. This chapter mainly discusses the scientific content, compares results with the existing literature, and establishes a mutual connection among the individual works.

4.1 Synthesis of templates

In **Article I**, PIL nanovesicles (NVs) are selected as the soft templates, which have been prepared through conventional dispersion polymerization. By simply tuning the initial monomer concentration (C_m) in polymerization, the overall size and shell thickness of the PIL NVs can be respectively controlled from 50 to 120 nm and 15 to 60 nm. The covalent linking of individual monomers enables the propagation of PIL chains. Once reaching above a critical molecular weight, the formed amphiphilic PIL chains will self-organize to well-ordered NVs in water, driven by the strong hydrophobic interaction from their alkyl side chains and electrostatic repulsion from their inherently charged backbones. Although the synthesis of polymer NVs has been carried out by many groups, the precise control of the overall size, particularly shell thickness remains challenging.[107-109] Most of the existing polymer NVs are synthesized using amphiphilic block polymers owing to their distinct boundary between the hydrophilic and hydrophobic blocks. Therefore, it is rather difficult to use homopolymers for the controllable synthesis of NVs. The scientific novelty in **Article I** is the good control over the shell thickness of NVs using PIL homopolymers. It is found that increasing C_m from 3 to 48 mg/mL triggers their morphologies transforming from hollow to solid spheres, eventually to one-dimensional solid worms. Although

a similar structure has been individually realized for PIL systems such as solid spheres or directional worms, the continuous variation of their morphologies using PIL homopolymers has been rarely reported in the literature.[24, 72, 110] To figure out the transformation mechanism, cryo-TEM, SAXS/WAXS, and DLS analysis have been conducted. Collectively, it reveals the strong correlation between the chain length of PILs and the shell thickness of NVs. Finally, PIL NVs have been selected as the soft templates for the preparation of the PILs/Cu composite catalyst for CO_2ER.

In addition to homopolymers in **Article I**, BCPs with well-defined molecular structures have been intensively investigated for the self-assembly of polymer particles. [77] Their phase behavior in the medium can be altered by tuning their molecular architecture, molecular weight and distribution of each block. In **Article II,** assembled PS-*b*-P2VP BCP particles have been used as the soft templates for the synthesis of MoS_2/C composites. The colloidal PS-*b*-P2VP BCP particles were first prepared by emulsifying PS-*b*-P2VP/toluene in water with additional surfactants (SDS). The hydrophobic interaction of BCPs and electrostatic repulsion from SDS drives the formation of primary particles. Considering the difference in the selectivity of each block (normally the minority block) to solvent, the chain movement (stretching or orientation) can be strongly influenced by the local osmotic pressure, caused by the interaction between BCP chains and solvent molecules in the vicinity. This provides the opportunity for the structural transformation of obtained BCP particles. Therefore, ethanol, a good solvent for the P2VP but a poor solvent for the PS block, has been used for the selective swelling of the PS-*b*-P2VP particles. The dependence of block fraction of P2VP (0.25 and 0.37) and swelling temperature (30 to 90 °C) have been systematically studied. Selective swelling of the BCP particles in ethanol has been found to induce their morphologic transformation. More interestingly, an open porous structure (inter-connected channels) has been realized by swelling PS-*b*-P2VP (P2VP fraction of 0.25) at 75 °C for 1 h.

Aside from the amphiphilic macromolecules used in **Article I** and **Article II**, amphiphilic small biomolecules also show potential in self-assembly and creation of versatile composites. In **Article III**, we chose biomolecule glycopeptides (GP) as the soft templates, which play a multi-functional role in the preparation of metal/CNTs composites. Specifically, the GP molecules are composed of a hydrophilic moiety (a trisaccharide with carboxyl and hydroxyl groups) and a hydrophobic counterpart (three phenylalanine). Through gentle sonication, the GP molecules are directly mixed with pristine CNTs in water, yielding a homogenous GP-CNTs dispersion. The coating of GP on

CNTs is driven by the hydrophobic interaction from the aromatic rings and slightly electrostatic repulsion from the carboxyl groups. It is worth mentioning again that although a qualified template usually shows a strong binding capability for metal particles, additional reducing agents are necessary for the formation of metal particles during the synthesis of metal-based composites. While the abundant hydroxyl groups in the trisaccharide moieties endow the GP molecules with noticeable reducibility towards metal ions. Therefore, the GP molecules in this article can not only disperse CNTs but also reduce metal ions to metallic particles and thus immobilize them on the CNTs surface. In short, the GP-functional CNTs then serve as versatile templates for the formation of metal/CNTs composites.

In summary, we demonstrate that both polymers (homopolymers in **Article I** or copolymers in **Article II**) and small molecules could serve as excellent soft templates for the creation of functional composites, as shown in **Table 4.1**. The similarity among these three templates is the distinctive amphiphilicity, derived from their unique chemical structures. However, the synthesis process of these featured templates differs significantly. The preparation method in **III** is relatively more straightforward, sustainable, and energy-efficient compared to that in **Articles I** and **II**. Water is the primary solvent for the fabrication of desired templates (as well as the final composites) in **Articles I** and **III.** Conversely, the involvement of organic solvents is typically inevitable in the self-assembly of BCPs, particularly toxic toluene has been used in **Article II**. Regarding the driving forces for the template formation, the preparation of PIL particles in **Article I** is determined by chemically covalent bonding (polymerization), physical electrostatic repulsion stemming from the ionic backbones, and hydrophobic interactions stemming from the pendant alkyl chains. However, in **Articles II** and **III,** only physical driving forces (mainly hydrophobic interaction and electrostatic repulsions) govern template formation. Despite the relatively complex synthesis, selective swelling in **Article II** could enable the fine modulation of the assembled BCP chains, yielding more diverse assembly structures. Beyond nanostructure, function of the obtained templates also plays a significant role in the preparation of desired composite materials. Compared with the templates used in **Articles I and II**, the templates in **Article III** display multiple functions. In addition to the fundamental supporting capability for catalytic components, the GP molecules in **Article III** could also reduce metal ions to catalytic metal NPs and further immobilize them on the CNTs surface. Overall, the design, synthesis, and properties of these three templates are primarily dictated by the final application in the catalytic reactions.

Further details about the fabrication of the final composites and their corresponding catalytic performance are discussed in the following **Sections 4.2** and **4.3**.

Table 4.1. Comparison of the synthetic templates in this thesis.

	Templates in Article I	**Templates in Article II**	**Templates in Article III**
Polymer or small molecules?	Homopolymers	Block copolymers	Small molecules
Synthetic methods	One-pot dispersion polymerization (75 °C, water, overnight)	Emulsion (room temperature, toluene/water), selective swelling (ethanol, 30-90 °C , 1 h)	Direct dispersion (room temperature, water, ~30 min)
Driving forces	Chemical and physical (covalent bonding, electrostatic repulsion, hydrophobic interaction)	Physical (electrostatic repulsion, hydrophobic interaction, osmotic pressure)	Physical (electrostatic repulsion, hydrophobic interaction)
Morphology	Vesicles (hollow, solid, or worms)	Spheres (solid, inter-connected channels)	Thin layers
Single or multi-function (s)?	Single (support/stabilize Cu NPs)	Single (support MoS_2)	Multiple (disperse CNTs, reduce metal precursors, immobilize metal NPs on CNTs)

4.2 CO_2 electroreduction

In **Article I**, we have successfully controlled the morphology and size of PIL templates by varying the initial C_m in polymerization. Based on these nanostructured PIL templates, various PIL/Cu composites have been prepared. Specifically, the charged nature of PIL NVs could enable the capture of copper ions. In addition, the imidazolium rings in PIL chains show a strong affinity to metallic Cu NPs. Therefore, the copper precursors ($CuAc_2$) have been first reduced by hydrazine to ultra-small size of Cu NPs (~1.8 nm), which has been subsequently immobilized in PIL particles. It is worth mentioning that the PIL NVs with different shell thicknesses show different loading amounts of Cu NPs. The PIL particles (a shell thickness of 18 nm) show a higher Cu loading of 19.2 wt%, which is much higher than that of those with a shell thickness of 60 nm (Cu loading of 8.9 wt%). This difference is mainly attributed to the relatively higher specific surface area resulting

from the hollow structure. Subsequently, the obtained PIL/Cu composites have been used as the electrocatalysts in CO_2ER.

As a result, our PILs/Cu composite particles show a 2.5-time increase in Faradic efficiency (FE, selectivity) towards C_1 products, compared to the pristine Cu NPs sample (amorphous bulk structure). Recently, PILs/Cu composite particles have been used as the electrocatalyst to tune the CO_2ER selectivity towards hydrocarbons in CO_2ER.[28] However, the reported Cu NPs are functionalized with PILs on their surface, thus presumably impairing the utilization of catalytically active Cu NPs. Conversely, the small size of Cu NPs in this article is immobilized in PIL templates. The catalytic Cu NPs could thus expose more active sites in the catalytic reactions, leading to a substantial increase in the production rate in CO_2ER. In our case, the PIL NVs/Cu indeed showed a much higher CH_4 production rate of ~38 mA mg^{-1} cm^{-2} compared to the pristine Cu NPs (~2 mA mg^{-1} cm^{-2}) at the applied cathodic potential of -1.2 V. Therefore, we demonstrate that the CO_2ER performance of metallic electrocatalysts can be tuned by using the well-defined PILs template.

4.3 Reduction of 4-nitrophenol

In **Article II**, the nanostructured BCP particles have been employed as the soft templates for the fabrication of MoS_2/C composite particles. Concretely, the $(NH_4)_2MoS_4$ precursor is deposited on the surface of polymer templates through coordination interactions with the polar pyridine groups in the PVP block. After calcination, most of the polymer framework (organic components) turns into amorphous carbon, resulting in the formation of hollow channels in the final composite particles. While the inorganic precursor is decomposed to be MoS_2 as the main active component for the following catalytic reactions. Eventually, the composite particles exhibit diverse morphologies including pomegranate-like, hollow, and open porous structures, mainly resulting from the structured polymer templates. Among these composite particles, the open porous MoS_2/C nanoparticles (PNPs) show a mesoporous structure (pore size of 10 - 20 nm) with a large specific surface area of 106.6 m^2/g, surpassing that of the bulk MoS_2 (36.3 m^2/g). Regarding nanostructure, the obtained porous MoS_2 particles show more intricate features, *i.e.*, open porous architectures with inter-connected hollow channels, when compared to the MoS_2 particles reported in the literature.[111, 112] In addition, most of the existing hollow or porous MoS_2 are prepared by hydrothermal treatment or chemical/mechanical exfoliation (**Table 4.2**). These procedures are

typically carried out under harsh conditions. By comparison, the MoS_2 synthesis presented in this article can be realized under relatively mild conditions, directly through thermal decomposition of precursor ions. Therefore, **Article II** presents a novel strategy for the facile synthesis of porous MoS_2 particles using assembled BCPs as the sacrificed soft templates.

Next, the as-prepared composite particles have been used as the catalyst for the reduction of 4-NP. To better compare with the MoS_2-based catalysts reported in the literature, herein we primarily calculated their rate constant (k_m), which represents k_{app} normalized with catalyst mass used in the reaction, as shown in **Table 4.2**. Compared with existing MoS_2-based catalysts, our MoS_2/C composite particles show good catalytic performance in the reduction of 4-NP. It is mainly due to the high porosity of the MoS_2/C particles (*i.e.*, sufficient specific surface area) and the fast diffusion of 4-NP molecules to the superficial/internal active sites. Again, it confirms that the active sites of composite catalysts can be altered using the BCP templates with tunable nanostructures. As discussed above, the reduction of 4-NP is a temperature-sensitive reaction. MoS_2 has been reported to convert solar energy to thermal energy upon light irradiation. The obtained MoS_2/C particles show a temperature increase of ~ 20 °C under NIR light irradiation (10 min, 808 nm, 3 W/cm^2), which is significantly higher than that of pure water (increase of ~5 °C). It demonstrates their good photothermal conversion capability. Therefore, we used the MoS_2/C composite particles as the catalyst for the reduction of 4-NP assisted by NIR light irradiation. As expected, the light irradiation (808 nm, 3 W/cm^2) could lead to a high reaction temperature of 37 ℃ in 10 min. Correspondingly, a k_{app} of 0.012 s^{-1} was observed, which is higher than the reaction conducted without light (k_{app} of 0.003 s^{-1}, room temperature). To illustrate the role of photothermal heating in the enhanced catalytic performance, the reduction was performed at the same temperature of 37 ℃ heated in a water bath. The reaction shows a k_{app} of 0.008 s^{-1}, which is still lower than the reaction conducted under NIR light irradiation. Overall, the incorporation of catalytic properties and photothermal conversion capabilities under NIR light irradiation makes MoS_2 a promising catalyst in the catalytic reaction. These two capabilities of the composite catalysts can be well-controlled using BCPs as soft templates with tunable nanostructures.

Table 4.2. Comparison of the catalytic activity of the MoS_2-based catalysts in the reduction of 4-NP at room temperature*.

Catalyst	Preparation method	Morphology/size	C_{NaBH4} (mM)	$C_{4\text{-}NP}$ (mM)	$k_m \times 10^3$ s^{-1} mg^{-1}	Ref.
Acetic acid-functionalized MoS_2	Electrochemical functionalization	Nanosheets (200×6 nm)	1100	1.2	168	[113]
MoS_2/ZnO	Exfoliation	Nanoflowers (200-500 nm)	132	0.5	0.486	[114]
MoS_2	Li- exfoliation	Nanosheets (300×1 nm)	72	0.12	56.18	[115]
Pd/MoS_2	Hydrothermal	Nanosheets (100-200 nm)	14.1	0.1	4.29	[116]
Fe_3O_4@MoS_2	Hydrothermal	Core-shell particles (~200 nm)	100	1	48.8	[117]
MoS_2-Fe_3O_4/Pt	Hydrothermal	Nanosheets (amorphous)	100	10	174.44	[118]
MoS_2/PMMT	Hydrothermal	Nanosheets (amorphous)	72	0.12	12.05	[119]
MoS_2/C	Calcination	Porous nanoparticles	20	0.1	80.46	This work

*C_{cat}, C_{NaBH4}, $C_{4\text{-}NP}$, and k_m are the catalyst concentration, $NaBH_4$ concentration, 4-NP concentration, and k_{app} normalized with the catalyst mass, respectively.

In **Article III**, photothermal CNTs have been functionalized with highly catalytic metal NPs to form metal/CNTs composites, which have been further employed as the catalyst for the reduction of 4-NP. Considering the amphiphilicity nature, the GP molecules are capable of stabilizing both CNTs and metal NPs. As the hydroxyl groups of sialyllactose show strong reducibility to noble metal ions, the GP molecules containing sialyllactose moieties in this article could also reduce metal ions to metallic particles. As expected, various metal NPs including Au, Ag, Pt, and Pd NPs have been successfully loaded on the surface of CNTs without any additional reducing agents at room temperature. The size and morphology of Au NPs can be also controlled by optimizing the GP/precursor concentration and reduction temperature. The obtained Au NPs in the GP-CNTs-Au composites and Pd NPs in the GP-CNTs-Au composites show an average size of 5.6 and 1.8 nm, respectively. In the literature, a few molecules (*e.g.* ascorbic acid) have shown one or two capabilities, *i.e.* stabilizing CNTs in water, reducing metal ions to metallic particles, and/or

stabilizing the formed metal NPs in aqueous solution. In this article, the GP molecules have demonstrated not only good reducibility to metal ions but also the capability to stabilize the formed metal NPs as well as CNTs in water. Therefore, the primary scientific novelty in this article is to realize the simple and green synthesis of metal/CNTs composites using multi-functional GP molecules.

For the reduction of 4-NP, the catalytic performance of the GP-CNTs-Pd and GP-CNTs-Au composites has been compared using surface area-normalized rate constant (k_1). As a result, GP-CNTs-Pd shows a much higher k_1 of 0.062 s^{-1} m^{-2} L than that of GP-CNTs-Au (k_1 value of 0.0081 s^{-1} m^{-2} L). It could result from the small size of Pd and its intrinsically catalytic activity when applied in the reduction of 4-NP. Furthermore, the photothermal conversion performance of the obtained GP-CNTs-Pd composites has been tested following the same procedures in **Article II**. The GP-CNTs-Pd composite dispersions show a 4.6-fold temperature increase compared to pure water under NIR light irradiation (15 min, 808 nm, 3 W/cm^2), demonstrating its excellent photothermal conversion performance. Similarly, the reduction of 4-NP has been further conducted under NIR light irradiation (808 nm, 3 W/cm^2). The reduction conducted under light irradiation (32 °C) shows a conversion of 91.2 % in 5 min, which is nearly 2.6 times than that of the reaction at the same temperature in a water bath without light illumination (conversion of 35.1%). It confirms that photothermal heating of CNTs significantly enhanced the catalytic performance of Pd NPs. In this case, the strong photothermal heating effects of the well-dispersed CNTs lead to localized heat, which quickly transports to the superficial catalytic metal NPs and reaction solution in the vicinity. Thus, the high surface temperature could substantially accelerate the reduction process. Overall, in addition to the design of MoS_2 in **Article II**, in **Article III** we demonstrate another promising strategy to enhance the degradation of 4-NPs by combining the photothermal CNTs with catalytic metal NPs using the versatile GP molecules as the soft templates.

In this thesis, various strategies have been developed to improve the catalytic activity of the composite catalysts in different reactions (**Table 4.3**). These approaches can be generally summarized as increasing the reaction active sites and elevating the local reaction temperature. First of all, increasing the active sites is a common theme across the three articles, which has been achieved by reducing the particle size or creating hollow/porous nanostructures. In **Articles I** and **III**, the abundant active reaction sites primarily originated from the small size of metal particles

(Cu, Au, and Pd). While the high specific surface of MoS_2 in **Article II** is enabled by the formation of hollow or open porous structures.

Table 4.3. Comparison of the composite catalysts in this thesis.

	Composites in Article I	**Composites in Article II**	**Composites in Article III**
Catalytic reaction	Electroreduction of CO_2	Reduction of 4-NP	Reduction of 4-NP
Strategies for enhancing the catalytic performance	Increase reaction active sites	Increase reaction active sites; elevate reaction temperature by photothermal conversion	Increase reaction active sites; elevate reaction temperature by photothermal conversion
Origin of catalytic sites	Small size of Cu NPs (~1.8 nm)	Open porous structure (mesopore size of 10-20 nm)	Small size of Pd NPs (~1.8 nm)
Synthetic conditions	Reduction by hydrazine, water phase, 80 °C	Calcination at 500 °C in an argon atmosphere	Reduction by GP, water phase, room temperature
Morphology	Vesicles (Cu NPs dotted in PIL NVs)	Mesoporous, pomegranate-like, or hollow particles	Nanotubes (GP and metal NPs on CNTs surface)
Components	Catalytic Cu NPs (~18.9 wt.%), PIL templates	Catalytic and photothermal MoS_2 (~61.1 wt.%), carbon	Catalytic metal NPs (Pd: ~13.2 wt.%), photothermal GP-CNTs templates

Besides increasing the active sites, elevating the local reaction temperature by photothermal heating can effectively enhance the reaction rate, as demonstrated in **Articles II** and **III**. Herein, the photothermal composite catalysts are designed through two different strategies. In **Article II,** we developed the nanostructured MoS_2/C composite catalysts that integrate the catalytic property of MoS_2 and its photothermal capability. These two characteristics have been intensified by creating open porous structures, which are realized by duplicating the nanostructure of BCP soft templates. Alternatively, in **Article III**, the metal/CNTs composites have been employed as the catalysts, combining the highly catalytic activity of metal NPs and photothermal CNTs. The excellent catalytic performance of the composite catalysts is thus enabled by using the ultra-small size of metal NPs as the catalytic species and well-dispersed CNTs template as the photothermal heating source. Different from **Article I**, no additional reducing agents are involved in the preparation of metal/CNTs composites in **Article III**. Also, the fabrication process can be conducted under mild conditions (room temperature and gentle stirring), which requires less

energy compared to that of the MoS_2/C composites in **Article II** (calcination at 500 °C). Regarding the final morphologies, the obtained composites in **Article II** show diverse morphologies, particularly open mesoporous structures. On the contrary, the final composites in **Article I** simply show similar morphology to the corresponding templates.

In conclusion, we have demonstrated that tailoring the catalyst performance can be realized by adjusting the number of reaction active sites and manipulating the reaction temperature, strongly influenced by the particle size or the surface/internal structures. These distinct morphologies of the composites can be created using soft templates (whether polymers or small molecules). A wide array of tools is available to create assembled templates with specific nanostructures and functionalities. Despite the differences in their synthetic strategies, the diversity and versatile functionalization of template candidates hold promise in the design of composite catalysts for various catalytic reactions.

5 Summary and Outlook

This cumulative thesis presents the synthesis of functional nanocomposites with desired novel nanostructures based on soft-template methods. Soft templates, including nanostructured poly(ionic liquid) (PILs) vesicles, polystyrene-*b*-poly(2-vinylpyridine) (PS-*b*-P2VP) particles, and glycopeptide (GP) biomolecules have been prepared and then utilized for the fabrication of PILs/Cu, molybdenum disulfide/carbon (MoS_2/C), and GP-carbon nanotubes-metal (GP-CNTs-metal) composites, respectively. As a step forward to explore their applications, these composites have been employed as catalysts in two typical reactions, *i.e.* reduction of 4-nitrophenol (4-NP) and CO_2 electroreduction (CO_2ER), respectively.

In **Article I**, a simple and scalable strategy towards the fabrication of PIL homopolymer nanovesicles (NVs) with a multi-lamellar chain packing structure has been demonstrated *via* free radical polymerization. The overall size and shell thickness of the PIL NVs have been controlled by tuning the initial monomer concentration (C_m) for polymerization. The increase in C_m drives the morphology of PIL NVs evolving from hollow to solid spheres, further to directional solid worms. This morphologic transformation of PIL NVs has been studied in detail, revealing a strong correlation between the polymerization degree of PILs and the shell thickness of NVs. It is also worth exploring the growth kinetics of particles in future work. Subsequently, the obtained PIL NVs with different shell thickness have been utilized as soft templates for the immobilization of ultra-small Cu nanoparticles (NPs, 1.8 nm on average) and used as electrocatalysts for CO_2ER. Remarkably, the hollow PILs/Cu composite electrocatalysts show a 2.5-fold increase in selectivity towards C_1 products (*e.g.* CH_4) compared to the pristine Cu NPs. This work opens opportunities for using assembled PILs as versatile templates in CO_2 conversion. To achieve deep insights into the CO_2ER activity based on PIL-functionalized metal catalysts, the size effect of Cu NPs on CO_2ER activity could be investigated through *in situ* Raman, density functional theory (DFT) simulations, and XPS analysis.

In **Article II**, self-assembled PS-*b*-P2VP block copolymer particles have been prepared *via* selective swelling. These featured polymer particles have been further employed as sacrificed soft templates for the formation of various nanostructured MoS_2/C composite particles. These particles show desired morphologies such as pomegranate-like, hollow, and open porous structures. These nanostructured MoS_2/C particles exhibit excellent photothermal conversion performance when

exposed to near infrared (NIR) light irradiation. Under the light illumination, the porous MoS_2/C particles exhibit a 1.5-fold enhancement in rate constant of reduction of 4-NP. The enhancement in catalytic performance is primarily attributed to their unique porous architecture and exceptional photothermal conversion performance of the MoS_2. This proposed strategy casts new aspects on using nanostructured MoS_2 for efficient photothermal-assisted catalysis. To deepen the understanding of the influence of the photo-induced charge transfer process of MoS_2/C on the catalytic behavior, a systematic study on the charge separation of MoS_2/C upon light irradiation and electron transfer pathway during the catalytic reaction could be carried out *via* electron spinning resonance, photoluminescence, XPS, and DFT simulations.

In **Article III**, a versatile GP-CNTs-metal composite has been fabricated using an amphiphilic GP biomolecule both as a stabilizer for CNTs in water and as a reducing agent for noble metal ions. Various metal ions can be reduced by GP under mild conditions, leading to the formation of metal NPs (*e.g.* Au, Ag, Pt, and Pd) on the CNTs surface. The incorporation of catalytic Pd NPs and photothermal CNTs makes GP-CNTs-Pd an ideal catalyst candidate for the degradation of organic pollutants, as demonstrated by a model reduction reaction of 4-NP. When employed as the catalyst in the reaction, the obtained GP-CNTs-Pd composite displays a 1.6-fold increase in its conversion with the assistance of NIR light illumination, owing to the strong photothermal heating effect of CNTs. This strategy demonstrates the potential for the design and synthesis of CNTs-based composite as an efficient and sustainable catalyst platform. To further enhance the multi-functionalization of CNTs, it would be valuable to investigate the influence of the molecular structure of the amphiphilic glycopeptides, which can be achieved by varying the number and type of peptide or carbohydrate units.

Overall, this thesis demonstrates that the utilization of soft templates enables the controllable synthesis of multi-functional nanocomposites with ordered structures and tailored properties. This study has established a clear relationship between the selected soft templates and final application performance. The proposed synthetic strategy broadens the application scope of composite materials in various catalytic processes. The findings of this thesis contribute to the development of materials science and catalysis, opening up new possibilities for the design and synthesis of novel and efficient catalysts.

6 Experimental

6.1 Chemicals and materials

Chemicals	Purity	Supplier
1-Bromodecane	≥ 99 %	Sigma-Aldrich
1-Vinylimidazole	≥ 99 %	Sigma-Aldrich
2,2'-Azobis[2-methyl-N-(2-hydroxyethyl) propionamide] (VA86)	≥ 99 %	FUJIFILM Wako Chemicals
2,6-Di-tert-butyl-4-methylphenol (BHT)	≥ 99 %	Sigma-Aldrich
3-Mercaptopropionic acid (3-MPA)	≥ 99 %	Sigma-Aldrich
4-Nitrophenol (4-NP)	≥ 99 %	Sigma-Aldrich
Ammonium tetrathiomolybdate ($(NH_4)_2MoS_4$)	≥ 99 %	Sigma-Aldrich
Carbon nanotubes (CNTs)	≥ 99.9 %	Timesnano
Copper acetate monohydrate ($CuAc_2 \bullet H_2O$)	≥ 99 %	Sigma-Aldrich
Gold chloride trihydrate ($HAuCl_4 \bullet 3H_2O$)	≥ 99 %	Sigma-Aldrich
Hydrazine hydrate solution ($N_2H_4 \bullet H_2O$)	35 wt.%	Sigma-Aldrich
Hydrochloric acid solution (HCl)	37 %	Sigma-Aldrich
Palladium chloride ($PdCl_2$)	97 %	Sigma-Aldrich
Polystyrene-*b*-poly(2-vinylpyridine) (PS-*b*-P2VP)	99 %	Polymer Source Inc.
Potassium bromide (KBr)	≥ 99.8 %	Sigma-Aldrich
Potassium hydrogen carbonate ($KHCO_3$)	99.7-100.5 wt.%	Sigma-Aldrich
Silver nitrate ($AgNO_3$)	99.9 %	Sigma-Aldrich
Sodium borohydride ($NaBH_4$)	≥ 99 %	Sigma-Aldrich
Sodium hydroxide (NaOH)	97 %	Sigma-Aldrich
Sulfuric acid (H_2SO_4)	≥ 99.8 %	Sigma-Aldrich
2-Propanol (PrOH)	≥ 99.8 %	Sigma-Aldrich
Diethyl ether	⩾99.0%	Sigma-Aldrich
Dimethyl sulfoxide-*d6* (DMSO-*d6*)	≥ 99.9 atom %D	Sigma-Aldrich
Ethanol (EtOH)	≥ 99.8 %	Sigma-Aldrich
Methanol (MeOH)	≥ 99 %	Sigma-Aldrich
Toluene	≥ 99.7 %	Sigma-Aldrich
Ultrapure water	18.20 MΩ·cm	Thermo Scientific

6.2 Material synthesis

6.2.1 Synthesis of PIL/Cu composites

6.2.1.1 Synthesis of the IL monomer

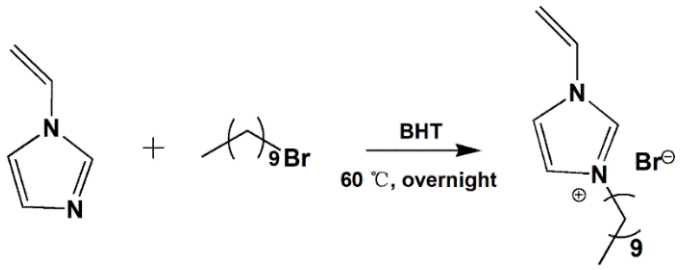

Figure 6.2.1. The synthetic reaction of IL monomers.

The synthesis of the IL monomer 3-*n*-decyl-1-vinylimidazolium bromide was shown in **Figure 6.2.1**.[73] 10 mL of 1-vinylimidazole and 10 mL of methanol were loaded into a 100 mL flask. 22.8 mL of *n*-decyl bromide and 50 mg of inhibitor (BHT) were introduced to the solution. The mixed solution was stirred at 300 rpm at 60 °C in an oil bath for 15 h. After cooli ng down, the mixed solution was slowly added to ~300 mL of diethyl ether. Next, the unreacted reactants in the supernatant layer were removed, while the precipitated product in the bottom layer was washed with diethyl ether 5 times. Finally, the obtained viscous yellow liquid was dried at 50 °C in a vacuum oven overnight to completely remove the residual solvent. The chemical structure of obtained IL monomers was confirmed by nuclear magnetic resonance (NMR) analysis (**Figure 6.2.2**). The reaction yield is *ca.* 34%. The obtained liquid product was stored in dark at 4 °C in a fridge for further use.

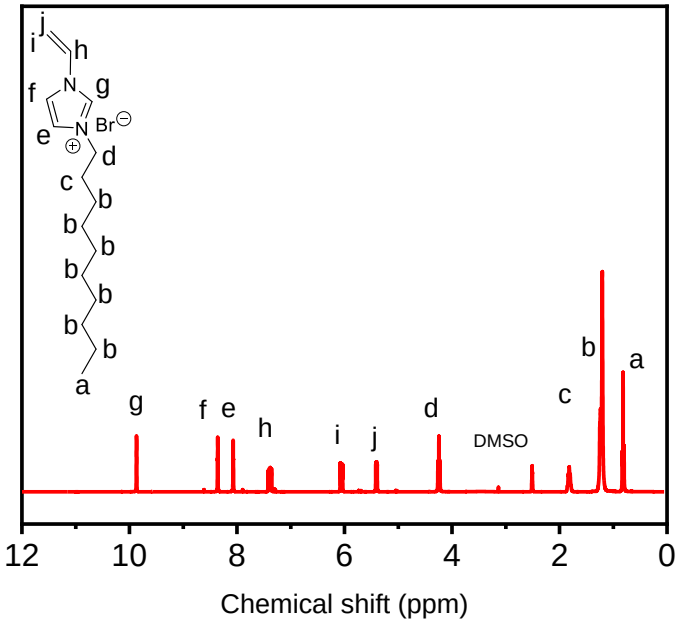

Figure 6.2.2. ^{1}H-NMR spectrum of the IL monomers dissolved in DMSO-*d6*.

6.2.1.2 Synthesis of PIL NVs

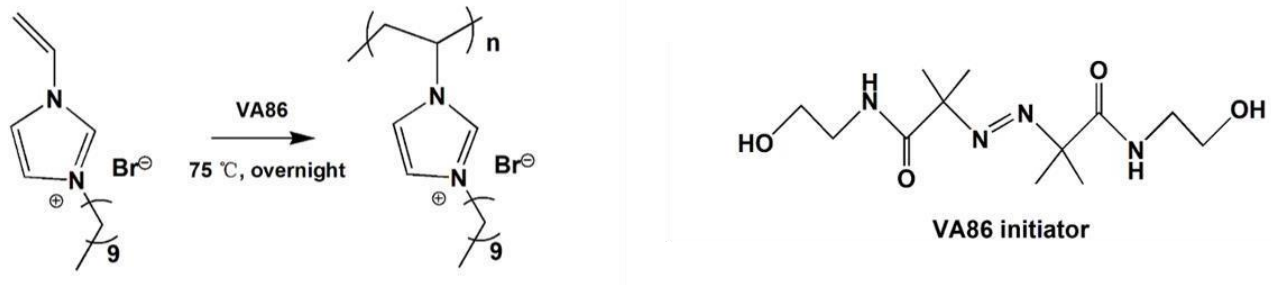

Figure 6.2.3. Free radical polymerization for the synthesis of PILs**.**

In a typical run, various amounts of IL monomers (0.3 - 4.8 g) were fully dissolved in 100 mL of deionized water in a 250 mL of Schlenk flask to form a homogenous solution. The monomer solution was mixed with 50 mg of thermo-initiator (VA86) under magnetic stirring at 250 rpm for 30 min. The mixture was completely deoxygenated by five cycles of nitrogen replacement. Afterwards, the mixture was stirred at 75 °C in an oil bath overnight for the formation of colloidal PIL dispersion. The polymerization reaction is depicted in **Figure 6.2.3**.

The colloidal PIL dispersion was exhaustively dialyzed against deionized water using a dialysis tubing (cellulose, diameter of 44 mm, thickness of 20 µm) until the conductivity of cleaning water was below 3 µS/cm. Eventually, the PIL dispersion was stored at 4 °C in the fridge for further use. The PIL dispersion was freeze-dried overnight, forming a PIL powder used for the NMR measurement. The corresponding ^{1}H-NMR spectrum of the obtained PILs is shown in **Figure 6.2.4**. The PIL NVs prepared at the monomer concentration (C_m) of 12 and 24 mg/mL are named as NVs and SNSs, respectively, according to their morphology under TEM characterization. To calculate the polymerization yield (Y), a desired amount of PIL dispersion at a given C_m (V mL) after dialysis was completely dried at 90 °C in an oven overnight until its weight remained constant (W g). Each sample was repeated 5 times to calculate the average value. Therefore, Y can be determined by:

$$Y = \frac{V \times c_m - W}{V \times c_m} \times 100\% \qquad (6.2.1)$$

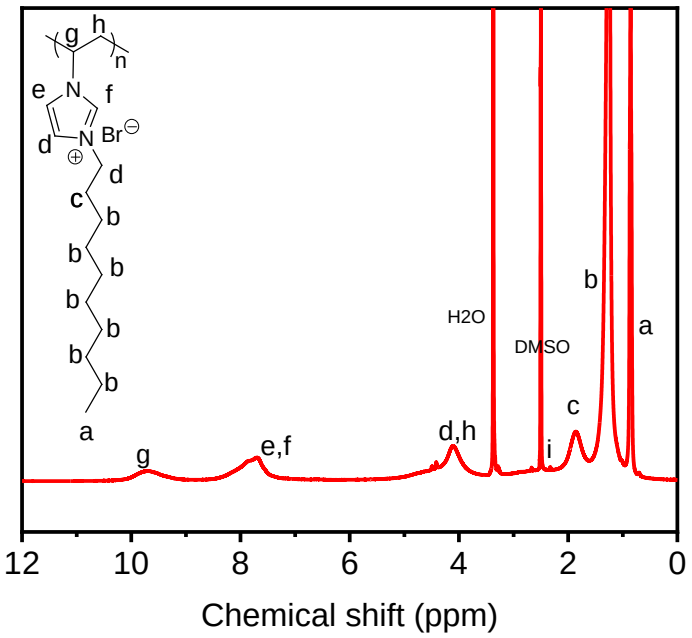

Figure 6.2.4. ^{1}H-NMR spectrum of the PILs prepared at C_m of 12 mg/mL dissolved in DMSO-*d6*.

6.2.1.3 Synthesis of PIL/Cu composite particles

The facile synthesis of colloidal PIL/Cu composite particles was conducted based on the previous study.[121] For PIL NVs (C_m of ~ 12 mg/mL), the obtained PIL dispersion (4 mL, 10 mg/mL) was diluted with 32 mL of deionized water. Then a fresh copper acetate ($CuAc_2$) solution (4 mL, 10 mg/mL) was slowly added to the dispersion under vigorous stirring at 500 rpm. The mixed dispersion was stirred at room temperature for 4 h, followed by quickly injecting an aqueous N_2H_4 solution (0.4 mL, 35 wt.%). The color of the mixed dispersion turned from light blue to pink. Afterwards, the mixed dispersion was heated at 80 °C in an oil bath under stirring at 250 rpm overnight to complete the reduction of Cu^{2+} ions. The color of the mixed dispersion changed to dark red the next day. After cooling down, the resulting dispersion was sonicated (30 W, 37 kHz) for 20 min. Subsequently, the dispersion was filtered off using a syringe filter (Acrodisc with Supor Membrane, polyethersulfone, 1.2 μm in pore size, and 25 mm in diameter) to remove any big aggregates. The dispersion was subjected to centrifugation at 8500 rpm for 30 min and washed with fresh water once, yielding the final product of PIL/Cu composite particles. The obtained composite particles were re-dispersed in 25 mL of fresh water before further use. For PIL SNSs (C_m of ~ 24 mg/mL), the as-synthesized PIL dispersion (2 mL, 20 mg/mL) was used for the

preparation of the corresponding PIL/Cu composite in the same manner as mentioned above. By comparison, the pristine Cu NPs were also prepared in the same way without any PIL templates. Cu NPs-decorated NVs and SNSs are denoted as NVs/Cu and SNSs/Cu, respectively.

6.2.2 Synthesis of MoS_2/C composites

6.2.2.1 Assembly of block copolymer as templates

Two block copolymers (BCPs) with different mass fractions of P2VP moiety have been used for the formation of assembled polymer particles, as shown in **Table 6.2.1**. Taking $PS_{48.5k}$-*b*-$P2VP_{16.5k}$ ($M_{n,\ PS}$ = 48.5 kg/mol, $M_{n,\ P2VP}$ = 16.5 kg/mol, M_w/M_n = 1.06) for an example, 40 mg of the as-purchased BCP powder was completely dissolved in 4 mL of toluene to form a homogenous BCP solution (10 mg/mL). The BCP solution was then introduced to 80 mL of deionized water containing 0.12 mL of a surfactant solution (SDS, 0.5 wt.%). The mixture was completely emulsified under sonication (30 W, 37 kHz) for 30 min to form a well-dispersed colloidal dispersion (2 mg/mL). The formed BCP dispersion was subjected to rotatory evaporation at 40 °C in a water bath for *ca.* 2 h to remove toluene and solidify the BCP particles. The solidified particles in water were collected by centrifugation at 9000 rpm for 2 h, followed by re-dispersing in *ca.* 80 mL of ethanol. The particle dispersion in ethanol was further heated at various temperature ranging from 30 to 90 °C in an oil bath for 1 h to induce the selective swelling of the BCP particles. After cooling down to room temperature, the BCP dispersion was condensed to *ca.* 4 mg/mL using the rotary evaporator at 40 °C in the water bath for *ca.* 2 h. For $PS_{38.5k}$-*b*-$P2VP_{23k}$ ($M_{n,\ PS}$ = 38.5 kg/mol, $M_{n,\ P2VP}$ = 23 kg/mol, M_w/M_n = 1.03), the BCP particles were obtained using the same protocol but swelling at 50 °C in ethanol.

Table 6.2.1. Selective swelling condition of the two PS-*b*-P2VP particles.

BCPs	**Swelling temperature (°C)**
$PS_{48.5k}$-*b*-$P2VP_{16.5k}$	30
$PS_{48.5k}$-*b*-$P2VP_{16.5k}$	50
$PS_{48.5k}$-*b*-$P2VP_{16.5k}$	75
$PS_{48.5k}$-*b*-$P2VP_{16.5k}$	90
$PS_{38.5k}$-*b*-$P2VP_{23k}$	50

6.2.2.2 Synthesis of nanostructured MoS_2/C composite particles

As shown in **Table 6.2.2**, the obtained BCP dispersion (4 mg/mL, 10 mL) was added in 140 mL of $(NH_4)_2MoS_4$ solution with the final concentration of $(NH_4)_2MoS_4$ maintained at 1, 1.5, and 3 mg/mL, respectively. The particle dispersion was stirred at 250 rpm for 30 min. Afterwards, an HCl solution (0.16 mL, 1 M) was added dropwise into the dispersion, resulting in the partial decomposition of the precursor into molybdenum sulfide (MoS_x, x = 2~3). To improve the hydrophilicity of the MoS_x in the aqueous solution, 100 μL of 3-MPA was added into the mixed dispersion under stirring at 550 rpm. The chemical reaction is shown in the equation (6.2.2). The mixed dispersion was stirred for ~30 min, followed by centrifugation at 8000 rpm for ~40 min and washing with fresh water 3 times. Next, the obtained brown particles were completely dried by freeze-drying overnight. The particles were then calcined at 500 °C in an argon atmosphere for 2 h at a heating rate of 3 °C/min, yielding t he final product of MoS_2 with carbon (termed as MoS_2/C), as shown in equation (6.2.3). In comparison to MoS_2/C composite particles prepared with various polymer templates, the bulk MoS_2 was fabricated by following the same process without any BCP templates. The MoS_2/C particles prepared with the final concentration of $(NH_4)_2MoS_4$ of 1, 1.5, and 3 mg/mL are denoted as MoS_2/C-1, MoS_2/C-1.5, and MoS_2/C-3, respectively.

$$MoS_4^{2-} + 2H^+ \rightarrow MoS_3 \downarrow + H_2S \uparrow \quad (6.2.2)$$

$$(NH_4)_2MoS_4 \xrightarrow{\Delta} MoS_2 + 2NH_3 \uparrow + H_2S \uparrow \quad (6.2.3)$$

Table 6.2.2. Preparation conditions of $(NH_4)_2MoS_4$ coated block copolymer particles.

Polymer templates	**$(NH_4)_2MoS_4$ concentration (mg/mL)**	**$(NH_4)_2MoS_4$ amount (mg)**
$PS_{48.5k}$-*b*-$P2VP_{16.5k}$ particles swollen at 75 °C	1	150
$PS_{48.5k}$-*b*-$P2VP_{16.5k}$ particles swollen at 75 °C	1.5	300
$PS_{48.5k}$-*b*-$P2VP_{16.5k}$ particles swollen at 75 °C	3	600
$PS_{48.5k}$-*b*-$P2VP_{16.5k}$ particles swollen at 50 °C	1.5	150
$PS_{38.5k}$-*b*-$P2VP_{23k}$ particles swollen at 50 °C	1.5	150

6.2.3 Synthesis of GP-CNTs-metal composites

The glycopeptide (GP) molecule was provided by our project collaborator Dr. Rongying Liu from Fudan University. It was synthesized according to the methods reported in the previous study.[46] In short, the GP molecule was prepared through a coupling reaction between the hydrazide group of the triphenylalanine and hydroxyl end of sialyllactose at 50 °C. The reaction yield is *ca.* 59%. As shown in **Figure 6.2.5**, ^{1}H-NMR (400 MHz, DMSO-*d6*, δ, ppm): 9.63 (d, 1H), 8.37 (d, *J* = 8.6 Hz, 1H), 8.17 (s, 1H), 7.87 (d, 1H), 7.26-7.16 (m, 15H), 6.90 (d, *J* = 8.9 Hz, 1H), 5.73 - 5.65 (m, 1H), 5.15 (d, *J* = 3.6 Hz, 1H), 4.89 (d, *J* = 6.0 Hz, 1H), 4.72 (d, *J* = 5.8 Hz, 1H), 4.63 - 4.48 (m, 7H), 4.42 (s, 1H), 4.35(t, *J* = 5.7 Hz, 1H), 4.28 (t, *J* = 5.4 Hz, 1H), 4.18 - 4.11 (m, 1H), 4.11 - 4.03 (m, 1H), 4.02-3.93 (m, 1H), 3.81 - 3.72(m, 2H), 3.70 (s, 1H), 3.66 - 3.54 (m, 7H), 3.53 - 3.42 (m, 4H), 3.22 - 3.17 (m, 4H), 3.03 - 3.00 (m, 2H), 2.95 - 2.90 (m, 1H), 2.89 - 2.85 (m, 1H), 2.84 - 2.73 (m, 4H), 2.64 - 2.57 (m, 1H), 1.90 (s, 3H), 1.26 (s, 9H).

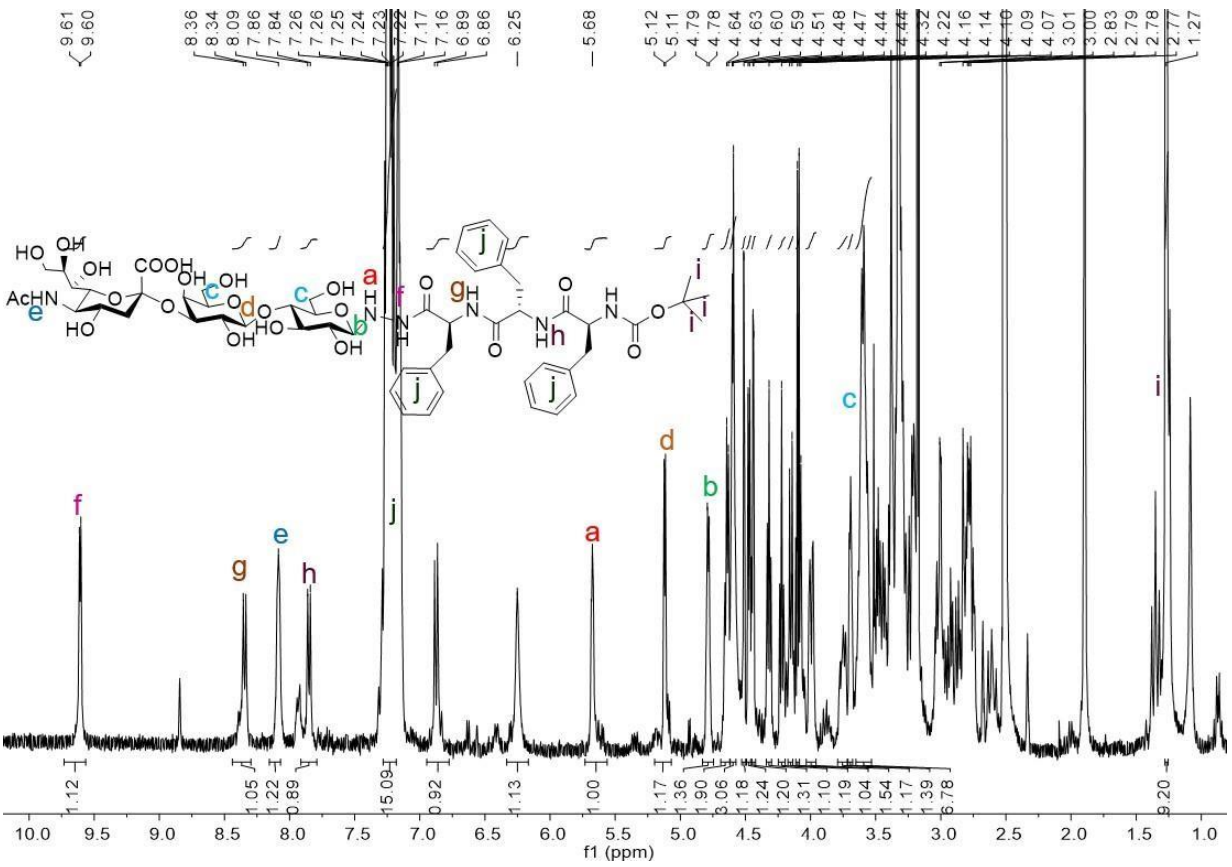

Figure 6.2.5. ^{1}H-NMR spectrum of the GP powder dissolved in DMSO-*d6*.

6.2.3.1 Synthesis of GP-CNTs in various states

To prepare the diluted CNTs dispersion, 1 mg of as-purchased multi-wall carbon nanotubes (MWCNTs, outer diameter of 10-30 nm, inner diameter of 3-5 nm, length of 10-50 μm) powders were added in 1 mL of fresh GP solution (1 mg/mL) and dispersed by sonication (30 W, 37 kHz) in an ice bath for 30 min. After centrifugation at 8000 rpm for 20 min to remove the residual bundle complexes, a diluted GP functionalized CNTs (termed as GP-CNTs) dispersion was obtained. The preparation of single-wall carbon nanotubes (SWCNTs, an average diameter of 1-2 nm, an average length of 5-30 μm) dispersion followed the same procedure as described above. As a control experiment, the pristine MWCNTs powders were directly dispersed in water without any GP molecules. To synthesize the GP-CNTs paste, the diluted GP-CNTs dispersion was concentrated further by centrifugation (8000 rpm, 40 min) to form a highly viscous state. The concentrated paste was subsequently coated onto an alumina foil and dried at 40 °C in an oven, ultimately yielding a uniform thin film. For the preparation of gel and dough, MWCNTs powder was directly mixed with GP molecules at the same weight ratio (1:1) but the total concentration in water increased from ~70 to 200 mg/mL or even higher and followed by simple hand-grinding in a mortar for ~30 min.

6.2.3.2 Synthesis of GP-CNTs-metal composites

The synthesis of GP-CNTs-metal particles is conducted under similar conditions. Taking Pd as an example, a $PdCl_2$ solution (50 μL, 10 mM) was directly mixed with the as-obtained GP-CNTs dispersion (4 mL, 0.05 mg/mL). The pH value of the GP-CNTs dispersion was adjusted to ~8.5 by adding NaOH. After stirring at 250 rpm at room temperature for 15 min, the Pd NPs coated GP-CNTs (denoted as GP-CNTs-Pd) were achieved by centrifugation at 8000 rpm for 20 min. For Au, Pt, and Ag, $HAuCl_4$ (60 μL, 10 mM), H_2PtCl_6 (60 μL, 10 mM), and $AgNO_3$ (60 μL, 5 mM) solution were respectively used as the precursor for the synthesis of Au NPs coated GP-CNTs (denoted as GP-CNTs-Au), Pt NPs coated GP-CNTs (denoted as GP-CNTs-Pt), and Ag NPs coated GP-CNTs (denoted as GP-CNTs-Ag).

6.3 Experiments

6.3.1 CO_2 electrochemical reduction

The pristine Cu NPs and PIL/Cu composite particles were used for the CO_2 electroreduction (CO_2ER). The as-prepared pristine Cu NPs and PIL/Cu dispersions (*ca.* 4 mg/mL) were deposited on a Freudenberg H1C49 gas diffusion layers (GDLs, 180 μm in thickness) using an ultrasonic atomizer (Sonaer, 130 kHz, low-flow tapered tip) connected with a LF130K focusing plume shaper. The GDLs were placed on a hot plate (150 °C) at a fixed distance of 15 cm between the nozzle tip and the surface of the hot plate. The dispersions were pumped through the nozzle using a Harvard Apparatus syringe pump at a flow rate of 0.5 mL/min. The compressed air supplied to the nozzle was at a pressure of 0.5 bar.

The CO_2ER measurements were conducted in an H-type electrochemical cell containing 0.1 M $KHCO_3$ aqueous solution (as electrolyte). The electrochemical setup is shown in **Figure 6.3.1**. The cathodic compartment was continuously purged with CO_2 gas at a flow rate of 20 mL/min to ensure the electrolyte solution was saturated with CO_2. The GDLs coated with either pristine Cu NPs or PIL/Cu particles were employed as the working electrode (WE), while a Pt wire and an Ag/AgCl electrode were used as the counter electrode (CE) and reference electrode (RE), respectively. The electrochemical bias was provided using SP-200 potentiostat (Biologic) under chronoamperometry mode. Reduction reaction takes place on WE. The reduction reaction of several main products can be expressed by:

$$2H^+ + 2e^- \rightarrow H_2(g) \quad (6.3.1)$$

$$CO_2 + 8H^+ + 8e^- \rightarrow CH_4(g) + 2H_2O \quad (6.3.2)$$

$$CO_2 + 12H^+ + 12e^- \rightarrow C_2H_4(g) + 4H_2O \quad (6.3.3)$$

Correspondingly, an oxidation reaction occurs on CE to complete the circuit within the electrochemical cell. The reaction is given by:

$$2H_2O \rightarrow O_2(g) + 4e^- \quad (6.3.4)$$

The gaseous and liquid products were then quantified using online gas chromatography (GC) and high-performance liquid chromatography (HPLC), respectively.[60]

85% of ohmic resistance (iR) was compensated automatically and the applied potentials were converted to reversible hydrogen electrode (RHE) according to the equation below:

$$E\ vs.RHE\ (V) = E\ vs.Ag/AgCl\ (V) + E^0\ vs.Ag/AgCl\ (V) + 0.059\ pH \quad (6.3.5)$$

where *E vs.* Ag/AgCl is the measured cationic potential and E_0 *vs.* Ag/AgCl is the standard potential of Ag/AgCl electrode (0.1976 V at 25 °C). The pH of the electrolyte (0.1 M $KHCO_3$) was measured to be 6.8. The samples were tested in the potential ranging from -0.8 to -1.2 V *vs.* RHE. The measured current density (*J*) was normalized to the geometric surface area of WE. The product analysis of CO_2ER is mainly conducted by Siddharth Gupta and Dr. Gumaa Nagar from HZB.

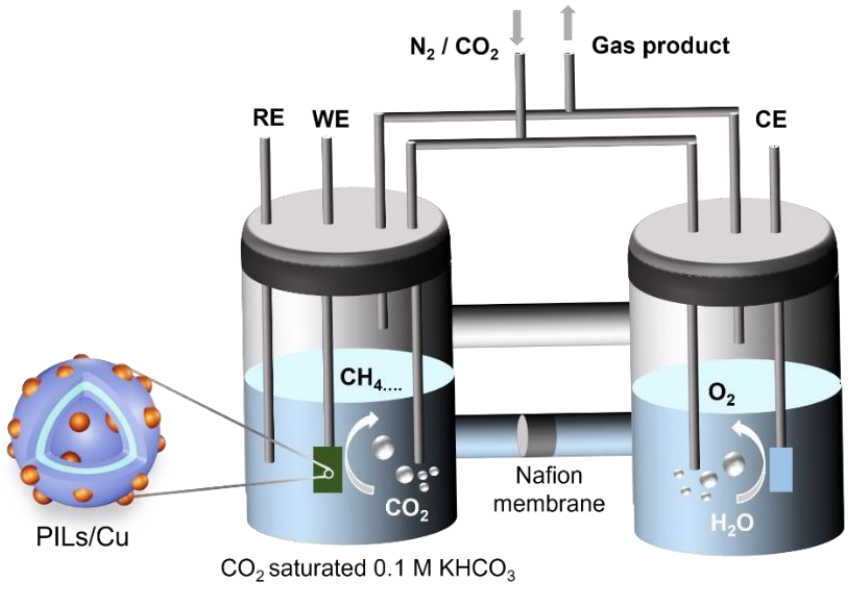

Figure 6.3.1. Setup scheme of a typical H-cell for CO_2ER.

6.3.2 Photothermal conversion performance

MoS_2/C composite particles: the photothermal conversion performance of the MoS_2/C composite particles was measured using their aqueous particle dispersions at various concentrations (0.05 - 0.5 mg/mL), as shown in **Figure 6.3.2**. Specifically, 1 mL of the desired dispersion was stirred at 300 rpm in a quartz cuvette (110-QS Hellma, 10 mm) under the near infrared (NIR) light irradiation using a NIR laser (PhotonTec Berlin, turn-key 808 nm diode laser system, wavelength of 808 nm) at various intensities (2 - 4 W/cm^2) for *ca.* 10 min. To avoid direct heating by light, the thermometer was kept far away from the laser spot, while the distance between the laser spot and the thermometer was fixed at *ca.* 6.5 cm. The temperature change of the dispersion was recorded by a digital thermometer (P300 Thermometer, Dostmann electronics) every 20 s. The IR camera (FLIR-E8 XT) was employed to visualize the temperature changes of the dispersion every 3 min.

GP-CNTs-metal composites: the photothermal conversion performance of metal/GP-CNTs composite was evaluated using the same setup as that for MoS_2/C particles. While, the obtained dispersions in the cuvette were stirred at various concentrations (1 mL, 0.01 - 0.12 mg/mL) under the NIR light irradiation at a fixed intensity of 3 W/cm^2.

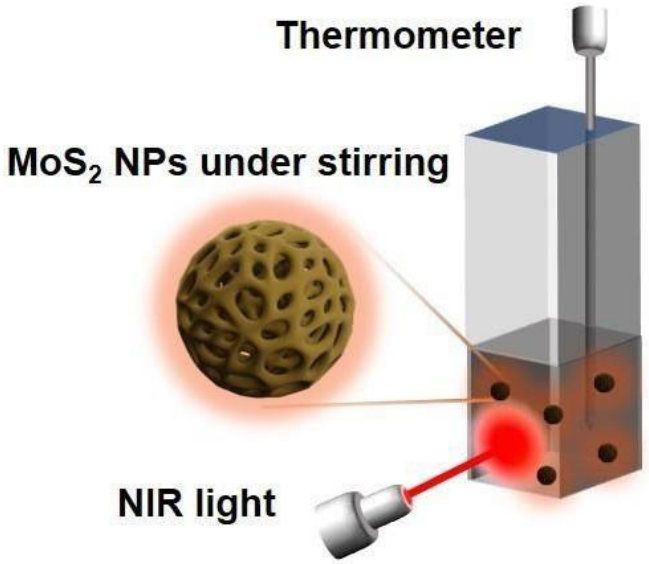

Figure 6.3.2. Setup scheme of photothermal conversion of the MoS_2/C particles (same setup for the metal/GP-CNTs sample).

To quantitatively evaluate the light-to-heat conversion of the obtained dispersions based on the heating-cooling profile (**Figure 6.3.3a**), the photothermal conversion efficiency (η) can be given by:

$$\eta = \frac{hs(T_{max}-T_{sur})-Q_{Dis}}{I(1-10^{A_{808}})} \quad (6.3.6)$$

where h, s, and Q_{Dis} are the heat transfer coefficient, surface area of the container, and heat dissipated from the light absorbed by the quartz sample cell containing pure water, respectively. I and A_{808} are the laser intensity and absorption of dispersion at the wavelength of 808 nm, respectively. T_{sur} and T_{max} are the surrounding temperature and highest temperature of the dispersion, respectively.[122, 123]

To calculate hs, a dimensionless parameter (θ) needs to be introduced and determined by:

$$\theta = \frac{T-T_{sur}}{T_{max}-T_{sur}} \quad (6.3.7)$$

$$t = -\tau_s ln\,(\theta) \tag{6.3.8}$$

where τ_s, t, and T are the time constant, time, and temperature during the cooling stage, respectively. Herein, τ_s can be determined from the slope of the cooling curve (**Figure 6.3.3b**). Then, hs can be determined by:

$$hs = \frac{m_D C_D}{\tau_s} \tag{6.3.9}$$

where m_D and C_D are the mass of water (1 g) and heat capacity (4.2 J/g·°C), respectively.

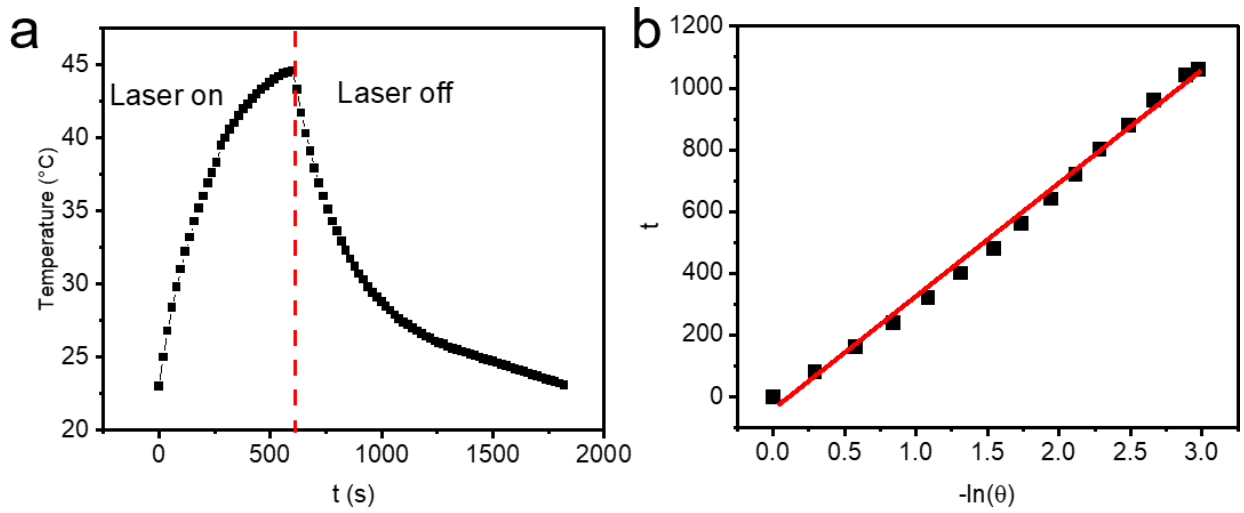

Figure 6.3.3. (a) Temperature variation of dispersion under NIR irradiation. (b) t versus $-ln(\theta)$ obtained from the cooling stage.

6.3.3 Catalytic reduction of 4-Nitrophenol

To exclude the influence of dissolved O_2 molecules in the solvent on the reduction reaction, all the solutions and dispersion were purged by fresh N_2 for 30 min to remove the dissolved O_2 before use.

6.3.3.1 Catalytic reaction in the absence of NIR light

MoS_2/C composite particles: appropriate amounts of MoS_2/C aqueous dispersions (0.1 - 0.25 mL, 1 mg/mL) were sonicated (30 W, 37 kHz) for ~15 min and then added into a clean quartz cuvette

(110-QS Hellma, 10 mm). A fresh 4-NP solution (0.25 mL, 1 mM) was introduced to the MoS_2/C dispersion under stirring at 300 rpm. The dispersion volume was fixed at 2.5 mL by adding the proper amount of fresh water. Finally, the reaction was initialized by quickly introducing a fresh $NaBH_4$ solution (0.5 mL, 0.1 M) at room temperature. The dispersion in the cuvette (light path of 10 mm) was measured by UV-Vis absorption spectroscopy.

GP-CNTs-metal composites: the catalytic reaction of the GP-CNTs-metal composites in the absence of light irradiation was evaluated using the same protocols as that for MoS_2/C particles. While, 1.75 mL of fresh water, 0.25 mL of 4-NP solution (1 mM), and an appropriate amount of GP-CNTs-metal dispersion (50 - 150 μL, 0.1 mg/mL) were successively introduced to a clean cuvette under stirring at 250 rpm. Next, a fresh $NaBH_4$ (0.5 mL, 0.1 M) solution was quickly injected to initialize the reduction reaction of 4-NP at room temperature. Finally, the mixed dispersion in the cuvette was then measured by UV-Vis absorption spectroscopy.

6.3.3.2 Catalytic reaction in the presence of NIR light

MoS_2/C composite particles: A MoS_2/C particle dispersion (0.05 mL, 1 mg/mL) was added in a 4-NP solution (0.5 mL, 2 mM) in a cuvette under stirring at 300 rpm. Next, 0.45 mL of fresh water was introduced to the dispersion. After being irradiated with the NIR laser at the intensity of 3 W/cm^2 for ~15 min, the temperature of the dispersion reached equilibrium. A fresh $NaBH_4$ solution (100 μL, 2 M) was then injected into the mixed dispersion to start the reaction. 0.1 mL of the reaction dispersion was taken out every 40 s and then quickly diluted in 1.9 mL of water. The MoS_2/C particles were then filtered out using the syringe with a filter (Acrodisc with Supor Membrane, polyethersulfone, 0.22 μm in pore size, and 13 mm in diameter), and the residual solution was tested *via* UV-Vis absorption spectroscopy. To calculate the activation energy (E_a) under different heating conditions, the MoS_2 dispersion (0.03 mg/mL) was heated by an external heating plate and NIR light (2 W/cm^2), and the reaction temperature was recorded by the thermometer. In comparison to the NIR-assisted reduction, the reaction without light irradiation was conducted at the same temperature as that under NIR light irradiation.

GP-CNTs-Pd composites: the catalytic reaction of GP-CNTs-Pd under NIR light irradiation was evaluated using the same protocols as that of MoS_2/C particles. While, 0.45 mL of fresh water, 0.5 mL of 4-NP solution (2 mM), and 0.03 mL of the GP-CNTs-Pd dispersion (1 mg/mL) was

successively added in a cuvette and stirred at 300 rpm. The mixed dispersion was irradiated by NIR light (3 W/cm^2) for ~15 min to reach a constant temperature. A fresh $NaBH_4$ solution (100 μL, 2 M) was rapidly introduced to trigger the reaction. To monitor the reduction progress, 0.1 mL of the reaction dispersion was extracted after 5 min and then diluted with 1.9 mL of fresh water. The resulting diluted dispersion was then subjected to filtration using the syringe with a filter (Acrodisc with Supor Membrane, polyethersulfone, 0.22 μm in pore size, and 13 mm in diameter). The remaining solution was eventually analyzed using UV-Vis absorption spectroscopy. In comparison to the NIR-assisted reduction, the non-irradiated reactions were conducted in a water bath heated at the same temperature as the same condition as above.

6.4 Characterization methods

6.4.1 UV-Vis spectroscopy

UV-Vis spectroscopy is commonly used in analytical chemistry for the quantitative or qualitative determination of diverse samples, such as plasmonic metal particles (*e.g.* Au, Ag, and Cu), transition metal ions, and conjugated organic compounds. The detector in a UV-Vis spectrophotometer measures and compares the intensity of light before and after passing through the sample. The intensity of the transmitted light decreases due to the light absorption by the samples at specific wavelengths. The absorbance of a sample solution is based on the Beer-Lambert law that can be given by:

$$A = \varepsilon cL = log_{10}(\frac{I_0}{I}) = log_{10}(\frac{1}{T}) \quad (6.4.1)$$

where A is the absorbance of the sample, L is the path length of the cuvette, c is the sample concentration, I_0 is the initial light intensity, I is the transmitted light intensity, T is the transmittance of the sample, and ε is the molar absorptivity.[124] When passing through a transparent cuvette filled with the sample solution, the light intensity is proportional to the sample concentration.

In this thesis, the dispersion samples were contained in a clean quartz cuvette (110-QS Hellma, 10 mm) and measured on a PerkinElmer Lambda 650 spectrometer at room temperature. The reference spectra of the corresponding composite samples were replaced with water.

6.4.2 Raman spectroscopy

Raman spectroscopy was used to detect the vibration modes of molecules, thus providing a both chemical and structural fingerprint of the samples. Raman spectroscopy detects scattered Raman light from the sample when irradiated by a laser.[125] Raman scattering rarely occurs (*ca.* 1 in 10 million photons), which is an inelastic scattering process with an energy transfer between the molecule and scattered photon (**Figure 6.4.1**). Generally, two types of scattering processes occur: Stokes and anti-Stokes scattering. Stokes Raman scattering refers to the scattering of photons that lose energy during the interaction with a measured molecule. Inversely, if the scattered photon gains from a molecule, its wavelength will decrease, which is often defined as anti-Stokes Raman scattering.

Herein, the Raman spectra were obtained on an InVia 2R9X81 Raman spectrometer with a detector of Renishaw Centrus 2MYA08 and a HeNe laser (a wavelength of 532 nm). Before measurement, the dispersion samples were completely dried on a clean silicon wafer overnight inside the fume hood.

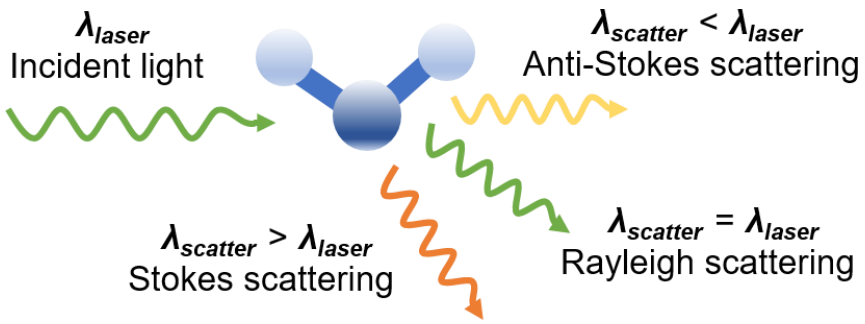

Figure 6.4.1. Three types of scattering processes that occur when the incident light interacts with a molecule.

6.4.3 Nuclear magnetic resonance

Nuclear magnetic resonance (NMR) measurements were used to determine the chemical structure of as-synthesized samples. The ^{1}H-NMR spectra were recorded at room temperature using a Bruker DPX-400 spectrometer operating at 400 MHz. Dimethyl sulfoxide-d_6 (DMSO-d_6) was used as the solvent to dissolve the samples (*i.e.* ILs, PILs, and GP molecules).

6.4.4 X-ray photoelectron spectroscopy

The quasi *in situ* X-ray photoelectron spectroscopy (XPS) measurements were carried out on a SPECS PHOIBOS 100 analyzer with Al K_α radiation (1486.74 eV). The CO_2ER experiments were conducted in an O_2-free glovebox using the H-type cell specified above and under the same conditions. After the electrolysis, the samples were completely dried and stored in the glovebox. Next, the samples were transferred to the XPS vacuum chamber using a transfer arm, which was kept in an inert atmosphere.[126] The oxidation state of Pd in the GP-CNTs-Pd composite was determined by XPS with an ESCA-Lab-220i-XL X-ray photoelectron spectrometer (Thermo Fisher Scientific) with Al K_α sources (hv = 1486.6 eV).

6.4.5 Gas chromatography

Gas chromatography (GC) was used to analyze the gaseous products (*e.g.* H_2, CO, CH_4, and C_2H_4) from CO_2ER. The products were measured on an online GC (Thermo Scientific, Trace 1310, double column) equipped with a flame ionization detector (FID) for multi-carbon (C_{2+}) products and a pulse discharge detector for light components (*e.g.* H_2, CO, CH_4). Helium (He) was used as the carrier gas. The mixed gas products were first diluted with pure CO_2 gas and then measured every 10 min for ~3h.[60]

6.4.6 High-performance liquid chromatography

High-performance liquid chromatography (HPLC) was employed to quantify the liquid products (*e.g.* methanol and formic acid) from CO_2ER. The measurement was performed on an HPLC (Thermo Scientific, UltiMate 3000 Series, Dionex, single column) equipped with a variable wavelength detector (VWD, UltiMate 3000, Dionex), a refraction index (RefractoMax 520, ERC) detector, and an automatic sampling unit. A fresh 5 mM H_2SO_4 solution was used as an eluent. After the reaction, 1 mL of the electrolyte solution containing the liquid products was collected in a clean glass vial and transferred to the automatic unit for the measurement.[60]

6.4.7 Differential scanning calorimetry

Differential scanning calorimetry (DSC) is a thermo-analytical technique that can be used to detect the phase transitions of samples. The IL monomer was measured on a Netzsch Phoenix F204 instrument at a heating rate of 10 °C /min under a continuous N_2 flow.

6.4.8 Thermogravimetric analysis

Thermogravimetric analysis (TGA) is applied to estimate the mass fraction of each component in the composite materials. During the high-temperature pyrolysis in a synthetic air atmosphere, organic polymers (*e.g.* BCPs) or carbon materials (*e.g.* amorphous carbon and CNTs) can be burned out, while the inorganic materials or inert metals would be left in the measured container.

Herein, the samples were measured on PerkinElmer (TGA 8000) in a temperature range of 25-900 °C at a heating rate of 10 °C/min in synthetic air. Vigorous oxidation reaction occurs during heating process in the air atmosphere.

For MoS_2/C samples, the chemical reactions are shown below:

$$3O_2(g) + MoS_2(s) \rightarrow MoO_3(s) + SO_3(g) \quad (6.4.2)$$

$$O_2(g) + C(s) \rightarrow CO_2(g) \quad (6.4.3)$$

Herein, we assume the initial amount of carbon and MoS_2 are *x* and *y*, respectively. The molar masses of MoS_2 and MoO_3 are 160.1 g/mol and 143.9 g/mol, respectively. If the final mass of the residual is *z* %, the mass equilibrium before and after calcination can be given by:

$$x + y = 100\ \% \quad (6.4.4)$$

$$\frac{143.9}{160.1} \times y = z\ \% \quad (6.4.5)$$

For PILs/Cu composite particles, PILs were burned out and metallic Cu was oxidized to CuO during calcination, respectively. The chemical reaction can be given by:

$$O_2(g) + 2Cu(s) \rightarrow 2CuO(s) \quad (6.4.6)$$

The molar masses of Cu and CuO are 64.5 g/mol and 79.5 g/mol, respectively. If the final mass determined from TGA curve after calcination is *x* %, the original mass fraction of Cu in the PILs/Cu composites (*i.e.* the loading amount of Cu) is thereby 0.8*x* %.

6.4.9 Gel permeation chromatography

Gel permeation chromatography (GPC) is a typical column chromatographic technique commonly used to determine the relative molecular weight and the corresponding distribution of polymer samples. The principle of GPC separation is based on the difference in polymer size or hydrodynamic volume (radius of gyration). As shown in **Figure 6.4.2**, the polymer sample is first dissolved in a good solvent that is also used as an eluent (*i.e.* mobile phase). The polymer solution after filtration is injected into the column composed of porous gel particles. Afterwards, larger sizes of polymer chains are excluded from penetrating the pores of gel particles, thus showing a shorter eluted time. While, smaller sizes of polymer chains can enter the porous channels, increasing their total retention time in the column.[127]

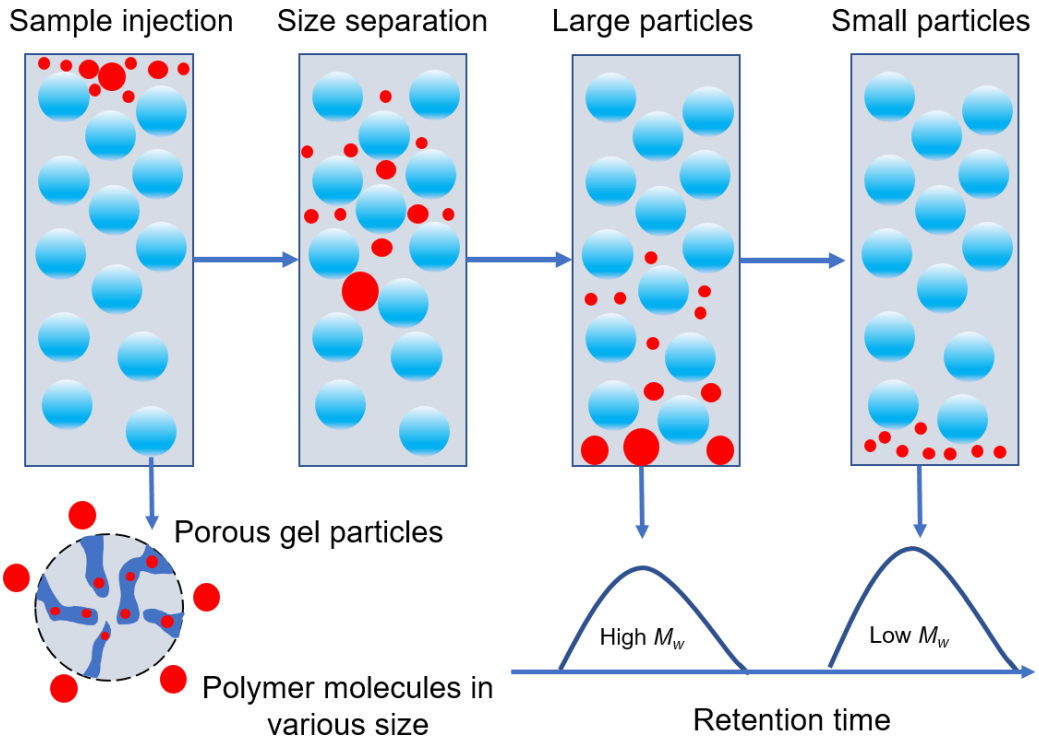

Figure 6.4.2. Scheme of the working mechanism of GPC.

Number-average molecular weight (M_n) and molecular weight distributions of the PIL samples were determined by GPC. The GPC equipment was equipped with a PSS SECcurity 1260 autosampler injector, a PSS SECcurity 1260 HPLC pump, and a PSS SECcurity 1260 differential refractometer (RID) detector using PSS columns (PSS GRAM, 10 mm, Guard + 100 Å + 2 × 10,000 Å). A fresh *N*, *N*-dimethylacetamide (DMAc) solution containing lithium bromide (LiBr,

10 mg/mL) was used as the eluent at a flow rate of 1.0 mL/min at 70 °C. [128] The PIL powder after freeze-drying was first dissolved in the DMAc/LiBr solution and kept shaking at 50 °C for *ca.* 1 h to ensure the complete dissolution. Afterwards, the solutions (*ca.* 3 mg/mL) were left overnight at room temperature for equilibration. The as-prepared solutions were filtered through a syringe filter (average pore size of 1.0 μm) before injection. The M_n and its distributions were calculated based on linear polystyrene standards (M_n = 470-2520000 g/mol) for calibration by a PSS WinGPC UniChrom Version 8.4 software.

6.4.10 Scanning electron microscopy

Scanning electron microscopy (SEM) is used to obtain information about composition, surface morphology, and geometry by scanning the samples with electron beams. Limited by the low resolution (δ) of optical microscopy, the electron microscope possesses a much higher resolution, which can be explained by:

$$\delta = \frac{0.61\lambda}{\mu \sin\beta} \tag{6.4.7}$$

where λ, μ, and β are the wavelength of the radiation, refractive index of the viewing medium, and semi-angle of collection of the magnifying lens ($\mu sin\beta$ also refers to the numerical aperture), respectively.[129] After approximation, the resolution is nearly equal to half the wavelength of incident light. The relationship between the wavelength and energy (E) of electrons accelerated in the microscope can be expressed by Louis de Broglie's equation if ignoring relativistic effects and inconsistency in units [130]:

$$\lambda = \frac{1.22}{\sqrt{E}} \tag{6.4.8}$$

Thus, a narrow beam of high-energy electrons accelerated by a high voltage (normally below 50 kV) source provides a high resolution to visualize the morphology of the samples. The excited electrons interact with atoms of the sample, which yields various characteristic signals including secondary electrons, backscattered electrons, and X-rays, as shown in **Figure 6.4.3**.

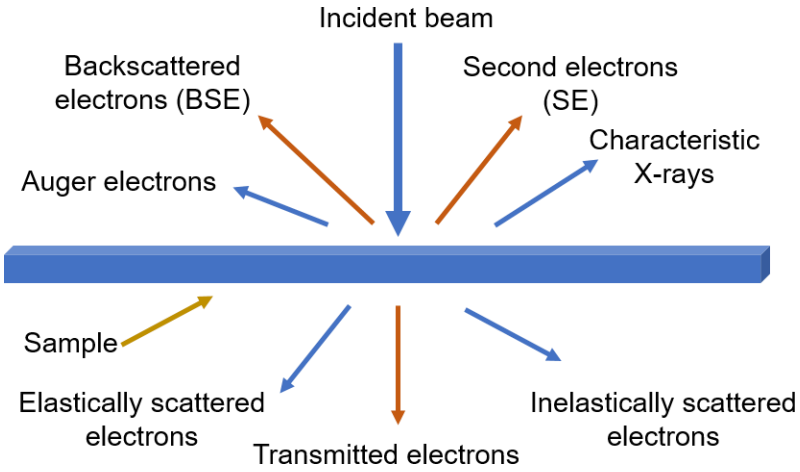

Figure 6.4.3. Various signals produced through the interactions between incident electrons with samples.

In SEM, the surface morphology of the samples is often spotted by secondary electrons (SE) and backscattered electrons (BSE). The energy or wavelength of these characteristic X-rays can be measured by Energy-dispersive X-ray spectroscopy (EDX), thus predominantly used to identify the elements and corresponding distributions in the sample.

In this work, the surface morphologies of the samples were recorded on a LEO GEMINI 1530 microscope equipped with an EDX (Zeiss) using an In-Lens detector (SE mode) operated at 3 - 10 kV. All the dispersion samples (~50 μL, 0.05 mg/mL) were dropped on a clean silicon wafer and fully dried at 60 °C in an oven for 4 h. Afterwards, the samples were coated with a thin carbon layer (*ca.* 5 nm) before imaging to enhance the conductivity using a carbon sprayer.

6.4.11 Transmission electron microscopy

Transmission electron microscopy (TEM) is a high-resolution imaging technique that can be used to obtain various information such as morphology, crystal structure, and chemical composition. Unlike SEM, the electron beams in TEM generated by much higher voltage (typically 100 - 300 kV) are able to transmit through a specimen to form a two-dimensional image. The imaging mechanism mainly relies on the contrast (or differences) in the thickness or density, atomic number, crystal structure or orientation, energy loss of transmitted electrons, and many more.

Normal TEM: The TEM measurements were performed on a JEOL JEM-2100 instrument operated at an accelerating voltage of 200 kV. Continuous carbon-coated copper TEM grids (200 mesh, Science Services, Germany) were used for conventional TEM measurements after treated with glow discharge for ~50 s. The sample dispersion (~5 μL, 0.1 wt.%) was dropped onto the grid to prepare the TEM specimen. After completely drying inside a fume hood for ~2 h (depending on the dispersion solvent), the specimen on the grid was loaded on the sample holder and then inserted into the column for imaging.

Cryogenic transmission electron microscopy (cryo-TEM): Native or fine structures of a soft matter (*e.g.* polymer assemblies) in dispersion are hard to maintain in conventional TEM due to the drying effect, cryo-TEM was thereby needed.[131] Cryo-TEM specimens were prepared by dropping 4 μL of a dispersion sample onto Lacey carbon-coated copper TEM grids (200 mesh, Science Services) and plunge-frozen into liquid ethane with an FEI Vitrobot Mark IV set at 4 °C and 95% humidity. Vitrified grids were either transferred directly to the microscope cryogenic transfer holder (Gatan 914, Gatan, Munich, Germany) or stored in a liquid N_2 tank. The TEM equipment was operated at an accelerating voltage of 200 kV with a defocus of the objective lens at 2.5 - 3 μm. The imaging process was carried out at *ca.* - 183 °C and the corresponding images were recorded using a bottom-mounted 4 k × 4 k CMOS camera (TemCam-F416, TVIPS, Gauting, Germany). The total electron dose in each micrograph was kept below 20 $e^-/Å^2$.

Scanning transmission electron microscopy (STEM): STEM was used to study the elemental mapping of the as-synthesized GP-CNTs-Pd sample. STEM for electron energy-loss spectroscopy (EELS) analysis was performed on a Nion HERMES microscope (Nion Co., Kirkland, WA, USA) equipped with a Dectris ELA direct electron detector (Dectris AG, Baden-Daettwil, Switzerland). Similar to the sample preparation for cryo-TEM, ~5 μL of the GP-CNTs-Pd dispersion was placed on a lacey carbon-coated copper grid (200 mesh, Electron Microscopy Sciences, Hatfield, PA) and followed by drying under mild conditions.

6.4.12 Powder X-ray diffraction

Powder X-ray diffraction (XRD) is a powerful method that can provide information such as phase identification, sample purity, and crystallite size of the samples. The incident X-ray beam at a certain angle enters (10 - 80°) the crystal lattice and is diffracted by the atom layers in the

samples.[132] This constructive interference phenomenon can be described by Bragg's equation (6.4.9):

$$n\lambda = d \sin\theta \quad (6.4.9)$$

where n, λ, d, and θ are the diffraction order, wavelength of X-ray, crystal spacing, and diffraction angle, respectively. The position of the diffraction peaks is determined by the distance between parallel crystal planes. The diffraction pattern of a mixture (or composite materials) is the sum of the diffraction patterns of each component.

The XRD measurements herein were mainly used to detect the crystal structure of the as-prepared samples. The XRD was conducted on Bruker D8 using a monochromatized X-ray beam with Cu K_α radiation at a scan rate of 0.05°/min at room temperature. All the samples were collected after freeze-drying and kept in an air-tight XRD holder (Bruker) to avoid possible oxidation of metal nanoparticles during measurement.

6.4.13 Small angle X-ray scattering and wide angle X-ray scattering

Small angle X-ray scattering (SAXS) and wide angle X-ray scattering (WAXS) measurements are conducted to obtain both the morphology and size information of the samples. In comparison to powder XRD, SAXS is typically recorded at smaller scattering angles (0.1-10°). Particularly, a crystalline sample is not essential in SAXS.[133, 134] Characteristic distances of partially ordered structures can be detected by SAXS/WAXS. The average distance (d) between repeated spacing (or long period) is then roughly as a function of the scattering vector (q), as presented in the following equations:

$$q = \frac{4\pi \sin\theta}{\lambda} \quad (6.4.10)$$

$$d = \frac{2\pi}{q} \quad (6.4.11)$$

where q, λ, and θ are the scattering vector, wavelength of X-ray, and scattering angle, respectively. When scattering from spherical particles dispersed in a medium, scattered intensity (I) can be expressed by:

$$I(q) = n\Delta\rho^2 V^2 P(q)\, S(q) \quad (6.4.12)$$

where *n, Δρ, V, P(q),* and *S(q)* are the number of scatters, the difference in electron density, form factor, and structure factor, respectively.[135] Therefore, the samples with higher electron density exhibit a stronger contribution to the scattering signal. The other parameters such as the form and structure factor also influence the overall scattering intensity in the system.

The PIL dispersions were measured at the four-crystal monochromator (FCM) beamline of Physikalisch-Technische Bundesanstalt (PTB) at the BESSY II synchrotron radiation facility (Helmholtz-Zentrum Berlin, Germany).[136] The PIL dispersions were measured in tightly sealed borosilicate glass cuvettes (Hilgenberg, Malsfeld, Germany, 80.0 × 4.2 × 1.25 mm^3). All the measurements were performed at a photon energy of 8000.0 ± 0.8 eV. The SAXS/WAXS images were recorded with a Pilatus 1M detector (Dectris Ltd., Baden, Switzerland) at a sample-to-detector (SD) distance of 5.107 ± 0.005 m for SAXS and a distance of 0.206 ± 0.002 m for WAXS measurement, respectively.[137] These SD distances were calibrated with the long-period spacing (001) peak of silver behenate by the triangulation method. To determine the scattering signal resulting from the used container and solvent, the empty cuvette and separated cuvette containing pure water were measured as background, respectively. In addition, the lower section of the cuvettes was filled with Fluorinert FC-3283 acquired from Iolitec (Heilbronn, Germany) to determine the optical path length of the cuvettes.[138] The SAXS/WAXS images were recorded on multiple spots along the cuvettes and averaged to eliminate the possible sedimentation effects. Each sample was repeated 3 times to detect potential X-ray damage to the PIL particles. The obtained SAXS/WAXS images were circularly averaged and the SAXS curves were accordingly fitted using custom-made software with a model for hollow spherical core-shell particles under the assumption of a log-normal size distribution. The uncertainties of the fit parameters for the overall diameter, shell thickness, and errors of the fits were determined based on the reduced χ^2- method.[139]

6.4.14 Dynamic light scattering

Dynamic light scattering (DLS) is a technique to measure the hydrodynamic size of particles in dispersion. Particles dispersed in a suitable solvent continuously undergo Brownian motion, resulting in a fluctuated light scattering over time. In addition, the size-dependent behavior of scattering intensity variations can provide information on the dynamics and motion of particles in a scattering system. Large particles tend to show a slower change in scattering intensity compared

to smaller particles.[140] Specifically, the velocity of the Brownian motion can be indicated by the translational diffusion coefficient (D), the hydrodynamic diameter (D_h) is thus calculated based on the Stokes-Einstein equation (6.4.13):

$$D_h = \frac{kT}{3\pi\eta D} \quad (6.4.13)$$

where k, η, and T are Boltzmann constant, viscosity, and absolute temperature of the dispersion, respectively.

The average D_h and distributions of PIL dispersions were determined by using a Malvern Zetasizer Nano ZS at room temperature. A HeNe laser (wavelength of 632.8 nm, output power of 25 mW) was utilized as the light source, and the scattered light was detected at a fixed angle of 173°. The PIL dispersion (~0.01 mg/mL) was filtered with a syringe filter (Acrodisc with Supor Membrane, 25 mm in diameter, and 5 μm in pore size) and subsequently placed in a disposable cuvette (DTS0012, polystyrene, 12 mm). Each measurement was repeated 5 times at room temperature.

6.4.15 Nitrogen adsorption/desorption

Nitrogen adsorption/desorption at low-temperature was used for porous structure analysis. N_2 adsorption/desorption isotherms were obtained using a Quantachrome Autosorb-1 system at 77 K. The specific surface area of porous MoS_2/C particles was calculated using Brunauer-Emmett-Teller (BET) method based on a multipoint analysis and the pore size distributions were obtained from Barrett-Joyner-Halenda (BJH) method. Before all measurements, samples were outgassed at 100 ºC for 12 h under vacuum.

List of Abbreviations

3-MPA	3-Mercaptopropionic acid
4-AMP	4-aminophenol
4-NP	4-Nitrophenol
AAO	Anodic aluminum oxide
Ag	Silver
$AgNO_3$	Silver nitrate
ATRP	Atom transfer radical polymerization
Au	Gold
BCPs	Block copolymers
BET	Brunauer-Emmett-Teller
BHT	2,6-Di-tert-butyl-4-methylphenol
BJH	Barrett-Joyner-Halenda
CNTs	Carbon nanotubes
CO_2ER	CO_2 electroreduction
cryo-TEM	Cryogenic transmission electron microscopy
Cu	Copper
$CuAc_2•H_2O$	Copper acetate monohydrate
DLS	Dynamic light scattering
DSC	Differential scanning calorimetry
EELS	Electron energy loss spectroscopy
FT-IR	Fourier transform infrared spectroscopy
GC	Gas chromatography
GP	Glycopeptide
GPC	Gel permeation chromatography
H_2SO_4	Sulfuric acid
HAADF	High-angle annular dark-field
$HAuCl_4•3H_2O$	Gold chloride trihydrate
HCl	Hydrochloric acid
HER	Hydrogen evolution reaction

HNPs	Hollow nanovesicles
HNVs	Hollow nanoparticles
HPLC	High-performance liquid chromatography
H_x	4-hydroxylamine
ILs	Ionic liquids
KBr	Potassium bromide
$KHCO_3$	Potassium hydrogen carbonate
LH model	Langmuir-Freundlich model
MoS_2	Molybdenum disulfide
$N_2H_4•H_2O$	Hydrazine hydrate solution
$NaBH_4$	Sodium borohydride
NaOH	Sodium hydroxide
$(NH_4)_2MoS_4$	Ammonium tetrathiomolybdate
NIR	Near infrared
NMP	Nitroxide-mediated polymerization
NMR	Nuclear magnetic resonance
NVs	Nanovesicles
Pd	Palladium
$PdCl_2$	Palladium chloride
PILs	Poly(ionic liquid)s
PISA	Polymerization-induced assembly
PLNPs	Pomegranate-like nanoparticles
PNPs	Porous nanoparticles
PS-*b*-P2VP	Polystyrene-*b*-poly(2-vinylpyridine)
RAFT	Reversible addition-fragmentation transfer
SAXS	Small-angle X-ray scattering
SD	Sample-to-detector
SEM	Scanning electron microscopy
SNSs	Solid nanospheres
STEM	Scanning transmission electron microscopy
TEM	Transmission electron microscopy

TGA	Thermogravimetric analysis
VA86	2,2'-Azobis[2-methyl-N-(2-hydroxyethyl) propionamide]
WAXS	Wide angle X-ray scattering
WS_2	Tungsten disulfide
XPS	X-ray photoelectron spectroscopy
XRD	X-ray diffraction

a	Size of the segregated domains
A	Arrhenius pre-factor
A_H	Hamaker constant
c	Concentration
d	Long period determined from Bragg' equation
D	Translational diffusion coefficient
D_h	Hydrodynamic diameter
D_0	Diameter
E	Standard potentials
E_a	Activation energy
ε	Interaction energies of each block
f	Volume fraction of one block
F	Faradaic constant
G	Attraction/repulsion energy between two particles
h	Distance between two particles
i	Current
I	Absorption/scattering intensity
J	Current density
K	Langmuir adsorption constant
k_1	Surface area-normalized rate constant
k_{app}	Apparent rate constant
l	Statistical segment length
L_0	Length
m	Electron transfer number
M_n	Number-averaged molecular weight

n	Number of charge density/scatters
$P(q)$	Form factor
q	Scattering vector
R	Radius
S	Normalized specific surface area
S_{BET}	Specific surface area based on BET method
$S(q)$	Structure factor
t	Time
T	Temperature
x	Molar ratio of one block
z	Boltzman constant
δ	Solubility parameter
η	Photothermal conversion efficiency
θ	Actual coverage fraction
κ	Debye-Hückel parameter
χ	Flory-Huggins interaction parameter
γ	Reduced surface potential

List of Publications

Related Articles:

I. **X. Pan**, Z. Kochovski, Y. Wang, R. M. Sarhan, E. Härk, S. Gupta, S. Stojkovikj, G. A. El - Nagar, M. T. Mayer, R. Schürmann, J. Deumer, C. Gollwitzer, J. Yuan, and Y Lu, Poly(ionic liquid) nanovesicles via polymerization induced self-assembly and their stabilization of Cu nanoparticles for tailored CO_2 electroreduction, *J. Colloid Interface Sci*. **2023**, 637, 408-420.

II. **X. Pan**, R. M. Sarhan, Z. Kochovski, G. Chen, A. Taubert, S. Mei, and Y. Lu, Template synthesis of dual-functional porous MoS_2 nanoparticles with photothermal conversion and catalytic properties, *Nanoscale* **2022**, 14, 6888.

III. **X. Pan**, R. Liu, Z. Yu, B. Haas, Z. Kochovski, S. Cao, R. M. Sarhan, G. Chen, and Y. Lu, Multi-functionalized carbon nanotubes towards green fabrication of heterogeneous catalyst platforms with enhanced catalytic properties under NIR light irradiation, submitted to *Nanoscale*, accepted (DOI: 10.1039/D3NR02607H).

Unrelated publications:

I. **X. Pan**, S. Mei, Y. Lu, J. Yuan, Synthetic advances of internally nanostructured polymer particles: From and beyond block copolymer, *Nano Select* **2020**, 1, 639-658.

II. M. Elibol, L. Jiang, D. Xie, S. Cao, **X. Pan**, E. Härk, and Y. Lu, Nickel oxide decorated halloysite nanotubes as sulfur host materials for lithium-sulfur batteries, *Global Challenges*, **2023**, 7, 2300005.

III. K. Kheirabad, **X. Pan**, S. Long, Z. Kochovski, S. Zhou, Y. Lu, G. McInerney, J. Yuan, Colloidal dispersion of poly(ionic liquid)/Cu composite particles for protective surface coating against SAR-CoV-2, *Nano Select* **2022**, 3, 227-232.

IV. D. Xie, Y. Xu, Y. Wang, **X. Pan**, E. Härk, Z. Kochovski, A. Eljarrat, J. M üller, C. T. Koch, J. Yuan, and Y. Lu, Poly(ionic liquid) nanovesicle-templated carbon nanocapsules functionalized with uniform iron nitride nanoparticles as catalytic sulfur host for Li-S batteries, *ACS Nano* **2022**, 16, 7, 10554-10565.

Acknowledgement

First of all, I would like to highly appreciate Prof. Dr. Yan Lu for providing me this precious opportunity to study at the University of Potsdam and Helmholtz-Zentrum Berlin. Without her patient instructions and constructive advice, I could never complete this thesis work.

I would like to thank Prof. Dr. Shilin Mei for his invaluable mentorship and inspiring insights into polymer assembly and functionalization. His guidance has encouraged me to overcome challenges and create novel materials with unique nanostructures. I am also deeply grateful to Prof. Dr. Jiayin Yuan for introducing me to the field of PILs, and to Prof. Dr. Guosong Chen for the continuous collaboration in biomaterial-based assemblies and composites.

I would like to express my appreciation to Dr. Zdravko Kochovski for his expertise in cryo-TEM and his invaluable and patient assistance throughout the measurement and analysis of electronic microscopy. His support in TEM significantly enhanced my understanding of the native architecture of soft matters.

I am grateful to Dr. Radwan M. Sarhan, Dr. Rongying Liu, and Dr. Zhilong Yu. Their expertise and collaboration have been significant in my work on photothermal plasmonic materials, biomolecule assembly, and CNTs processing, respectively. Furthermore, I am grateful for the support and collaboration with Siddharth Gupta, Dr. Gumaa Nagar, and Dr. Matthew Mayer in our work on CO_2 conversion. I would like to thank Dr. Robin Schürmann and D r. Christian Gollwitzer from PTB and Dr. Eneli Härk in SAXS/WAXS measurement and data interpretation.

I also thank my current and former labmates, Dongjiu Xie, Ping Feng, Sijia Cao, Lihong Jiang, Dr. Henry Halim, Dr. Yaolin Xu, Dr. Shengxuan Lin, Yael Rodriguez Ayllon, Dr. Chenxiao Lin, Dr. Ting Quan, Dr. Yuhang Zhao, and many more, for their strong support throughout our work and leisure time. I would also like to extend my sincere appreciation to our secretary Linda Schmalz for her constant support in the administration of the institute.

I would like to acknowledge the joint project from Deutsche Forschungsgemeinschaft (DFG) for the financial support during these years.

Finally, I would like to express my deepest gratitude to my family for their long-term support and encouragement throughout my PhD life.

Selbstständigkeitserklärung

Hiermit erkläre ich die vorliegende Arbeit selbst verfasst und nur unter Zuhilfenahme der angegebenen Hilfsmittel angefertigt zu haben.

Ferner erkläre ich, dass ich nicht anderweitig mit oder ohne Erfolg versucht habe, eine Dissertation einzureichen oder mich einer Doktorprüfung zu unterziehen.

Potsdam, 2023

Xuefeng Pan

Bibliography

1. N. Pal and A. Bhaumik, *Adv. Colloid Interface Sci.*, 2013, **189-190**, 21-41.
2. L. Zhang, L. Jin, B. Liu and J. He, *Frontiers in chemistry*, 2019, **7**, 22.
3. A. Thomas, F. Goettmann and M. Antonietti, *Chem. Mater.*, 2008, **20**, 738-755.
4. Y. Li, J. Liu, S. Wang, L. Zhang and B. Shen, *Composites Part B: Engineering*, 2020, **182**, 107615.
5. H. Yabu, *Polym. J.*, 2013, **45**, 261-268.
6. R. R. Poolakkandy and M. M. Menamparambath, *Nanoscale Adv.*, 2020, **2**, 5015-5045.
7. B. R. Thompson, T. S. Horozov, S. D. Stoyanov and V. N. Paunov, *J. Mater. Chem. A*, 2019, **7**, 8030-8049.
8. S.-Y. Zhang, Q. Zhuang, M. Zhang, H. Wang, Z. Gao, J.-K. Sun and J. Yuan, *Chem. Soc. Rev.*, 2020, **49**, 1726-1755.
9. N. V. Plechkova and K. R. Seddon, *Chem. Soc. Rev.*, 2008, **37**, 123-150.
10. J. Yuan, D. Mecerreyes and M. Antonietti, *Prog. Polym. Sci.*, 2013, **38**, 1009-1036.
11. W. Qian, J. Texter and F. Yan, *Chem. Soc. Rev.*, 2017, **46**, 1124-1159.
12. J. Yuan, S. Soll, M. Drechsler, A. H. E. Müller and M. Antonietti, *J. Am. Chem. Soc.*, 2011, **133**, 17556-17559.
13. H. Luo, Y. V. Kaneti, Y. Ai, Y. Wu, F. Wei, J. Fu, J. Cheng, C. Jing, B. Yuliarto and M. Eguchi, *Adv. Mater.*, 2021, **33**, 2007318.
14. Y. Mai and A. Eisenberg, *Chem. Soc. Rev.*, 2012, **41**, 5969-5985.
15. A. Levin, T. A. Hakala, L. Schnaider, G. J. L. Bernardes, E. Gazit and T. P. J. Knowles, *Nature Reviews Chemistry*, 2020, **4**, 615-634.
16. M. C. Herrera-Beurnio, J. Hidalgo-Carrillo, F. J. López -Tenllado, J. Martin-Gómez, R. C. Estévez, F. J. Urbano and A. Marinas, *Catalysts*, 2021, **11**, 1364.
17. A. Freeman, *Biomimetics*, 2017, **2**, 14.
18. Y. Fu, X. Wang, J. Zhang and W. Li, *Curr. Opin. Biotechnol.*, 2014, **28**, 33-38.
19. Z. Lei, B. Chen, Y.-M. Koo and D. R. MacFarlane, *Journal*, 2017, **117**, 6633-6635.
20. S. K. Singh and A. W. Savoy, *J. Mol. Liq.*, 2020, **297**, 112038.
21. S.-h. Liu, H. Wang, J.-k. Sun, M. Antonietti and J. Yuan, *Acc. Chem. Res.*, 2022, **55**, 3675-3687.
22. M. G. Cowan, D. L. Gin and R. D. Noble, *Acc. Chem. Res.*, 2016, **49**, 724-732.
23. J. Yuan and M. Antonietti, *Polymer*, 2011, **52**, 1469-1482.
24. J.-K. Sun, Z. Kochovski, W.-Y. Zhang, H. Kirmse, Y. Lu, M. Antonietti and J. Yuan, *J. Am. Chem. Soc.*, 2017, **139**, 8971-8976.
25. Y. Lu and W. Chen, *Chem. Soc. Rev.*, 2012, **41**, 3594-3623.
26. P. Hervés, M. Pérez -Lorenzo, L. M. Liz-Marzán, J. Dzubiella, Y. Lu and M. Ballauff, *Chem. Soc. Rev.*, 2012, **41**, 5577-5587.
27. X.-F. Yang, A. Wang, B. Qiao, J. Li, J. Liu and T. Zhang, *Acc. Chem. Res.*, 2013, **46**, 1740-1748.
28. X.-Q. Li, G.-Y. Duan, J.-W. Chen, L.-J. Han, S.-J. Zhang and B.-H. Xu, *Appl. Catal. B*, 2021, **297**, 120471.
29. H. Tian, S. Zhu, F. Xu, W. Mao, H. Wei, Y. Mai and X. Feng, *ACS App. Mater. Interfaces*, 2017, **9**, 43975-43982.
30. R. Barik and P. P. Ingole, *Current Opinion in Electrochemistry*, 2020, **21**, 327-334.
31. J. Joo, T. Kim, J. Lee, S. I. Choi and K. Lee, *Adv. Mater.*, 2019, **31**, 1806682.

32. S. Chandrasekaran, L. Yao, L. Deng, C. Bowen, Y. Zhang, S. Chen, Z. Lin, F. Peng and P. Zhang, *Chem. Soc. Rev.*, 2019, **48**, 4178-4280.
33. J.-W. Xu, K. Yao and Z.-K. Xu, *Nanoscale*, 2019, **11**, 8680-8691.
34. L.-Q. Zhang, S.-G. Yang, L. Li, B. Yang, H.-D. Huang, D.-X. Yan, G.-J. Zhong, L. Xu and Z.-M. Li, *ACS App. Mater. Interfaces*, 2018, **10**, 40156-40167.
35. Q. Liu, X. Liu, H. Feng, H. Shui and R. Yu, *Chem. Eng. J.*, 2017, **314**, 320-327.
36. Y. J. Tang, M. R. Gao, C. H. Liu, S. L. Li, H. L. Jiang, Y. Q. Lan, M. Han and S. H. Yu, *Angew. Chem.*, 2015, **127**, 13120-13124.
37. A. Brito, S. Kassem, R. L. Reis, R. V. Ulijn, R. A. Pires and I. Pashkuleva, *Chem*, 2021, **7**, 2943-2964.
38. S. Gim, Y. Zhu, P. H. Seeberger and M. Delbianco, *Wiley Interdisciplinary Reviews: Nanomedicine and Nanobiotechnology*, 2019, **11**, e1558.
39. M. A. Khalilzadeh, S. Y. Kim, H. W. Jang, R. Luque, R. S. Varma, R. A. Venditti and M. Shokouhimehr, *Materials Today Chemistry*, 2022, **24**, 100869.
40. L. Su, Y. Feng, K. Wei, X. Xu, R. Liu and G. Chen, *Chem. Rev.*, 2021, **121**, 10950-11029.
41. H. Unal Gulsuner, H. Ceylan, M. O. Guler and A. B. Tekinay, *ACS App. Mater. Interfaces*, 2015, **7**, 10677-10683.
42. S. Ji, W. Shen, L. Chen, Y. Zhang, X. Wu, Y. Fan, F. Fu and G. Chen, *Colloids Surf. Physicochem. Eng. Aspects*, 2019, **564**, 59-68.
43. S. Sivakova and S. J. Rowan, *Chem. Soc. Rev.*, 2005, **34**, 9-21.
44. A. Ciesielski, M. El Garah, S. Masiero and P. Samorì, *Small*, 2016, **12**, 83-95.
45. A. Mittal, S. Prasad, P. K. Mishra, S. K. Sharma and B. Parshad, *Materials Advances*, 2021, **2**, 3459-3473.
46. R. Liu, R. Zhang, L. Li, Z. Kochovski, L. Yao, M.-P. Nieh, Y. Lu, T. Shi and G. Chen, *J. Am. Chem. Soc.*, 2021, **143**, 6622-6633.
47. J. Zhang, K. Zhou, Y. Zhang, M. Du and Q. Wang, *Adv. Mater.*, 2019, **31**, 1901485.
48. L. Zhang, X. Yue, N. Li, H. Shi, J. Zhang, Z. Zhang and F. Dang, *Anal. Chim. Acta*, 2019, **1088**, 63-71.
49. J. Cai, S. Kimura, M. Wada and S. Kuga, *Biomacromolecules*, 2009, **10**, 87-94.
50. G. Biliuta and S. Coseri, *Coord. Chem. Rev.*, 2019, **383**, 155-173.
51. A. Michalcová, L. Machado, I. Marek, M. Martinec, M. Sluková and D. Vojtěch, *J. Phys. Chem. Solids*, 2018, **113**, 125-133.
52. I. V. Yentekakis and F. Dong, *Frontiers in Environmental Chemistry*, 2020, **1**.
53. S. Zhang, Q. Fan, R. Xia and T. J. Meyer, *Acc. Chem. Res.*, 2020, **53**, 255-264.
54. I. Sullivan, A. Goryachev, I. A. Digdaya, X. Li, H. A. Atwater, D. A. Vermaas and C. Xiang, *Nature Catalysis*, 2021, **4**, 952-958.
55. M. Jouny, W. Luc and F. Jiao, *Industrial & Engineering Chemistry Research*, 2018, **57**, 2165-2177.
56. R. Sen, A. Goeppert, S. Kar and G. K. S. Prakash, *J. Am. Chem. Soc.*, 2020, **142**, 4544-4549.
57. A. J. Garza, A. T. Bell and M. Head-Gordon, *ACS Catalysis*, 2018, **8**, 1490-1499.
58. Y. A. Alsunni, A. W. Alherz and C. B. Musgrave, *J. Phys. Chem. C*, 2021, **125**, 23773-23783.
59. H. Xu, D. Rebollar, H. He, L. Chong, Y. Liu, C. Liu, C.-J. Sun, T. Li, J. V. Muntean, R. E. Winans, D.-J. Liu and T. Xu, *Nature Energy*, 2020, **5**, 623-632.

60. S. Stojkovikj, G. A. El-Nagar, F. Firschke, L. C. Pardo Pérez, L. Choubrac, M. Najdoski and M. T. Mayer, *ACS App. Mater. Interfaces*, 2021, **13**, 38161-38169.
61. D. Kim, C. S. Kley, Y. Li and P. Yang, *Proceedings of the National Academy of Sciences*, 2017, **114**, 10560-10565.
62. D. Raciti and C. Wang, *ACS Energy Letters*, 2018, **3**, 1545-1556.
63. Z. Gu, H. Shen, L. Shang, X. Lv, L. Qian and G. Zheng, *Small Methods*, 2018, **2**, 1800121.
64. S. Nitopi, E. Bertheussen, S. B. Scott, X. Liu, A. K. Engstfeld, S. Horch, B. Seger, I. E. L. Stephens, K. Chan, C. Hahn, J. K. Nørskov, T. F. Jaramillo and I. Chorkendorff, *Chem. Rev.*, 2019, **119**, 7610-7672.
65. R. Reske, H. Mistry, F. Behafarid, B. Roldan Cuenya and P. Strasser, *J. Am. Chem. Soc.*, 2014, **136**, 6978-6986.
66. R. Schlögl, *Angew. Chem. Int. Ed.*, 2015, **54**, 3465-3520.
67. H. He, K. Rahimi, M. Zhong, A. Mourran, D. R. Luebke, H. B. Nulwala, M. Möller and K. Matyjaszewski, *Nat. Commun.*, 2017, **8**, 14057.
68. H. He, D. Luebke, H. Nulwala and K. Matyjaszewski, *Macromolecules*, 2014, **47**, 6601-6609.
69. S. Levine, *Proceedings of the Royal Society of London. Series A. Mathematical and Physical Sciences*, 1939, **170**, 165-182.
70. A. Langford, M. Bruchsaler and M. Gupta, in *Practical Aspects of Vaccine Development*, eds. P. Kolhe and S. Ohtake, Academic Press, 2022, DOI: https://doi.org/10.1016/B978-0-12-814357-5.00008-8, pp. 225-266.
71. M. Boström, V. Deniz, G. Franks and B. Ninham, *Adv. Colloid Interface Sci.*, 2006, **123**, 5-15.
72. W. Zhang, Z. Kochovski, Y. Lu, B. V. K. J. Schmidt, M. Antonietti and J. Yuan, *ACS Nano*, 2016, **10**, 7731-7737.
73. J. Yuan and M. Antonietti, *Macromolecules*, 2011, **44**, 744-750.
74. M. Koebe, M. Drechsler, J. Weber and J. Yuan, *Macromol. Rapid Commun.*, 2012, **33**, 646-651.
75. C. Cummins, R. Lundy, J. J. Walsh, V. Ponsinet, G. Fleury and M. A. Morris, *Nano Today*, 2020, **35**, 100936.
76. T. Liu and G. Liu, *J. Mater. Chem. A*, 2019, **7**, 23476-23488.
77. X.-H. Hu and S. Xiong, *Frontiers in Nanotechnology*, 2022, **4**, 762996.
78. F. S. Bates and G. H. Fredrickson, *Annu. Rev. Phys. Chem.*, 1990, **41**, 525-557.
79. J.-P. Xu and J.-T. Zhu, *Chin. J. Polym. Sci.*, 2019, **37**, 744-759.
80. C. M. Hansen, *Eur. Polym. J.*, 2008, **44**, 2741-2748.
81. M. Belmares, M. Blanco, W. Goddard Iii, R. Ross, G. Caldwell, S. H. Chou, J. Pham, P. Olofson and C. Thomas, *J. Comput. Chem.*, 2004, **25**, 1814-1826.
82. T. I. Morozova and A. Nikoubashman, *Langmuir*, 2019, **35**, 16907-16914.
83. R. Deng, S. Liu, F. Liang, K. Wang, J. Zhu and Z. Yang, *Macromolecules*, 2014, **47**, 3701-3707.
84. A. Steinhaus, R. Chakroun, M. Müllner, T.-L. Nghiem, M. Hildebrandt and A. H. Gröschel, *ACS nano*, 2019, **13**, 6269-6278.
85. D. Hu, Y. Wang, J. Liu, Y. Mao, X. Chang and Y. Zhu, *Nanoscale*, 2022, **14**, 6291-6298.
86. S. E. Chung, W. Park, S. Shin, S. A. Lee and S. Kwon, *Nat. Mater.*, 2008, **7**, 581-587.
87. L. Li, K. Matsunaga, J. Zhu, T. Higuchi, H. Yabu, M. Shimomura, H. Jinnai, R. C. Hayward and T. P. Russell, *Macromolecules*, 2010, **43**, 7807-7812.

88. B.-H. Wu, L.-W. Zhu, Y. Ou, W. Tang, L.-S. Wan and Z.-K. Xu, *J. Phys. Chem. C*, 2015, **119**, 1971-1979.
89. M. Ma, E. L. Thomas, G. C. Rutledge, B. Yu, B. Li, Q. Jin, D. Ding and A.-C. Shi, *Macromolecules*, 2010, **43**, 3061-3071.
90. P. Hou, H. Fan and Z. Jin, *Macromolecules*, 2015, **48**, 272-278.
91. H. Jo, N. Haberkorn, J.-A. Pan, M. Vakili, K. Nielsch and P. Theato, *Langmuir*, 2016, **32**, 6437-6444.
92. B. Yu, P. Sun, T. Chen, Q. Jin, D. Ding, B. Li and A.-C. Shi, *Phys. Rev. Lett.*, 2006, **96**, 138306.
93. C. Mijangos, R. Hernández and J. Martin, *Prog. Polym. Sci.*, 2016, **54**, 148-182.
94. S. Mei, X. Feng and Z. Jin, *Macromolecules*, 2011, **44**, 1615-1620.
95. E. J. Cornel, J. Jiang, S. Chen and J. Du, *CCS Chemistry*, 2021, **3**, 2104-2125.
96. M. Destarac, *Polym. Chem.*, 2018, **9**, 4947-4967.
97. N. J. Warren, O. O. Mykhaylyk, D. Mahmood, A. J. Ryan and S. P. Armes, *J. Am. Chem. Soc.*, 2014, **136**, 1023-1033.
98. F. d'Agosto, J. Rieger and M. Lansalot, *Angew. Chem. Int. Ed.*, 2020, **59**, 8368-8392.
99. P. B. Zetterlund, S. C. Thickett, S. Perrier, E. Bourgeat-Lami and M. Lansalot, *Chem. Rev.*, 2015, **115**, 9745-9800.
100. A. S. Oliveira, P. V. Mendonça, S. Simões, A. C. Serra and J. F. Coelho, *J. Polym. Sci.*, 2021, **59**, 211-229.
101. C. Liu, C.-Y. Hong and C.-Y. Pan, *Polym. Chem.*, 2020, **11**, 3673-3689.
102. M. Lages, N. Gil, P. Galanopoulo, J. Mougin, C. Lefay, Y. Guillaneuf, M. Lansalot, F. D'Agosto and J. Nicolas, *Macromolecules*, 2022, **55**, 9790-9801.
103. K. Matyjaszewski, *Macromolecules*, 2012, **45**, 4015-4039.
104. W. Zhang, Y. Hu, L. Ma, G. Zhu, Y. Wang, X. Xue, R. Chen, S. Yang and Z. Jin, *Adv. Sci.*, 2018, **5**, 1700275.
105. R. Kortlever, J. Shen, K. J. P. Schouten, F. Calle-Vallejo and M. T. M. Koper, *J. Phys. Chem. Lett.*, 2015, **6**, 4073-4082.
106. S. Mei, Z. Kochovski, R. Roa, S. Gu, X. Xu, H. Yu, J. Dzubiella, M. Ballauff and Y. Lu, *Nano-Micro Lett.*, 2019, **11**, 83.
107. X. Pan, Z. Kochovski, Y.-L. Wang, R. M. Sarhan, E. Härk, S. Gupta, S. Stojkovikj, G. A. El-Nagar, M. T. Mayer, R. Schürmann, J. Deumer, C. Gollwitzer, J. Yuan and Y. Lu, *J. Colloid Interface Sci.*, 2023, **637**, 408-420.
108. Y. Zhu, L. Fan, B. Yang and J. Du, *ACS Nano*, 2014, **8**, 5022-5031.
109. Y. Zhu, B. Yang, S. Chen and J. Du, *Prog. Polym. Sci.*, 2017, **64**, 1-22.
110. K. Manojkumar, D. Mecerreyes, D. Taton, Y. Gnanou and K. Vijayakrishna, *Polym. Chem.*, 2017, **8**, 3497-3503.
111. C. Gao, Y. Han, K. Zhang, T. Wei, Z. Jiang, Y. Wei, L. Yin, F. Piccinelli, C. Yao, X. Xie, M. Bettinelli and L. Huang, *Adv. Sci.*, 2020, **7**, 2002444.
112. Z. Lv, N. Mahmood, M. Tahir, L. Pan, X. Zhang and J.-J. Zou, *Nanoscale*, 2016, **8**, 18250-18269.
113. S. García -Dalí, J. I. Paredes, S. Villar -Rodil, A. Martínez -Jódar, A. Martínez -Alonso and J. M. D. Tascón, *ACS App. Mater. Interfaces*, 2021, **13**, 33157-33171.
114. M. R, J. R. J. Uc, D. Pinheiro and S. Devi Kr, *Applied Surface Science Advances*, 2022, **10**, 100265.

115. L. Guardia, J. I. Paredes, J. M. Munuera, S. Villar-Rodil, M. Ayán -Varela, A. Martínez - Alonso and J. M. D. Tascón, *ACS App. Mater. Interfaces*, 2014, **6**, 21702-21710.
116. X.-Q. Qiao, Z.-W. Zhang, F.-Y. Tian, D.-F. Hou, Z.-F. Tian, D.-S. Li and Q. Zhang, *Crystal Growth & Design*, 2017, **17**, 3538-3547.
117. T. Lin, J. Wang, L. Guo and F. Fu, *J. Phys. Chem. C*, 2015, **119**, 13658-13664.
118. Z. Cheng, B. He and L. Zhou, *J. Mater. Chem. A*, 2015, **3**, 1042-1048.
119. K. Peng, L. Fu, H. Yang, J. Ouyang and A. Tang, *Nano Res.*, 2017, **10**, 570-583.
120. X. Cui, Q. Ruan, X. Zhuo, X. Xia, J. Hu, R. Fu, Y. Li, J. Wang and H. Xu, *Chem. Rev.*, 2023, **123**, 6891-6952.
121. A. Khorsand Kheirabad, X. Pan, S. Long, Z. Kochovski, S. Zhou, Y. Lu, G. McInerney and J. Yuan, *Nano Select*, 2022, **3**, 227-232.
122. X. Liu, B. Li, F. Fu, K. Xu, R. Zou, Q. Wang, B. Zhang, Z. Chen and J. Hu, *Dalton Transactions*, 2014, **43**, 11709-11715.
123. G. M. Neelgund and A. Oki, *Industrial & Engineering Chemistry Research*, 2018, **57**, 7826-7833.
124. P. Misra and M. A. Dubinskii, in *Ultraviolet Spectroscopy and UV lasers*, CRC Press, 2002, pp. 398-450.
125. P. Graves and D. Gardiner, *Springer*, 1989, **10**, 978-973.
126. L. C. Pardo Pérez, A. Arndt, S. Stojkovikj, I. Y. Ahmet, J. T. Arens, F. Dattila, R. Wendt, A. Guilherme Buzanich, M. Radtke, V. Davies, K. Höflich, E. Köhnen, P. Tockhorn, R. Golnak, J. Xiao, G. Schuck, M. Wollgarten, N. López and M. T. Mayer, *Adv. Energy Mater.*, 2022, **12**, 2103328.
127. J. Ma, G. Sun, D. Sun, F. Yu, M. Hu and T. Lu, *Construction and Building Materials*, 2021, **278**, 122386.
128. H. He, M. Zhong, B. Adzima, D. Luebke, H. Nulwala and K. Matyjaszewski, *J. Am. Chem. Soc.*, 2013, **135**, 4227-4230.
129. B. A. CARTER, D. B. Williams, C. B. Carter and D. B. Williams, *Transmission electron microscopy: a textbook for materials science. Diffraction. II*, Springer Science & Business Media, 1996.
130. P. E. Champness, *Electron diffraction in the transmission electron microscope*, Garland Science, 2020.
131. Z. Kochovski, G. Chen, J. Yuan and Y. Lu, *Colloid. Polym. Sci.*, 2020, **298**, 707-717.
132. R. E. Marsh, *Science*, 1955, **121**, 162-162.
133. V. M. Burger, D. J. Arenas and C. M. Stultz, *Sci. Rep.*, 2016, **6**, 29040.
134. J. S. Pedersen, *Adv. Colloid Interface Sci.*, 1997, **70**, 171-210.
135. A. G. Kikhney and D. I. Svergun, *FEBS Lett.*, 2015, **589**, 2570-2577.
136. M. "Krumrey and G. "Ulm, *Nuclear Instruments and Methods in Physics Research. Section A, Accelerators, Spectrometers, Detectors and Associated Equipment*, 2001, Medium: X; Size: page(s) 1175-1178.
137. J. Wernecke, C. Gollwitzer, P. Muller and M. Krumrey, *J. Synchrotron Radiat.*, 2014, **21**, 529-536.
138. A. Schavkan, C. Gollwitzer, R. Garcia-Diez, M. Krumrey, C. Minelli, D. Bartczak, S. Cuello-Nuñez, H. Goenaga -Infante, J. Rissler, E. Sjöström, G. B. Baur, K. Vasilatou and A. G. Shard, *Nanomaterials*, 2019, **9**, 502.
139. I. Hughes, *Journal*, 2010.

140. B. J. Berne and R. Pecora, *Dynamic light scattering: with applications to chemistry, biology, and physics*, Courier Corporation, 2000.

Appendix

Article I: Poly(ionic liquid) nanovesicles *via* polymerization induced self-assembly and their stabilization of Cu nanoparticles for tailored CO_2 electroreduction

Article II: Template synthesis of dual-functional porous MoS_2 nanoparticles with photothermal conversion and catalytic properties

Article III: Multi-functionalized carbon nanotubes towards green fabrication of heterogeneous catalyst platforms with enhanced catalytic properties under NIR light irradiation

Journal of Colloid and Interface Science 637 (2023) 408–420

Contents lists available at ScienceDirect

Journal of Colloid and Interface Science

journal homepage: www.elsevier.com/locate/jcis

Poly(ionic liquid) nanovesicles *via* polymerization induced self-assembly and their stabilization of Cu nanoparticles for tailored CO_2 electroreduction

Xuefeng Pan [a,g], Zdravko Kochovski [a], Yong-Lei Wang [a], Radwan M. Sarhan [a,d], Eneli Härk [a], Siddharth Gupta [b,c], Sasho Stojkovikj [b,c], Gumaa A. El-Nagar [b,d,⇑], Matthew T. Mayer [b], Robin Schürmann [e], Jérôme Deumer [e], Christian Gollwitzer [e], Jiayin Yuan [f,⇑], Yan Lu [a,g,⇑]

[a] Department for Electrochemical Energy Storage, Helmholtz-Zentrum Berlin für Materialien und Energie, Hahn-Meitner-Platz 1, 14109 Berlin, Germany
[b] Helmholtz Young Investigator Group: Electrochemical Conversion, Helmholtz-Zentrum Berlin für Materialien und Energie, Hahn-Meitner-Platz 1, 14109 Berlin, Germany
[c] Institut für Chemie und Biochemie, Freie Universität Berlin, Arnimallee 22, D-14195 Berlin, Germany
[d] Chemistry Department, Faculty of Science, Cairo University, Egypt
[e] Physikalisch-Technische Bundesanstalt (PTB), Abbestr. 2-12, 10587 Berlin, Germany
[f] Department of Materials and Environmental Chemistry (MMK), Stockholm University, Svante Arrhenius väg 16C, 10691 Stockholm, Sweden
[g] Institute of Chemistry, University of Potsdam, Karl-Liebknecht-Str. 24-25, 14476 Potsdam, Germany

graphical abstract

This study casts new aspects on using nanostructured PILs as new electrocatalyst supports in CO_2 conversion to C_1 products.

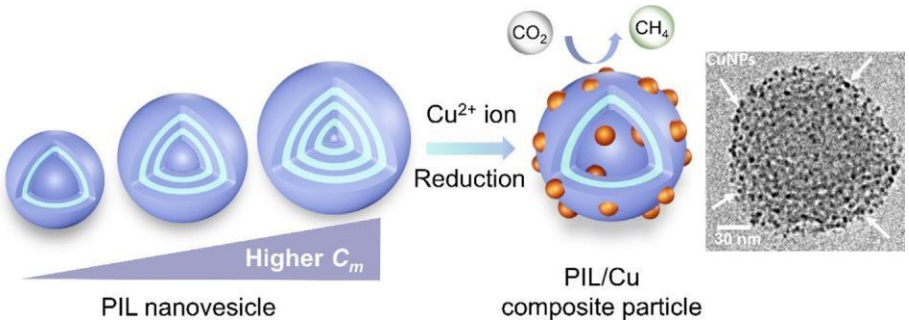

ARTICLE INFO

Article history:
Received 7 November 2022
Revised 18 January 2023
Accepted 20 January 2023
Available online 21 January 2023

Keywords:
Poly(ionic liquid)
Nanovesicles
Polymerization-induced self-assembly
Nanoparticles
CO_2 electroreduction

ABSTRACT

Herein, we report a straightforward, scalable synthetic route towards poly(ionic liquid) (PIL) homopolymer nanovesicles (NVs) with a tunable particle size of 50 to 120 nm and a shell thickness of 15 to 60 nm *via* one-step free radical polymerization induced self-assembly. By increasing monomer concentration for polymerization, their nanoscopic morphology can evolve from hollow NVs to dense spheres, and finally to directional worms, in which a multilamellar packing of PIL chains occurred in all samples. The trans- formation mechanism of NVs' internal morphology is studied in detail by coarse-grained simulations, revealing a correlation between the PIL chain length and the shell thickness of NVs. To explore their potential applications, PIL NVs with varied shell thickness are *in situ* functionalized with ultra-small (1 ~ 3 nm in size) copper nanoparticles (CuNPs) and employed as electrocatalysts for CO_2 electroreduc- tion. The composite electrocatalysts exhibit a 2.5-fold enhancement in selectivity towards C_1 products (*e.g.*, CH_4), compared to the pristine CuNPs. This enhancement is attributed to the strong electronic

* Corresponding authors.
E-mail addresses: gumaa.el-nagar@helmholtz-berlin.de (G.A. El-Nagar), jiayin.yuan@mmk.su.se (J. Yuan), yan.lu@helmholtz-berlin.de (Y. Lu).

https://doi.org/10.1016/j.jcis.2023.01.097
0021-9797/

interactions between the CuNPs and the surface functionalities of PIL NVs. This study casts new aspects on using nanostructured PILs as new electrocatalyst supports in CO_2 conversion to C_1 products.

1. Introduction

Polymer nanovesicles (NVs) self-assembled from amphiphilic polymers have aroused intensive interest in diverse research areas such as drug delivery, cell mimicking, nanoreactors, and water remediation.[1–5] Owing to their inherent hollow shape, polymer NVs possess light weight, large surface area, and a unique compartmentalized cavity.[6–8] These structural characteristics are directly associated with their mechanical stability, membrane permeability, and encapsulating capability, which impact their material performance.[9–11] For instance, when it comes to nanoreactors, the tiny cavity of the NVs is beneficial for achieving higher reaction rates and potentially better catalytic performance due to the shortened transport distance for the reaction medium and reactants.[12,13] Recently, various synthetic approaches toward precise control over the size of NVs have been developed, including the solvent exchange method, template-assisting route, and microfluidics.[14–17] However, from the applicative perspective, the involvement of organic solvents and/or complex devices in the above-mentioned approaches is undesirable and may limit their future practical use.

From the structural perspective, in addition to the dimension of the NVs, the shell thickness is essential in regulating the shape robustness and mass transport into and out of NVs. As the majority of vesicles are made up of amphiphilic block polymers *via* the default concept of block copolymer self-assembly, it is common to alter the relative and absolute length scale of the hydrophilic and hydrophobic blocks to dictate the shell thickness.[18,19] How- ever, the tedious, time-intensive synthetic protocols for block copolymers *via* multistep polymerizations are the apparent dilemma and bottleneck for real-life applications. By contrast, efforts have been rarely directed to tailor shell thickness by the homopolymer approach, which is often ignored in the NV synthesis for lack of qualified homopolymers and the fuzzy boundary between hydrophobic and hydrophilic moieties within the same repeating unit.

Poly(ionic liquid)s (PILs), as a fascinating group of functional ionic polymers, have been actively employed in multiple research areas including ionic liquids (ILs), polymer science, materials chemistry, sensing technology, and analytic chemistry, just to name a few.[20–25] In terms of molecular structure design, a series of PIL homopolymers has been fabricated from diverse IL mono- mers; these PIL homopolymers typically carry cationic backbones (*e.g.*, polyimidazolium, polypyridinium, and polyphosphonium) with side alkyl chains of various lengths and counter anions (*e.g.*, halides, acetate, and hexafluorophosphate).[26,27] The amphiphilicity of PILs is readily modulated by the choice of the alkyl chain length and counterion type, without varying the syn- thetically complex backbone.[28–30] Taking advantage of a large number of existent amphiphilic IL monomers, a couple of PIL homopolymers in vesicular nanostructures have been indeed made.[31] The microphase separation of PILs during their polymer- ization gives rise to the simultaneous formation of NVs, that is to say, the chemical polymerization drives the physical self- assembly process. This straightforward technique for polymer assembly is often defined as "polymerization induced self- assembly" (PISA), which due to its easiness in implementation has been prevailing for preparing nanoparticles of a rich library of morphologies at a broad polymer concentration window.[32] Nevertheless, the essential factors affecting the internal structures and self-assembled morphologies of PILs *via* PISA remain mysterious and lack in-depth investigation.

In addition to the prominent advantages in vesicle assembly, PILs find versatile applications including drug delivery, catalyst supports, and CO_2 sorption/conversion.[26,33–35] In light of the growing demand for clean energy sources, the electrochemical conversion of CO_2 (CO_2ER) into valuable chemicals provides an auspicious approach to mitigating the negative impacts of excess CO_2 emissions. [36–38] A primary technological challenge is to design selective electrocatalysts with high stability and production rates. Tackling the undesired parasitic hydrogen evolution reaction (HER) is crucial to mitigate the aforementioned-challenges.[39,40] Copper (Cu) is the only known metal that enables CO_2 electroreduction to high-value hydrocarbons (*e.g.,* CH_4 and C_2H_4) with considerable production rates, despite its poor selectivity towards specific products.[41–43] A variety of approaches, including surface functionalization, surface nano-structuring, and alloying, have been used to enhance the selectivity of Cu catalysts.[44–46] Very recently, copper nanoparticles (CuNPs) functionalized with PILs have been used to tune CO_2ER selectivity towards hydrocarbons. [47] In addition, PILs are an excellent stabilizer and carrier for metal nanoparticles, and are capable of efficiently tailoring their particle size.[48–51]

Herein, we finely modulated the CO_2ER selectivity of CuNPs by *in situ* synthesis and anchoring them into structurally well-defined PIL NVs with specific surface functional groups. Concretely, we first systematically investigated the morphological transformation of PIL homopolymer NVs *via* free radical polymerization by varying the concentration of monomer 3-*n*-decyl-1-vinylimidazolium bromide ($3 \leq C_m \leq 48$ mg/mL) (Scheme 1). Intriguingly, multilamellar NVs with controllable overall size and shell thickness were obtained *via* PISA, and the corresponding formation mechanism was proposed and validated *via* coarse-grained simulations. As a step forward to explore the utilization of such exquisitely constructed nanostructures, the PIL NVs with different shell thicknesses were *in situ* decorated by uniform ultra-small CuNPs of $1 \sim 3$ nm in size for CO_2ER. The synthesized hollow PIL/Cu composite particles exhibited an enhanced selectivity towards C_1 products, especially CH_4 as a crucial chemical feedstock. Moreover, quasi *in situ* X-ray photoelectron spectroscopy has been adopted to probe the surface speciation changes of the prepared PIL/Cu composite catalyst and correlating them to the CO_2ER processes.

2. Materials and methods

2.1. Chemicals

1-Vinylimidazole (99 %), 1 bromodecane (99 %), diethyl ether (≥99 %), methanol (≥99 %), 2,6-di-*tert*-butyl-4-methylphenol (BHT, ≥99 %), copper (II) acetate monohydrate ($CuAc_2{\cdot}H_2O$), and hydrazine hydrate (N_2H_4, 35 wt%) solution in water were purchased from Sigma-Aldrich. 2,2′ -Azobis[2-methyl-N-(2-hydroxyethyl) propionamide] (VA86, ≥99 %) was purchased from FUJIFILM Wako Chemicals. Ultrapure water with a resistance of 18.20 MΩ·cm was purified using the Thermo Scientific Barnstead GenPurex CAD Plus system). 2-propanol (≥99.8 wt%), sulfuric acid (H_2SO_4, ≥98 wt%, EMSURE® purity), and potassium hydrogen carbonate ($KHCO_3$, 99.7–100.5 wt% ACS, EMSURE® purity) were pur-

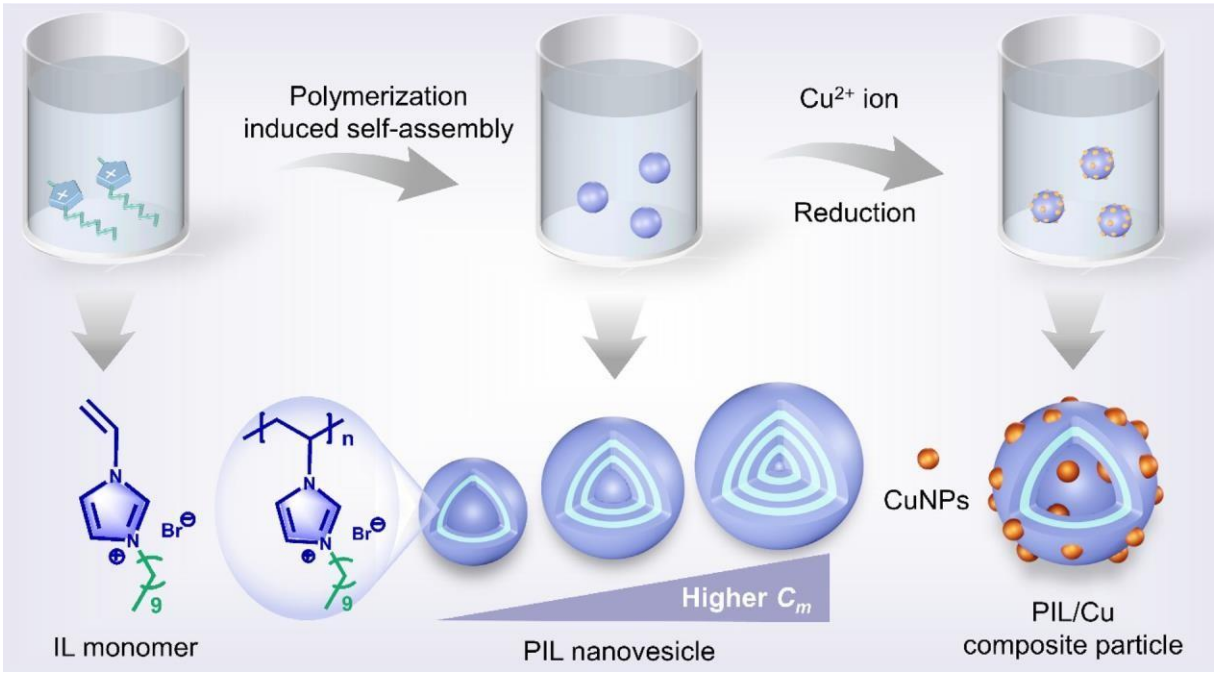

Scheme 1. Synthetic scheme of PIL NVs from its IL monomer at varied concentrations and their functionalization by CuNPs.

chased from Merck. Carbon dioxide (CO_2) gas with 4.8 purity was purchased from Linde. All chemicals were used without any further purification.

2.2. Synthesis of the IL monomer

The synthesis of the IL monomer 3-*n*-decyl-1-vinylimidazolium bromide was follow our previous report,[52] and briefly described as follows. 0.1 mol of 1-vinylimidazole and 10 mL of methanol were loaded into a 100 mL of flask. 0.1 mol of *n*-decyl bromide and 50 mg of inhibitor (BHT) were introduced to the solution. The mixture was stirred at 60 °C in an oil bath for 15 h. After cooling down, the reaction mixture was slowly added into an excess amount of diethyl ether. Then, the supernatant layer was removed and the precipitate was washed with diethyl ether 5 times. Finally, the obtained viscous liquid was dried into a brown solid under vacuum overnight to completely remove the residual solvent. The yield is *ca.* 34 %.

2.3. Synthesis of PIL NVs

In a typical run, various amounts of monomer (0.3–4.8 g) were dissolved in 100 mL of water in a 250 mL of Schlenk flask. The monomer solution was mixed with 50 mg of initiator (VA86) for *ca.* 30 min under magnetic stirring at 250 rpm. The mixture was completely deoxygenated by five cycles of the freeze–pump thaw procedure. Subsequently, the mixture was continuously stirred at 75 °C in an oil bath overnight. After cooling down, the final colloid dispersion was exhaustively dialyzed against deionized water until the conductivity of water is below 3 μS/cm. The PIL dispersion was collected and stored in the fridge at 4 °C for further use. The PIL nanovesicles (termed ''NVs") and solid nanospheres (termed ''SNSs") were first prepared at a monomer concentration (C_m) of 12 and 24 mg/mL respectively, according to their morphology observed in TEM characterization. To calculate the polymerization yield (Y), the desired amount of PIL dispersion at a given C_m (V mL) after dialysis was contained in a clean dry vial and placed in an oven at 90 °C until its weight was kept constant (W). Each sample was repeated 5 times to calculate the average value. Therefore, Y can be determined by the following equation (1):

$$Y = \frac{V \times c_m - W}{V \times c_m} \times 100\% \quad (1)$$

2.4. Synthesis of PIL/Cu composite particles

The facile synthesis of colloidal PIL/Cu composite particles was conducted based on our recent study.[53] For PIL NVs ($C_m \sim 12$ mg/mL), the colloidal dispersion (4 mL, 10 mg/mL) was diluted with 32 mL of deionized water. Then a fresh $CuAc_2$ solution (4 mL, 10 mg/mL) was slowly added to the dispersion under stirring. After stirring at 250 rpm at room temperature for 4 h, an aqueous N_2H_4 solution (0.4 mL, 35 wt%) was quickly injected into the mixture. The color of the solution turned from light blue to pink. Afterwards, the solution was placed in an oil bath under stirring at 250 rpm at 80 °C overnight to complete the reduction. The color of the solution gradually changed to wine-like. After cooling down, the dispersion was sonicated again for 20 min. Subsequently, the dispersion was filtered off using a syringe with a filter (an average pore size of 1.2 μm) to remove any big aggregates. After centrifugation at 8500 rpm for 30 min and washing with fresh water, the precipitated PIL/Cu composite particles were redispersed in 25 mL of fresh water before further use. For PIL SNSs ($C_m \sim 24$ mg/mL), the synthesized dispersion (2 mL, 20 mg/mL) was used for synthesis of copper nanoparticles (CuNPs) in the same manner as mentioned above. For comparison, the pristine CuNPs were also prepared in the same way without any PIL templates. CuNP-decorated NVs and SNSs are denoted as NVs/Cu and SNSs/Cu, respectively.

2.5. CO_2 electrochemical reduction

Electrode preparation by spray coating: the as-prepared pristine CuNPs and PIL/Cu dispersions (*ca.* 4 mg/mL) were deposited onto a Freudenberg H1C49 gas diffusion layers (GDLs, 180 μm in thickness) using an ultrasonic atomizer (Sonaer 130 kHz Low Flow tapered tip atomizer) was used in conjunction with a focusing

plume shaper LF130K). The GDLs were placed on a hot plate (150 °C) while maintaining a distance of 15 cm from the nozzle tip. The dispersions were pumped through the nozzle using a Harvard Apparatus syringe pump at a flow rate of 0.5 mL/min. The compressed air supplied to the nozzle was at a pressure of 0.5 bar. The CO_2 electrochemical reduction (CO_2ER) tests were performed in an H-type two-compartment electrochemical cell filled with 0.1 M $KHCO_3$ aqueous solution. The cathodic compartment was continuously purged with CO_2 gas at a flow rate of 20 mL/min. The as-prepared pristine CuNPs and PIL/Cu composite particles deposited GDL substrate acts as a working electrode fully immersed in the electrolyte, while Pt wire and Ag/AgCl were used as counter and reference electrodes, respectively. The electrochemical bias was provided using SP-200 potentiostat (Biologic) under chronoamperometry mode. 85 % of ohmic resistance (iR) was compensated automatically and all applied potentials were converted with respect to the Reversible Hydrogen Electrode (RHE). The cathodic gaseous products (H_2, CO, CH_4, and C_2H_4) were quantified using an online gas chromatograph (GC, Thermo Scientific) equipped with a flame ionization detector (FID) and a pulse discharge detector (PDD). The quantification interval was 10 min. Liquid products contained in the electrolyte were quantified using a high-performance liquid chromatography (HPLC) with a UV detector for the non-volatile ($HCOO^-$) and head-space gas chromatography (GC-HS) with FID detector for the volatile ones (*e.g.*, alcohols). A more detailed description of the electrochemical setup and quantification methods can be found in our previous report.[54]

2.6. Characterization methods

Nuclear magnetic resonance (NMR): ^{1}H NMR spectra were recorded at room temperature using a Bruker DPX-400 spectrometer operating at 400 MHz. Dimethyl sulfoxide-d_6 (DMSO d_6) was used as a solvent to dissolve both the IL monomer and the corresponding PIL.

Differential scanning calorimetry (DSC): DSC measurements were conducted on a Netzsch Phoenix F204 instrument at a heating rate of 10 K min^{-1} under an N_2 flow.

Gel permeation chromatography (GPC): Number-average molecular weight (M_n) and molecular weight distributions of PIL samples were determined by GPC. The GPC equipment is equipped with a PSS SECcurity 1260 autosampler injector, a PSS SECcurity 1260 HPLC pump, and a PSS SECcurity 1260 differential refractometer (RID) detector using PSS columns (PSS GRAM, 10 mm, Guard + 10 0 Å + 2 × 10,000 Å). The eluent is *N*, *N*-dimethylacetamide (DMAc) containing 10 g/L of lithium bromide (LiBr) at a flow rate of 1.0 mL/min at 70 °C.[55] The PIL powders after freeze-drying were first dissolved in eluent and kept shaking at 50 °C for *ca.* 1 h to ensure complete dissolution. Afterwards, the solutions (*ca.* 3 mg/mL) were left overnight at room temperature for equilibration. The as-prepared solutions were filtered through a PTFE syringe filter (an average pore size of 1.0 lm) before injection. The M_n and its distributions were calculated using linear polystyrene standards (M_n = 470–2520000 g/mol) for calibration by a PSS WinGPC UniChrom Version 8.4 software.

Dynamic light scattering (DLS): The average hydrodynamic diameter (D_h) and distributions were determined by using a Malvern Zetasizer Nano ZS. The scattered light was detected at an angle of 173°.

Scanning electron microscopy (SEM): The morphologies of the PIL samples were recorded on a LEO GEMINI 1530 microscope operated at 3 kV. All the samples were coated with a thin carbon layer (*ca.* 5 nm) before measurement.

Transmission electron microscopy (TEM): Conventional TEM, high-resolution TEM (HRTEM), and cryogenic transmission electron microscopy (cryo-TEM) were performed on a JEOL JEM-2100 instrument operated at an acceleration voltage of 200 kV. Cryo-TEM specimens were prepared by applying a 4 μL drop of a dispersion sample to Lacey carbon-coated copper TEM grids (200 mesh, Science Services) and plunge-frozen into liquid ethane with an FEI Vitrobot Mark IV set at 4 °C and 95 % humidity. Vitrified grids were either transferred directly to the microscope cryogenic transfer holder (Gatan 914, Gatan, Munich, Germany) or stored in liquid nitrogen. Imaging was carried out at temperatures around 90 K. The TEM was operated at an acceleration voltage of 200 kV, and a defocus of the objective lens of about 2.5–3 lm was used to increase the contrast. Cryo-TEM micrographs were recorded at a number of magnifications with a bottom-mounted 4 k × 4 k CMOS camera (TemCam-F416, TVIPS, Gauting, Germany). The total electron dose in each micrograph was kept below 20 $e^-/Å^2$.

Small angle X-ray scattering (SAXS) and wide angle X-ray scattering (WAXS): SAXS/WAXS measurements of the PIL dispersions have been performed at the four crystal monochromator (FCM) beamline of the PTB at the BESSY II synchrotron radiation facility (Helmholtz-Zentrum Berlin, Germany).[56] The PIL dispersions have been measured in sealed 80.0 × 4.2 × 1.25 mm^3 borosilicate glass cuvettes purchased from Hilgenberg (Malsfeld, Germany, a wall thickness of *ca.* 120 μm). All measurements have been performed at a photon energy of (8000.0 ± 0.8) eV. The SAXS data have been recorded at a sample detector distance of (5.107 ± 0.005) m with a Pilatus 1 M detector (Dectris ltd., Baden, Switzerland) and a distance of (0.206 ± 0.002) m for WAXS measurement.[57] Distance from sample to detectors has been determined with the long-period spacing (001) peak of silver behenate by the triangu- lation method. To determine the scattering from the solvent and the glass-cuvettes, prior measurements of the empty cuvettes and pure water in a separate cuvette have been performed. In all measurements, the lower section of the cuvettes was filled with Fluorinert FC-3283 acquired from Iolitec (Heilbronn, Germany) to determine the optical path length of the cuvettes.[58] The SAXS and WAXS scattering images have been recorded on multiple spots along the cuvettes and averaged to reveal possible effects of sedimentation. The whole sequence of measurements was repeated three times to detect potential X-ray damage of the PIL NVs. The scattering images have been circularly averaged and the resulting SAXS data curves have been accordingly fitted using custom-made software with a model for hollow spherical core–shell particles under the assumption of a log-normal size distribution. The uncertainties of the fit parameters for the overall diameter and shell thickness and the errors of the fits of the SAXS data have finally been determined by the reduced v^2- method.[59]

X-ray diffraction analysis (XRD): The powder XRD measurements were conducted on Bruker D8 using a monochromatized X-ray beam with Cu Ka radiation at a scan rate of 0.05°/min. The PIL/ Cu samples were collected after freeze-drying and kept in an air-tight XRD holder from Bruker.

UV–vis absorption spectra: the colloidal dispersions of PILs and PIL/Cu composite samples were contained in a clean quartz cuvette (110-QS Hellma, 10 mm) and measured on a PerkinElmer Lambda 650 spectrometer at room temperature.

Thermogravimetric analysis (TGA): the fully dried PIL template and PIL/Cu composite samples were measured on PerkinElmer (TGA 8000) in a temperature range of 25–900 °C at a heating rate of 10 °C/min under synthetic air. The copper loading of PIL/Cu sam- ples is calculated based on the mass of CuO residual after calcina- tion in air.[53]

Quasi in situ X-ray photoelectron spectroscopy (XPS): the XPS measurements were carried out in a SPECS PHOIBOS 100 analyzer with Al Kα radiation (1486.74 eV). For the quasi *in situ* XPS measurements, the CO_2ER experiments were carried out in an O_2-free glovebox using the H-type cell specified above and under the same conditions. After the electrolysis, the samples were completely

dried and stored in the glovebox. The samples were then transferred to the XPS vacuum chamber using a transfer arm, which was kept under an inert atmosphere. Further details on the quasi *in situ* XPS measurements are referred to our previously published work.[60]

Coarse-grained simulations for self-assembled PIL NVs: The coarse-grained (CG) model for PILs is constructed with the following principles: the planar imidazolium ring is represented by a single bead carrying a partial charge of + 1.0 e; the Br^- anion is mapped into a single CG bead carrying a partial charge of —1.0 e; each ethyl or ethylene unit is coarsened into one neutral CG bead. The bonded and non-bonded interaction potentials between CG beads are described by the AMBER FF format. The effective interaction parameters between these CG beads were determined following the similar procedures described in the previous work.[61] In brief, the relative positions and sizes of these CG beads are determined from the center-of-mass of the corresponding atomistic units. The bonded interaction parameters between virtually bonded CG beads including bond stretching and angle bending terms were calibrated to reproduce probability distributions of bond lengths and angles of atomistic groups in ILs derived from extensive atomistic reference simulations. The non-bonded interaction parameters between CG beads were determined to reproduce microstructures (*e.g.*, radial distribution functions) of atomistic modeling systems at varied thermodynamic states.[61]

The CG MD simulations of the self-assembly behavior of PILs in an aqueous solution were performed using the GALAMOST package.[62] The equations of motion were integrated using a classical velocity Verlet leap-frog integration algorithm with a time step of 2.0 fs to accelerate CG MD simulations of PILs modelling systems at extended spatiotemporal scales with a modest computational cost. A cut-off distance of 1.6 nm was set for short-range *van der Waals* interactions and real-space electrostatic interactions between point charges. The ENUF method, an abbreviation for the Ewald summation based on the non-uniform fast Fourier transform technique, was employed to handle long-range electrostatic interactions in reciprocal space calculations.[63,64]

Each modeling system contains ~375,000 CG beads and the number concentration of ion pair beads is kept at 20 %. The degree of polymerization (n) of PIL chains varies from 1 (IL monomer) to 50 to explore its overall effect on the self-assembled structures at constant C_m. Additional CG MD computations were performed for PILs consisting of 2, 4, 6, 12, and 30 IL monomers. All modeling systems were first energetically minimized using a steepest descent algorithm, and subsequently annealed gradually from 600 K to target temperatures within 10 ns. Afterwards, the system was equilibrated in an isothermal-isobaric ensemble for 20 ns of physical time maintained using Nose-Hoover thermostat and Parrinello-Rahman barostat with time coupling constants of 0.4 ps and 0.2 ps, respectively, to control temperatures and pressure at 1 atm. All CG MD simulations were sampled in a canonical ensemble for 20 ns, and simulation trajectories were recorded at an interval of 100 fs for further structural and dynamical analysis.

3. **Results and discussion**

3.1. Formation of PIL NVs via PISA

Polymerization induced self-assembly (PISA) of amphiphilic PIL homopolymers in an aqueous solution triggers the facile synthesis of well-defined PIL structures from a surfactant-like IL monomer. Without any externally added stabilizer in polymerization, stably dispersed PIL homopolymer particles in different forms were prepared in water, driven by incompatibility between the hydrophilic charged backbones and the hydrophobic neutral long alkyl substituents.[32] Herein, we began with the chemical synthesis of the amphiphilic IL monomer 3-*n*-decyl-l-vinylimidazolium bromide, followed by its free radical homopolymerization in an aqueous solution. The successful preparation of this monomer and its corresponding PIL (C_m at 12 mg/mL for initial tests) was confirmed by ^{1}H NMR measurements (see details in Fig. S1). Their thermal behavior and relative stabilities were subsequently characterized by DSC and TGA, as summarized in Fig. S2 and S3. A distinct melting peak at *ca.* 33 °C (below 100 °C) for the IL monomers was observed in the DSC curve, which classifies itself into the group of ionic liquids. Besides, no apparent weight loss (up to 200 °C) in its TGA curve was found for the as-synthesized PILs, indicating their good thermal stability (Fig. S3).

The self-assembly of the PIL can be controlled by simply polymerizing the IL monomer at chosen C_m. The morphologies of these featured PIL nanoparticles prepared at specific C_m in aqueous solution were first characterized by conventional TEM and SEM, as shown in Fig. S4 and S5, respectively. The samples for electron microscopies were prepared by drying their dispersions at room temperature. We observed that the particle size increased along with C_m from 3 to 6 mg/mL (Fig. S4). Subsequently, their shape was transformed from hollow NVs at C_m ~ 12 mg/mL, to dense spheres at C_m ~ 24 mg/mL, and finally into directional worms (at C_m ~ 48 mg/mL). Generally speaking, when polymerizing the IL monomer at both low (3 to 6 mg/mL) and medium C_m (from 6 to 12 mg/mL), the observed lighter contrast in the center area of PIL particles than their edge in TEM images indicates a hollow core that was filled with water before drying. The morphology of collapsed thin shells after drying under ambient conditions was similarly spotted in SEM images (Fig. S5). Interestingly, in the case of high C_m (from 12 to 24 mg/mL), the center void gradually shrank in size and eventually disappeared at C_m ~ 24 mg/mL or above to form only dense particles. A further increase of C_m to 48 mg/mL triggers the formation of linear PIL aggregates, *i.e.*, one-dimensional PIL fibers with a length of up to ~ 10 μm and a diameter of (110 ± 13) nm. A similar morphology was observed in our previous report of a different PIL system.[65]

Due to the ambient-condition drying effect in the TEM sample preparation step, the authentic architecture, particularly the hollow inner structure of the PIL particles, is hard to be convincingly verified by conventional TEM. A morphology-verification step by cryo-TEM is thus required.[66] As shown in Fig. 1a-b, e-f, and S6, large spherical cavities inside PIL NVs were found at both low (3 to 6 mg/mL) and medium (6 to 12 mg/mL) C_m. In high C_m range (from 12 to 24 mg/mL), the ordered curved multilamellar wall gradually extended its thickness to downsize the central void (C_m at ~ 16 mg/mL), and eventually filled in the hollow interior to form solid nanospheres (SNSs) at C_m ~ 24 mg/mL, as shown in Fig. 1c-d, and g-h. Beyond this concentration, *e.g.*, at C_m ~ 48 mg/mL, the linear attachment of primary PIL nanoparticles occurred and gave rise to hierarchical structures, namely primary nanoparticles formed first and next fused into nanoworms (Fig. 1i-k). For all PIL nanoparticles prepared in this work, a general molecular organization in the form of an alternating multilamellar packing of polymer chains was identified under the cryo-TEM conditions. The hydrophobic alkyl substituent as a side chain covalently tethered to the ionic polymer backbone accounts for the lighter lamellae domain in the cryo-TEM images, while the darker rings (or planes) stem from the polymer backbone made up of the imidazolium bromide ion pairs of a higher electron density.[65] The average bilayer spacing of NVs (C_m ~ 12 mg/mL) is measured to be (3.1 ± 0.1) nm from cryo-TEM images (see the detailed bilayer structure in Fig. S7).

By carefully analyzing the cryo-TEM images, we identify that the overall diameter and shell thickness of NVs (*i.e.,* the total thickness of the multilamellar layers shown in Fig. 2a) strongly depends on C_m in the polymerization. The particle sizes and size distribu-

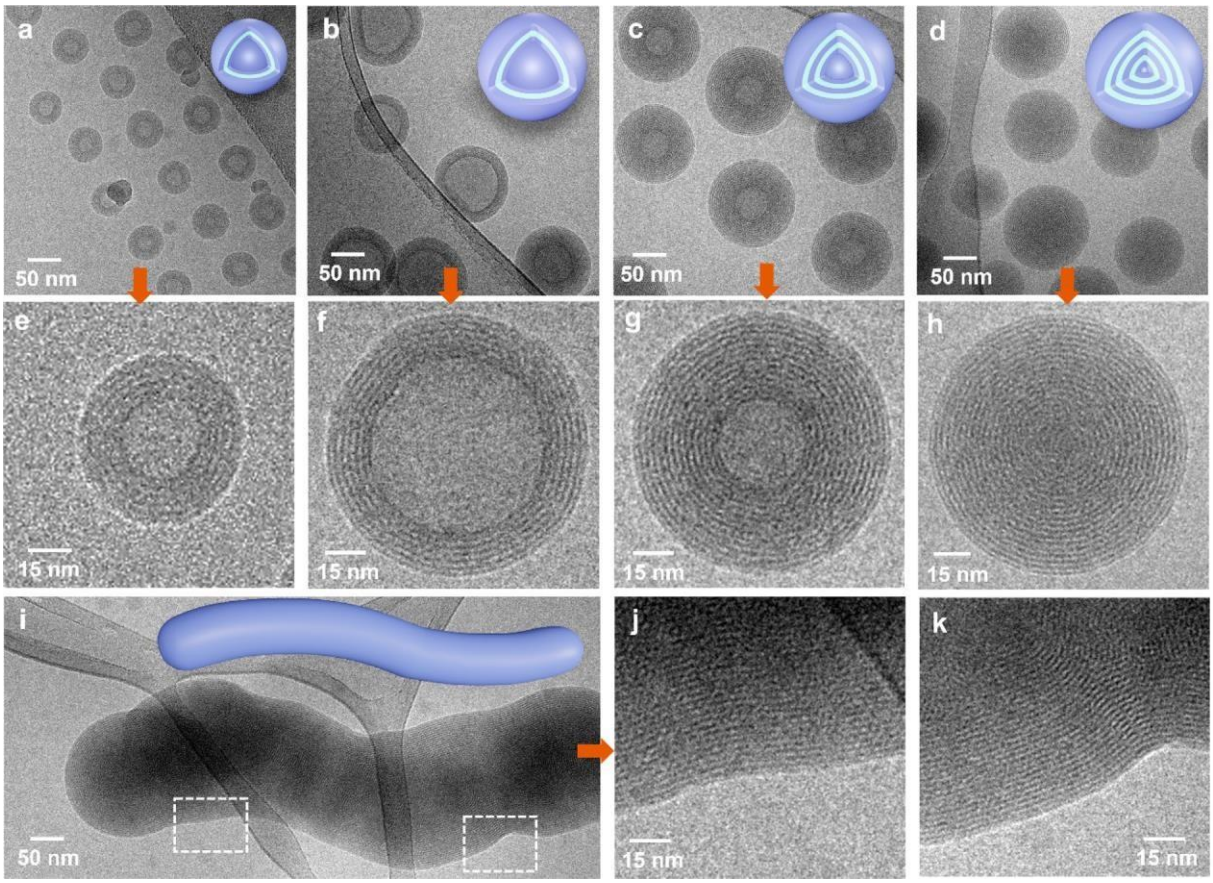

Fig. 1. Cryo-TEM images of the PIL NVs prepared *via* PISA method at various monomer concentrations (C_m): (a, e) 3 mg/mL, (b, f) 12 mg/mL, (c, g) 16 mg/mL, (d, h) 24 mg/mL, and (i-k) 48 mg/mL. The insets are the corresponding 3D models.

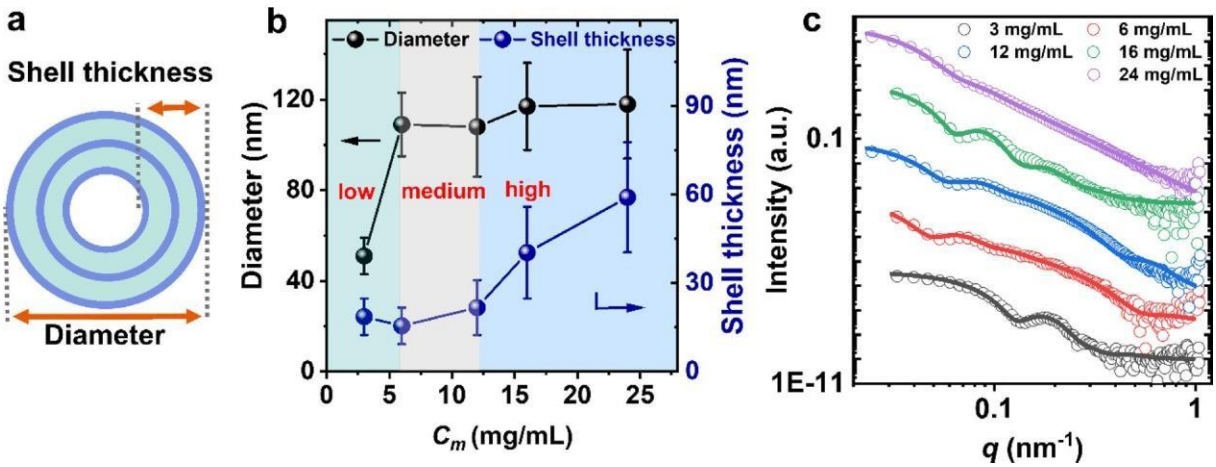

Fig. 2. (a) Scheme of the cross-section of the multilamellar PIL NVs. (b) Plots of the diameter and shell thickness of the PIL particles as a function of C_m. (c) SAXS profiles (scatter patterns) of the PIL dispersions prepared at various C_m plotted together with the analytical fit (solid lines) using a core–shell form factor. Scattering curves are vertically shifted for clarity.

tions determined from cryo-TEM analysis are shown in Fig. 2b and S8. Specifically, increasing C_m in the low range of 3 to 6 mg/mL leads to an initially dramatic expansion of the NVs size from (51 ± 8) to (109 ± 14) nm. In the medium C_m range (6 to 12 mg/ mL), the diameter of PIL particles does not change significantly from (109 ± 14) to (108 ± 22) nm. Meanwhile at high C_m (12 to 24 mg/mL), the diameter increases slightly to (118 ± 28) nm at C_m ~ 24 mg/mL. It is worth noting that the shell thickness undergoes a slight decrease ranging from (18 ± 6) to (16 ± 6) nm in the low concentration zone (C_m of 3 to 6 mg/mL) and is followed by a minor jump to (22 ± 9) nm at medium C_m of 6 to 12 mg/mL. At higher C_m above 12 mg/mL till the C_m at which the hollow space is fully filled, the shell thickness sharply rises to a maximum value of (59 ± 14) nm. The D_h and distributions of these assembled nanoparticles were also determined by DLS and plotted against C_m (Fig. S9), and the results are in good agreement with cryo-

TEM analysis. Hence, it can be addressed that in the low C_m zone (below 6 mg/mL), the addition of more monomers only enlarges particle size. In the medium C_m zone (from 6 to 12 mg/mL), neither the particle size nor the shell thickness of PIL particles exhibits any drastic change. Polymerization at a high C_m (beyond 12 mg/mL) will vary the internal nanostructure by thickening the shell, trig- gering the complete transformation of NVs to SNSs (Fig. 1f-h and 2b). In short, the C_m is correlated with the shell thickness and the diameter of PIL NVs, which offers a useful tool to manipulate the dimension and morphology of PISA-induced PIL homopolymer nanostructure.

To verify the structural information, the colloidal dispersions of the PIL particles were further investigated by synchrotron-based SAXS/WAXS measurements. Fig. 2c displays their corresponding SAXS profiles at various C_m. Taking PIL NVs prepared at C_m ~ 3 mg/mL as an example, their SAXS plot has been fitted in the region from 0.04 to 0.8 nm^{-1} with an analytical form factor of a core–shell particle F_{cs} according to the following equation (2):

$$F_{CS}(q, R, \nu) = F_{Sphere}(q, R) - (1 - \mu) F_{Sphere}(q, \nu \cdot R) \quad (2)$$

where $F_{Sphere}(q, R)$ is the form factor of a sphere with an overall radius R, q is the scattering vector, μ is the electron density difference between core and solvent relative to the shell contrast, and ν is the ratio of the core radius to R.[67] To simplify the model, the PIL vesicle is assumed to logically adopt a hollow core ($\mu = 0$) filled with water as a solvent. Moreover, a homogeneous shell is assumed here and the scattering from the internal lamellar layers is not considered in the simplified form factor of the fit.[68] The particle size distribution is further given in the form of a log-normal distribution. The fit of the SAXS profile reveals an average diameter of (56.1 ± 3.8) nm with a size distribution of *ca.* 7.9 nm, which resem- bles the results of cryo-TEM at (51 ± 8) nm. The shell thickness is determined to be (16.0 ± 2.2) nm, which also agrees well with that of cryo-TEM. The overall diameter and shell thickness of all the PIL particles were summarized in Table S1, generally following a similar trend to that of cryo-TEM analysis. In addition, the prominent peak is located at a q value of *ca.* 2.1 nm^{-1} in the WAXS data originated from the bilayer spacing of the NVs (Fig. S10). The average bilayer spacing is calculated to be (3.0 ± 0.1) nm based on Bragg's law, which is in good accordance with the value of (3.1 ± 0.1) nm determined in the cryo-TEM analysis.[69] The bilayer spacing of all the PIL assemblies shows only a slightly different value of 2.9 to 3.1 nm, confirming that the bilayer spacing stays constant, independent on the final morphologies of the assembled PIL NVs (Table S2).

3.2. Evolution mechanism of PIL NVs

Generally speaking, the morphology transformation and structural characteristics of polymer vesicles strongly correlate with the chain structure and polymer concentration.[9,70,71] In the current study, a higher C_m indicates a higher polymer concentration (see Table S3). At a low C_m window ranging from 3 to 6 mg/mL, we found a sharp increase in overall diameter but little change in thickness (Fig. 2b). Before polymerization, the 1- vinylimidazolium cations in IL monomer in water are reported to be associated with counter anions *via* Coulombic interaction.[72] The subsequent polymerization leads to the spontaneous self- organization of PIL chains packing into layered assemblies (as pri- mary particles) due to the strong hydrophobic interaction of the long alkyl groups.[65] Meanwhile, the propagating PIL chains can be diffusively captured by the primary PIL vesicles until all the IL monomers are depleted. In addition, the primary particles tend to coalesce together and eventually form stabilized particles. Both effects could contribute to the appreciable size expansion of PIL vesicles when increasing C_m. In the medium C_m zone (from 6 to 12 mg/mL), however, neither the diameter nor the shell thickness of the PIL vesicles shows the drastic change. A possible explanation is that the number of the PIL particles increased due to the enhanced polymer concentration.[9]

At an even high C_m (from 12 to 24 mg/mL), we observed only a significant increase in shell thickness but a slight change in ultimate diameter. Particle coalescence or diffusion capture of PIL chains could not fully explain the increase in the shell thickness rather than diameter. It is essential to gain a deeper insight into the structural evolution in a molecular chain level. Chain length of amphiphilic homopolymers has been reported to affect their final assembly morphologies.[73,74] GPC (see Fig. S11 and Table S4) was thereby used to determine the number-averaged molecular weight (M_n) of PIL chains. Elevating C_m from 12 to 24 mg/mL increases their M_n from 43 to 49 kg/mol. Note that the M_n reported here stands for an apparent molecular weight using polystyrene standard for lack of suitable PIL standards, which can sufficiently reflect the relative length of PIL chains. When keeping the initiator concentration constant, a high C_m in free radical homopolymerization leads to a high propagating rate and therefore the formation of long PIL chains.[75] As a result, the PIL chain length (or M_n) is suggested to play a dominant role in the internal organization at high C_m, which will be further discussed in the latter simulation part. In principle, the increase in shell thickness could be separately or simultaneously realized in two possible ways: one mainly results from the expansion of the bilayers, which is commonly found in block copolymers; [76,77] the other primar- ily comes from the folding of more bilayers into the vesicle center. Evidently, the shell thickening of our PIL homopolymer NVs will merely expand in the latter manner. Independent on the C_m, the bilayer spacing keeps practically constant for all PIL NVs, which has been proved by cryo-TEM and WAXS analyses (Table S2). When the C_m keeps increasing (up to 48 mg/mL), the strong Hamaker force induced by charge polarization promotes the align- ment organization of the neighboring particles due to the liquid character of their interior. Thus, the PIL particles partially deform and fuse into directional worms, as described in our previous study.[65]

Extensive coarse-grained (CG) molecular dynamics simulations were performed to confirm the dependence of self-assembled structures of PILs on the polymerization degree (n), *i.e.*, chain length of PILs. The adopted CG model for the IL monomer cation 3-*n*-decyl-l-vinylimidazolium is depicted in Fig. 3a. The principles for constructing such a CG model and determining the effective interaction potentials between CG beads were detailed in our previous work.[61] The relevant computational methodology is provided in Supporting Information. On account of the high bending energy, short PIL chains will require a long time to mediate their spatial distributions and coordinate with anions and solvent molecules.[78] In comparison to neutral polymers, our cationic PILs by virtue of their ionic nature present a more complex molecular organization behavior. For polyelectrolytes, the electrostatic interactions between and inside polymer chains have been documented to result in counterion condensation.[79,80] The number of condensed counterions increases with the polymerization degree and polymer concentration. The strong condensation effect is likely to weaken the intrachain repulsion, thus driving severe deformation of polymer chains (mostly shrunk, collapsed, or unfolded chains).[81,82] In our case, as the presence of long side chains attached to the PIL backbone provides a strong steric hindrance between the neighboring PIL chains; it could favor retaining their layered packing rather than complete collapse during assembly. Therefore, the interplay of the effects as mentioned above presumably jointly facilitates the formation of well-defined vesicular nanostructures with anions and solvent molecules encapsulated inside (Fig. 3b and 3c).

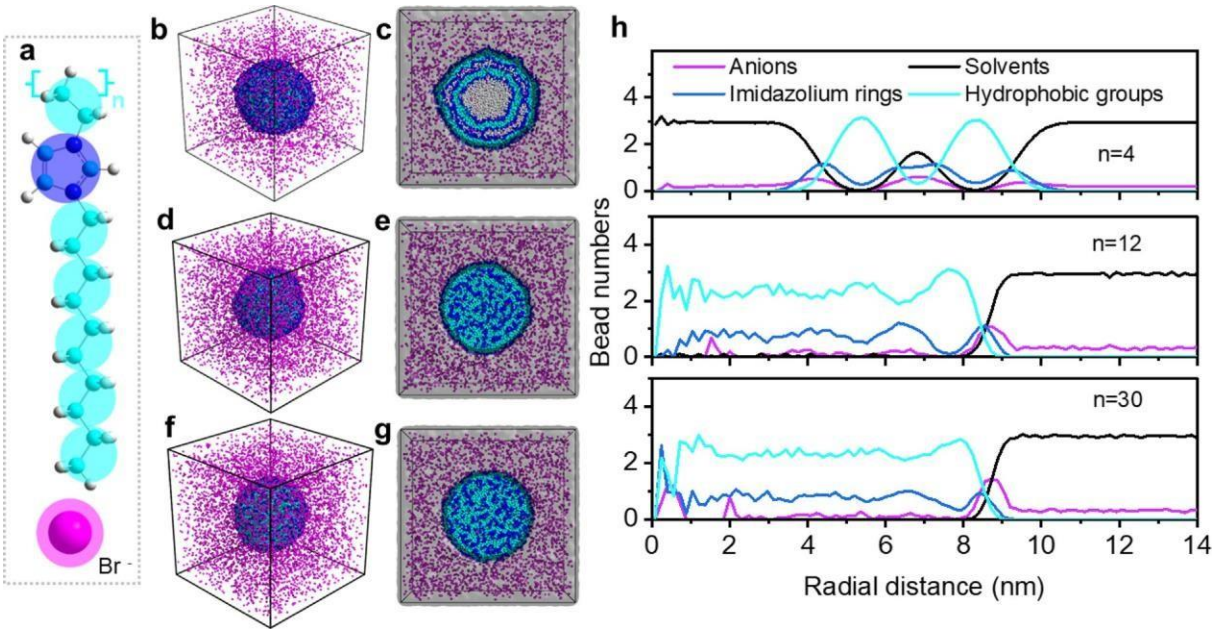

Fig. 3. (a) The constructed CG model for 3-*n*-decyl-1-vinylimidazolium bromide. Full and cross-section views of the self-assembled structure of PILs in an aqueous solution. PIL (b, c) with $n = 4$, (d, e) $n = 12$, and (f, g) $n = 30$. The solvent molecules encapsulated within and outside the self-assembled PIL particles are indicated by a gray medium. (h) Number density distributions of the CG beads in PILs, anions, and solvent molecules in modeling systems.

It is noticeable that a gradual increase in chain length from monomeric to an oligomeric chain with 6 repeating units (*i.e.*, *n* of 1 to 6) promotes a considerable expansion of the inner space of vesicular structures, and thereafter a substantial decrease in the inner volume with a further lengthening of PIL chains (Fig. S12). It resembles the experimental results of PIL NVs with the C_m increasing from 3 to 6 mg/mL. PILs with intermediate chain length ($n = 12$ in Fig. 3d and 3e) are self-assembled into solid spheres with residual solvent molecules incorporated inside, which is in line with the transformation of PIL NVs to SNSs (C_m of 12 to 24 mg/mL). PILs with an even longer chain ($n = 30$ in Fig. 3f and 3 g) tend to form solid self-assembled structures with less solvent encapsulated than the PIL NVs. On the basis of these findings, we may argue that the PIL chains with relatively higher *n* are more likely to extend into the center of the vesicle due to their better flexibilities and weaker intrachain repulsions, thus diminishing the central cavity. The number density distributions of representative CG beads in modeling systems (Fig. 3h) demonstrate that the self-assembled structures from PILs with intermediate and long backbones are characterized by structure-less interior and stripe-patterned shells, which are probably relevant to the residual solvent molecules inside the self-assembled PIL particles. Therefore, we demonstrated that the polymerization degree of PIL homopolymers plays an essential role in dictating the overall shell thickness (*i.e.*, the number of folded bilayers), thus enabling the transformation of their morphology.

3.3. PIL NVs-supported ultra-small CuNPs for CO_2ER

PIL NVs were further explored as a template to immobilize and stabilize ultra-small CuNPs. The obtained PIL/Cu composite particles were utilized as electrocatalysts for CO_2ER. Briefly, the PIL templates were incubated with $CuAc_2$ salt in an aqueous solution for 4 h to ensure sufficient enrichment of the Cu^{2+} ions into the PIL particles. Subsequently, the copper ions were reduced into metallic copper in the presence of N_2H_4 as a strong reducing agent at 80 °C (Fig. 4a).[53] As a result, ultra-small CuNPs (highlighted by white arrows in Fig. 4b) were directly immobilized into the PIL nanostructures. In addition, the multilamellar structure in PIL NVs was observed to be slightly distorted in the composite particles. While N_2H_4 treatment can hardly influence the morphology of PIL NVs (Fig. S13), penetration of Cu^{2+} ions into the neighboring PIL layers is likely the drive for deforming the PIL internal structure. The CuNPs in NVs (denoted as NVs/Cu thereafter) and in SNSs (denoted as SNSs/Cu thereafter) show an average particle size of (1.8 ± 0.4) and (1.7 ± 0.5) nm, respectively (Fig. 4c and S14). The successful incorporation of CuNPs within the PIL templates is supported by the observation of a weak absorption peak at 200 to 300 nm in the UV–vis absorption spectra (Fig. 4d).[49] To confirm the presence of CuNPs, the PIL/Cu composite particles and the pristine PIL templates were characterized by X-ray diffraction (XRD). As shown in Fig. 3e, three distinct peaks at 43°, 55°, and 74° are observed for both PIL/Cu composite particles, which can be assigned to the (111), (200), and (220) reflections of face- centered cubic (*fcc*) metallic Cu, respectively. The pure PIL tem- plates show no reflection at all due to their amorphous nature, which is in line with the DSC analysis (Fig. S2). The amount of cop- per loading in PIL NVs/Cu and SNSs/Cu is 19.2 and 8.9 wt%, respec- tively, calculated from the aerobic residual (CuO) in the TGA test (Fig. 4f and S15). The PIL NVs show a higher Cu loading than that of SNSs, as expected for a hollow structure with a relatively higher specific surface area (Fig. S16) to provide more surface area to load CuNPs as active sites for CO_2ER. As reference, pristine CuNPs were prepared using the same protocol but without any PIL template. Only Cu particles with an irregular morphology were obtained. Their much larger size was revealed by SEM and TEM images (Fig. S17), emphasizing the essential role of PIL NVs in controlling the ultra-small size of CuNPs in the composite particles.

The as-prepared pristine CuNPs and NVs/Cu particles were directly spray-coated on GDLs. The coated GDLs were served as the working electrode for CO_2ER experiments (Fig. 5a). The CO_2ER activity was examined in a CO_2-saturated 0.1 M $KHCO_3$ solution using a conventional H-cell configuration (Fig. S18). The product distributions (Faradaic efficiency, FE) of the CO_2ER as a function of the applied potential of the synthesized catalyst materials are summarized in Fig. 5b and S19. At low negative potentials between

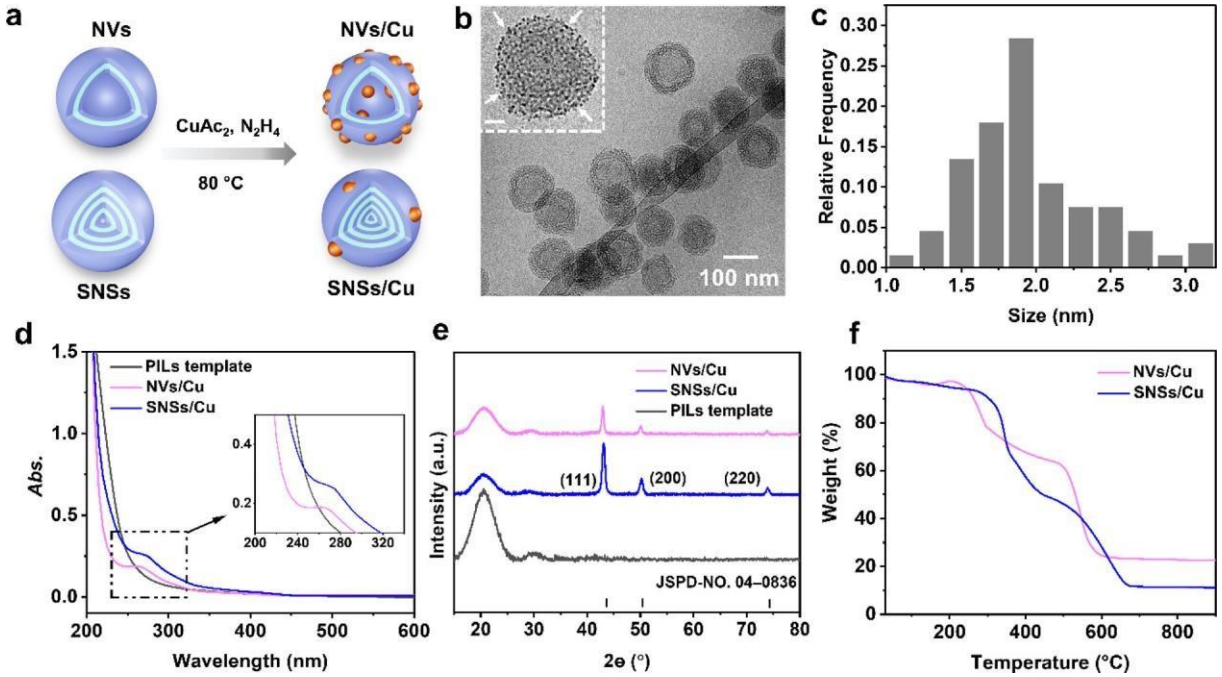

Fig. 4. (a) Scheme of the synthesis of the colloidal PIL/Cu composite particles. (b) Cryo-TEM images of the PIL NVs/Cu composite particles. The inset is a close view with a scale bar of 30 nm and some tiny CuNPs are indicated by white arrows. (c) The corresponding size distribution histogram of CuNPs (calculated from over 100 particles) in PIL NVs/Cu determined from its cryo-TEM image. (d) UV–vis absorption spectra of the dispersions of PIL template, NVs/Cu, and SNSs/Cu. (e) XRD diagrams of the PIL templates, NVs/Cu, and SNSs/Cu powders after a thorough freeze-dry, which are referenced to the JSPD card (Cu: 04–0836). (f) TGA curves measured under synthetic air of the NVs/Cu and SNSs/Cu powder after freeze-drying.

—0.8 and —0.9 V *vs* RHE, a mixture of H_2 and C_1 products (CO, CH_4, and $HCOO^-$) were the major products in the case of all studied electrocatalysts. For the PIL NVs/Cu electrodes, with the applied potential increasing from —0.8 to —1.1 V the total FE of all C_1 products increased from ~ 38 % to ~ 58 %, concurring with decreasing H_2 FE. It is notable that the FE of CH_4 significantly increased from ~ 6 % to ~ 34 % when the potential increased from —0.8 to —1.2 V for NVs/Cu, while the FE of CH_4 of the pristine CuNPs remained below 8 % (Fig. 5b). Upon increasing the applied cathodic bias, the FE of the pristine CuNPs shifts from C_1 products (CO and $HCOO^-$ as main products) towards C_2/C_{2+} products (mainly C_2H_4), see Fig. S19. In other words, the FE of the pristine CuNPs entirely shifts to C_{2+} products at the expense of C_1 products, while the FE of the PIL NVs/Cu shifts from CO and $HCOO^-$ to CH_4 as a major product (Fig. 5b and S19). Note that the PIL SNSs/Cu shows higher selectivity towards H_2 generation despite having similar CH_4 selectivity to that of NVs/Cu (Fig. S20). Thus, we focused on PIL NVs/Cu for further study. Overall, our PIL/Cu composite particles show relatively high CH_4 selectivity compared with the current reports, as shown in Table S5.

To gain deep insights into the CO_2ER behavior of the pristine CuNPs and PIL NVs/Cu, the partial current densities (*i.e.*, production rates) of their main products are displayed in Fig. 5c and d. An increase in H_2 production was observed for both catalysts upon increasing the applied cathodic potential. The PIL NVs/Cu showed a significant surge in CH_4 production rate from ~ 2.0 to 38 mA mg^{-1} cm^{-2} when the applied cathodic potential increased from —0.9 to —1.2 V. As shown in Fig. S21, the PIL NVs/Cu also exhibited higher specific current density than the commercial CuNPs (40–60 nm in size). Additionally, the FE ratio of CH_4/C_2H_4 on PIL NVs/Cu particles was enhanced by a factor of 22 at —1.2 V in comparison with that of pristine CuNPs, highlighting the significant impacts of PIL templates on the CuNPs electrocatalytic behavior for CO_2ER.

Apart from the structural merits of the hollow nanovesicle, the chemical nature of PIL NVs is expected to crucially facilitate the CO_2ER process. The enhanced selectivity of CO_2ER towards CH_4 on NVs/Cu could be attributed to one (or more) of the following effects: (1) special surface defects (low coordinated sites) provided by the small size of CuNPs in PILs; (2) stabilizing effect of key intermediates for CH_4 by surface functionalities of PILs; (3) electronic interactions between the PILs and the CuNPs. It has been reported in recent works that a strong interfacial electric field induced by the imidazolium moieties at the PIL/Cu interface could stabilize key intermediates in CO_2ER.[47,83] Quasi *in situ* XPS was employed here to investigate the interplay between the CuNPs and PILs, and to examine the induced surface speciation changes of PIL/Cu induced during CO_2ER. The results are displayed in Fig. 6 and Fig. S22. As-prepared pristine CuNPs (in the absence of PILs) showed a mixture of Cu^{2+}, which is indicated by the observed shoulder peak at 934.2 eV, and Cu^+/Cu^0 as demonstrated by the strong sharp peak at 932.3 eV. On the other hand, the as- synthesized PIL NVs/Cu exhibited merely a single peak at 936.0 eV, which is strongly shifted to higher binding energy than the observed Cu^{2+} peak of the pristine CuNPs (see Fig. 6a and c). This may suggest an intense electronic interaction between Cu and the polyimidazolium backbone *via* the formation of copper 1,3-dialkylimidazol-2 ylidene carbene complex, which is different from the copper oxide species (*e.g.*, CuO and $Cu(OH)_2$).[49,84] The absence of the metallic Cu surface species in the case of pris- tine CuNPs was further indicated by fitting the Auger region, see Fig. 6d. Following the application of the cathodic bias, both the pristine CuNPs and the NVs/Cu exclusively exhibited metallic Cu surface species, as indicated by the absence of the Cu^{2+} shoulder and its related strong satellite on the Cu 2p spectra. The full reduc- tion of the oxidized copper surface species of both electrodes (pris- tine CuNPs and NVs/Cu) during CO_2ER is further indicated by their respective fitted Auger regions (Fig. 6b and d). The post XPS surface analysis of the NVs/Cu catalyst after CO_2ER (air-exposed) shows a surface consisting of a mixture of Cu^{2+} and Cu^+ species resembling the as-prepared pristine CuNPs. The related peaks for the Cu^{2+} and

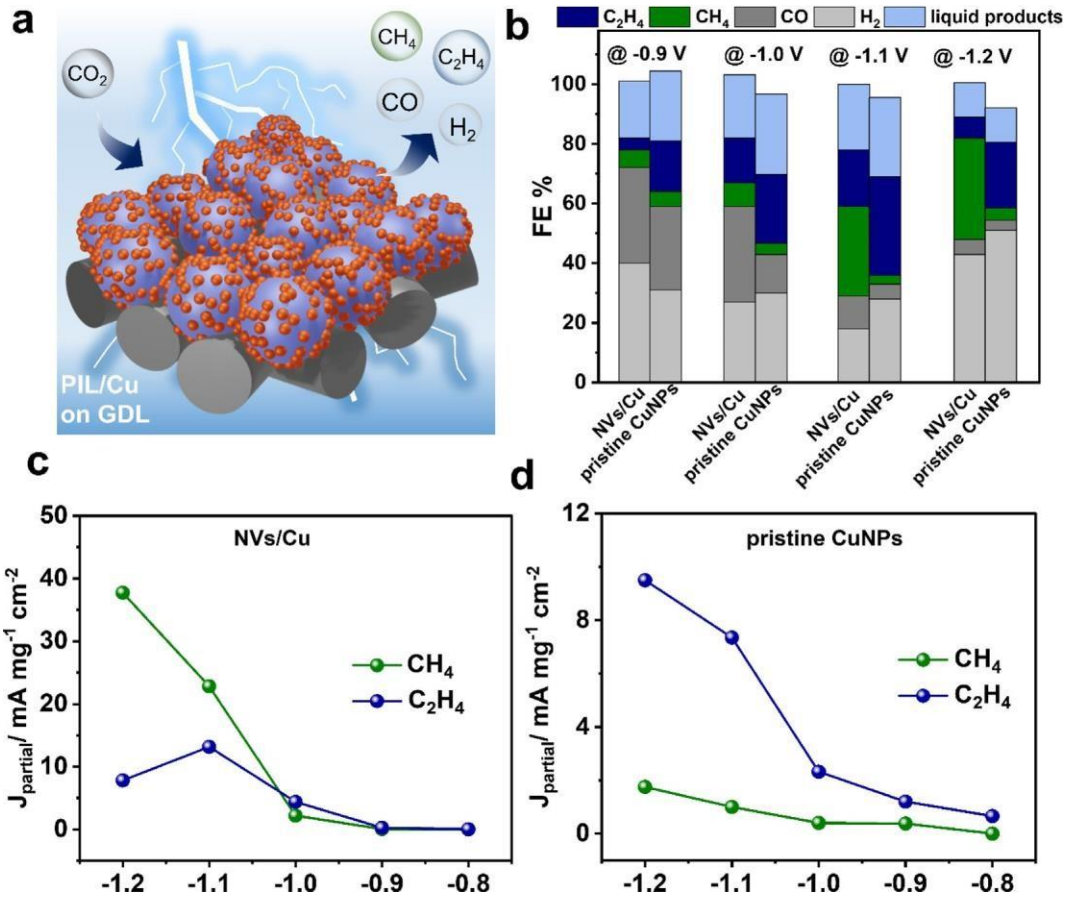

Fig. 5. (a) Scheme of CO_2ER using PIL/Cu composite particles after coating on GDLs. (b) Summary of the CO_2ER activity trend for various catalysts, highlighting the tunable selectivity toward CH_4. The complete dataset is found in Fig. S19. FE% of the PIL NVs/Cu and pristine CuNPs coated GDLs is measured in CO_2-saturated 0.1 M $KHCO_3$ solution at applied potentials (V *vs* RHE). Partial current density toward the generation of CH_4 and C_2H_4 on (c) NVs/Cu, (d) pristine CuNPs as a function of applied potential.

Cu^+ surface species were observed at 932.5 eV and 934.6 eV, respectively, which are still positively shifted (~0.2 eV) compared to that of the pristine CuNPs. The appearance of the mixture of Cu^+ and Cu^{2+} for the PIL/Cu catalysts after CO_2ER instead of the strong positively shifted peak may indicate the transformation of the PILs under CO_2ER measuring conditions. The transformation of PILs under bias was also evidenced by the observed significant changes in the obtained C 1 s spectra of PIL NVs/Cu before and after CO_2ER, see Fig. S22. Regardless, retesting the same electrode after removal of bias in a fresh electrolyte still showed a high FE towards CH_4 (33 % FE). Based on these XPS results, the enhanced C_1 selectivity of the PIL NVs/Cu electrode might be attributable to the strong electronic interaction between PILs and CuNPs as well as the ultra-small size of CuNPs, resulting from *in situ* reduction of PIL NVs/Cu complex under CO_2 electrolysis conditions. The enhanced CH_4 production due to the reduction of Cu from copper complexes is also in line with previous findings.[85,86]

4. Conclusion

In summary, we successfully fabricated PIL homopolymer NVs with a characteristic multilamellar chain stacking *via* free radical homopolymerization, which is in line with our previous studies. [30,52] Their morphologies were tailored from hollow to solid spheres, further to directional solid worms by simply increasing C_m applied in polymerization. Manipulation of the overall size and shell thickness of PIL NVs has been achieved by tuning the C_m, which has been scarcely reported before. Next, we systematically studied the influence of the C_m on their size variation and morphological transformation. The formation mechanism of PIL NVs has been further confirmed by CG simulations, illustrating the essential role of polymerization degree of PIL chains in directing the assembly behavior. Our well-defined PIL NVs with a hollow interior enabled high loading amounts of ultra-small CuNPs (1–3 nm in size) that were used for CO_2ER. Large pristine CuNPs and PIL-functionalized CuNPs (above 30 nm) have been reported to improve the selectivity towards C_2 products in CO_2ER. [47,83] In our study, PIL/Cu composite particles exhibited a high FE towards C_1 products, especially CH_4 (FE of ~ 34 % at —1.2 V). The XPS analysis showed that the strong electronic interactions between the imidazolium units of PILs and the surface Cu atoms of CuNPs results in the high FE towards CH_4. This contribution highlights the potential of future research interest in the use of well- defined PILs to tune the selectivity of metallic electrocatalysts for CO_2 reduction. Future work is expected to deepen our understand- ing *via* a systematic study on the role of PIL and the size effect of CuNPs on CO_2ER performance by *in situ* Raman and XPS.

CRediT authorship contribution statement

Xuefeng Pan: Conceptualization, Writing – original draft. **Zdravko Kochovski**: Resources, Software. **Yong-Lei Wang**: Methodology, Visualization, Software. **Radwan M. Sarhan**: Investigation, Validation. **Eneli Härk**: Resources, Data curation. **Siddharth Gupta**: Investigation, Validation. **Sasho Stojkovikj**: Validation, Resources. **Gumaa A. El-Nagar**: Formal analysis, Writing – review

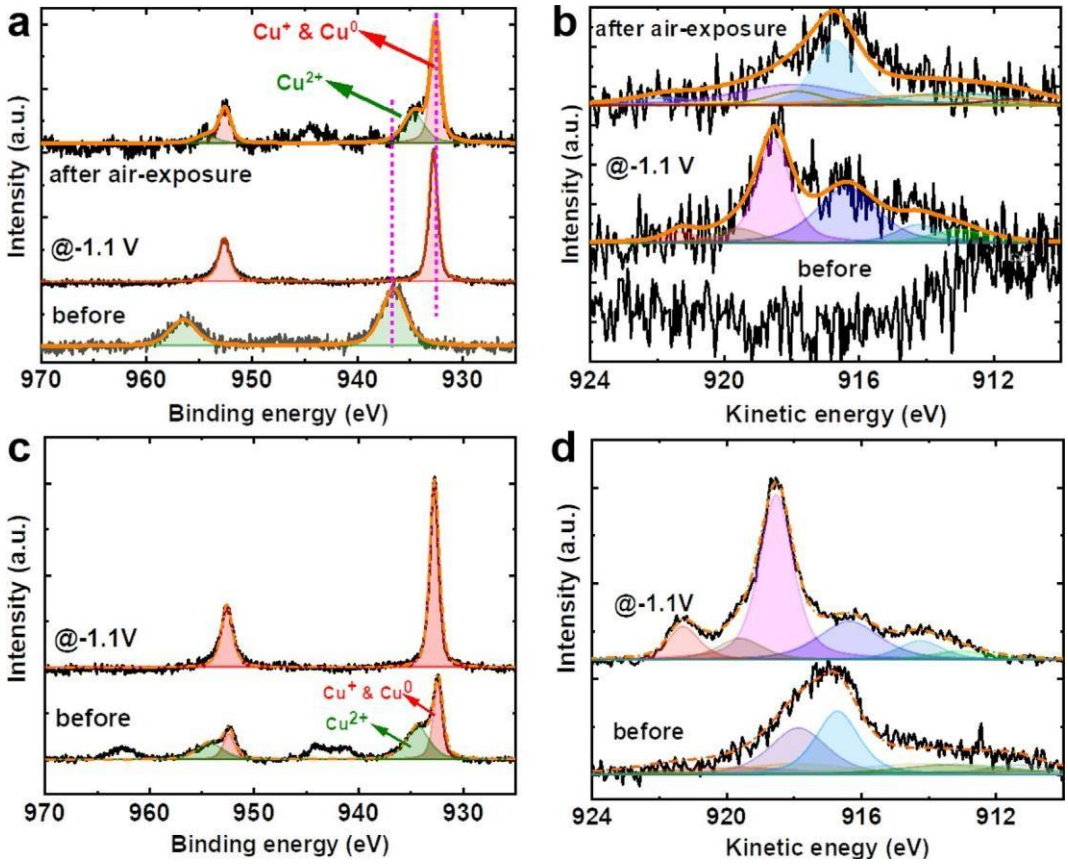

Fig. 6. Quasi *in situ* XPS results of (a, b) the NVs/Cu and (c, d) the pristine CuNPs: (a, c) the Cu 2p XPS spectra and (b, d) the respective Cu Auger regions.

& editing. **Matthew T. Mayer**: Funding acquisition, Writing – review & editing. **Robin Schürmann**: Visualization, Methodology. **Jérôme Deumer**: Resources, Data curation. **Christian Gollwitzer**: Validation, Writing – review & editing. **Jiayin Yuan**: Supervision, Writing – review & editing. **Yan Lu**: Project administration, Supervision, Funding acquisition, Writing – review & editing.

Data availability

Data will be made available on request.

Declaration of Competing Interest

The authors declare that they have no known competing financial interests or personal relationships that could have appeared to influence the work reported in this paper.

Acknowledgements

The authors thank Flora Haun from Freie Universität Berlin for the great help in electrochemical experiments. The authors also thank Ms. Qiong Fang and Yi Chen for the suggestions in 3D modelling. Y. L. also thanks the Deutsche Forschungsgemeinschaft (DFG, German Research Foundation) - Project number 410871749 for financial support. The authors also thank the Joint Lab for Structural Research at the Integrative Research Institute for the Sciences (IRIS Adlershof) for cryo-TEM measurements. J. Y. appreciates the financial support of the Knut and Alice Wallenberg Foundation under the program Wallenberg Academy Fellow (WAF2017.0166) and the European research council consolidator grant (PARIS-101043485), and computations were performed using computational resources provided by Swedish National Infrastructure for Computing (SNIC) at PDC, HPC2N, and NSC partially funded by Swedish Research Council through grant agreement no. 2016-07213. This work was supported in part by the Helmholtz Association's Initiative and Networking Fund (Helmholtz Young Investigator Group VH-NG-1225) and the European Union's Horizon 2020 research and innovation program project FlowPhotoChem (grant agreement 862453). The material presented and views expressed here are the responsibilities of the author (s) only; the EU Commission takes no responsibility for any use made of the information set out.

Appendix A. Supplementary data

Supplementary data to this article can be found online at https://doi.org/10.1016/j.jcis.2023.01.097.

References

[1] R.M. Gorgoll, K. Harano, E. Nakamura, Nanoscale Control of Polymer Assembly on a Synthetic Catalyst-Bilayer System, J. Am. Chem. Soc. 138 (30) (2016) 9675–9681.
[2] A. Joseph, C. Contini, D. Cecchin, S. Nyberg, L. Ruiz-Perez, J. Gaitzsch, G. Fullstone, X. Tian, J. Azizi, J. Preston, G. Volpe, G. Battaglia, Chemotactic synthetic vesicles: Design and applications in blood-brain barrier crossing, Sci. Adv. 3 (8) (2017) e1700362.
[3] Y. Zhu, L. Fan, B. Yang, J. Du, Multifunctional Homopolymer Vesicles for Facile Immobilization of Gold Nanoparticles and Effective Water Remediation, ACS Nano 8 (5) (2014) 5022–5031.
[4] P. Tanner, P. Baumann, R. Enea, O. Onaca, C. Palivan, W. Meier, Polymeric Vesicles: From Drug Carriers to Nanoreactors and Artificial Organelles, Acc. Chem. Res. 44 (10) (2011) 1039–1049.
[5] M. Fauquignon, E. Courtecuisse, R. Josselin, A. Mutschler, A. Brûlet, M. Schmutz, J.-F. Le Meins, Large hybrid Polymer/Lipid Unilamellar vesicle (LHUV) at the

nanoscale: An insight into the lipid distribution in the membrane and permeability control, J. Colloid Interface Sci. 604 (2021) 575–583.
[6] Y. Zhu, B. Yang, S. Chen, J. Du, Polymer vesicles: Mechanism, preparation, application, and responsive behavior, Prog. Polym. Sci. 64 (2017) 1–22.
[7] M. Sasidharan, K. Nakashima, Core–Shell–Corona Polymeric Micelles as a Versatile Template for Synthesis of Inorganic Hollow Nanospheres, Acc. Chem. Res. 47 (1) (2014) 157–167.
[8] R.A. Ramli, Hollow polymer particles: a review, RSC Adv. 7 (83) (2017) 52632–52650.
[9] T. Nishimura, S. Shishi, Y. Sasaki, K. Akiyoshi, Thermoresponsive Polysaccharide Graft Polymer Vesicles with Tunable Size and Structural Memory, J. Am. Chem. Soc. 142 (27) (2020) 11784–11790.
[10] Q. He, D.-H. Tuo, Y.-F. Ao, Q.-Q. Wang, D.-X. Wang, Vesicles Constructed with Chiral Amphiphilic Oxacalix[2]arene[2]triazine Derivatives for Enantioselective Recognition of Organic Anions, ACS App. Mater. Interfaces 10 (4) (2018) 3181–3185.
[11] W. Jiang, Y. Zhou, D. Yan, Hyperbranched polymer vesicles: from self- assembly, characterization, mechanisms, and properties to applications, Chem. Soc. Rev. 44 (12) (2015) 3874–3889.
[12] D. Gaur, N.C. Dubey, B.P. Tripathi, Biocatalytic self-assembled synthetic vesicles and coacervates: From single compartment to artificial cells, Adv. Colloid Interface Sci. 299 (2022) 102566.
[13] Q. Chen, H. Schönherr, G.J. Vancso, Block-Copolymer Vesicles as Nanoreactors for Enzymatic Reactions, Small 5 (12) (2009) 1436–1445.
[14] C.K. Wong, A.D. Martin, M. Floetenmeyer, R.G. Parton, M.H. Stenzel, P. Thordarson, Faceted polymersomes: a sphere-to-polyhedron shape transformation, Chem. Sci. 10 (9) (2019) 2725–2731.
[15] S. So, T.P. Lodge, Size Control and Fractionation of Ionic Liquid Filled Polymersomes with Glassy and Rubbery Bilayer Membranes, Langmuir 32 (19) (2016) 4959–4968.
[16] J. He, L. Wang, Z. Wei, Y. Yang, C. Wang, X. Han, Z. Nie, Vesicular Self-Assembly of Colloidal Amphiphiles in Microfluidics, ACS App. Mater. Interfaces 5 (19) (2013) 9746–9751.
[17] J.R. Howse, R.A.L. Jones, G. Battaglia, R.E. Ducker, G.J. Leggett, A.J. Ryan, Templated formation of giant polymer vesicles with controlled size distributions, Nat. Mater. 8 (6) (2009) 507–511.
[18] C. Lebleu, L. Rodrigues, J.-M. Guigner, A. Brûlet, E. Garanger, S. Lecommandoux, Self-Assembly of PEG-b-PTMC Copolymers: Micelles and Polymersomes Size Control, Langmuir 35 (41) (2019) 13364–13374.
[19] L. Ma, A. Eisenberg, Relationship between Wall Thickness and Size in Block Copolymer Vesicles, Langmuir 25 (24) (2009) 13730–13736.
[20] J. Yuan, M. Antonietti, Poly(ionic liquid)s: Polymers expanding classical property profiles, Polymer 52 (7) (2011) 1469–1482.
[21] J. Yuan, D. Mecerreyes, M. Antonietti, Poly(ionic liquid)s: An update, Prog. Polym. Sci. 38 (7) (2013) 1009–1036.
[22] S.-Y. Zhang, H. Miao, H.-M. Zhang, J.-H. Zhou, Q. Zhuang, Y.-J. Zeng, Z. Gao, J. Yuan, J.-K. Sun, Accelerating Crystallization of Open Organic Materials by Poly (ionic liquid)s, Angew. Chem. Int. Ed. 59 (49) (2020) 22109–22116.
[23] J.-K. Sun, Y.I. Sobolev, W. Zhang, Q. Zhuang, B.A. Grzybowski, Enhancing crystal growth using polyelectrolyte solutions and shear flow, Nature 579 (7797) (2020) 73–79.
[24] D. Xie, Y. Xu, Y. Wang, X. Pan, E. Härk, Z. Kochovski, A. Eljarrat, J. Müller, C.T. Koch, J. Yuan, Y. Lu, Poly(ionic liquid) Nanovesicle-Templated Carbon Nanocapsules Functionalized with Uniform Iron Nitride Nanoparticles as Catalytic Sulfur Host for Li–S Batteries, ACS Nano 16 (7) (2022) 10554–10565.
[25] Y. Jiang, D. Li, Y. Zhao, J. Sun, Hydrogen bond donor functionalized poly(ionic liquids)@MIL-101 for the CO2 capture and improving the catalytic CO2 conversion with epoxide, J. Colloid Interface Sci. 618 (2022) 22–33.
[26] W. Qian, J. Texter, F. Yan, Frontiers in poly(ionic liquid)s: syntheses and applications, Chem. Soc. Rev. 46 (4) (2017) 1124–1159.
[27] T.M. Ukarde, J.S. Mahale, P.H. Pandey, A. Vasishta, A.M.J.C. Harrish, H.S. Pawar, Facile Synthesis of Novel Polyethyleneimine Functionalized Polymeric Protic Ionic Liquids (PolyE-ILs) with Protagonist Properties for Acid Catalysis, ChemistrySelect 6 (36) (2021) 9616–9624.
[28] K. Manojkumar, K.T. Prabhu Charan, A. Sivaramakrishna, P.C. Jha, V.M. Khedkar, R. Siva, G. Jayaraman, K. Vijayakrishna, Biophysical Characterization and Molecular Docking Studies of Imidazolium Based Polyelectrolytes–DNA Complexes: Role of Hydrophobicity, Biomacromolecules 16 (3) (2015) 894–903.
[29] K. Manojkumar, D. Mecerreyes, D. Taton, Y. Gnanou, K. Vijayakrishna, Self- assembly of poly(ionic liquid) (PIL)-based amphiphilic homopolymers into vesicles and supramolecular structures with dyes and silver nanoparticles, Polym. Chem. 8 (22) (2017) 3497–3503.
[30] W. Zhang, Z. Kochovski, Y. Lu, B.V.K.J. Schmidt, M. Antonietti, J. Yuan, Internal Morphology-Controllable Self-Assembly in Poly(Ionic Liquid) Nanoparticles, ACS Nano 10 (8) (2016) 7731–7737.
[31] M. Koebe, M. Drechsler, J. Weber, J. Yuan, Crosslinked Poly(ionic liquid) Nanoparticles: Inner Structure, Size, and Morphology, Macromol. Rapid Commun. 33 (8) (2012) 646–651.
[32] E.J. Cornel, J. Jiang, S. Chen, J. Du, Principles and characteristics of polymerization-induced self-assembly with various polymerization techniques, CCS Chemistry 3 (4) (2021) 2104–2125.
[33] X. Zhou, J. Weber, J. Yuan, Poly(ionic liquid)s: Platform for CO2 capture and catalysis, Curr. Opin. Green Sust. 16 (2019) 39–46.
[34] Y. Xie, J. Liang, Y. Fu, M. Huang, X. Xu, H. Wang, S. Tu, J. Li, Hypercrosslinked mesoporous poly(ionic liquid)s with high ionic density for efficient CO2 capture and conversion into cyclic carbonates, J. Mater. Chem. A 6 (15) (2018) 6660–6666.
[35] E. Ewins, R.B. Lira, W. Zhang, J. Yuan, M. Antonietti, T. Robinson, R. Dimova, Poly(Ionic Liquid) Nanoparticles Selectively Disrupt Biomembranes, Adv. Sci. 6 (4) (2019) 1801602.
[36] I. Sullivan, A. Goryachev, I.A. Digdaya, X. Li, H.A. Atwater, D.A. Vermaas, C. Xiang, Coupling electrochemical CO2 conversion with CO2 capture, Nat. Catal. 4 (11) (2021) 952–958.
[37] M. Jouny, W. Luc, F. Jiao, General Techno-Economic Analysis of CO2 Electrolysis Systems, Ind. Eng. Chem. Res. 57 (6) (2018) 2165–2177.
[38] R. Sen, A. Goeppert, S. Kar, G.K.S. Prakash, Hydroxide Based Integrated CO2 Capture from Air and Conversion to Methanol, J. Am. Chem. Soc. 142 (10) (2020) 4544–4549.
[39] A.J. Garza, A.T. Bell, M. Head-Gordon, Mechanism of CO2 Reduction at Copper Surfaces: Pathways to C2 Products, ACS Catal. 8 (2) (2018) 1490–1499.
[40] Y.A. Alsunni, A.W. Alherz, C.B. Musgrave, Electrocatalytic Reduction of CO2 to CO over Ag(110) and Cu(211) Modeled by Grand-Canonical Density Functional Theory, J. Phys. Chem. C 125 (43) (2021) 23773–23783.
[41] D. Kim, C.S. Kley, Y. Li, P. Yang, Copper nanoparticle ensembles for selective electroreduction of CO2 to C2–C3 products, Proc. Nat. Acad. Sci. 114(40) (2017) 10560-10565.
[42] D. Raciti, C. Wang, Recent Advances in CO2 Reduction Electrocatalysis on Copper, ACS Energy Lett. 3 (7) (2018) 1545–1556.
[43] Z. Gu, H. Shen, L. Shang, X. Lv, L. Qian, G. Zheng, Nanostructured Copper-Based Electrocatalysts for CO2 Reduction, Small Methods 2 (11) (2018) 1800121.
[44] S. Nitopi, E. Bertheussen, S.B. Scott, X. Liu, A.K. Engstfeld, S. Horch, B. Seger, I.E. L. Stephens, K. Chan, C. Hahn, J.K. Nørskov, T.F. Jaramillo, I. Chorkendorff, Progress and Perspectives of Electrochemical CO2 Reduction on Copper in Aqueous Electrolyte, Chem. Rev. 119 (12) (2019) 7610–7672.
[45] Y. Ye, Y. Liu, Z. Li, X. Zou, H. Wu, S. Lin, Highly selective and active Cu-In2O3/C nanocomposite for electrocatalytic reduction of CO2 to CO, J. Colloid Interface Sci. 586 (2021) 528–537.
[46] W. Wang, S. Gong, J. Liu, Y. Ge, J. Wang, X. Lv, Ag-Cu aerogel for electrochemical CO2 conversion to CO, J. Colloid Interface Sci. 595 (2021) 159– 167.
[47] X.-Q. Li, G.-Y. Duan, J.-W. Chen, L.-J. Han, S.-J. Zhang, B.-H. Xu, Regulating electrochemical CO2RR selectivity at industrial current densities by structuring copper@poly(ionic liquid) interface, Appl. Catal. B 297 (2021) 120471.
[48] K.T. Prabhu Charan, N. Pothanagandhi, K. Vijayakrishna, A. Sivaramakrishna, D. Mecerreyes, B. Sreedhar, Poly(ionic liquids) as "smart" stabilizers for metal nanoparticles, Eur. Polym. J. 60 (2014) 114–122.
[49] J.-K. Sun, Z. Kochovski, W.-Y. Zhang, H. Kirmse, Y. Lu, M. Antonietti, J. Yuan, General Synthetic Route toward Highly Dispersed Metal Clusters Enabled by Poly(ionic liquid)s, J. Am. Chem. Soc. 139 (26) (2017) 8971–8976.
[50] Y. Gong, H. Zhong, W. Liu, B. Zhang, S. Hu, R. Wang, General Synthetic Route toward Highly Dispersed Ultrafine Pd–Au Alloy Nanoparticles Enabled by Imidazolium-Based Organic Polymers, ACS App. Mater. Interfaces 10 (1) (2018) 776–786.
[51] D. Parida, C. Bakkali-Hassani, E. Lebraud, C. Schatz, S. Grelier, D. Taton, J. Vignolle, Tuning the activity and selectivity of polymerised ionic liquid-stabilised ruthenium nanoparticles through anion exchange reactions, Nanoscale 14 (12) (2022) 4635–4643.
[52] J. Yuan, M. Antonietti, Poly(ionic liquid) Latexes Prepared by Dispersion Polymerization of Ionic Liquid Monomers, Macromolecules 44 (4) (2011) 744–750.
[53] A. Khorsand Kheirabad, X. Pan, S. Long, Z. Kochovski, S. Zhou, Y. Lu, G. McInerney, J. Yuan, Colloidal dispersion of poly(ionic liquid)/Cu composite particles for protective surface coating against SAR-CoV-2, Nano Select 3 (1) (2022) 227–232.
[54] S. Stojkovikj, G.A. El-Nagar, F. Firschke, L.C. Pardo Pérez, L. Choubrac, M. Najdoski, M.T. Mayer, Electrocatalyst Derived from Waste Cu–Sn Bronze for CO2 Conversion into CO, ACS App. Mater. Interfaces 13 (32) (2021) 38161–38169.
[55] H. He, M. Zhong, B. Adzima, D. Luebke, H. Nulwala, K. Matyjaszewski, A Simple and Universal Gel Permeation Chromatography Technique for Precise Molecular Weight Characterization of Well-Defined Poly(ionic liquid)s, J. Am. Chem. Soc. 135 (11) (2013) 4227–4230.
[56] M. Krumrey, G. Ulm, High-accuracy detector calibration at the PTB four-crystal monochromator beamline, Nucl. Instruments Methods Phys. Res. Sect. A, Accelerators, Spectrometers, Detectors Associated Equipment (2001) 1175–1178. Medium: X; Size:.
[57] J. Wernecke, C. Gollwitzer, P. Muller, M. Krumrey, Characterization of an in-vacuum PILATUS 1M detector, J. Synchrotron Radiat. 21 (3) (2014) 529–536.
[58] A. Schavkan, C. Gollwitzer, R. Garcia-Diez, M. Krumrey, C. Minelli, D. Bartczak, S. Cuello-Nuñez, H. Goenaga-Infante, J. Rissler, E. Sjöström, G.B. Baur, K. Vasilatou, A.G. Shard, Number Concentration of Gold Nanoparticles in Suspension: SAXS and spICPMS as Traceable Methods Compared to Laboratory Methods, Nanomaterials 9 (4) (2019) 502.
[59] C. Gollwitzer, D. Bartczak, H. Goenaga-Infante, V. Kestens, M. Krumrey, C. Minelli, M. Pálmai, Y. Ramaye, G. Roebben, A. Sikora, Z. Varga, A comparison of techniques for size measurement of nanoparticles in cell culture medium, Anal. Methods 8 (26) (2016) 5272–5282.
[60] L.C. Pardo Pérez, A. Arndt, S. Stojkovikj, I.Y. Ahmet, J.T. Arens, F. Dattila, R. Wendt, A. Guilherme Buzanich, M. Radtke, V. Davies, K. Höflich, E. Köhnen, P. Tockhorn, R. Golnak, J. Xiao, G. Schuck, M. Wollgarten, N. López, M.T. Mayer,

Determining Structure-Activity Relationships in Oxide Derived Cu-Sn Catalysts During CO2 Electroreduction Using X-Ray Spectroscopy, Adv. Energy Mater. 12 (5) (2022) 2103328.
[61] Y.-L. Wang, B. Li, A. Laaksonen, Coarse-grained simulations of ionic liquid materials: from monomeric ionic liquids to ionic liquid crystals and polymeric ionic liquids, PCCP 23 (35) (2021) 19435–19456.
[62] Y.-L. Wang, Y.-L. Zhu, Z.-Y. Lu, A. Laaksonen, Electrostatic interactions in soft particle systems: mesoscale simulations of ionic liquids, Soft Matter 14 (21) (2018) 4252–4267.
[63] S.-C. Yang, B. Li, Y.-L. Zhu, A. Laaksonen, Y.-L. Wang, The ENUF method—Ewald summation based on nonuniform fast Fourier transform: Implementation, parallelization, and application, J. Comput. Chem. 41 (27) (2020) 2316–2335.
[64] Y.-L. Wang, A. Laaksonen, Z.-Y. Lu, Implementation of non-uniform FFT based Ewald summation in dissipative particle dynamics method, J. Comput. Phys. 235 (2013) 666.
[65] J. Yuan, S. Soll, M. Drechsler, A.H.E. Müller, M. Antonietti, Self-Assembly of Poly (ionic liquid)s: Polymerization, Mesostructure Formation, and Directional Alignment in One Step, J. Am. Chem. Soc. 133 (44) (2011) 17556–17559.
[66] Z. Kochovski, G. Chen, J. Yuan, Y. Lu, Cryo-Electron microscopy for the study of self-assembled poly(ionic liquid) nanoparticles and protein supramolecular structures, Colloid Polym. Sci. 298 (7) (2020) 707–717.
[67] I. Bressler, J. Kohlbrecher, A.F. Thunemann, SASfit: a tool for small-angle scattering data analysis using a library of analytical expressions, J. Appl. Cryst. 48 (5) (2015) 1587–1598.
[68] Z. Varga, Y. Yuana, A.E. Grootemaat, E. van der Pol, C. Gollwitzer, M. Krumrey, R. Nieuwland, Towards traceable size determination of extracellular vesicles, J. Extracell. Vesicles 3 (1) (2014) 23298.
[69] V. Delhorbe, D. Bresser, H. Mendil-Jakani, P. Rannou, L. Bernard, T. Gutel, S. Lyonnard, L. Picard, Unveiling the Ion Conduction Mechanism in Imidazolium- Based Poly(ionic liquids): A Comprehensive Investigation of the Structure-to- Transport Interplay, Macromolecules 50 (11) (2017) 4309–4321.
[70] R. Bleul, R. Thiermann, M. Maskos, Techniques To Control Polymersome Size, Macromolecules 48 (20) (2015) 7396–7409.
[71] T. Nishimura, Y. Sasaki, K. Akiyoshi, Biotransporting Self-Assembled Nanofactories Using Polymer Vesicles with Molecular Permeability for Enzyme Prodrug Cancer Therapy, Adv. Mater. 29 (36) (2017) 1702406.
[72] Z. Huang, M. Yi, Y. Liu, P. Qi, A. Song, J. Hao, Magnetic polymerizable surfactants: thermotropic liquid crystal behaviors and construction of nanostructured films, New J. Chem. 44 (38) (2020) 16537–16545.
[73] Y. Kimura, M. Takenaka, M. Ouchi, T. Terashima, Self-Sorting of Amphiphilic Block-Pendant Homopolymers into Sphere or Rod Micelles in Water, Macromolecules 53 (12) (2020) 4942–4951.
[74] Y. Kimura, T. Terashima, Morphology transition of amphiphilic homopolymer self-assemblies in water triggered by pendant design and chain length, Eur. Polym. J. 139 (2020) 110001.
[75] C. Barner-Kowollik, G.T. Russell, Chain-length-dependent termination in radical polymerization: Subtle revolution in tackling a long-standing challenge, Prog. Polym. Sci. 34 (11) (2009) 1211–1259.
[76] C. Gonzato, M. Semsarilar, E.R. Jones, F. Li, G.J.P. Krooshof, P. Wyman, O.O. Mykhaylyk, R. Tuinier, S.P. Armes, Rational Synthesis of Low-Polydispersity Block Copolymer Vesicles in Concentrated Solution via Polymerization- Induced Self-Assembly, J. Am. Chem. Soc. 136 (31) (2014) 11100–11106.
[77] M. Xiao, J. Liu, J. Yang, R. Wang, D. Xie, Biomimetic membrane control of block copolymer vesicles with tunable wall thickness, Soft Matter 9 (8) (2013) 2434–2442.
[78] Q. Ge, D. Lou, S. Lu, W. Zhang, L. Zhang, X. Wang, Aggregation behavior of N-alkyl imidazolium-based poly(ionic liquid)s in an organic solvent, RSC Adv. 6 (90) (2016) 87461–87468.
[79] A.V. Dobrynin, M. Rubinstein, Theory of polyelectrolytes in solutions and at surfaces, Prog. Polym. Sci. 30 (11) (2005) 1049–1118.
[80] A.V. Dobrynin, Effect of Counterion Condensation on Rigidity of Semiflexible Polyelectrolytes, Macromolecules 39 (26) (2006) 9519–9527.
[81] M. Satoh, J. Komiyama, T. Iijima, Counterion condensation in polyelectrolyte solution: a theoretical prediction of the dependences on the ionic strength and the degree of polymerization, Macromolecules 18 (6) (1985) 1195–1200.
[82] N.V. Brilliantov, D.V. Kuznetsov, R. Klein, Chain Collapse and Counterion Condensation in Dilute Polyelectrolyte Solutions, Phys. Rev. Lett. 81 (7) (1998) 1433–1436.
[83] G.-Y. Duan, X.-Q. Li, G.-R. Ding, L.-J. Han, B.-H. Xu, S.-J. Zhang, Highly Efficient Electrocatalytic CO2 Reduction to C2+ Products on a Poly(ionic liquid)-Based Cu0–CuI Tandem Catalyst, Angew. Chem. Int. Ed. 61 (9) (2022) e202110657.
[84] F. Hannig, G. Kehr, R. Fröhlich, G. Erker, Formation of chiral ionic liquids and imidazol-2-ylidene metal complexes from the proteinogenic aminoacid l-histidine, J. Organomet. Chem. 690 (24) (2005) 5959–5972.
[85] Z. Weng, Y. Wu, M. Wang, J. Jiang, K. Yang, S. Huo, X.-F. Wang, Q. Ma, G.W. Brudvig, V.S. Batista, Y. Liang, Z. Feng, H. Wang, Active sites of copper-complex catalytic materials for electrochemical carbon dioxide reduction, Nat. Commun. 9 (1) (2018) 415.
[86] Z. Weng, J. Jiang, Y. Wu, Z. Wu, X. Guo, K.L. Materna, W. Liu, V.S. Batista, G.W. Brudvig, H. Wang, Electrochemical CO2 Reduction to Hydrocarbons on a Heterogeneous Molecular Cu Catalyst in Aqueous Solution, J. Am. Chem. Soc. 138 (26) (2016) 8076–8079.

Supporting Information

Poly(ionic liquid) nanovesicles *via* polymerization induced self-assembly and their stabilization of Cu nanoparticles for tailored CO_2 electroreduction

Xuefeng Pan[a,g], Zdravko Kochovski[a], Yong-Lei Wang[a], Radwan M. Sarhan[a,d], Eneli Härk [a], Siddharth Gupta[b,c], Sasho Stojkovikj[b,c], Gumaa A. El-Nagar[b,d*], Matthew T. Mayer[b], Robin Schürmann [e], Jérôme Deumer [e], Christian Gollwitzer[e], Jiayin Yuan[f*] and Yan Lu[a,g*]

[a]*Department for Electrochemical Energy Storage, Helmholtz-Zentrum Berlin für Materialien und Energie, Hahn-Meitner-Platz 1, 14109 Berlin, Germany.*
[b]*Helmholtz Young Investigator Group: Electrochemical Conversion, Helmholtz-Zentrum Berlin für Materialien und Energie, Hahn-Meitner-Platz 1, 14109 Berlin, Germany.*
[c]*Institut für Chemie und Biochemie, Freie Universität Berlin, Arnimallee 22, D -14195 Berlin, Germany.*
[d]*Chemistry department, Faculty of science, Cairo University, Egypt.*
[e]*Physikalisch-Technische Bundesanstalt (PTB), Abbestr. 2-12, 10587 Berlin, Germany.*
[f]*Department of Materials and Environmental Chemistry (MMK), Stockholm University, Svante Arrhenius väg 16C, 10691 Stockholm, Sweden.*
[g]*Institute of Chemistry, University of Potsdam, Karl-Liebknecht-Str. 24-25, 14476 Potsdam, Germany.*

E-mails:
Yan Lu: yan.lu@helmholtz-berlin.de
Jiayin yuan: jiayin.yuan@mmk.su.se
Gumaa A. El-Nagar: gumaa.el-nagar@helmholtz-berlin.de

1. Supplementary data

1.1 Supplementary figures

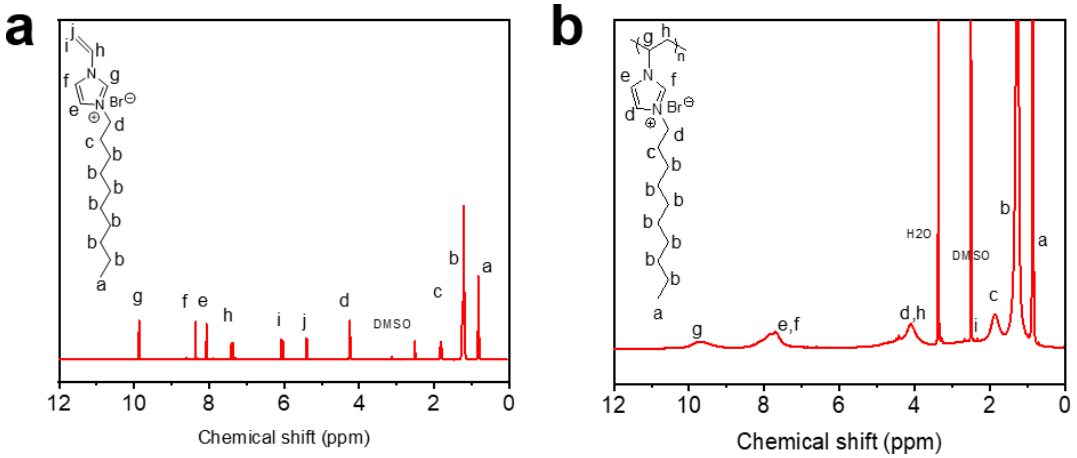

Fig. S1. (a) ^{1}H-NMR spectra of the IL monomers and (b) the corresponding PILs prepared at the C_m of 12 mg/mL.

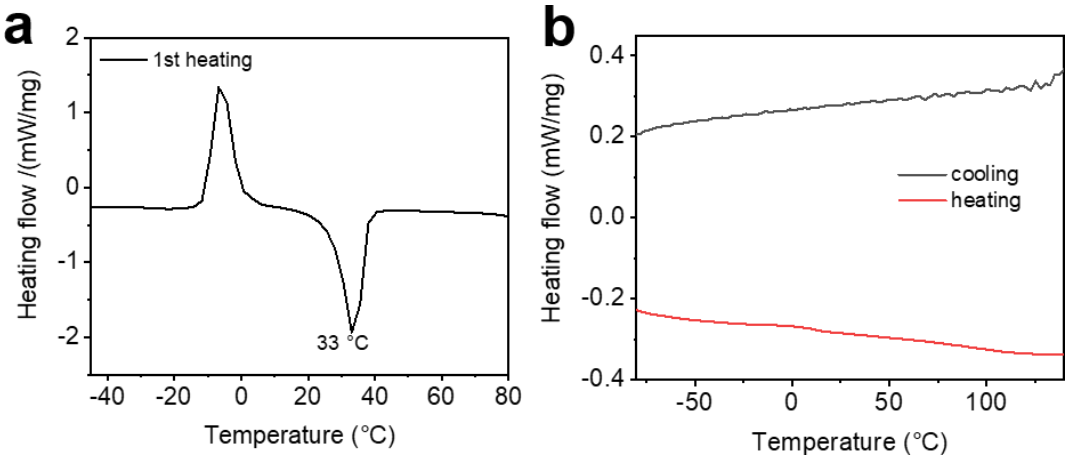

Fig. S2. DSC curves of (a) IL monomer and (b) corresponding PIL prepared at the C_m of 12 mg/mL after freeze-drying.

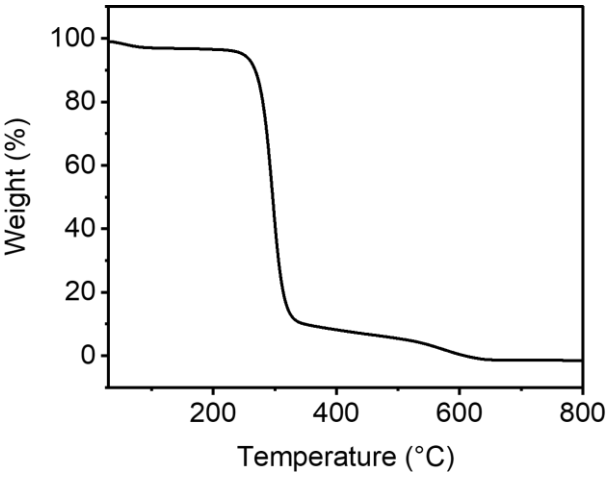

Fig. S3. TGA curves measured under synthetic air of the PIL sample prepared at the C_m of 12 mg/mL after freeze-drying.

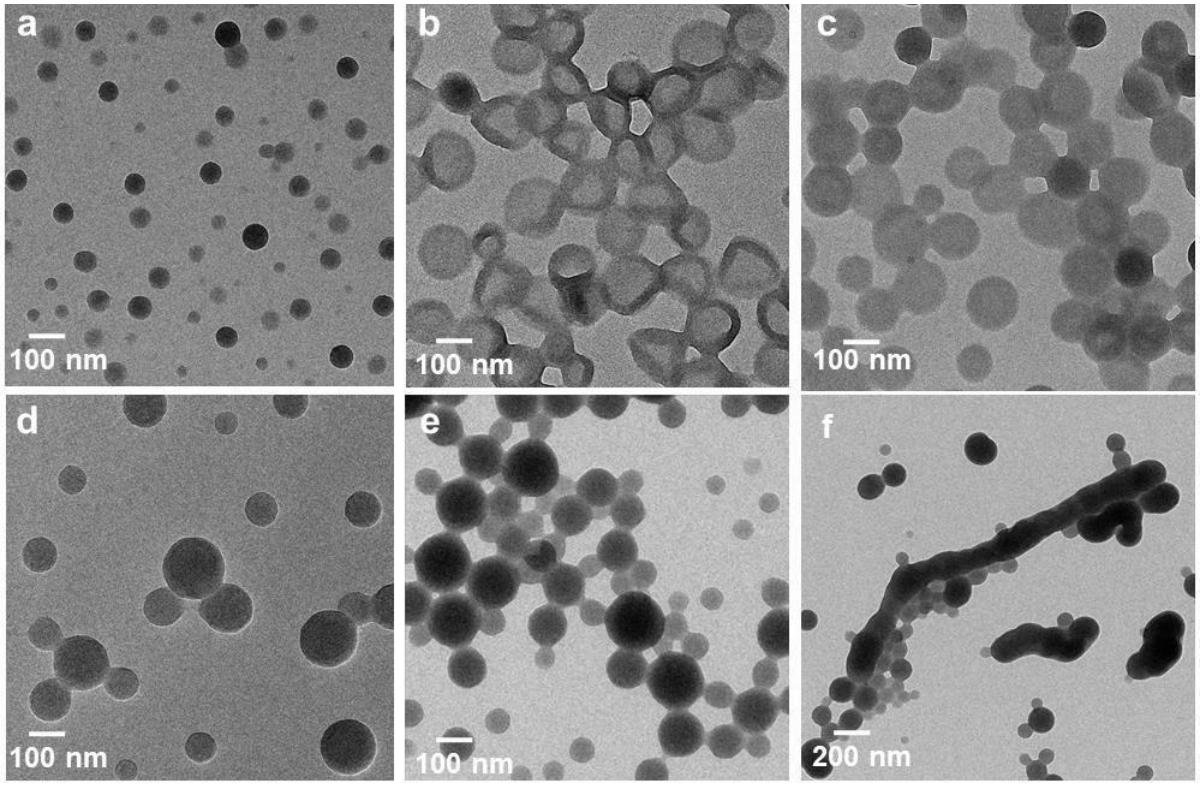

Fig. S4. TEM images of the PIL NVs prepared at various C_m: (a) 3 mg/mL, (b) 6 mg/mL, (c) 12 mg/mL, (d) 16 mg/mL, (e) 24 mg/mL, and (f) 48 mg/mL.

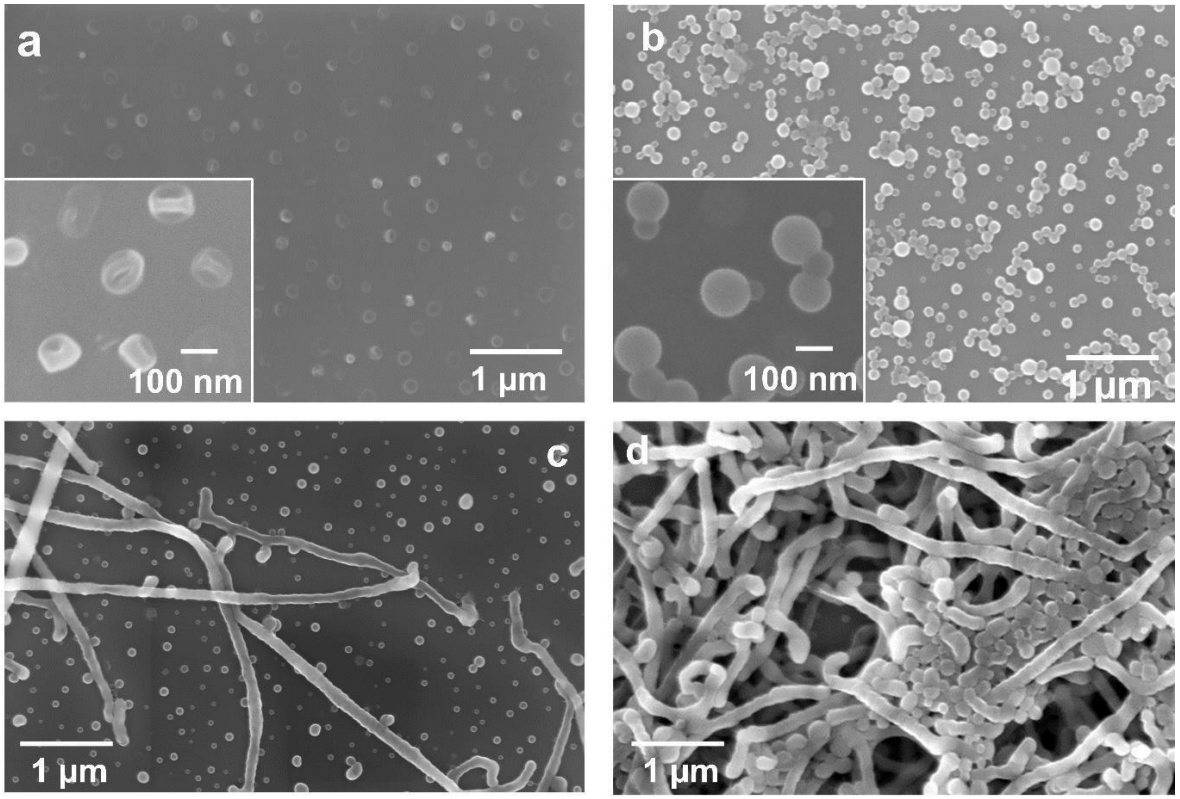

Fig. S5. SEM images of the PIL NVs prepared at various C_m: (a) 12 mg/mL, (b) 24 mg/mL, and (c, d) 48 mg/mL.

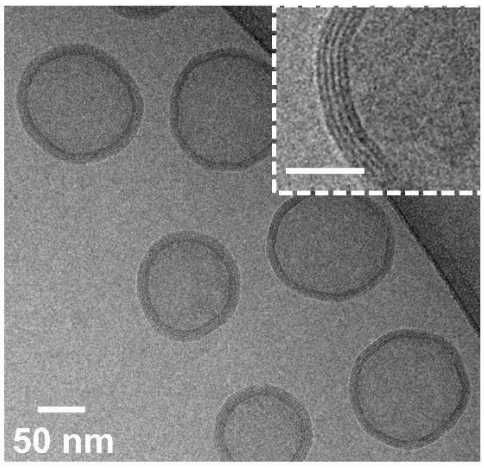

Fig. S6. Cryo-TEM image of the PIL NVs prepared at C_m of 6 mg/mL. The inset is the corresponding high magnification image with a scale bar of 25 nm.

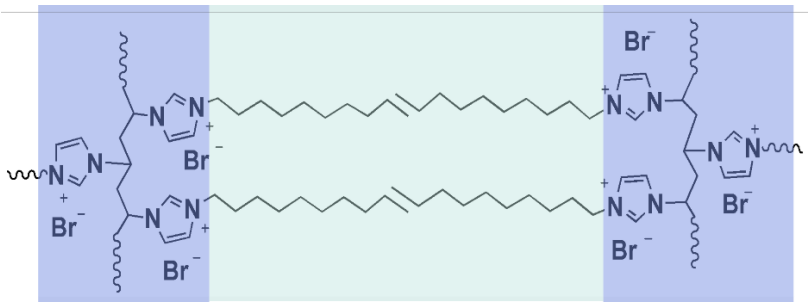

Fig. S7. Molecular packing scheme of the bilayer structure of PIL NVs.

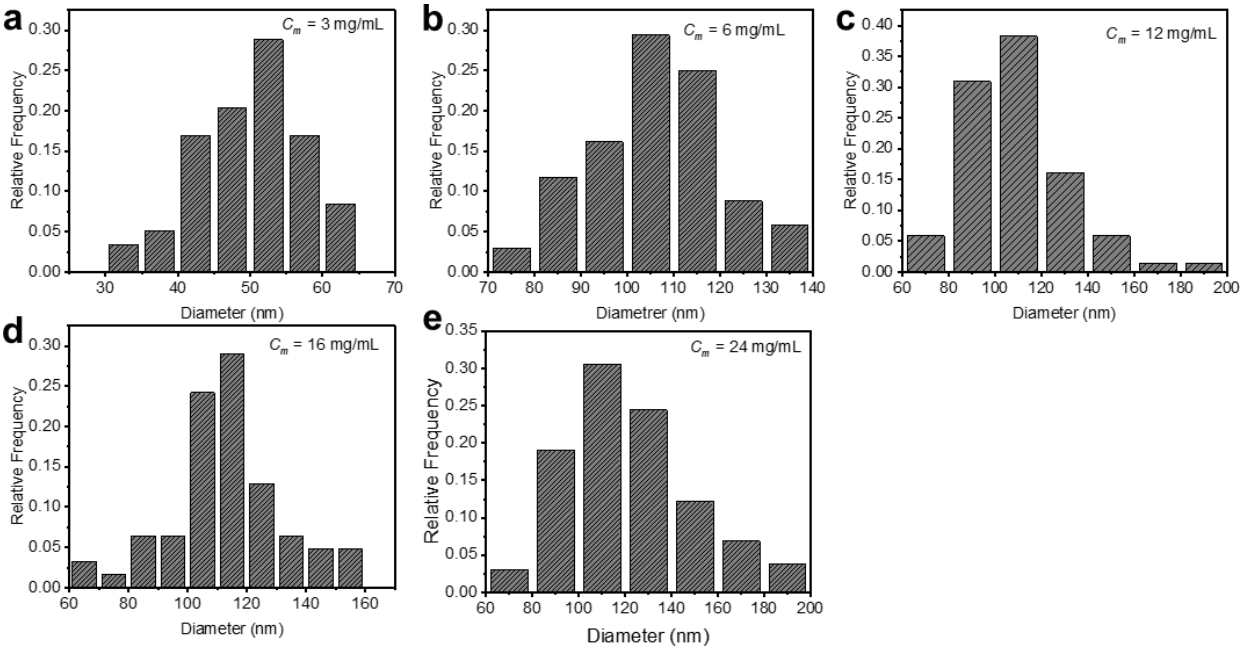

Fig. S8. Particle size distribution histograms (based on over 100 particles) determined from the cryo-TEM images of the PIL NVs prepared at various C_m.

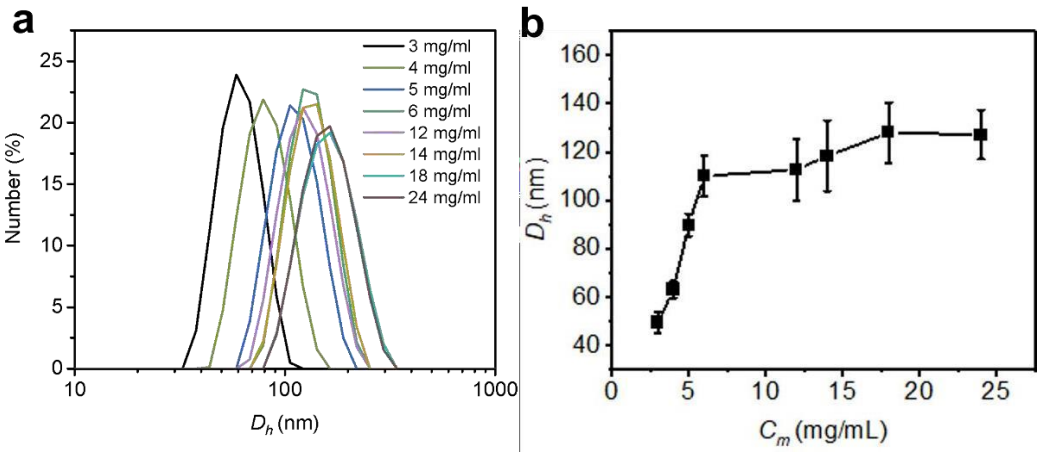

Fig. S9. DLS plots of the PIL NVs prepared at various C_m: (a) size distribution and (b) Hydrodynamic diameter (D_h). Each test has been repeated for 3 times to obtain the average value.

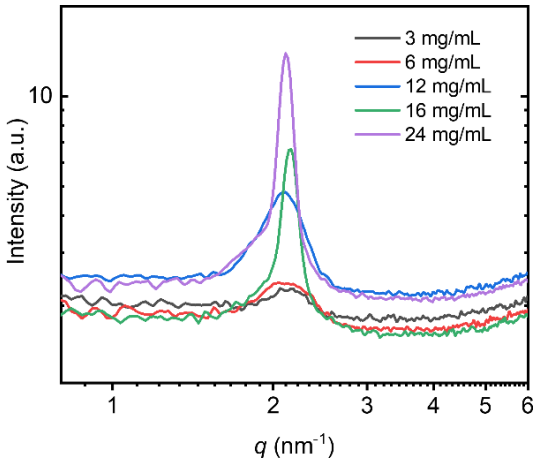

Fig. S10. WAXS profiles of the PIL NVs prepared at various C_m.

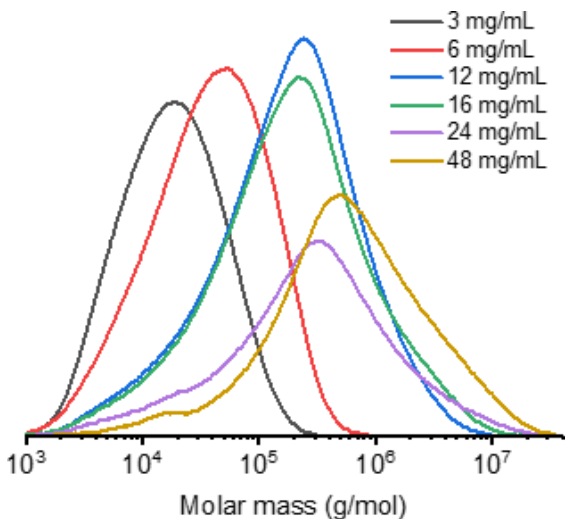

Fig. S11. Molecular weight distributions of the PILs prepared at various C_m after freeze-drying.

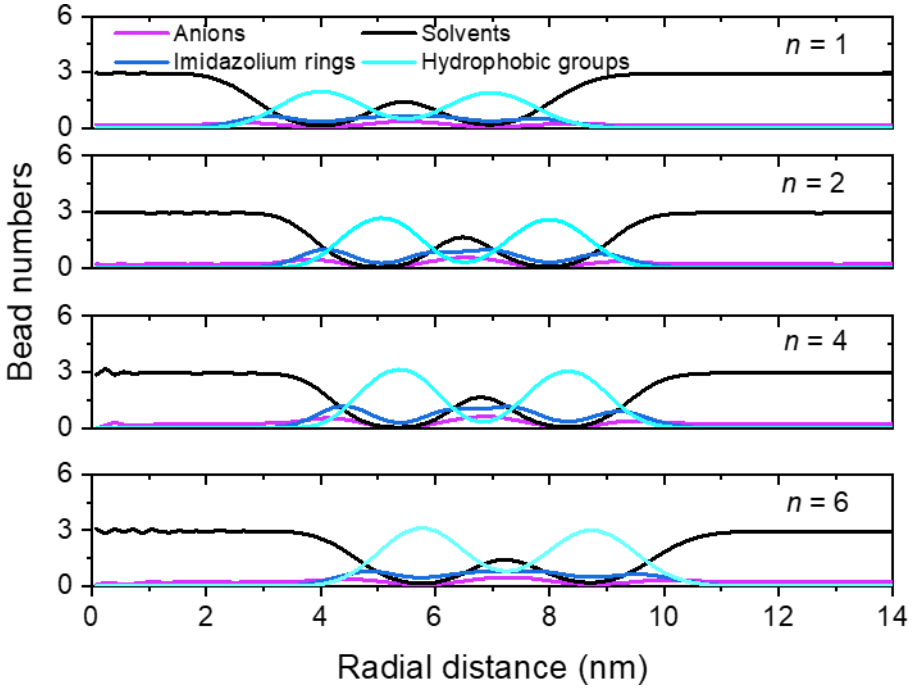

Fig. S12. Number density distributions of CG beads in PILs, anions, and solvent molecules in modeling systems of *n* varying from 1 to 6 (*n* for polymerization degree).

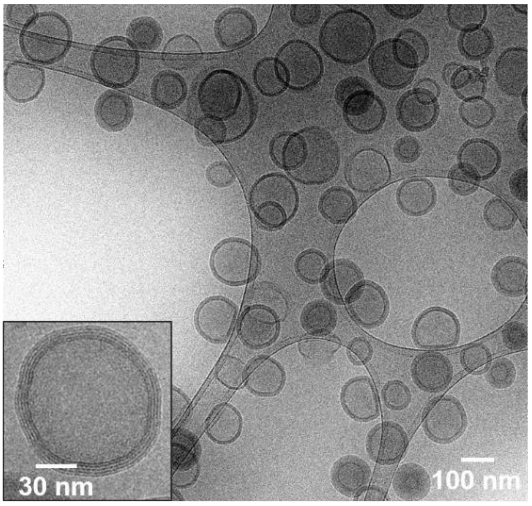

Fig. S13. Cryo-TEM images of the PIL NVs after treated with N_2H_4 at 80 ℃ overnight.

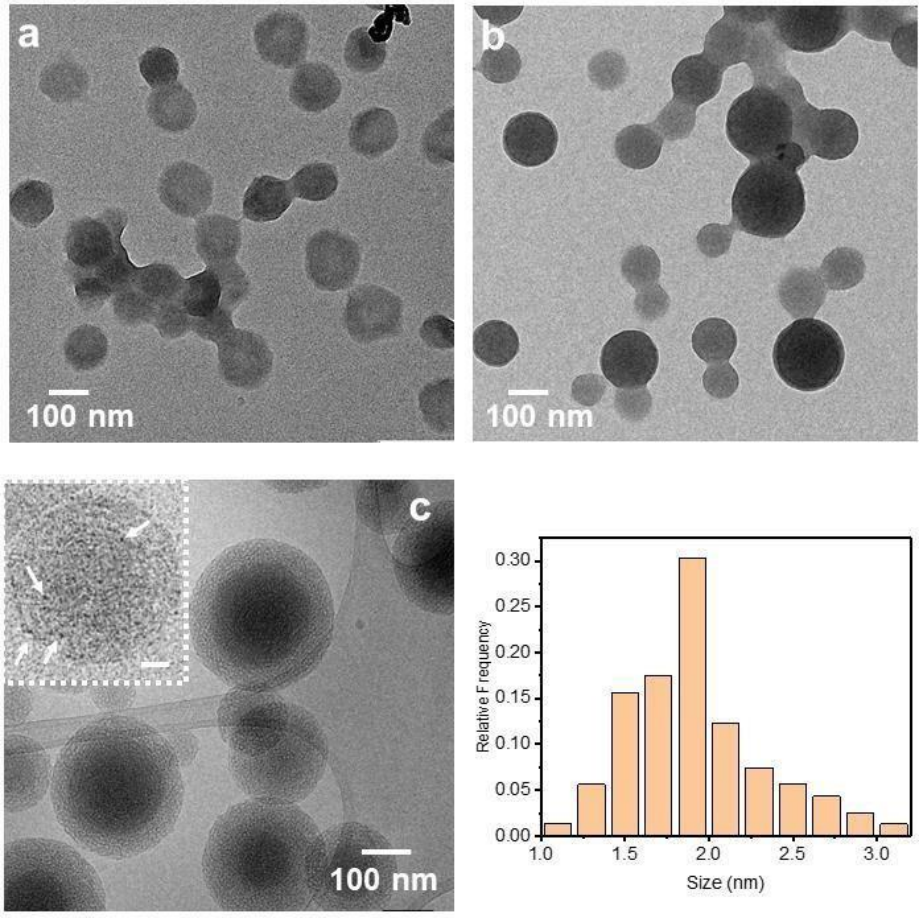

Fig. S14. TEM images of (a) NVs/Cu and (b) SNSs/Cu particles. (c) Cryo-TEM image of PIL SNSs/Cu particles. The inset is a high magnification image with a scale bar of 30 nm, and the CuNPs are indicated by white arrows. (d) Size distribution (based on over 100 particles) of the CuNPs in SNSs/Cu determined from the corresponding cryo-TEM image.

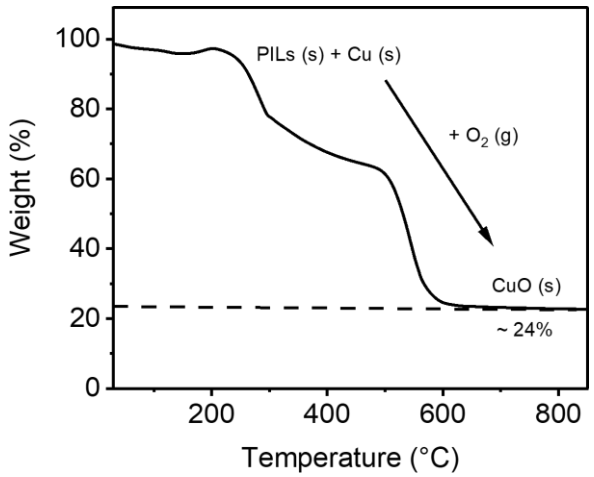

Fig. S15. TGA curve (under synthetic air) of the PIL NVs/Cu after freeze-drying.

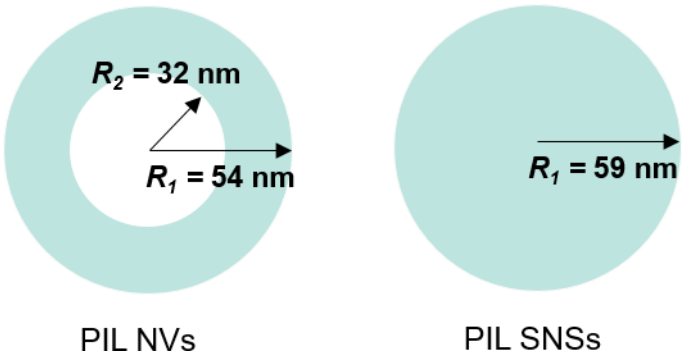

Fig. S16. Scheme of a single NV and SNS particle.

$$S = 4\pi R_1^2 + 4\pi R_2^2 \quad (1)$$

$$V = \frac{4}{3}\pi R_1^3 - \frac{4}{3}\pi R_2^3 \quad (2)$$

$$m = \rho V \quad (3)$$

$$SSA = \frac{S}{m} = \frac{3(R_1^2+R_2^2)}{\rho(R_1^3-R_2^3)} \quad (4)$$

where *S*, *V*, *m*, ρ is the total surface area, volume, mass, and density, respectively. Then, if we assume $\rho \approx 1\ g/cm^3$ for both particles and take R_1 and R_2 from cryo-TEM results, the specific surface area (*SSA*) of PIL NVs and SNSs is estimated to be 95.9 and 50.8 m^2/g, respectively, according to Equation (1)-(4). The theoretical specific surface area of PIL NVs is *ca.* 1.9-fold of PIL SNSs.

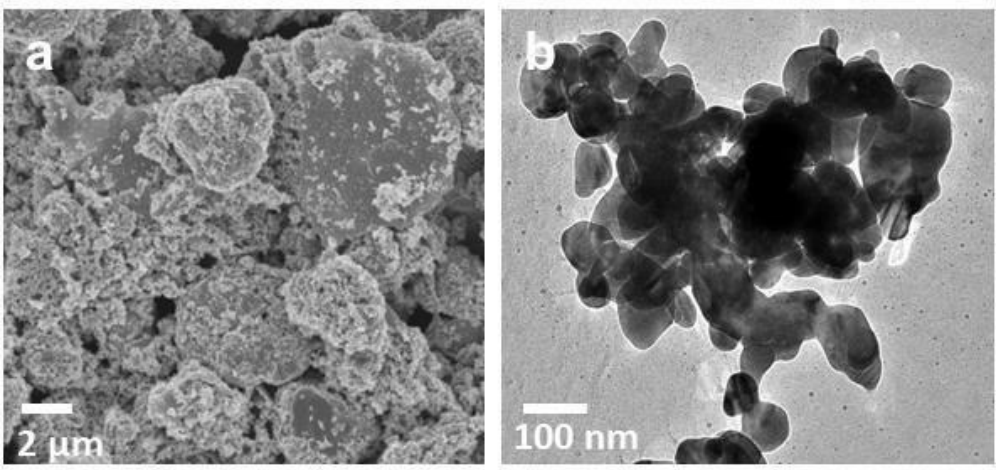

Fig. S17. (a) SEM and (b) TEM images of the pristine CuNPs.

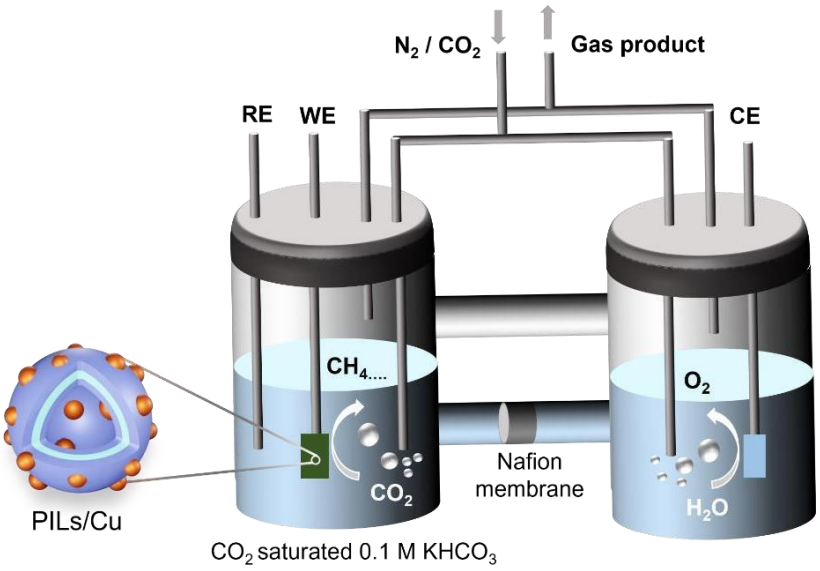

Fig. S18. Scheme of the setup of CO_2 electrochemical reduction.

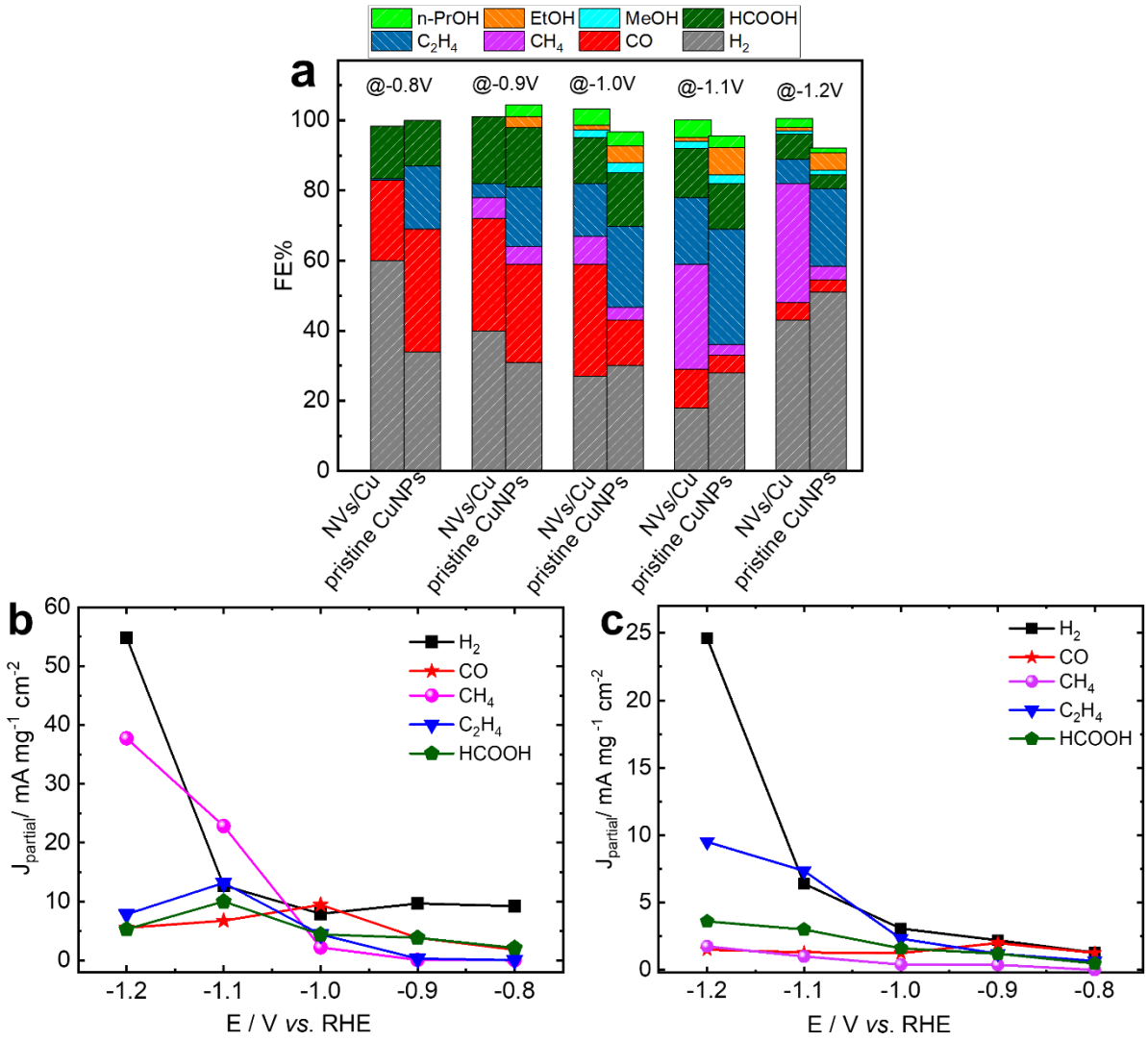

Fig. S19. Summary of CO_2ER activity trends for various catalysts. FE% of the NVs/Cu and pristine CuNPs coated GDLs measured in CO_2-saturated 0.1 M $KHCO_3$ solution at several applied potentials (V *vs.* RHE). Partial current density toward the generation of the main products on (b) NVs/Cu and (c) pristine CuNPs as a function of applied potential.

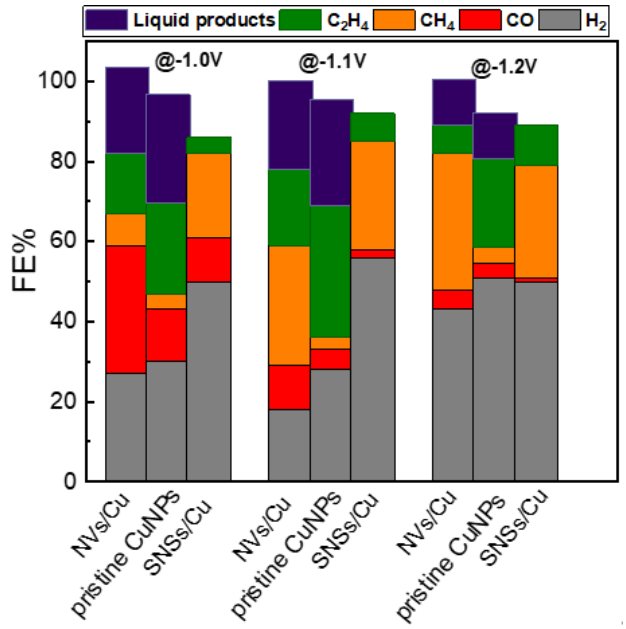

Fig. S20. Summary of the products of CO_2ER for the pristine CuNPs, PILs NVs/Cu and SNSs/Cu catalysts at various applied cathodic potentials.

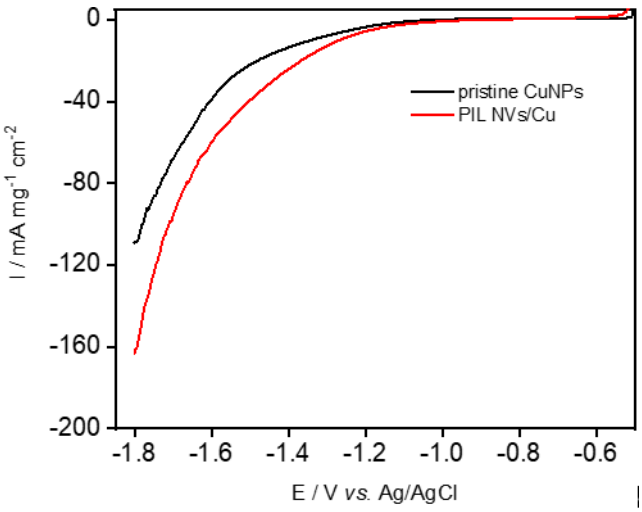

Fig. S21. Linear sweep voltammetries (LSVs) of the commercial CuNPs (40-60 nm in size) and PIL NVs/Cu in 0.1 M $KHCO_3$ at a scan rate of 10 mV s^{-1}.

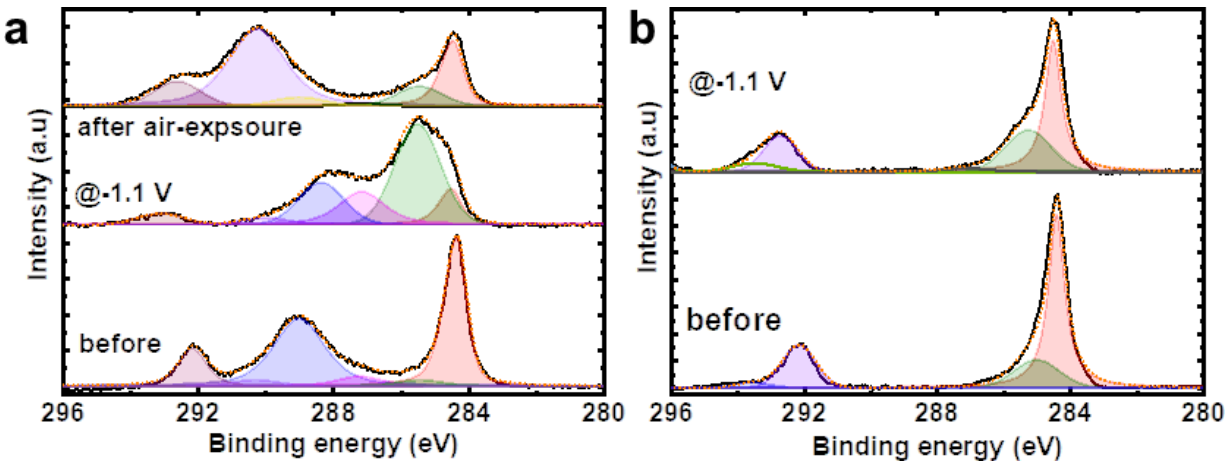

Fig. S22. C 1s high-resolution XPS spectra of (a) PIL NVs/Cu and (b) pristine CuNPs.

1.2 Supplementary tables

Table S1. Summary of diameter, bilayer spacing, and shell thickness obtained from cryo-TEM and SAXS/WAXS. The values for the cryo-TEM measurement are given in terms of the mean and the standard deviation of the individual vesicle, whereas the values for the SAXS measurements represent the mean and the standard uncertainty of the mean as determined by the reduced χ^2-method.[1] The SAXS curve of the PIL SNSs (C_m = 24 mg/mL) does not exhibit clear features possibly due to the polydispersity of the particle size. Each test has been repeated for 3 times to obtain the average value.

	Cryo-TEM		**SAXS**			
C_m **(mg/mL)**	**Diameter (nm)**	**Size distribution (nm)**	**Diameter (nm)**	**Size distribution (nm)**	***v***	**Shell thickness (nm)**
3	50.8	7.8	56.1 ± 3.8	7.9	0.43 ± 0.08	16.0 ± 2.2
6	108.6	14.3	116.5 ± 7.2	22.4	0.84 ± 0.03	9.3 ± 1.7
12	107.8	22.6	99.4 ± 4.1	20.2	0.74 ± 0.02	12.9 ± 1.0
16	117.1	19.2	120.2 ± 7.5	15.6	0.31 ± 0.07	41.5 ± 4.2
24	117.8	28.0	(113.2)	26.3	0	(56.6)

Table S2. Bilayer spacing calculated from WAXS. Each test has been repeated for 3 times to obtain the average value.

C_m **(mg/mL)**	**Bilayer spacing (nm)**
3	2.95 ± 0.1
6	2.98 ± 0.1
12	3.00 ± 0.1
16	2.92 ± 0.1
24	2.98 ± 0.1

Table S3. Yield and final polymer concentration of PILs prepared at various C_m. Note that *ca.* 50 wt.% of PILs aggregate was obtained resulting from precipitation when it comes to C_m at 48 mg/mL. Therefore, only PILs dispersed in water were included for the calculation of polymer concentration and GPC measurement. Each test has been repeated for 3 times to obtain the average value.

C_m (mg/mL)	Yield (%)	Polymer concentration (mg/mL)
3	90 ± 9	3 ± 1
6	92 ± 7	6 ± 1
12	93 ± 7	11± 1
16	94 ± 5	15 ± 1
24	93 ± 4	22 ± 2
48	95 ± 2	(24± 3)

Table S4. GPC results of PIL samples at various C_m.

C_m (mg/mL)	M_n (kg/mol)
3	11
6	17
12	43
16	44
24	49
48	110

Table S5. Comparison of various Cu-based catalysts in CO_2ER.

Catalyst	FE (%)		FE ratio of CH_4/C_2H_4	Potential (V)	Electrolyte	Reference
	CH_4	C_2H_4				
Copper mesh	15	7	2.1	-1.9	0.1 M $KHCO_3$	[2]
CuNPs (50-100 nm) on Cu film	1	37	0.03	-1.1	0.1 M $KClO_4$	[3]
20 wt% Cu/SWCNT (~20 nm)	30	30	1	-2.0	0.1 M $KHCO_3$	[4]
Cu nanocubes on rGO	10	20	0.5	-1.1	0.1 M $KHCO_3$	[5]
CuNPs	22	10	2.2	-0.9	0.5 M $KHCO_3$	[6]
PDA coated Cu nanowires	29	15	1.9	-0.9	0.1 M $KHCO_3$	[7]
Cu nanowires with carbon black	55	<5	>11	-1.3	0.1 M $KHCO_3$	[8]
CuNPs (1-3 nm)	34	7	4.9	-1.1	0.1 M $KHCO_3$	This work

References in Supporting Information

[1] I. Hughes, Measurements and their uncertainties: a practical guide to modern error analysis, in: T.P.A. Hase (Ed.) Oxford University Press, Oxford; 2010.
[2] M.R. Gonçalves, A. Gomes, J. Condeço, T.R.C. Fernandes, T. Pardal, C.A.C. Sequeira, J.B. Branco, Electrochemical conversion of CO2 to C2 hydrocarbons using different ex situ copper electrodeposits, Electrochim. Acta 102 (2013) 388-392.
[3] W. Tang, A.A. Peterson, A.S. Varela, Z.P. Jovanov, L. Bech, W.J. Durand, S. Dahl, J.K. Nørskov, I. Chorkendorff, The importance of surface morphology in controlling the selectivity of polycrystalline copper for CO2 electroreduction, Phys. Chem. Chem. Phys. 14(1) (2012) 76-81.
[4] O.A. Baturina, Q. Lu, M.A. Padilla, L. Xin, W. Li, A. Serov, K. Artyushkova, P. Atanassov, F. Xu, A. Epshteyn, T. Brintlinger, M. Schuette, G.E. Collins, CO2 Electroreduction to Hydrocarbons on Carbon-Supported Cu Nanoparticles, ACS Catalysis 4(10) (2014) 3682-3695.
[5] S. Kuang, M. Li, R. Xia, L. Xing, Y. Su, Q. Fan, J. Liu, E.J.M. Hensen, X. Ma, S. Zhang, Stable Surface-Anchored Cu Nanocubes for CO2 Electroreduction to Ethylene, ACS Applied Nano Materials 3(8) (2020) 8328-8334.
[6] R. Kas, R. Kortlever, H. Yılmaz, M.T.M. Koper, G. Mul, Manipulating the Hydrocarbon Selectivity of Copper Nanoparticles in CO2 Electroreduction by Process Conditions, ChemElectroChem 2(3) (2015) 354-358.
[7] H. Liu, K. Xiang, Y. Liu, F. Zhu, M. Zou, X. Yan, L. Chai, Polydopamine Functionalized Cu Nanowires for Enhanced CO2 Electroreduction Towards Methane, ChemElectroChem 5(24) (2018) 3991-3999.
[8] Y. Li, F. Cui, M.B. Ross, D. Kim, Y. Sun, P. Yang, Structure-Sensitive CO2 Electroreduction to Hydrocarbons on Ultrathin 5-fold Twinned Copper Nanowires, Nano Lett. 17(2) (2017) 1312-1317.

Nanoscale

PAPER

View Article Online
View Journal | View Issue

Cite this: *Nanoscale*, 2022, 14, 6888

Template synthesis of dual-functional porous MoS_2 nanoparticles with photothermal conversion and catalytic properties †

Xuefeng Pan,[a,b] Radwan M. Sarhan,[a] Zdravko Kochovski,[a] Guosong Chen,[c] Andreas Taubert,[b] Shilin Mei*[a] and Yan Lu*[a,b]

Advanced catalysis triggered by photothermal conversion effects has aroused increasing interest due to its huge potential in environmental purification. In this work, we developed a novel approach to the fast degradation of 4-nitrophenol (4-Nip) using porous MoS_2 nanoparticles as catalysts, which integrate the intrinsic catalytic property of MoS_2 with its photothermal conversion capability. Using assembled polystyrene-*b*-poly(2-vinylpyridine) block copolymers as soft templates, various MoS_2 particles were prepared, which exhibited tailored morphologies (*e.g.*, pomegranate-like, hollow, and open porous structures). The photothermal conversion performance of these featured particles was compared under near-infrared (NIR) light irradiation. Intriguingly, when these porous MoS_2 particles were further employed as catalysts for the reduction of 4-Nip, the reaction rate constant was increased by a factor of 1.5 under NIR illumination. We attribute this catalytic enhancement to the open porous architecture and light-to-heat conversion performance of the MoS_2 particles. This contribution offers new opportunities for efficient photothermal-assisted catalysis.

Received 22nd February 2022,
Accepted 29th March 2022

DOI: 10.1039/d2nr01040b

rsc.li/nanoscale

Introduction

Over the past decades, solar-driven photothermal conversion has attracted intensive attention, which enables broad applications such as environmental remediation, water desalination and photothermal-assisted catalysis under mild conditions with high efficiency.[1–4] Therefore, it is essential to develop photothermal conversion catalysts that can strongly harvest solar energy ranging from UV to the visible light, and even to the near-infrared light (NIR) to accelerate the degradation of water contaminants by the converted heat.[5–7] In principle, the rational design of efficient photothermal conversion-assisted catalysts includes, but is not limited to, active composition as well as structural optimization. Nowadays, various solar absorbers including plasmonic noble metals (*e.g.*, gold and silver),[8,9] narrow bandgap semiconductors (*e.g.*, copper sulfide and tungsten oxide),[10–12] carbon-based nanostructures (*e.g.*, carbon nanotubes and graphenes),[13,14] and organic compounds (*e.g.*, polyaniline (PANI), polypyrrole and polydopamine (PDA)) with outstanding photothermal conversion performance are successfully fabricated.[15–17] For instance, a bismuth vanadate photocatalyst modified with PANI was applied in the water oxidation reaction under NIR light irradiation. The water oxidation photocurrent was increased by more than 300% than that of pristine catalysts with the assistance of photothermal heating of PANI.[17] Recently, our group has successfully developed a gold@PDA nanoreactor for the fast reduction of 4-nitro- phenol (4-Nip). The photoheating caused by PDA under NIR irradiation greatly enhanced the reduction reaction catalyzed by the gold nanoparticles embedded inside the nanoreactor.[18] Generally, the catalyst and the photothermal converter are often two different species according to the above-mentioned reports. A hybridization process is usually required to combine the unique function of each material, which often involves complicated synthetic routes and is undesirable from the economic point of view. Furthermore, the activity of the catalytic species is possibly being impaired due to the modification by the photothermal conversion components, which may reduce the active surface or induce diffusion-controlled sluggish kinetics. Therefore, developing a dual-functional catalyst utilizing its intrinsic photothermal conversion and catalytic properties is in great demand.

Among various photothermal conversion materials, molybdenum disulfide (MoS_2) has shown great potential in the fields

[a]*Department for Electrochemical Energy Storage, Helmholtz-Zentrum Berlin für Materialien und Energie, Hahn-Meitner-Platz 1, Berlin 14109, Germany. E-mail: yan.lu@helmholtz-berlin.de, shilin.mei@helmholtz-berlin.de*
[b]*Institute of Chemistry, University of Potsdam, Potsdam 14476, Germany*
[c]*The State Key Laboratory of Molecular Engineering of Polymers and Department of Macromolecular Science, Fudan University, Shanghai 200433, China*
† Electronic supplementary information (ESI) available. See DOI: https://doi.org/10.1039/d2nr01040b

of hydrogen generation, pollutant degradation and photothermal therapy due to its tunable chemical and physical properties.[19–24] The photothermal effect of MoS_2 is mainly explained by the generation of electron-hole pairs upon light excitation and their relaxation *via* a non-radiative decay mechanism.[25–27] In addition, MoS_2 exhibits a good catalytic performance in the reduction of 4-Nip.[28] The surface area and crystallinity of the catalytic surface are additional important parameters that determine their performances. Large surface area with a plenty of exposed edges can provide abundant active sites for the catalytic reaction.[29] In addition, metallic 1T-phase MoS_2 has been reported to exhibit a stronger NIR absorption and a higher photothermal conversion efficiency than those of the 2H-phase.[22] However, their instability and tedious synthesis protocol are inevitable. For the more stable 2H phase of MoS_2, the unsaturated sulfur (S) atoms at the edge sides of MoS_2 nanosheets determine the catalytic activity, while the other S atoms in bulk MoS_2 contribute little to the overall activity.[30,31] Thus, fabrication of MoS_2 with abundant exposed active edges is an effective method to improve the catalytic performance. Furthermore, several approaches including bandgap engineering, defect design, and structural heterojunction *via* hybridization with other nanomaterials such as titanium oxide and nickel oxide have been developed to simultaneously optimize their catalytic and photothermal conversion performance.[26,32,33] Inevitably, these modification approaches also involve complicated synthetic procedures, which lead to additional production costs. Thus, facile fabrication of MoS_2 catalysts with efficient photothermal conversion effects and rich active sites on the catalytic surface remains a challenge.

Recently, it has been revealed that the rational design of nanostructured MoS_2 (*e.g.*, hollow structure) could enable enhanced light scattering and capturing, reduced distance for charge migration, and abundant surface reactive area.[34–36] However, less efforts have been made to explore the more complicated surface/internal nanostructure of MoS_2 due to the limitation of commonly used synthetic methods (*e.g.*, hard template, hydrothermal method, and physical deposition). In contrast, soft templates such as surfactant micelles, organic molecules, and polymer assemblies are good alternatives to prepare novel nanostructures.[37,38] Unlike the harsh conditions needed to remove the hard templates, soft polymer templates can be readily eliminated by solvent dissolution or direct calcination. In particular, block copolymers open up new possibilities for the construction of advanced architectures due to their tunable microphase-separation when serving as soft templates.

In this work, we developed a series of dual-functional MoS_2 particles with well-designed nanostructures, combining the photothermal conversion effect and catalytic property using a soft-template strategy (Scheme 1). Polystyrene-*b*-poly(2-vinylpyridine) (PS-*b*-P2VP) nanoparticles with tunable swollen structures were first fabricated and then used as soft templates.[39] Different volume fractions (determined by the molecular weight) of the P2VP moiety and swelling conditions were applied to tailor the microphase separation of the PS-*b*-P2VP particles, inducing a series of soft templates with significantly different nanostructures.[40] The template can be directly complexed with the ammonium tetrathiomolybdate ($(NH_4)_2MoS_4$) as the MoS_2 precursor. After calcination, MoS_2 nanoparticles with pomegranate-like, hollow, and open porous structures

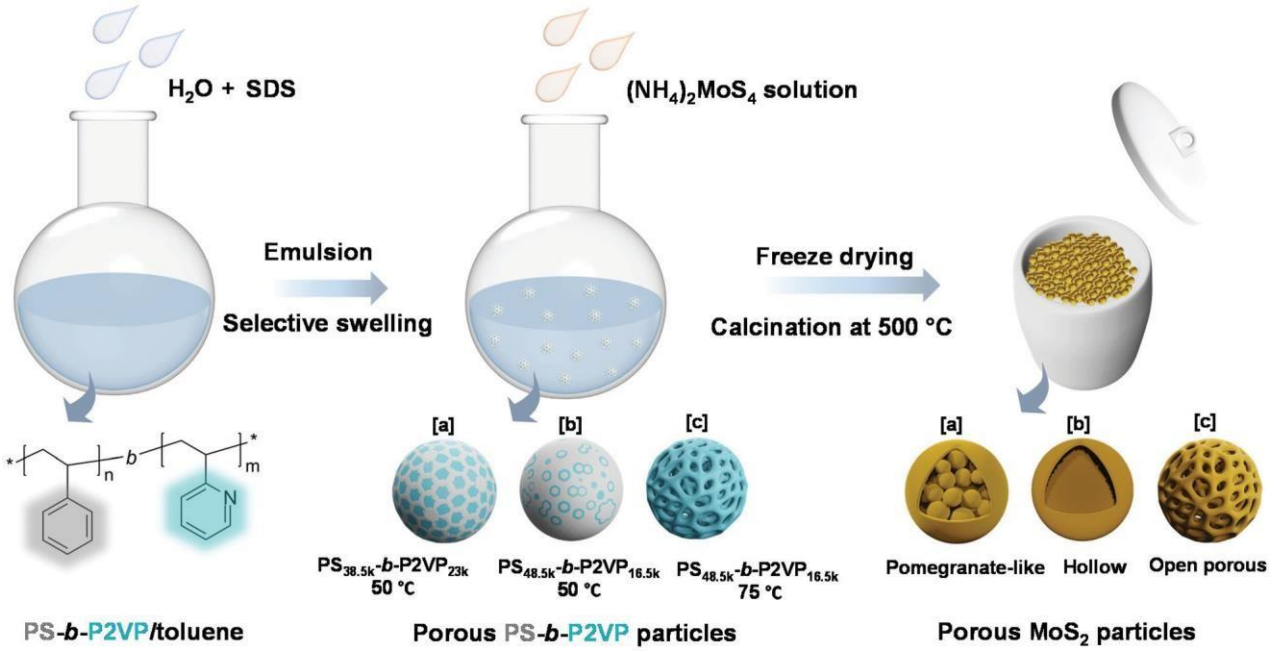

Scheme 1 Synthesis strategy of MoS_2 particles with various morphologies using PS-*b*-P2VP as a sacrificial soft template.

were successfully constructed. The dependence of the photothermal conversion effect as well as the catalytic performance on their morphologies was systematically investigated, demonstrating the importance of structure–property relationship in the photothermal conversion-assisted catalysis.

Results and discussion

Material synthesis and characterization

Block copolymers composed of two (or more) covalently bonded homopolymer chains show rich functional groups and microphase separation structure, promoting their increasing application in the formation of ordered hybrid structures and porous functional materials.[41–47] A simple pore-generating method termed "selective swelling" has shown its great potential in extending the micropattern diagram as well as the porous structure of block copolymers.[48,49] The methodology is based on the difference in polarity (or interaction) of the constituent blocks and the swelling solvent. The pores/voids are typically derived from deformed domains of the minor component dispersed in the continuous phase of the major component. In this contri- bution, PS-*b*-P2VP particles with two different molecular weight fractions of the P2VP moiety were generated by a deli- cate emulsion-swelling method (Fig. S1a and S1b†). Ethanol, which has strong interaction with the P2VP block but poor interaction with the PS block, was applied as the selective swelling solvent. For $PS_{38.5k}$-*b*-$P2VP_{23k}$ and $PS_{48.5k}$-*b*-$P2VP_{16.5k}$, the template particles tend to form solid nanostructures upon swelling in ethanol at 50 °C (Fig. S1c and S1d†). It is also found that dense and spherical P2VP nanodomains (~20 nm) were uniformly distributed inside the polymer particles in $PS_{38.5k}$-*b*-$P2VP_{23k}$. For $PS_{48.5k}$-*b*-$P2VP_{16.5k}$, an irregular hollow space was also generated inside. In this scenario, swelling of both polymer particles results in only slight deformation, and therefore, no porous structures were obtained under this mild condition (Fig. 1a and b). This is mainly due to the slight swelling degree of the P2VP chains at this temperature (50 °C). Moreover, the osmotic pressure of the slightly swollen P2VP domains is too weak to drive the plastic deformation of the rigid PS domains. Therefore, solid or non-porous complex nanostructures of MoS_2 can be expected using these featured polymer particles as templates for the subsequent step of MoS_2 generation. Notably, when the temperature increased from 50 to 75 °C, an open porous nanostructure with interconnected micellar fibers was fabricated (Fig. 1c). At this temperature, a strong chain movement is triggered, which gives rise to the structural reorganization of the polymer chains into network-like spheres. Accordingly, an open porous structure of MoS_2 particles can be obtained by applying these porous particles as synthetic templates. Note that a lower temperature (30 °C) led to a slight swelling of the polymer chains, which is similar to that performed at 50 °C (Fig. S1e †). In contrast, a higher temperature (90 °C) led to the deformation of the polymer particles (Fig. S1f†).

Block copolymers have been reported to serve as templates for the synthesis of nanoparticles *via* coordination with inorganic precursors.[50,51] Benefiting from the good affinity of the P2VP block to the inorganic precursors, anionic MoS^{2-} was simply complexed with the PS-*b*-P2VP template with selec- tive loading onto the P2VP domain.[52,53] After the thorough incorporation of a molybdenum precursor into the PS-*b*-P2VP particle, the introduction of a trace amount of H^+ and 3-MPA into the solution leads to the decomposition of MoS^{2-} into MoS_x (x = 2–3). In this experiment, 3-MPA can serve as a stabil- izer and prevent the aggregation of the composite particles. Finally, MoS_2 particles with various internal nanostructures were obtained after calcination in an argon atmosphere. During the calcination step, MoS^{2-} was pyrolyzed into MoS_2 as the backbone, while much of the polymer template was calcined, leaving a small amount of carbon residues and hollow channels. For $PS_{38.5k}$-*b*-$P2VP_{23k}$ particles swollen at 50 °C, MoS^{2-} cations diffused inside the polymer particle and coordinated with small spherical P2VP domains due to the relatively large volume fraction of the P2VP block (37.4%), compared to $PS_{48.5k}$-*b*-$P2VP_{16.5k}$ with a fraction of 25.4%. This results in the formation of pomegranate-like nanoparticles (PLNPs) that contain a solid outer layer (~25 nm thick) with numerous dense nanospheres (~30 nm) inside, as shown in Fig. 1d and g. A limited free space was also observed in PLNPs.

In contrast, MoS_2 hollow nanoparticles (HNPs) were obtained using $PS_{48.5k}$-*b*-$P2VP_{16.5k}$ particles swollen at 50 °C as tem- plates (Fig. 1e). The HNP particles possess a thin layer of MoS_2 shell (~9 nm), without any visible internal MoS_2 spheres (Fig. 1h). The observed small particles also exhibit the same internal structure as the big ones (Fig. S2a† and 2b). This might be ascribed to the fact that few MoS_4^{2-} cations can diffuse into the internal part of $PS_{48.5k}$-*b*-$P2VP_{16.5k}$ particles primarily limited by their thicker blocking layer (rigid PS layers) compared with $PS_{38.5k}$-*b*-$P2VP_{23k}$. When it comes to $PS_{48.5k}$-*b*-$P2VP_{16.5k}$ particles swollen at 75 °C, the MoS_2 porous nanoparticles (PNPs) preserve the original loose structure of the polymer template (Fig. 1f). Due to the free space between interlocked fibers, the MoS_4^{2-} cations can easily diffuse and adsorb onto the internal part of the porous polymer template. After calcination, the polymer was burnt out leading to the for- mation of the MoS_2 particles with multi-interconnected hollow channels (Fig. 1i). The open porous MoS_2 particles with an interconnected hollow channel structure show several advan- tages when compared with particles of other morphologies including high porosity, light weight, and large accessible surface area. These are of special relevance to the practical applications including drug delivery, water purification, and surface catalysis. To further optimize the particle structure, we successfully tuned the thickness of the deposited MoS_2 layers by varying the concentration of the inorganic precursor during the synthesis. Fig. 2a–c show the SEM images of a series of MoS_2 particles prepared with different MoS_4^{2-} concentrations. The MoS_2 PNPs prepared with different concentrations of $(NH_4)_2MoS_4$ (1, 1.5, and 3 mg mL^{-1}) are denoted as MoS_2-1, MoS_2-1.5 and MoS_2-3 PNPs, respectively. These three samples

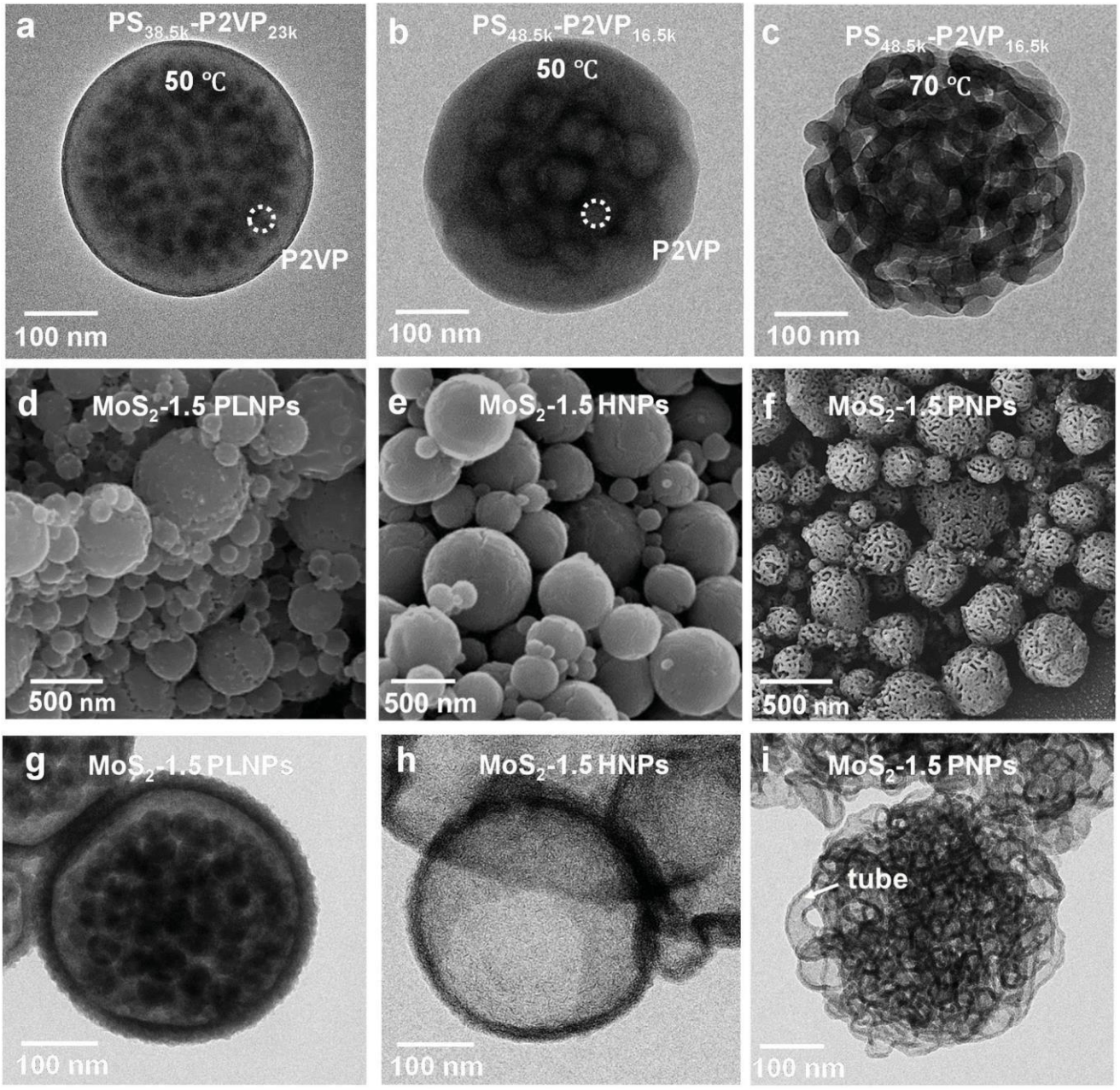

Fig. 1 TEM images of (a) $PS_{38.5k}$-*b*-$P2VP_{23k}$ and (b) $PS_{48.5k}$-*b*-$P2VP_{16.5k}$ particles obtained by swelling at 50 °C, and (c) $PS_{48.5k}$-*b*-$P2VP_{16.5k}$ particles obtained by swelling at 75 °C. The polymer particles were stained with I_2 vapor for 20 min. The dark contrast shows the distribution of P2VP domains. (d) SEM and (g) TEM images of the MoS_2-1.5 PLNPs. (e) SEM and (h) TEM images of the MoS_2-1.5 HNPs. (f) SEM and (i) TEM images of the MoS_2-1.5 PNPs.

show a broad size distribution with a similar trend that the diameter of the majority concentrates between 200 and 500 nm (Fig. S2c–e†). By increasing the precursor concen- tration, more MoS_4^{2-} were coordinated onto the PS-*b*-P2VP par- ticles and the distance between the separated micellar fibers became narrower. The layer thickness of the hollow channels in the particles increased from ~7 to 12 nm on average, when the concentration of precursor increased from 1 to 3 mg mL^{-1}. The presence of tiny MoS_2 flakes with generally single-layered structures was identified from the HRTEM images (Fig. 2d), suggesting the abundance of exposed active edges. The outer and inner diffraction rings as observed from the selected-area electron diffraction (SAED) pattern correspond to the (110) and (100) reflection of MoS_2, respectively (Fig. 2e). It is worth noting that the isolated MoS_2 nanoflakes (short sheets of length ~5 nm) of the MoS_2-1.5 PNPs might be favorable for the utilization of active edges. Carbon generated from the polymer template during calcination also prevents the aggregation of

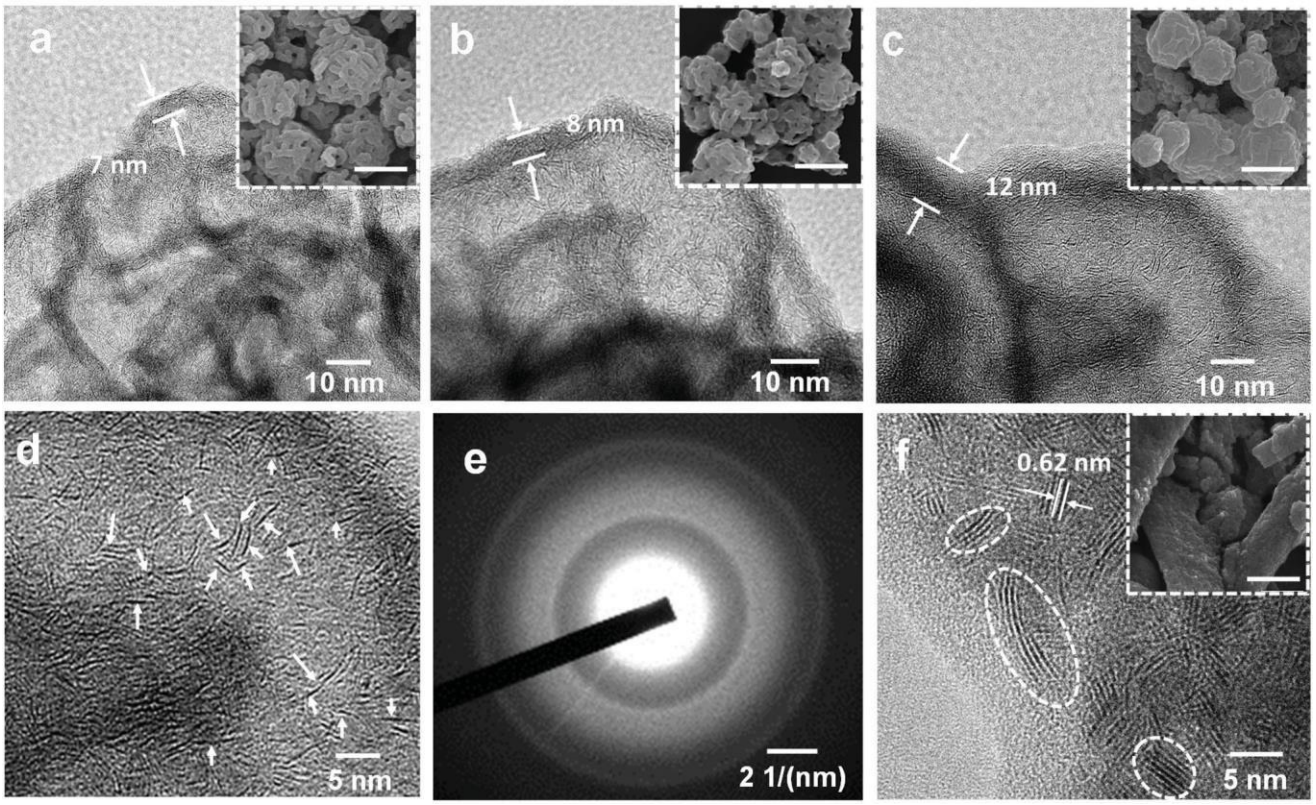

Fig. 2 TEM images of MoS_2 PNPs prepared at precursor concentrations of (a) 1, (b) 1.5, and (c) 3 mg mL^{-1}. The insets are the corresponding SEM images with a scale bar of 500 nm. (d) HRTEM image and (e) SAED pattern of MoS_2-1.5 PNPs. (f) HRTEM image of bulk MoS_2 prepared without any polymer template; the inset is the corresponding SEM image with a scale bar of 500 nm.

the MoS_2 nanoflakes. On the contrary, the nanoflakes of bulk MoS_2 (Fig. 2f) fabricated without any polymer template show a huge tendency to fuse together, resulting in the formation of a few layers of stacked multilayers (long sheets of length ~9 nm). Besides, an irregular bulk phase without any defined structure was found from the inset SEM image.

Taking MoS_2-1.5 PNPs, for example, the X-ray diffraction (XRD) profile verifies that MoS_2 in all the PNPs exhibits a typical 2H phase (Fig. 3a, see the others in Fig. S3†).[54] The main diffraction peaks at 32° and 56.8° correspond to the (100) and (110) reflections, respectively. Moreover, the weak (002) reflection at 14.4° indicates the relatively limited layers of MoS_2. The chemical composition of the obtained MoS_2-1.5 PNPs was further confirmed by Raman spectroscopy, as shown in Fig. 3b. The two Raman peaks at 1345 and 1587 cm^{-1} represent the D and G bands of sp^2 carbon, respectively, while the Raman peaks at around 377 and 403 cm^{-1}, correspond to the E^1_{2g} and out-of-plane A^1_g vibration modes of the MoS_2.[55] The amount of carbon and MoS_2 was calculated based on the molybdenum oxide residue from the TGA measurement in air (Fig. 3c and S4†). The MoS_2-1.5 PNPs show ~38.9 wt% of carbon species, corresponding to 61.1 wt% of MoS_2 in the particles. In contrast, ~69.2 wt% of MoS_2 was left in the MoS_2-3 PNPs on account of higher amounts of MoS_4^{2-} precursors during coordination, as summarized in Table S1.† From the N_2 adsorption/desorption isotherm curves in Fig. 3d, a distinct hysteresis loop can be observed with a typical type-IV isotherm, referring to a mesoporous structure. The pore size distribution curve displays a narrow range of mesopores centered at ~5 nm and a broad range (10–20 nm) centered at ~15 nm. The specific surface area (S_{BET}) of these MoS_2 particles calculated according to the BET equation is summarized in Fig. S5 and Table S2.† There is a clear decreasing tendency of S_{BET} for the MoS_2-1, MoS_2-1.5 and MoS_2-3 PNPs. The S_{BET} of MoS_2-1.5 PNPs was calculated to be 106.6 $m^2\ g^{-1}$, which is around 1.3-fold of that of the MoS_2-3 PNPs. Meanwhile, the bulk MoS_2 possesses the lowest S_{BET} of 36.3 $m^2\ g^{-1}$. The S_{BET} apparently decreased with the increase in the layer thickness, mainly due to the gradually diminished gap between the thick MoS_2 frameworks of the particles. Consequently, a reduced porosity as well as a lower specific surface area was obtained, as confirmed from the above-mentioned SEM and TEM images.

Photothermal conversion performance

To assess the photothermal conversion performance of the MoS_2 particles, we monitored the temperature change of the MoS_2 dispersion upon light irradiation as illustrated in Fig. 4a. A NIR-laser (808 nm, 3 W cm^{-2}) was adopted to irradiate the dispersions of the MoS_2 particles placed in a quartz cuvette, while the temperature was simultaneously recorded using a

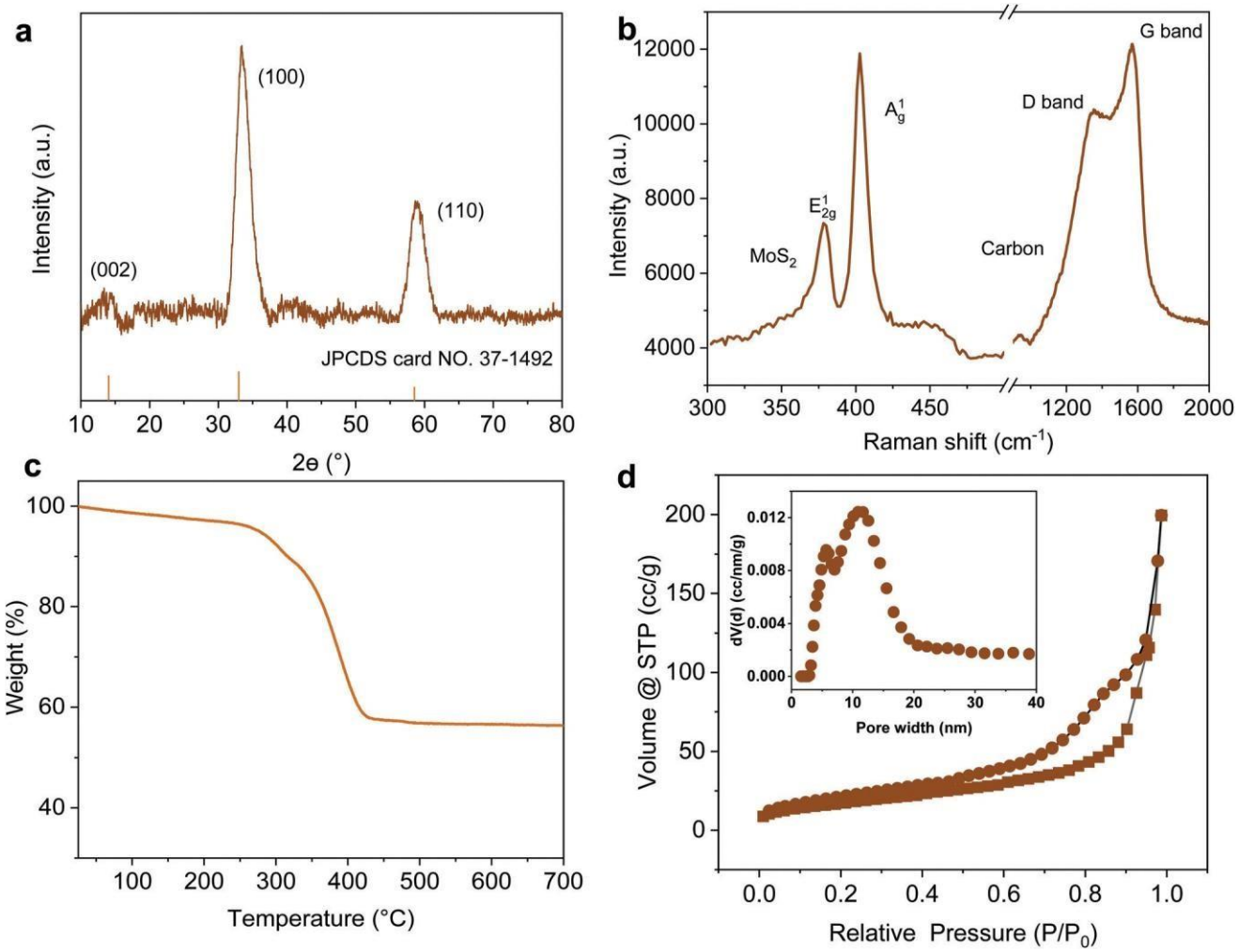

Fig. 3 (a) XRD pattern, (b) Raman spectrum, (c) TGA in air and (d) N_2 adsorption/desorption isotherm curves of MoS_2-1.5 PNPs; the inset is the curve of pore size distribution.

thermocouple connected to a digital thermometer. The thermal evolution of the MoS_2-1.5 PNP dispersion with time was first visualized using an IR camera (Fig. 4b). The tempera- ture of MoS_2 particle dispersions clearly increased with the irradiation time. To precisely track the temperature variation of the MoS_2 dispersion during NIR irradiation, quantitative results were further collected from the digital thermometer. Fig. 4c displays the photothermal heating curves of MoS_2 par- ticles fabricated with different polymer templates. The temp-

erature of the MoS_2 PNP dispersion increased by ~20 °C, while the dispersion containing the same concentration of MoS_2-1.5 HNPs and MoS_2-1.5 PLNPs exhibited a temperature increase of ~16 °C. The bulk MoS_2 particle synthesized without any polymer template showed a much lower temperature increment of ~11 °C. As a reference, the pure water displayed a temperature change of ~5 °C under the same light intensity. Moreover, when the laser is off, the temperature profile of the MoS_2 particle dispersions decreased slowly compared to that of the bulk MoS_2, showing that their defined hollow and porous structures may lead to a better thermal insulating effect (Fig. S6†). These results indicate the dependence of the photothermal conversion performance on the surface/internal structure of the MoS_2 particles. It has been reported that hollow nanostructures improve the light harvesting *via* multiple scattering of the photons.[56,57] This, in turn, will enhance the light-to-heat conversion efficiency. The hollow architectures facilitate localization and harvesting of the light, resulting in a relatively high particle temperature. Subsequently, the solution temperature increases as the heat dissipates to the solution. Therefore, our nanostructured MoS_2 particles (MoS_2- 1.5 PLNPs, MoS_2-1.5 PNPs and MoS_2-1.5 HNPs) show better photothermal conversion performance than that of bulk MoS_2. For MoS_2-1.5 PLNPs, however, the conversion efficiency could be limited by the insufficient free space. In addition, the MoS_2-1.5 PNP particles possess more complicated porous construction than that of the MoS_2-1.5 HNPs, which is likely to lead to efficient light scattering and capture. The complex open architecture of the MoS_2-1.5 PNPs efficiently accelerates the mass and heat transport, resulting in a higher overall temperature of the dispersion. Hence, the photothermal con-

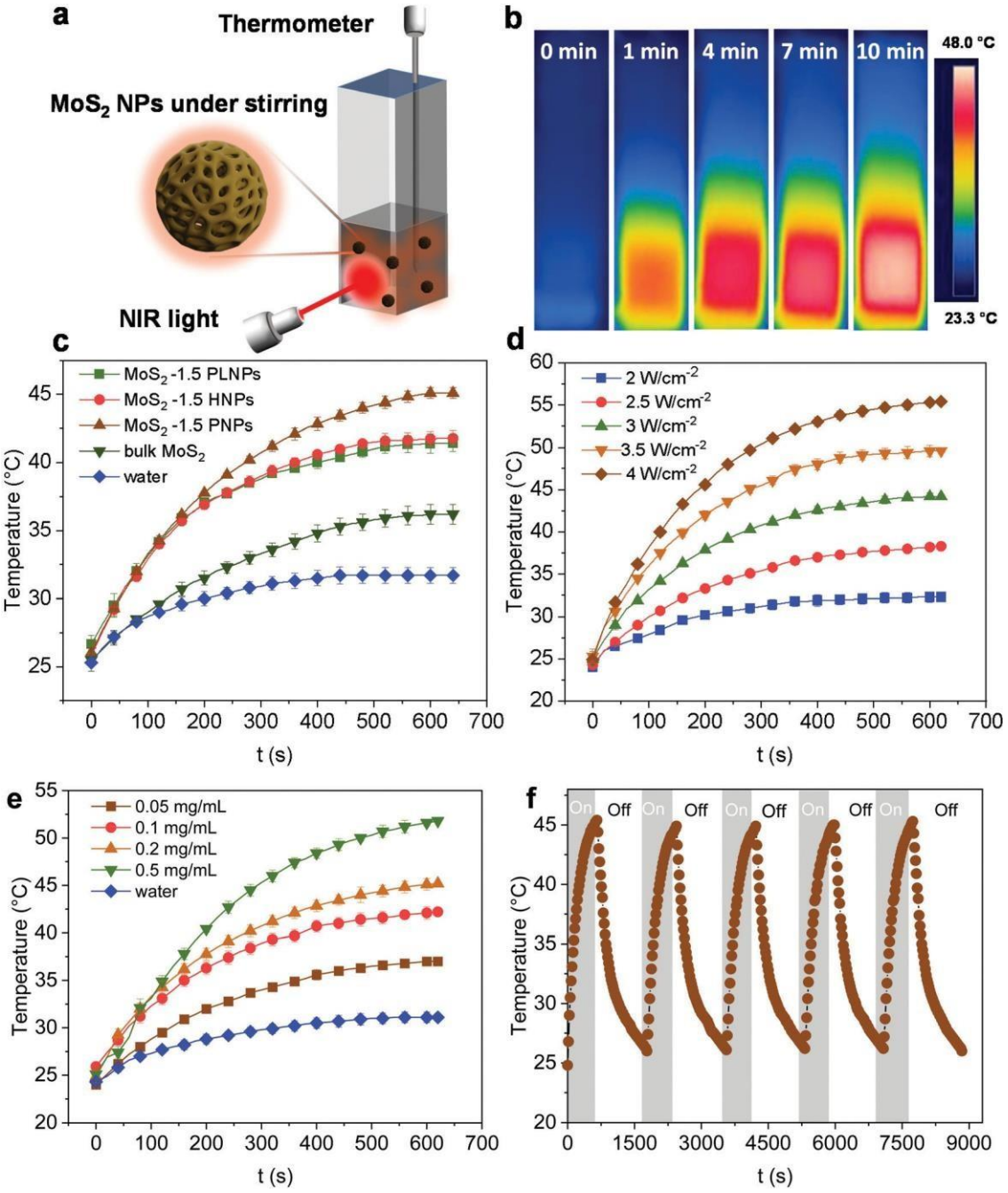

Fig. 4 (a) Schematic of the photothermal conversion setup. (b) Temperature variation of the MoS_2-1.5 PNP dispersion at 0.1 mg mL^{-1} visualized using an IR camera. (c) Photothermal curves of the MoS_2 particles with different morphologies at 0.1 mg mL^{-1} and 3 W cm^{-2}. (d) Photothermal curves of the MoS_2-1.5 PNP dispersion at 0.1 mg mL^{-1} in response to different intensities of NIR light. (e) Photothermal curves of the MoS_2-1.5 PNP dispersion in response to different concentrations at 3 W cm^{-2}. (f) Stability test of the MoS_2-1.5 PNP dispersion at 0.1 mg mL^{-1} and 3 W cm^{-2}.

version performance of the MoS_2-1.5 PNPs stands out among these three featured MoS_2 particles.

We further investigated the dependence of the photothermal effect on the irradiation power and the particle concentration. As shown in Fig. 4d, when the laser intensity increased from 2 to 4 W cm^{-2}, a temperature increment from ~5 to ~32 °C was observed for the MoS_2-1.5 PNP dispersion. Additionally, when the concentration of the MoS_2 PNP dispersion was elevated from 0.05 to 0.5 mg mL^{-1}, the temperature increment of the dispersions increased from ~14 to ~29 °C under a constant laser power of 3 W cm^{-2} (Fig. 4e). This strongly implies the tunable capability of the photothermal behavior of our MoS_2 particles, which is of great importance for many applications including photothermal-assisted catalysis and photothermal cancer therapy. In addition to the enhanced photothermal performance, MoS_2 PNPs showed

excellent stability over a long irradiation period. The temperature increment of the particles displayed a stable reversible behavior using successive ON/OFF irradiation cycles (Fig. 4f). No obvious structural change was observed from the TEM image (Fig. S7†). It is noteworthy that the dispersions of the MoS_2 PNPs with different wall thicknesses exhibited similar photothermal conversion performances and a temperature ~10 °C higher than that of the bulk MoS_2 dispersion under the same irradiation conditions (Fig. S8†).

Catalytic reduction of 4-Nip

As a classic model reaction, the reduction of 4-Nip into 4-aminophenol (4-Amp) can be conducted under ambient conditions by $NaBH_4$ in the presence of a catalyst. In addition, this reduction reaction can be facilely monitored by UV-vis absorption spectroscopy and commonly used as a benchmark to compare the catalytic performance of various catalysts.[58,59] In this work, this model reaction was employed to unfold the catalytic efficiency of our MoS_2 particles with different morphologies. Importantly, we also evaluated the catalytic performance under NIR irradiation by taking advantage of the high photothermal efficiency of the MoS_2 particles. Unlike conventional heating over a large macroscopic area, nanoscale heating by laser irradiation highly localizes the heat around the particles compared to the bulk solution and, therefore, might accelerate the rate of surface catalytic reactions.[60,61] It is noteworthy that the distinctive structure of the porous surface as well as the interconnected hollow channels in the MoS_2 PNPs increases the exposed active MoS_2 edges and accessible surface area for the catalytic surface reactions. In addition, these open porous particles also exhibit excellent photother- mal performance. On the basis of these considerations, the catalytic performance of MoS_2 PNPs was thereafter explored in the presence/absence of NIR light.

Fig. 5a displays the typical time-dependent UV-vis absorption spectra of 4-Nip after introducing MoS_2 PNPs particles as catalysts. As shown, at time zero, a distinct peak of the absorption spectrum is located at 400 nm, assigned to the 4-nitrophenolate ions.[62] As the reaction proceeds, a new peak appears at 290 nm and increases in absorption intensity, confirming the gradual reduction of 4-Nip into 4-Amp. After 15 minutes, the absorption peak of the 4-Nip at 400 nm was diminished, revealing that 4-Nip molecules were completely converted into 4-Amp. First, the reaction was performed in the darkness to compare the catalytic activity of the three MoS_2 PNPs with different wall thicknesses by comparing the reaction rates, as shown in Fig. 5b. The pseudo-first-order reaction was ensured by an excess amount of $NaBH_4$ and the apparent reduction rate (k_{app}) of 4-Nip was calculated by monitoring the absorbance intensity at 400 nm over time according to eqn (1):[28]

$$ln\frac{c}{c_0} = ln\frac{I}{I_0} = -k_{app}t \quad (1)$$

where c and c_0 are the concentrations and I and I_0 are the absorption intensities at 400 nm of 4-Nip at time t and the start of the reaction, respectively. k_{app} is the apparent rate constant, which is directly obtained from the linear relationship between $\ln(c/c_0)$ and t. Fig. 5b shows a comparison of the reaction rate constants using different MoS_2 particles as a function of the catalyst concentration (see summary of k_{app} in Table S3†). Notably, MoS_2-1.5 PNPs displayed the highest cata- lytic performance among the various MoS_2 PNPs. In contrast, the MoS_2-3 PNPs exhibited the lowest rate constant with different catalyst concentrations, which is very similar to that of the bulk MoS_2 particles. It is worth noting that the MoS_2-1 PNPs are relatively easy to aggregate and cluster in aqueous dispersions, which could deteriorate their catalytic performance (Fig. S9†). Therefore, we speculate that small clusters could also form microscopically at a short time scale (15 min), which relatively limits the accessible active surface of MoS_2 particles. No doubt that a larger surface area is more favorable for the surface-catalyzed reduction reaction, which can boost the reaction kinetics by providing more accessible catalytic sites. However, the overall reaction rate is determined by a series of factors, including but not limited to, accessible surface area, total active sites, and medium transfer pathway. Thus, the substantial catalytic enhancement of the MoS_2-1.5 PNPs is attributed to the porosity of the particles as well as to the accessibility of the reactant 4-Nip molecules to the internal active sites. The use of excess amount of MoS_4^{2-} precursor in the MoS_2-3 PNPs relatively reduced the surface porosity of the synthesis template ($PS_{48.5k}$-*b*-$P2VP_{16.5k}$ swollen at 75 °C), which hinders the diffusion of 4-Nip molecules and retards their reactivity. The stability and the recyclability of the catalyst represent another important parameter required for the practical applications. In this work, the stability of MoS_2-1.5 PNPs was investigated, where the particles were recovered and reused for five consecutive catalytic cycles. As shown in Fig. 5c, the conversion efficiency of particles remained above 90% after five cycles, suggesting the excellent catalytic stability of the particles, which makes it possible for them to serve as efficient and reusable nanocatalysts. Moreover, no visible changes were observed in the morphology of MoS_2-1.5 PNPs after 5 catalytic cycles, as examined by TEM (Fig. 5d, S10a and 10b†). In addition, the XRD patterns of the particles remained unchanged after being utilized for the catalytic reaction (Fig. S10c†), demonstrating their good chemical stability. Collectively, the structural and chemical stability contribute to the catalytic stability of MoS_2 during recycling.

Furthermore, the effect of the photoheating on the catalytic performance of the particles under light irradiation was explored. The MoS_2-1.5 PNPs were utilized for the catalytic measurements with light due to the best catalytic performance in the darkness at room temperature. The MoS_2-1.5 PNP dispersion was first continuously stirred and irradiated with NIR light for 15 minutes to ensure a stable temperature (here triggered after the introduction of $NaBH_4$ under continuous light irradiation, and the reaction was simultaneously monitored using UV-vis spectroscopy (Fig. S11b†). It is worth mentioning that the absorption of 4-Nip showed no changes in the absence of $NaBH_4$, indicating that the light solely cannot

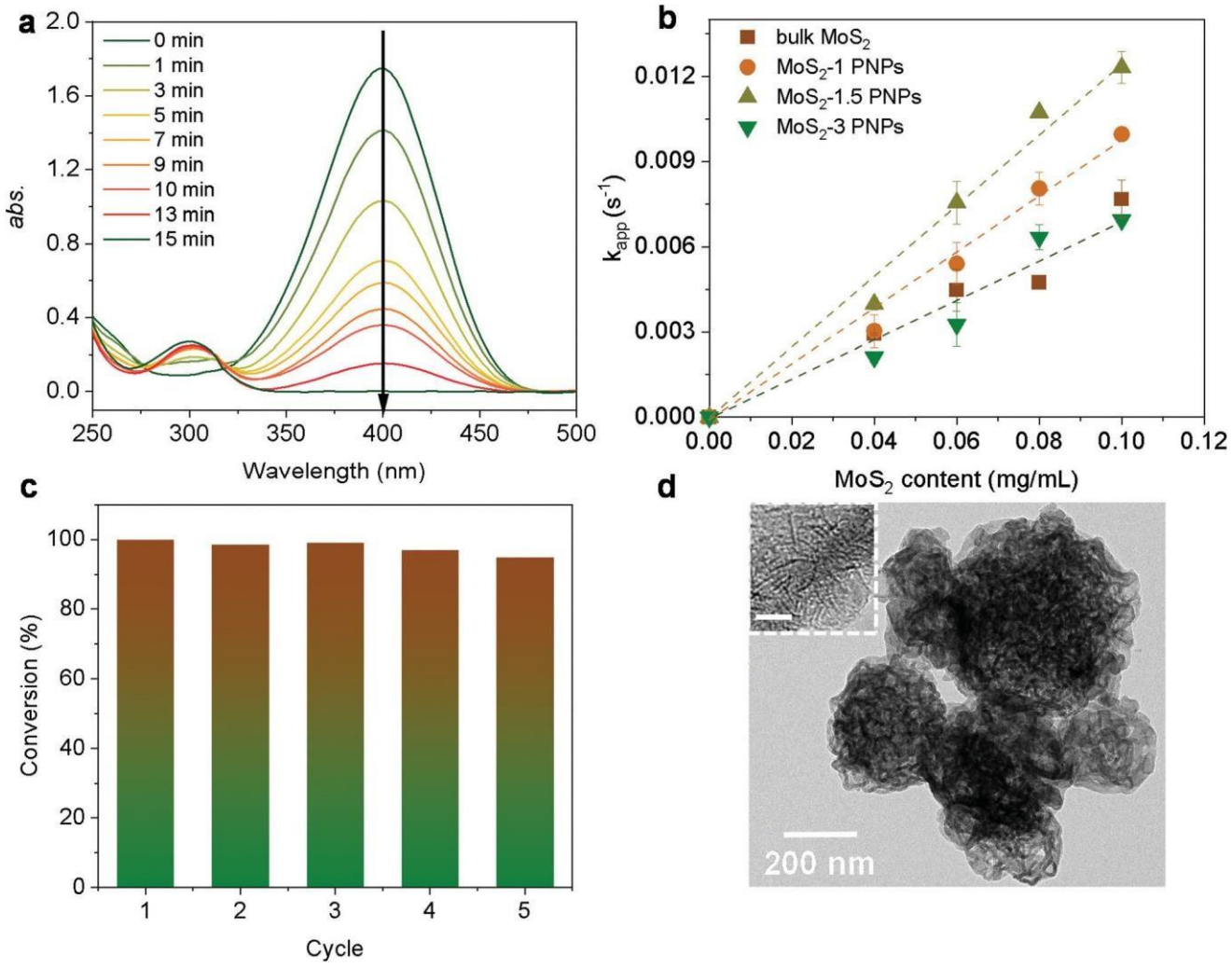

Fig. 5 (a) UV-vis absorption spectra of the reduction of 4-Nip with the concentration of the MoS_2-1.5 PNPs at 0.05 mg mL^{-1}, 4-Nip at 0.1 mM, and $NaBH_4$ at 20 mM at room temperature. (b) Rate constants, k_{app}, of different MoS_2 PNPs as a function of catalytic concentration. (c) Catalytic recycling test of the MoS_2-1.5 PNPs at 0.05 mg mL^{-1}. (d) TEM image of the MoS_2-1.5 PNPs after the recycling tests; the inset is the corresponding HRTEM image with a scale bar of 5 nm.

initiate the reaction (Fig. S11c and 11d†). As shown in Fig. 6a and S12†, light irradiation has led to a higher reduction rate of 0.012 s^{-1}, which obviously surpassed the rate of the reaction performed in the darkness (0.003 s^{-1}). The temperature of the reaction solution also increased from 20 to 37 °C by light irradiation. The enhanced reaction rate could therefore be ascribed to the high temperature induced by the photothermal conversion performance of the MoS_2 particles. To elucidate the role of the photoheating effect, the reaction was performed in the darkness with external heating at 37 °C in a water bath, as observed in the irradiation experiment. As a result, the reaction rate increased from 0.003 to 0.008 s^{-1}, suggesting the strong influence of the operating temperature. However, the reaction rate is still much lower than that of the photo-irradiated samples. It is also worth mentioning that photo-generated charges could possibly contribute to the reaction and enhance the reduction rate.[63] If this is true, the activation energy (E_a) of the reaction should be reduced significantly.[64] To ease this concern, we compared the E_a of the reaction in the presence/absence of light. The reactions were conducted at different operating temperatures with/without light irradiation and the corresponding reaction rates were further determined from the linear slope of $\ln(c/c_0)$ *vs.* *t*, as shown in Fig. 6b and c. These reaction rates were determined in the form of a typical Arrhenius plot in Fig. 6d (see summary of k_{app} in Table S4†) to calculate the E_a from the linear slopes according to the following eqn (2):[65]

$$-ln\left(k_{app}\right) = \frac{E_a}{RT} - ln\,(A) \quad (2)$$

where *T* is the total solution temperature in Kelvin, *R* is the gas constant, k_{app} is the apparent rate constant and *A* is the Arrhenius pre-factor. Thus, a significant reduction of the E_a upon illumination would be plausibly expected if the photo-

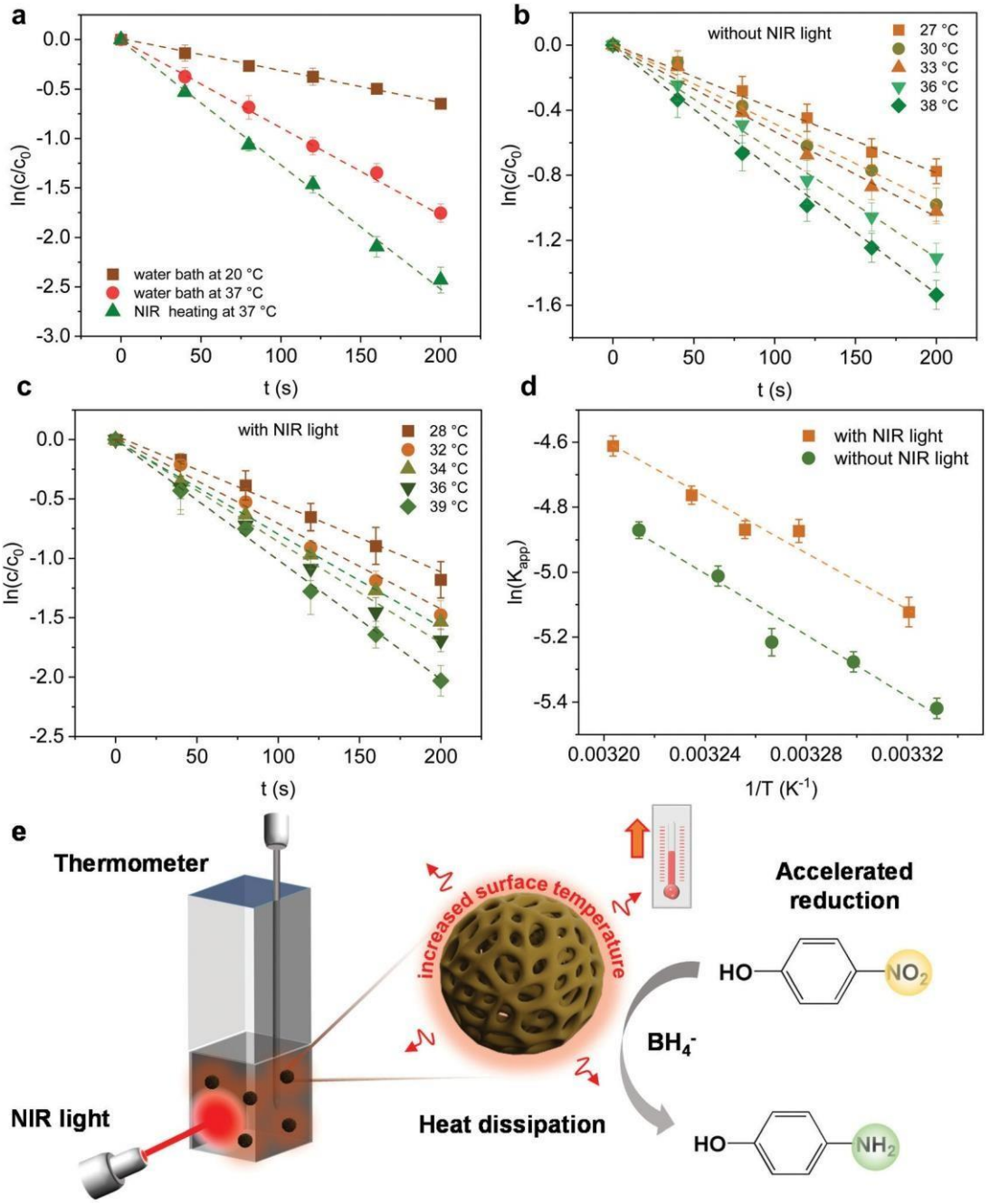

Fig. 6 (a) Plots of c/c_0 *versus* reaction time with the concentration of MoS_2-1.5 PNPs at 0.05 mg mL^{-1}, 4-Nip at 1 mM, and $NaBH_4$ at 0.2 M under different heating conditions. (b) Plots of I/I_0 *versus* reaction time in the darkness. (c) Plots of I/I_0 *versus* reaction time in the presence of light. (d) Reaction rates as a function of temperature in the presence (yellow line) and absence (green line) of 808 nm laser irradiation. The concentrations of MoS_2-1.5 PNPs, 4-Nip and $NaBH_4$ are 0.03 mg mL^{-1}, 1 mM and 0.2 M, respectively. (e) Scheme of the reduction reaction of 4-Nip under NIR irradiation.

generated charges are involved in the reaction. In the current study, however, the E_a in the presence/absence of light was calculated to be 34.7 ± 3.6 and 38.7 ± 4.6 kJ mol^{-1}, respectively. The comparable results of E_a point out that the photoheating effect could be the dominant mechanism of the reaction acceleration. In conclusion, the reduction reaction of 4-Nip into 4-Amp has been reported to occur on the particle surface following the Langmuir–Hinshelwood model,[66] as $NaBH_4$ provides the reactants with the necessary hydrogen species (Fig. 6e). The borohydride ions adsorb onto the catalytic surface to produce active hydrogen species, which subsequently reduce the adsorbed 4-Nip molecules into 4-Amp. Considering that the reduction of 4-Nip is a temperature-dependent process, the reaction rate is therefore enhanced by

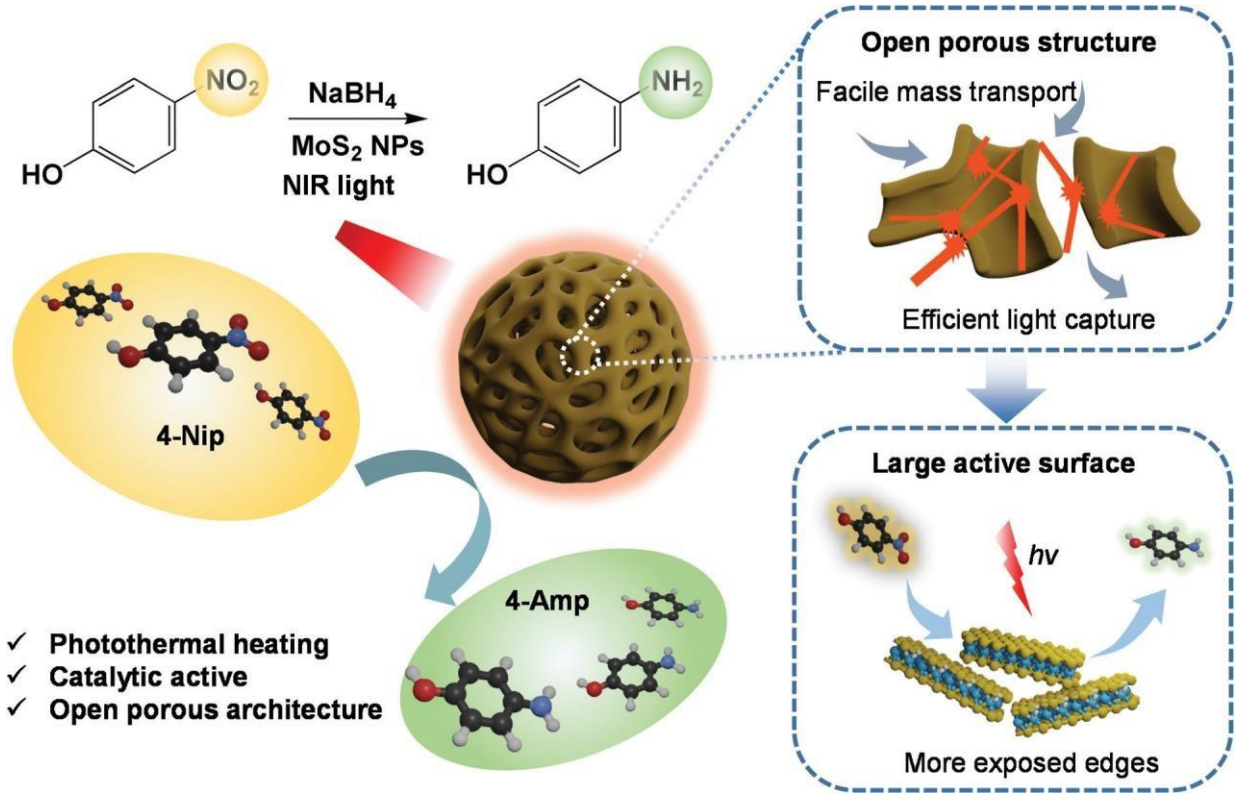

Scheme 2 Schematic of 4-Nip reduction with porous MoS_2 under NIR light illumination.

the increased reaction temperature benefiting from the surface local heat of the MoS_2 particles.[67] Overall, we demonstrate that our MoS_2 catalysts with well-designed porous nanostructures can serve as efficient dual-functional catalysts for the enhanced reduction of 4-Nip, benefiting from the fast diffusion of reactants,[68,69] photo-induced heat and improved utility of active surface (Scheme 2). In other words, combining with the intrinsically catalytic property of MoS_2, the strong photoheating effect induced by NIR light irradiation further greatly accelerates the catalytic reduction reaction. The porous nanostructure of MoS_2 enables the dual-functional MoS_2 to be employed in the fast degradation of 4-Nip.

Conclusions

In summary, we have designed a series of dual-functional MoS_2 particles including pomegranate-like, hollow, and open porous particles using a soft PS-*b*-P2VP template. These nanoparticles with different well-defined internal structures show an efficient photoheating effect. The porous MoS_2 nanoparticles displayed the highest photothermal conversion performance, benefitting from the localization of the light in their internal network-like structures. Moreover, this high photothermal conversion behavior has been demonstrated to accelerate the reduction reaction of 4-Nip under NIR light irradiation, confirming the synergistic properties of these MoS_2 particles. Thus, the open porous MoS_2 particles with interconnecting nanochannels were shown to serve as efficient nanocatalysts, while their abundant active sites, fast reactant diffusion pathway and local surface heating play a key role in enhancing the overall catalytic performance.

Experimental section/methods

Assembled block copolymer nanospheres

For $PS_{48.5k}$-*b*-$P2VP_{16.5k}$, 40 mg of the polymer powder was dissolved in 4 mL of toluene and introduced to 80 mL of de-ionized water with 0.12 mL of the surfactant solution (SDS, 0.5 wt%). The mixture was left to emulsify under sonication for 30 min. The solution was then evaporated using a rotary evaporator at 40 °C in a water bath, resulting in solidified polymer nanospheres dispersed in water. To completely remove toluene, the solution was left at 40 °C overnight. The dispersion was centrifuged at 9000 rpm for 2 h, and the obtained particles were redispersed in 80 mL of ethanol. The particle dispersion was further heated at 50 and 75 °C for 1 h to induce the porous structure, respectively. After cooling down, the polymer dispersion was then evaporated to remove ethanol. For $PS_{38.5k}$-*b*-$P2VP_{23k}$, the particles were obtained using the same protocol, while the swelling of the polymer was only performed in ethanol at 50 °C.

Nanostructured MoS_2 particles

First, 150 mL of $(NH_4)_2MoS_4$ solution was added to the as-prepared polymer dispersion (30 mg mL^{-1}, 15 mL) with final concentrations of $(NH_4)_2MoS_4$ maintained at 1, 1.5 and 3 mg mL^{-1}, respectively. After stirring at 250 rpm for 30 min, HCl (0.16 mL, 1 M) was added dropwise into the solution, resulting in the decomposition of a slight amount of the precursor into molybdenum sulfide (MoS_x, x = 2–3). To improve the hydrophilicity of MoS_2 in the aqueous solution, 100 μL of 3-MPA was added into the solution under stirring. After stirring for 30 min, the brown solution was separated by centrifugation at 8000 rpm for 40 min and washed three times with fresh water. The obtained dark brown particles were freeze-dried overnight. The final product of MoS_2 particles was obtained by calcination at 500 °C in an argon atmosphere for 2 h at a rate of 3 °C min^{-1}. In comparison to MoS_2 particles prepared with different polymer templates, bulk MoS_2 was fabricated by following the same process without any polymer template.

Photothermal conversion performance

The photothermal conversion performance of the MoS_2 particles was measured using an aqueous dispersion of the particles with different concentrations (0.05–0.5 mg mL^{-1}). First, 1 mL of the dispersion was placed in a quartz cuvette under 300 rpm of stirring and directly irradiated under 808 nm NIR laser (PhotonTec Berlin, turn-key 808 nm diode laser system) with different intensities (2.0–4.0 W cm^{-2}) for approximately 10 min. To avoid direct heating by light, the thermometer was kept far away from the laser spot, while the distance between the laser spot and the thermometer was fixed at *ca*. 6 cm. The temperature changes of the dispersion were recorded using a digital thermometer (P 300 Thermometer, Dostmann electronics) every 20 seconds. The IR camera (FLIR-E8 XT) was employed to visualize the temperature changes of the dispersion every 3 min.

Catalytic reduction of 4-nitrophenol

Catalytic reaction in darkness. All the solutions and dispersion were purged with fresh N_2 for 30 min to remove oxygen before use. An appropriate amount of MoS_2 aqueous dispersion (0.1–0.25 mL, 1 mg mL^{-1}) was sonicated for 15 min and then added into a clean quartz cuvette. The 4-Nip solution (0.25 mL, 1 mM) was introduced into the MoS_2 dispersion under 300 rpm of stirring. The reducing agent $NaBH_4$ (0.5 mL, 0.1 M) was then quickly injected to initialize the reduction reaction at room temperature. The total volume of the dispersion was fixed at 2.5 mL. The dispersion in the cuvette was measured using an UV-vis absorption spectrophotometer (PerkinElmer, Lambda 650 spectrometer) in the darkness. For the catalytic recycling test, the MoS_2 catalysts after reaction in one cycle were collected by centrifugation at 9000 rpm for 15 min. Afterwards, the MoS_2 particles were redispersed in fresh water with sonication for 15 min and then used for the next catalytic cycle.

Catalytic reaction in the presence of NIR light irradiation. A MoS_2 particle dispersion (0.05 mL, 1 mg mL^{-1}) was added into a 4-Nip solution (0.5 mL, 2 mM) in the cuvette under 300 rpm of stirring. Then, 0.45 mL of fresh water was introduced into the dispersion. After irradiation with the NIR laser at an intensity of 3 W cm^{-2} for about 15 min, the temperature of the dispersion remained constant. A freshly prepared $NaBH_4$ solution (100 μL, 2 M) was then quickly injected into the mixed dispersion. Following this, 0.1 mL of the reaction dispersion was taken out at regular time intervals and then quickly diluted with 1.9 mL of water. The catalysts were then filtered out using a syringe filter (pore size of 0.22 μm), and the residual solution was tested using the UV-vis absorption spectrum. For the calculation of activation energy, the MoS_2 dispersion (0.03 mg mL^{-1}) was heated by an external heating plate and NIR light (2 W cm^{-2}), and the reaction temperature was recorded using a thermometer. In comparison to the NIR-assisted reduction, the reaction without light irradiation was conducted in a water bath heating at a corresponding temperature to that under NIR light irradiation by following the same process.

Materials characterization

X-ray diffraction analysis (XRD, Bruker D8) measurements were conducted using a monochromatic X-ray beam with CuKa radiation at a scan rate of 0.05° min^{-1}. N_2 adsorption/desorption isotherms were obtained using a Quantachrome Autosorb-1 system at 77 K. The specific surface area was calculated using the Brunauer-Emmett-Teller (BET) method based on a multipoint analysis. Transmission electron microscopy (TEM) and high-resolution TEM (HRTEM) were performed using a JEOL JEM-2100 instrument operating at an accelerating voltage of 200 kV. Scanning electron microscopy (SEM) measurement was carried out using a LEO Gemini 1530 microscope operating at 5 kV. Thermogravimetric analysis (TGA) was performed using a Mettler Toledo TGA 1 Stare thermal instrument in the temperature range of 25–900 °C at a heating rate of 10 °C min^{-1} in air. The Raman spectra were recorded using an InVia 2R9X81 Raman spectrometer equipped with a detector of Renishaw Centrus 2MYA08 and a HeNe laser (a wavelength of 532 nm).

Conflicts of interest

The authors declare no competing financial interests.

Acknowledgements

The authors acknowledge Mr. J. Yang at Department of Chemistry/Functional Materials, Technische Universität Berlin for the TGA measurement. The authors also thank Mr. Z. Zhang at Department of Chemistry, Humboldt- Universität zu Berlin for the Raman measurement. Y. Lu thank the Deutsche Forschungsgemeinschaft (DFG, German Research Foundation) – Project number 410871749 for finan- cial support.

References

1 X. Liu, J. Iocozzia, Y. Wang, X. Cui, Y. Chen, S. Zhao, Z. Li and Z. Lin, *Energy Environ. Sci.*, 2017, 10, 402–434.
2 N. Meng, J. Ren, Y. Liu, Y. Huang, T. Petit and B. Zhang, *Energy Environ. Sci.*, 2018, 11, 566–571.
3 M. Gao, L. Zhu, C. K. Peh and G. W. Ho, *Energy Environ. Sci.*, 2019, 12, 841–864.
4 M. Tan, J. Wang, W. Song, J. Fang and X. Zhang, *J. Mater. Chem. A*, 2019, 7, 1244–1251.
5 T. Zhang, F. Meng, M. Gao, W. L. Ong, K.-G. Haw, T. Ding, G. W. Ho and S. Kawi, *EcoMat*, 2021, 3, e12152.
6 Y. Cao, M. Derakhshani, Y. Fang, G. Huang and C. Cao, *Adv. Funct. Mater.*, 2021, 31, 2106231.
7 H. Liu, H.-G. Ye, M. Gao, Q. Li, Z. Liu, A.-Q. Xie, L. Zhu, G. W. Ho and S. Chen, *Adv. Sci.*, 2021, 8, 2101232.
8 K. Xu, J. Wu, C. F. Tan, G. W. Ho, A. Wei and M. Hong, *Nanoscale*, 2017, 9, 11574–11583.
9 S. Hu, B.-J. Liu, J.-M. Feng, C. Zong, K.-Q. Lin, X. Wang, D.-Y. Wu and B. Ren, *J. Am. Chem. Soc.*, 2018, 140, 13680–13686.
10 D. Mateo, J. Albero and H. García, *Energy Environ. Sci.*, 2017, 10, 2392–2400.
11 Z. Zhang, X. Jiang, B. Liu, L. Guo, N. Lu, L. Wang, J. Huang, K. Liu and B. Dong, *Adv. Mater.*, 2018, 30, 1705221.
12 L. Jiang, X. Yuan, G. Zeng, J. Liang, X. Chen, H. Yu, H. Wang, Z. Wu, J. Zhang and T. Xiong, *Appl. Catal., B*, 2018, 227, 376–385.
13 Y. Yang, R. Zhao, T. Zhang, K. Zhao, P. Xiao, Y. Ma, P. M. Ajayan, G. Shi and Y. Chen, *ACS Nano*, 2018, 12, 829–835.
14 H. Yuan, F. Liu, G. Xue, H. Liu, Y. Wang, Y. Zhao, X. Liu, X. Zhang, L. Zhao, Z. Liu, H. Liu and W. Zhou, *Appl. Catal., B*, 2021, 283, 119647.
15 Y. Chai, H. Ma, X. Ma, X. Zhang, Y. He, Y. Wang, Q. Jiang, X. Wang, J. Ji and M. Xue, *J. Mater. Chem. A*, 2020, 8, 10891–10897.
16 S. Mei, X. Xu, R. D. Priestley and Y. Lu, *Chem. Sci.*, 2020, 11, 12269–12281.
17 M. Zhao, T. Chen, B. He, X. Hu, J. Huang, P. Yi, Y. Wang, Y. Chen, Z. Li and X. Liu, *J. Mater. Chem. A*, 2020, 8, 15976–15983.
18 S. Mei, Z. Kochovski, R. Roa, S. Gu, X. Xu, H. Yu, J. Dzubiella, M. Ballauff and Y. Lu, *Nano-Micro Lett.*, 2019, 11, 83.
19 Y.-C. Chen, A.-Y. Lu, P. Lu, X. Yang, C.-M. Jiang, M. Mariano, B. Kaehr, O. Lin, A. Taylor, I. D. Sharp, L.-J. Li, S. S. Chou and V. Tung, *Adv. Mater.*, 2017, 29, 1703863.
20 J. Ke, J. Liu, H. Sun, H. Zhang, X. Duan, P. Liang, X. Li, M. O. Tade, S. Liu and S. Wang, *Appl. Catal., B*, 2017, 200, 47–55.
21 D. A. Reddy, H. Park, S. Hong, D. P. Kumar and T. K. Kim, *J. Mater. Chem. A*, 2017, 5, 6981–6991.
22 Z. Zhou, B. Li, C. Shen, D. Wu, H. Fan, J. Zhao, H. Li, Z. Zeng, Z. Luo, L. Ma and C. Tan, *Small*, 2020, 16, 2004173.
23 M.-H. Wu, L. Li, N. Liu, D.-J. Wang, Y.-C. Xue and L. Tang, *Process Saf. Environ. Prot.*, 2018, 118, 40–58.
24 X. Li, L. Kong, W. Hu, C. Zhang, A. Pich, X. Shi, X. Wang and L. Xing, *J. Adv. Res.*, 2022, 37, 255–266.
25 D. Xu, Z. Li, L. Li and J. Wang, *Adv. Funct. Mater.*, 2020, 30, 2000712.
26 J. Wang, Y. Li, L. Deng, N. Wei, Y. Weng, S. Dong, D. Qi, J. Qiu, X. Chen and T. Wu, *Adv. Mater.*, 2017, 29, 1603730.
27 X. Yang, Y. Yang, L. Fu, M. Zou, Z. Li, A. Cao and Q. Yuan, *Adv. Funct. Mater.*, 2018, 28, 1704505.
28 S. García -Dalí, J. I. Paredes, J. M. Munuera, S. Villar-Rodil, A. Adawy, A. Martínez -Alonso and J. M. D. Tascón, *ACS Appl. Mater. Interfaces*, 2019, 11, 36991–37003.
29 X. Hai, W. Zhou, K. Chang, H. Pang, H. Liu, L. Shi, F. Ichihara and J. Ye, *J. Mater. Chem. A*, 2017, 5, 8591–8598.
30 J. Xie, H. Zhang, S. Li, R. Wang, X. Sun, M. Zhou, J. Zhou, X. W. Lou and Y. Xie, *Adv. Mater.*, 2013, 25, 5807–5813.
31 W. Bao, N. J. Borys, C. Ko, J. Suh, W. Fan, A. Thron, Y. Zhang, A. Buyanin, J. Zhang and S. Cabrini, *Nat. Commun.*, 2015, 6, 1–7.
32 R. Asahi, T. Morikawa, T. Ohwaki, K. Aoki and Y. Taga, *Science*, 2001, 293, 269–271.
33 M. Guo, Z. Xing, T. Zhao, Z. Li, S. Yang and W. Zhou, *Appl. Catal., B*, 2019, 257, 117913.
34 X. Yu, R. Du, B. Li, Y. Zhang, H. Liu, J. Qu and X. An, *Appl. Catal., B*, 2016, 182, 504–512.
35 T. Quan, N. Goubard-Bretesché, E. Härk, Z. Kochovski, S. Mei, N. Pinna, M. Ballauff and Y. Lu, *Chem. – Eur. J.*, 2019, 25, 4757–4766.
36 M. Xiao, Z. Wang, M. Lyu, B. Luo, S. Wang, G. Liu, H.-M. Cheng and L. Wang, *Adv. Mater.*, 2019, 31, 1801369.
37 R. R. Poolakkandy and M. M. Menamparambath, *Nanoscale Adv.*, 2020, 2, 5015–5045.
38 Y. Cui, T. Zhu, A. Li, B. Liu, Z. Cui, Y. Qiao, Y. Tian and D. Qiu, *ACS Appl. Mater. Interfaces*, 2018, 10, 6956–6964.
39 S. Mei, L. Wang, X. Feng and Z. Jin, *Langmuir*, 2013, 29, 4640–4646.
40 S. Mei and Z. Jin, *Small*, 2013, 9, 322–329.
41 H. Fan and Z. Jin, *Macromolecules*, 2014, 47, 2674–2681.
42 W. Han, P. Hou, S. Sadaf, H. Schäfer, L. Walder and M. Steinhart, *ACS Appl. Mater. Interfaces*, 2018, 10, 7451–7458.
43 L. Guo, Y. Wang and M. Steinhart, *Chem. Soc. Rev.*, 2021, 50, 6333–6348.
44 N. Hampu, J. R. Werber, W. Y. Chan, E. C. Feinberg and M. A. Hillmyer, *ACS Nano*, 2020, 14, 16446–16471.
45 H. Yang, X. Shi, S. Chu, Z. Shao and Y. Wang, *Adv. Sci.*, 2021, 8, 2003096.
46 D. Liu, Y. Liao, E. J. Cornel, M. Lv, T. Wu, X. Zhang, L. Fan, M. Sun, Y. Zhu, Z. Fan and J. Du, *Chem. Mater.*, 2021, 33, 7972–7985.
47 E. Kang, B. Graczykowski, U. Jonas, D. Christie, L. A. G. Gray, D. Cangialosi, R. D. Priestley and G. Fytas, *Macromolecules*, 2019, 52, 5399–5406.
48 Y. Wang, U. Gösele and M. Steinhart, *Chem. Mater.*, 2008, 20, 379–381.

49 J. Zhou and Y. Wang, *Macromolecules*, 2020, 53, 5–17.
50 Y. Liu, J. Wang, M. Zhang, H. Li and Z. Lin, *ACS Nano*, 2020, 14, 12491–12521.
51 X. Li, J. Iocozzia, Y. Chen, S. Zhao, X. Cui, W. Wang, H. Yu, S. Lin and Z. Lin, *Angew. Chem., Int. Ed.*, 2018, 57, 2046–2070.
52 S. Mei, J. Cao and Y. Lu, *J. Mater. Chem. A*, 2015, 3, 3382–3389.
53 T. Quan, Y. Xu, M. Tovar, N. Goubard-Bretesché, Z. Li, Z. Kochovski, H. Kirmse, K. Skrodczky, S. Mei, H. Yu, D. Abou-Ras, M. Wagemaker and Y. Lu, *Batter. Supercaps*, 2020, 3, 747–756.
54 D. Yang and R. F. Frindt, *J. Appl. Phys.*, 1996, 79, 2376–2385.
55 X. Zheng, J. Xu, K. Yan, H. Wang, Z. Wang and S. Yang, *Chem. Mater.*, 2014, 26, 2344–2353.
56 S. H. Hwang, J. Yun and J. Jang, *Adv. Funct. Mater.*, 2014, 24, 7619–7626.
57 J. Sun, J. Zhang, M. Zhang, M. Antonietti, X. Fu and X. Wang, *Nat. Commun.*, 2012, 3, 1139.
58 S. Wunder, Y. Lu, M. Albrecht and M. Ballauff, *ACS Catal.*, 2011, 1, 908–916.
59 P. Hervés, M. Pérez-Lorenzo, L. M. Liz-Marzán, J. Dzubiella, Y. Lu and M. Ballauff, *Chem. Soc. Rev.*, 2012, 41, 5577–5587.
60 W. Feng, L. Chen, M. Qin, X. Zhou, Q. Zhang, Y. Miao, K. Qiu, Y. Zhang and C. He, *Sci. Rep.*, 2015, 5, 17422.
61 N. R. S. Sibuyi, K. L. Moabelo, M. Meyer, M. O. Onani, A. Dube and A. M. Madiehe, *J. Nanobiotechnol.*, 2019, 17, 122.
62 R. D. Neal, R. A. Hughes, P. Sapkota, S. Ptasinska and S. Neretina, *ACS Catal.*, 2020, 10, 10040–10050.
63 Q. Xiao, S. Sarina, A. Bo, J. Jia, H. Liu, D. P. Arnold, Y. Huang, H. Wu and H. Zhu, *ACS Catal.*, 2014, 4, 1725–1734.
64 N. Li, Z. Liu, M. Liu, C. Xue, Q. Chang, H. Wang, Y. Li, Z. Song and S. Hu, *Inorg. Chem.*, 2019, 58, 5746–5752.
65 Z. A. Piskulich, O. O. Mesele and W. H. Thompson, *J. Phys. Chem. A*, 2019, 123, 7185–7194.
66 S. Wunder, F. Polzer, Y. Lu, Y. Mei and M. Ballauff, *J. Phys. Chem. C*, 2010, 114, 8814–8820.
67 J. Lü, Y. Fu, Y. Song, D. Wang and C. Lü, *RSC Adv.*, 2016, 6, 14247–14252.
68 L. Forni, *Catal. Today*, 1999, 52, 147–152.
69 Y. Zhou, Q. Ji, H. Liu and J. Qu, *Environ. Sci. Technol.*, 2018, 52, 7477–7485.

Supporting Information

Templating synthesis of dual-functional porous MoS_2 nanoparticles with photothermal conversion and catalytic properties

*Xuefeng Pan[a], Radwan M. Sarhan[a], Zdravko Kochovski[a], Guosong Chen[b], Andreas Taubert[c], Shilin Mei[a]*and Yan Lu[a,c*]*

[a] Department for Electrochemical Energy Storage, Helmholtz-Zentrum Berlin für Materialien und Energie, Hahn-Meitner-Platz 1, Berlin 14109, Germany

[b] The State Key Laboratory of Molecular Engineering of Polymers and Department of Macromolecular Science, Fudan University, Shanghai 200433, China

[c] Institute of Chemistry, University of Potsdam, Potsdam 14476, Germany

E-mails: shilin.mei@helmholtz-berlin.de (S.M.), Current contact: shilin.mei@bit.edu.cn yan.lu@helmholtz-berlin.de (Y. L.)

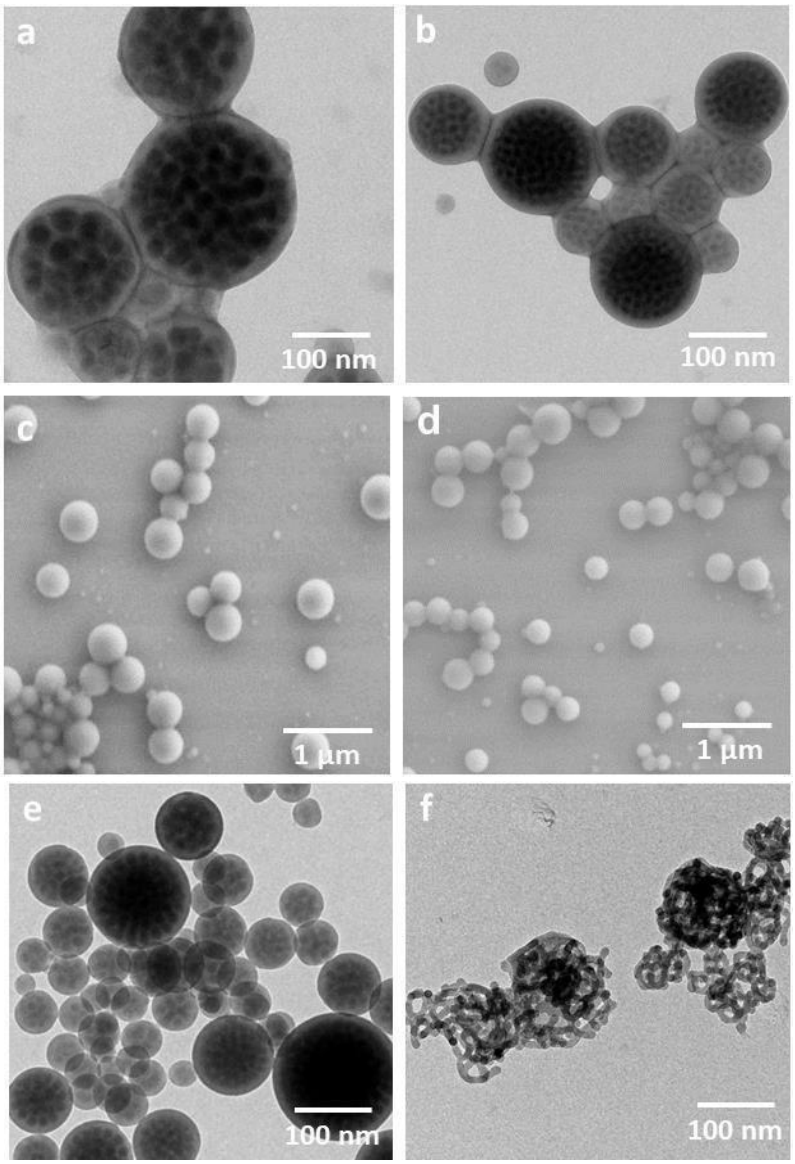

Fig. S1 TEM images of (a) $PS_{38.5k}$-*b*-$P2VP_{23k}$ and (b) $PS_{48.5k}$-*b*-$P2VP_{16.5k}$ particles before swelling. The polymer particles were stained by I_2 vapor for 20 min. The dark contrast shows the distribution of P2VP domains. SEM image of (c) $PS_{38.5k}$-*b*-$P2VP_{23k}$ and (d) $PS_{48.5k}$-*b*-$P2VP_{16.5k}$ particles after swelling at 50 °C. TEM images of the $PS_{48.5k}$-*b*-$P2VP_{16.5k}$ particles swelling at (e) 30 and (f) 90 °C.

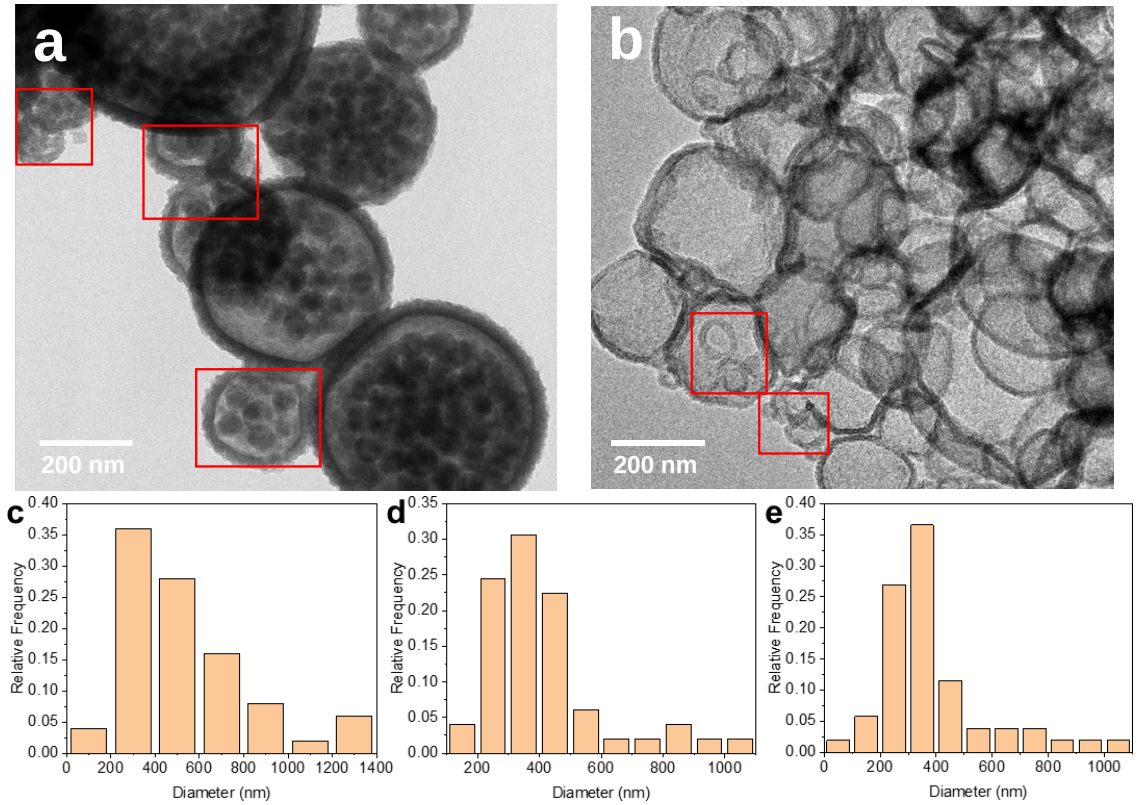

Fig. S2 TEM images of (a) MoS_2 PLNPs and (b) MoS_2 HNPs. The histograms of particle size distribution of the MoS_2 PNPs prepared at the precursor concentration of (c) 1, (d) 1.5 and (e) 3 mg/mL.

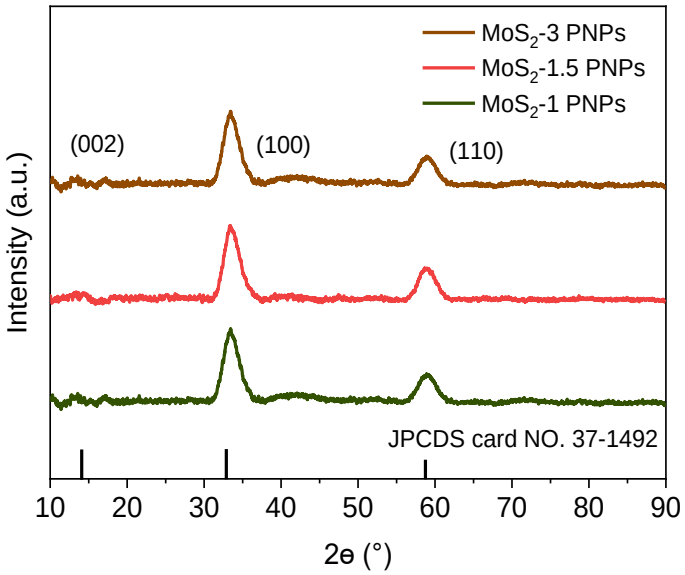

Fig. S3 XRD patterns of various MoS_2 PNPs.

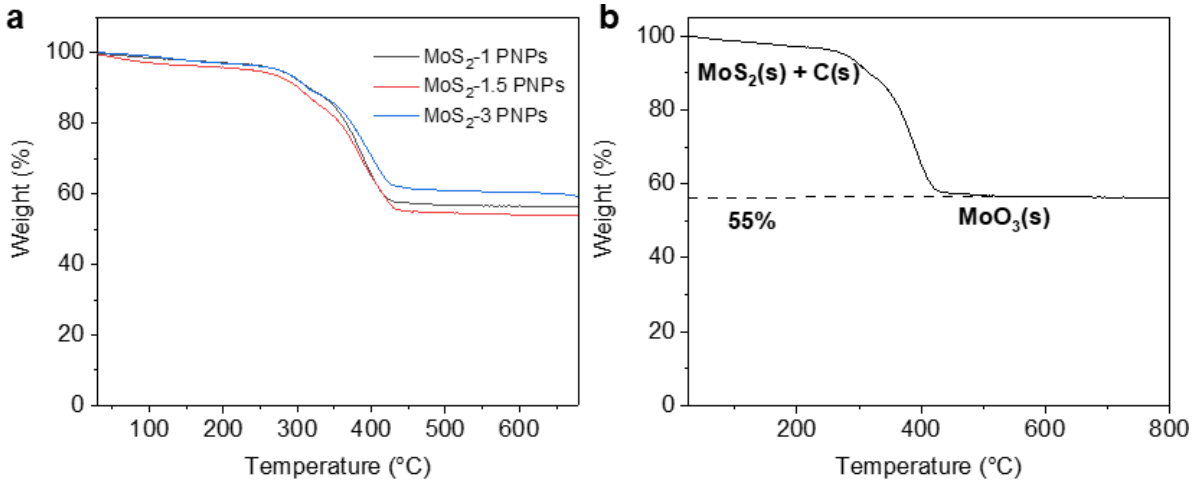

Fig. S4 TGA curves of (a) various MoS_2 particles and (b) the chemical variation of the MoS_2-1.5 PLNPs particles during calcination.

Taking MoS_2-1.5 PLNPs for example, the components change during calcination is as below:

$$3O_2(g) + MoS_2(s) \rightarrow MoO_3(s) + SO_3(g)$$

$$O_2(g) + C(s) \rightarrow CO_2(g)$$

Here we assume the initial amount of carbon and MoS_2 is x and y, respectively. The molar masses of MoS_2 and MoO_3 are 160.1 g/mol and 143.9 g/mol, respectively. Then the calculation equations of the mass equilibrium before and after calcination is below:

$$x + y = 100\%$$

$$\frac{143.9}{160.1} \times y = 55\%$$

Therefore, the amount of carbon and MoS_2 is calculated to be 38.9 % and 61.1 %. The results of various MoS_2 PNPs are summarized in **Table S1**.

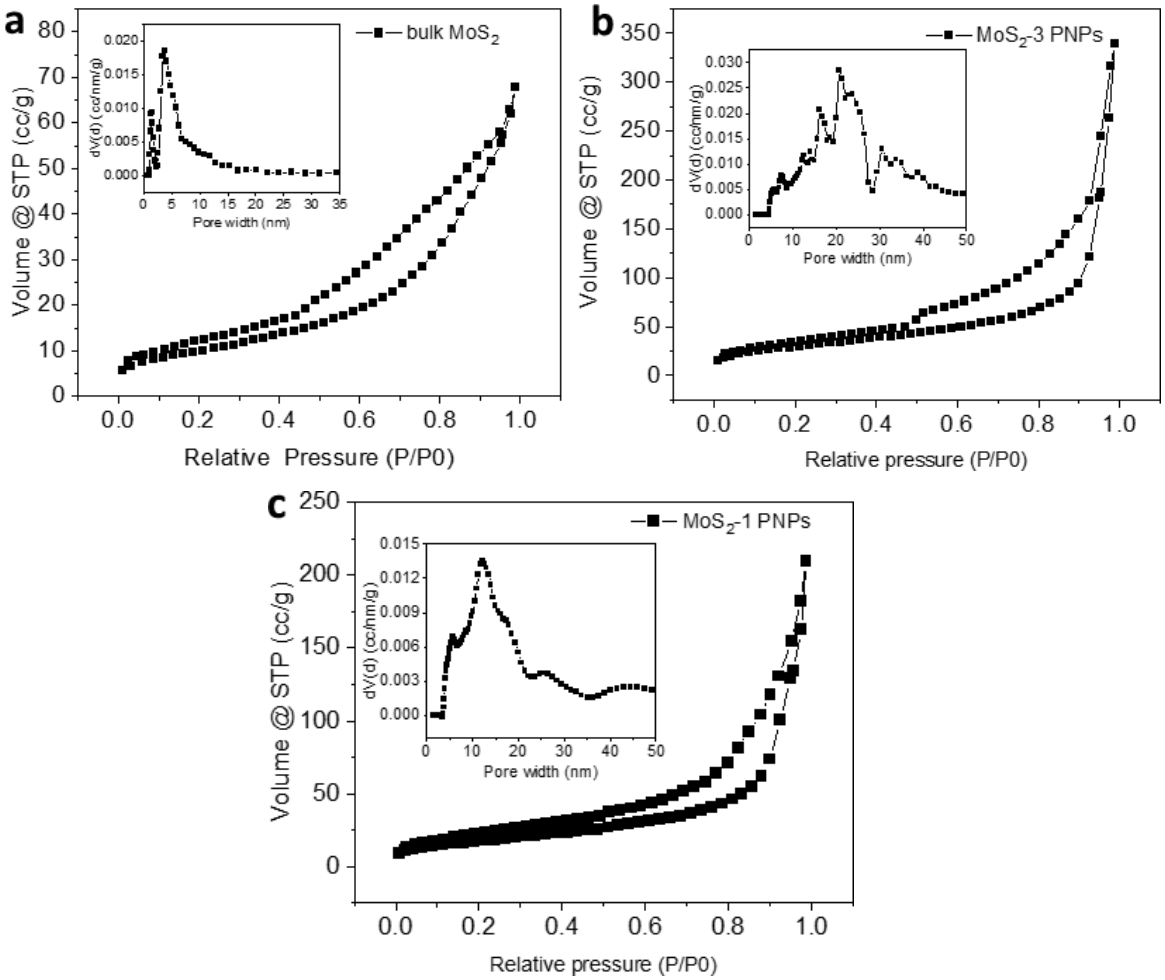

Fig. S5 Isothermal N_2 adsorption and desorption of various MoS_2 particles. The insets are the corresponding curves of pore size distribution.

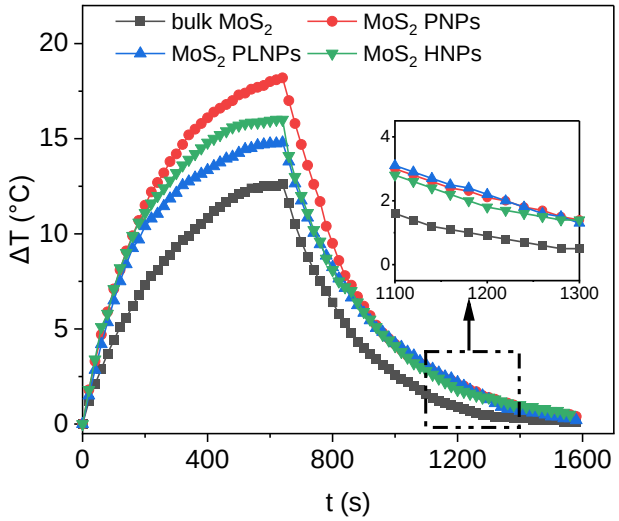

Fig. S6 Temperature change *vs.* time of MoS_2 particles with various morphologies when the laser on and off.

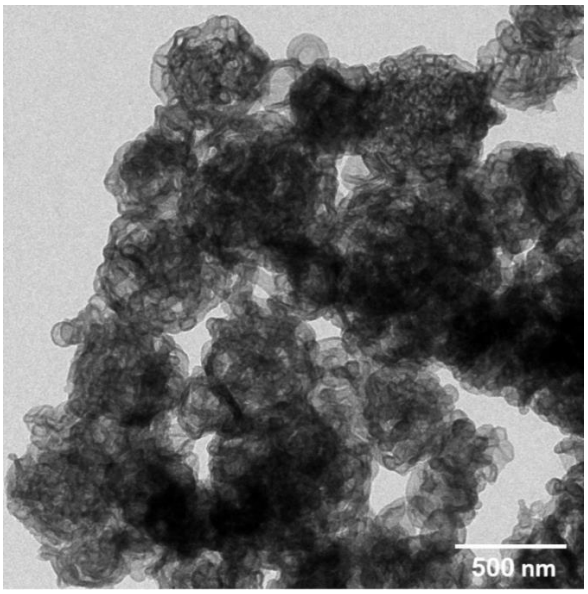

Fig. S7 TEM image of the MoS_2 -1.5 PNPs after 5 photothermal test cycles.

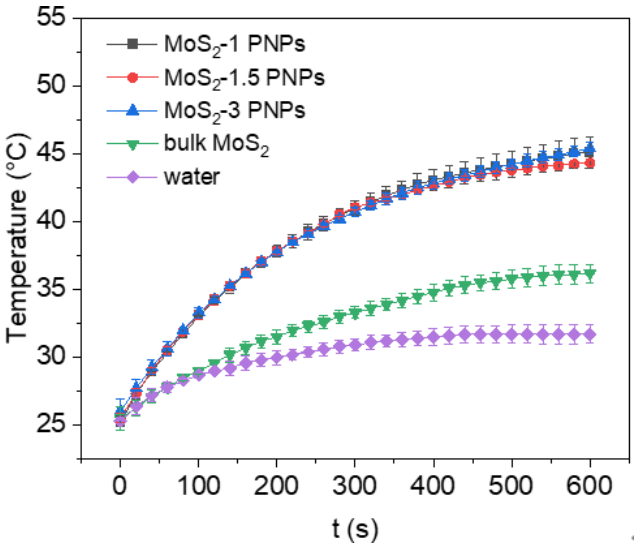

Fig. S8 Temperature change of water and various MoS_2 PNPs at 0.1 mg/ml under NIR irradiation at 3 W/cm^2.

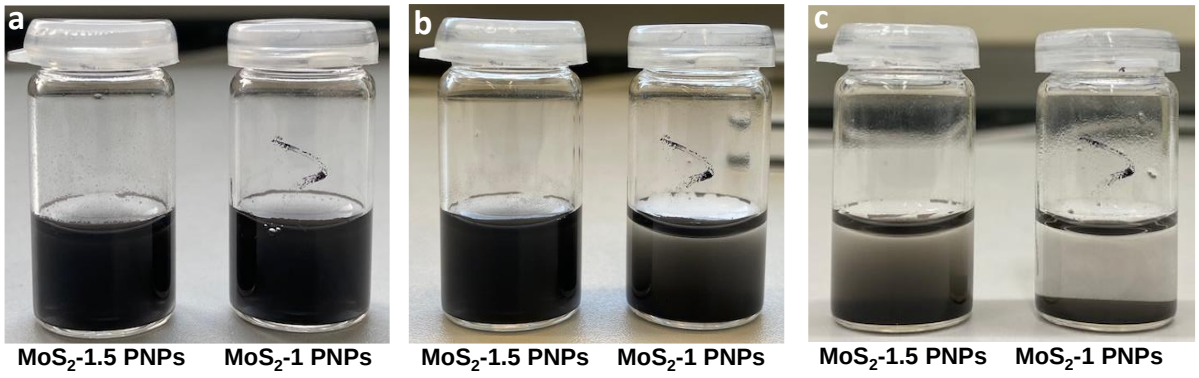

Fig. S9 Photos of MoS_2 dispersions after storing for (a) 0 h, (b) 1.5 h and (c) 3h.

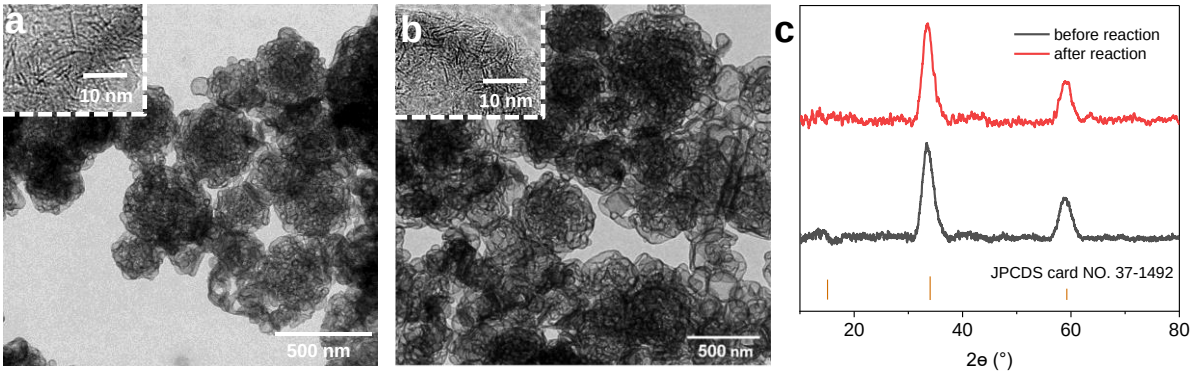

Fig. S10 TEM image of the MoS_2 -1.5 PNPs (a) before and (b) after 5 catalytic cycles. (c) XRD patterns before and after catalytic reactions.

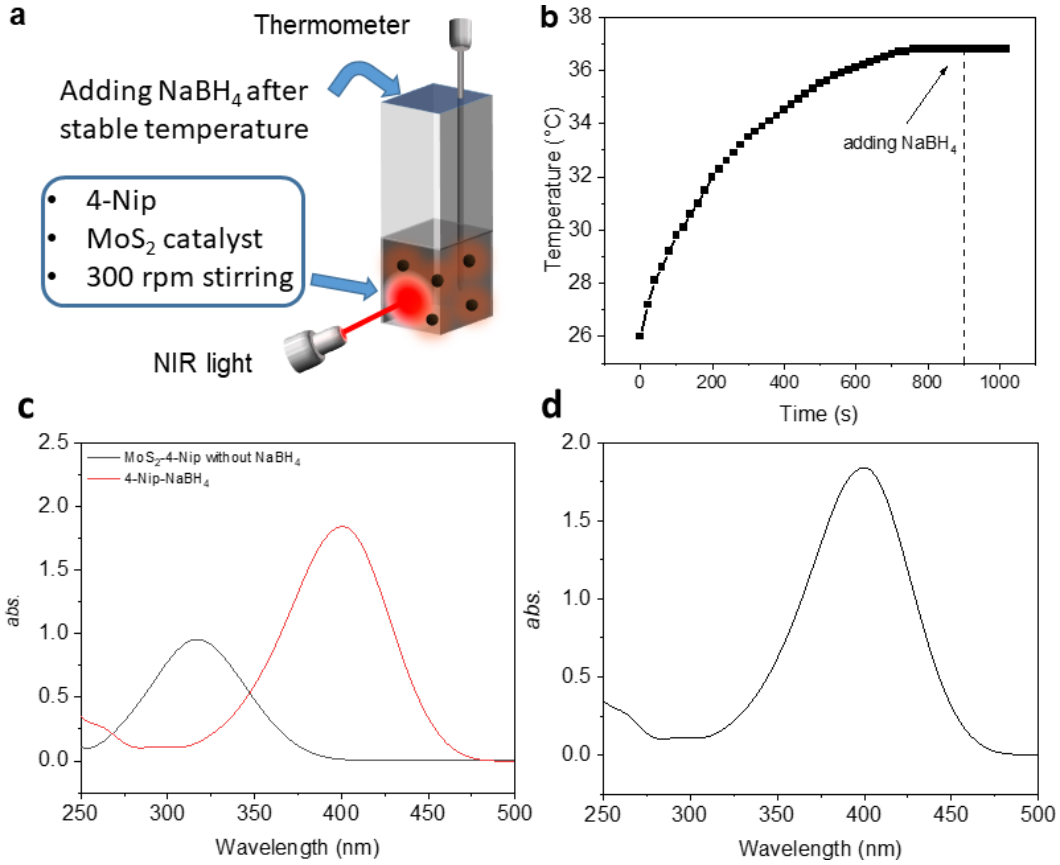

Fig. S11 (a) Schematic illustration of the catalytic reduction reaction under NIR light irradation at 0.05 mg/ml and 3 W/cm^2. (b) Photoheating curve of MoS_2-1.5 PNPs. UV-vis absorption spectra of the reaction solution (c) without $NaBH_4$ or MoS_2-1.5 PNPs, and (d) when $NaBH_4$ was replaced by NaOH (0.5 mM) after irradiation for 15 min.

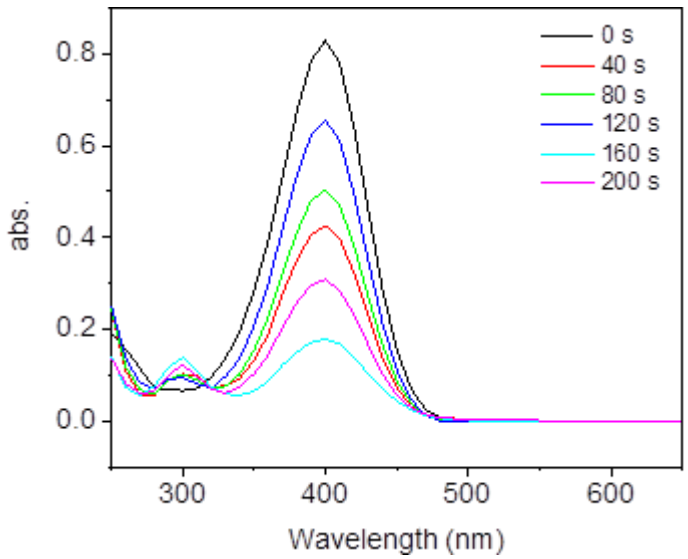

Fig. S12 UV-vis absorption spectra of the reduction of 4-Nip with MoS_2-1.5 PNPs at 0.05 mg/ml and 3 W/cm^2 within 200 s.

Table S1 Mass fraction of carbon and MoS_2 in various particles.

Sample	**MoS_2 (%)**	**Carbon (%)**
MoS_2-1 PNPs	63.3	36.7
MoS_2-1.5 PNPs	61.1	38.9
MoS_2-3 PNPs	69.2	30.8

Table S2 Specific surface area of various MoS_2 PNPs.

Sample	**Specific surface area(m^2/g)**
bulk MoS_2	36.3
MoS_2-1 PNPs	139.9
MoS_2-1.5 PNPs	106.6
MoS_2-3 PNPs	81.6

Table S3 Summary of k_{app} of various MoS_2 PNPs.

Content (mg/mL)	**k_{app} (s^{-1})**			
	bulk MoS_2	**MoS_2-1 PNPs**	**MoS_2-1.5 PNPs**	**MoS_2-3 PNPs**
0.04	$2.93\times10^{-3}\pm5.8\times10^{-4}$	$3.03\times10^{-3}\pm4.1\times10^{-5}$	$3.98\times10^{-3}\pm2.1\times10^{-4}$	$2.11\times10^{-3}\pm1.9\times10^{-4}$
0.06	$4.47\times10^{-3}\pm7.4\times10^{-4}$	$5.41\times10^{-3}\pm7.4\times10^{-4}$	$7.55\times10^{-3}\pm7.4\times10^{-4}$	$3.26\times10^{-3}\pm7.7\times10^{-4}$
0.08	$4.74\times10^{-3}\pm5.8\times10^{-4}$	$8.05\times10^{-3}\pm1.6\times10^{-4}$	$10.74\times10^{-3}\pm1.6\times10^{-4}$	$6.34\times10^{-3}\pm4.3\times10^{-4}$
0.1	$7.67\times10^{-3}\pm2.1\times10^{-4}$	$9.97\times10^{-3}\pm5.6\times10^{-4}$	$12.31\times10^{-3}\pm5.6\times10^{-4}$	$6.95\times10^{-3}\pm1.7\times10^{-4}$

Table S4 Summary of k_{app} of MoS_2-1.5 PNPs in the presence/absence of NIR light illumination.

1/T (K^{-1})	**k_{app} without NIR light (s^{-1})**	**1/T (K^{-1})**	**k_{app} with NIR light (s^{-1})**
0.00333	$4.43\times10^{-3}\pm2.31\times10^{-4}$	0.00332	$5.96\times10^{-3}\pm2.66\times10^{-4}$
0.00330	$5.11\times10^{-3}\pm2.03\times10^{-4}$	0.00328	$7.65\times10^{-3}\pm2.57\times10^{-4}$
0.00327	$5.43\times10^{-3}\pm6.02\times10^{-4}$	0.00326	$7.68\times10^{-3}\pm3.38\times10^{-4}$
0.00325	$6.66\times10^{-3}\pm3.61\times10^{-4}$	0.00323	$8.54\times10^{-3}\pm3.58\times10^{-4}$
0.00321	$7.66\times10^{-3}\pm2.04\times10^{-4}$	0.00320	$9.94\times10^{-3}\pm5.52\times10^{-4}$

Nanoscale

Accepted Manuscript

This article can be cited before page numbers have been issued, to do this please use: X. Pan, R. Liu, Z. Yu, B. Haas, Z. Kochovski, R. M. Sarhan, S. Cao, G. Chen and Y. Lu, *Nanoscale*, 2023, DOI: 10.1039/D3NR02607H.

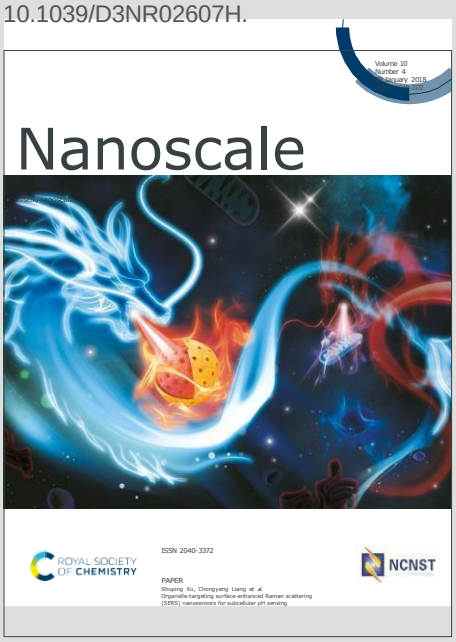

View Article Online
DOI: 10.1039/D3NR02607H

ARTICLE

Multi-functionalized carbon nanotubes towards green fabrication of heterogeneous catalyst platforms with enhanced catalytic properties under NIR light irradiation

Received 00th January 20xx,
Accepted 00th January 20xx

DOI: 10.1039/x0xx00000x

Xuefeng Pan[a,d†], Rongying Liu[b†], Zhilong Yu[a], Benedikt Haas[c], Zdravko Kochovski[a], Sijia Cao[a,d], Radwan M. Sarhan[a], Guosong Chen[b]*, and Yan Lu[a,d]*

Metal/carbon nanotubes (CNTs) have been attractive hybrid systems due to their high specific surface area and exceptional catalytic activity, but the challenging synthesis and dispersion impede their extensive applications. Herein, we report a facile and green approach towards the fabrication of metal/CNTs composites, which utilizes versatile glycopeptide (GP) both as stabilizer for CNTs in water and as reducing agent for noble metal ions. The abundant hydrogen bonds in GP bestow the formed GP-CNTs with excellent plasticity, enabling the availability of polymorphic CNTs species from dispersion to viscous paste, gel, and even to dough by increasing their concentration. The GP molecules can reduce metal precursors at room temperature without additional reducing agents, enabling the *in situ* immobilization of metal nanoparticles (*e.g.* Au, Ag, Pt, and Pd) on the CNTs surface. The combination of excellent catalytic property of Pd particles with photothermal conversion capability of CNTs makes the Pd/CNTs composite a promising catalyst for fast degradation of organic pollutants, as demonstrated by a model catalytic reaction using 4-nitrophenol (4-NP). The conversion of 4-NP using the Pd/CNTs composite as the catalyst has increased by 1.6-fold under near infrared light illumination, benefiting from the strong light-to-heat conversion effect of CNTs. Our proposed strategy opens a new avenue for the synthesis of CNTs composite as a sustainable and versatile catalyst platform.

Introduction

Metal functionalized carbon nanotubes (CNTs) composites have been proven as excellent heterogeneous catalytic platforms for various reactions, such as hydrogenation, oxidation, and reduction reactions, due to the integral merits from the intrinsic high specific surface area of CNTs and catalytically active metal nanoparticles (NPs).[1-4] Rational design of stable and highly active metal/CNTs hybrid catalysts has become one of the most prevailing works today. Generally, three critical steps are involved in the fabrication of metal/CNTs composites, including effective dispersion of CNTs, reduction/stabilization of metal NPs, and immobilization of metal NPs on the CNTs. The strong Van der Waals interactions inherent to CNTs result in their super high propensity to form aggregated bundles in a variety of solvents, particularly in water.[5-8] Therefore, a pivotal prerequisite for the production of metal/CNTs is to disperse bulk CNTs *via* a feasible strategy.[9] The most frequently reported strategy for spatially disassembling the CNTs bundles is to oxidize CNTs with strong acids, thus chemically etching the inherently hydrophobic CNTs towards the introduction of some hydrophilic oxygen-based functional moieties (*e.g.* carboxylic, hydroxyl, and phenolic groups) on their surface.[10-12] However, the daunting manipulation of the number and type of functional groups still hinders the controllable fabrication of CNTs-based composites.[13] In addition, irreversible damage to the aromatic rings of CNTs caused by harsh chemical modification usually impairs their intrinsic conductivity and catalytic activity. Moreover, the use of strong acids in these strategies is not environmentally friendly. Therefore, it is essential to develop a sustainable and eco-friendly approach towards simultaneously dispersing CNTs and preserving their structural integrity.

Alternatively, non-covalent physical modification using amphiphilic surfactants, polymers, or biomolecules such as DNA and proteins has been demonstrated to be effective not only in dispersing CNTs in aqueous solution but also in maintaining their structure intact.[14-18] In such a scenario, the hydrophobic moieties tend to attach to the surface of CNTs *via* hydrophobic interactions, while the hydrophilic ones are inclined to actively interact with water molecules, thus efficiently stabilizing CNTs in water.[17] Nevertheless, the use of wrapped polymers or surfactants may lead to toxicity, non-degradability, and arduous elimination from CNTs dispersion, consequently posing

[a] *Department for Electrochemical Energy Storage, Helmholtz-Zentrum Berlin für Materialien und Energie, Hahn-Meitner-Platz 1, 14109 Berlin, Germany*
[b] *The State Key Laboratory of Molecular Engineering of Polymers and Department of Macromolecular Science, Fudan University, Shanghai 200433, China*
[c] *Department of Physics & IRIS Adlershof, Humboldt-Universität zu Berlin, Newtonstr. 15, 12489 Berlin, Germany*
[d] *Institute of Chemistry, University of Potsdam, Karl-Liebknecht-Str. 24-25, 14476 Potsdam, Germany*

† *These two authors contribute equally to this manuscript.*

Electronic Supplementary Information (ESI) available: [details of any supplementary information available should be included here]. See DOI: 10.1039/x0xx00000x

View Article Online
DOI: 10.1039/D3NR02607H

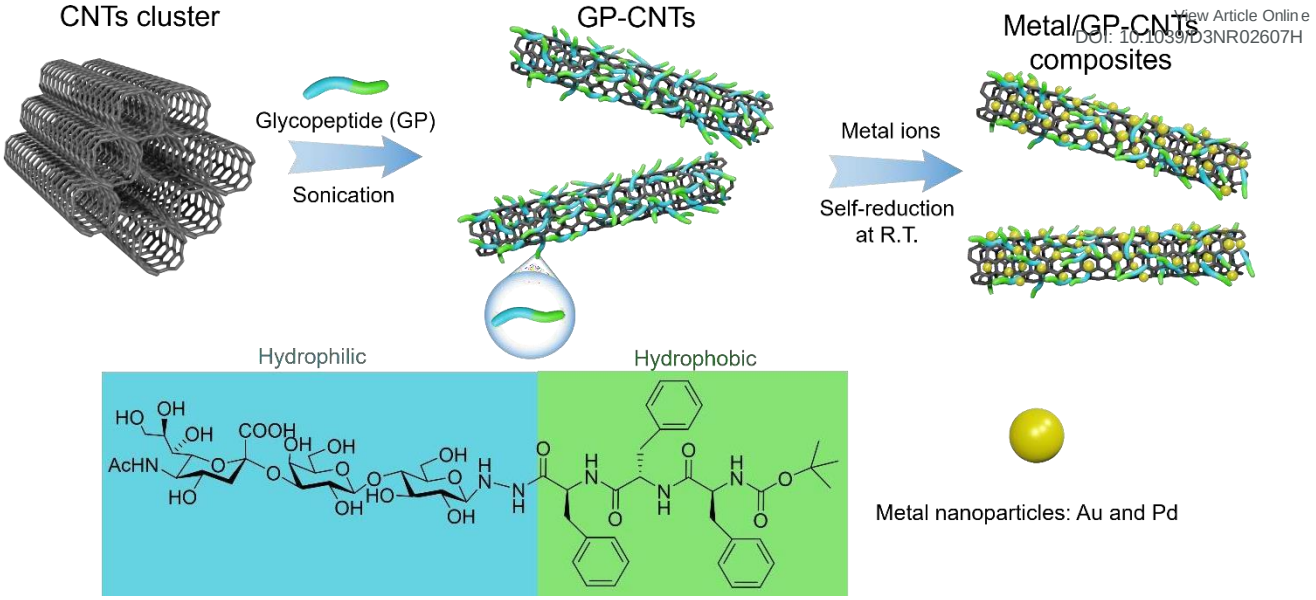

Scheme 1. Synthetic strategy of GP-CNTs and their functionalization with metal particles.

environmental sustainability and green chemistry concerns. Moreover, the intrinsic polydispersity and mono-functionality of naturally occurring biomolecules limit their wide application in such area. Therefore, environment-friendly and versatile dispersants are in great demand for the functionalization of CNTs.

When it comes to the reduction, stabilization, and immobilization of metal NPs on CNTs, direct reduction of metal precursor ions by reducing agents (*e.g.* sodium borohydride – $NaBH_4$) *via* wet chemistry often involves toxic chemicals or additional heating.[2, 19] Meanwhile, amphiphilic surfactants or polymers are commonly employed to control the formation/growth of metal NPs and improve their colloidal stability. Subsequent binding agents are also necessary to immobilize metal NPs on the surface of CNTs, potentially causing additional energy consumption and environmental pollution.[20] Conventional synthetic protocols such as hydrothermal, electrochemical deposition, or plasma reduction methods are either time-consuming or equipment- demanding.[21-24] Therefore, the development of a novel strategy that could integrally perform these abovementioned three critical steps in a green and sustainable fashion will be essential for the advance of CNTs-based heterogeneous catalysis.

In this work, we prepared an amphiphilic glycopeptide (GP) biomolecule composed of a hydrophilic trisaccharide and a hydrophobic triphenylalanine to efficiently disperse CNTs in aqueous solution (Scheme 1). Furthermore, the GP molecules on CNTs surface could capture various metal ions and subsequently reduce them into catalytic metal NPs at room temperature. The obtained metal NPs were simultaneously stabilized and immobilized on CNTs by the GP molecules, enabling the green fabrication of heterogeneous catalytic platforms. Unexpectedly, the introduction of GP molecules also significantly enhances the plasticity of CNTs and thus provides access to the rational construction of various CNTs entities with enhanced processability from paste to gel, and even dough by increasing their concentration. Besides, the hydroxyl groups of GP molecules endow the CNTs template with an excellent capability to accommodate a wide range of noble metal NPs *e.g.* gold (Au), silver (Ag), and palladium (Pd) on their surface under mild conditions. Eventually, the catalytic potential of the fabricated heterogeneous platforms also has been demonstrated *via* degradation of a typical organic pollutant, 4- nitrophenol (4-NP), in water with the assistance of near-infrared (NIR) light irradiation. The method here opens a new avenue to multi-functionalizing CNTs towards the fabrication of heterogeneous catalytic systems through a green approach.

Results and discussion

GP-stabilized CNTs dispersion

Considering the aromatic scaffold nature of hydrophobic CNTs, amphiphilic molecules containing aromatic groups appear to be ideal dispersant candidates to effectively adhere to the surface of CNTs and thus disperse them in water *via* aromatic-aromatic interactions between amphiphilic molecules and CNTs. Herein, we prepared an amphiphilic glycopeptide (GP) molecule comprising a hydrophilic moiety (*i.e.* a trisaccharide with carboxyl and hydroxyl groups) and a hydrophobic part (*i.e.* three phenylalanine) to disperse CNTs in water. The GP molecule was synthesized according to the methods reported in our previous study.[25, 26] As an initial test, we directly dispersed the as- purchased multi-wall CNTs (MWCNTs) powders (*i.e.* pristine CNTs cluster, 1 mg) with amphiphilic GP molecules (1 mg) in water (1 mL). A homogenous CNTs dispersion was obtained after simple treatment with sonication and centrifugation (Fig. 1a). A thin layer of GP molecules (~2 nm) was found to be wrapped on the surface of CNTs *via* high-resolution

View Online
10.1039/C3NR02607H

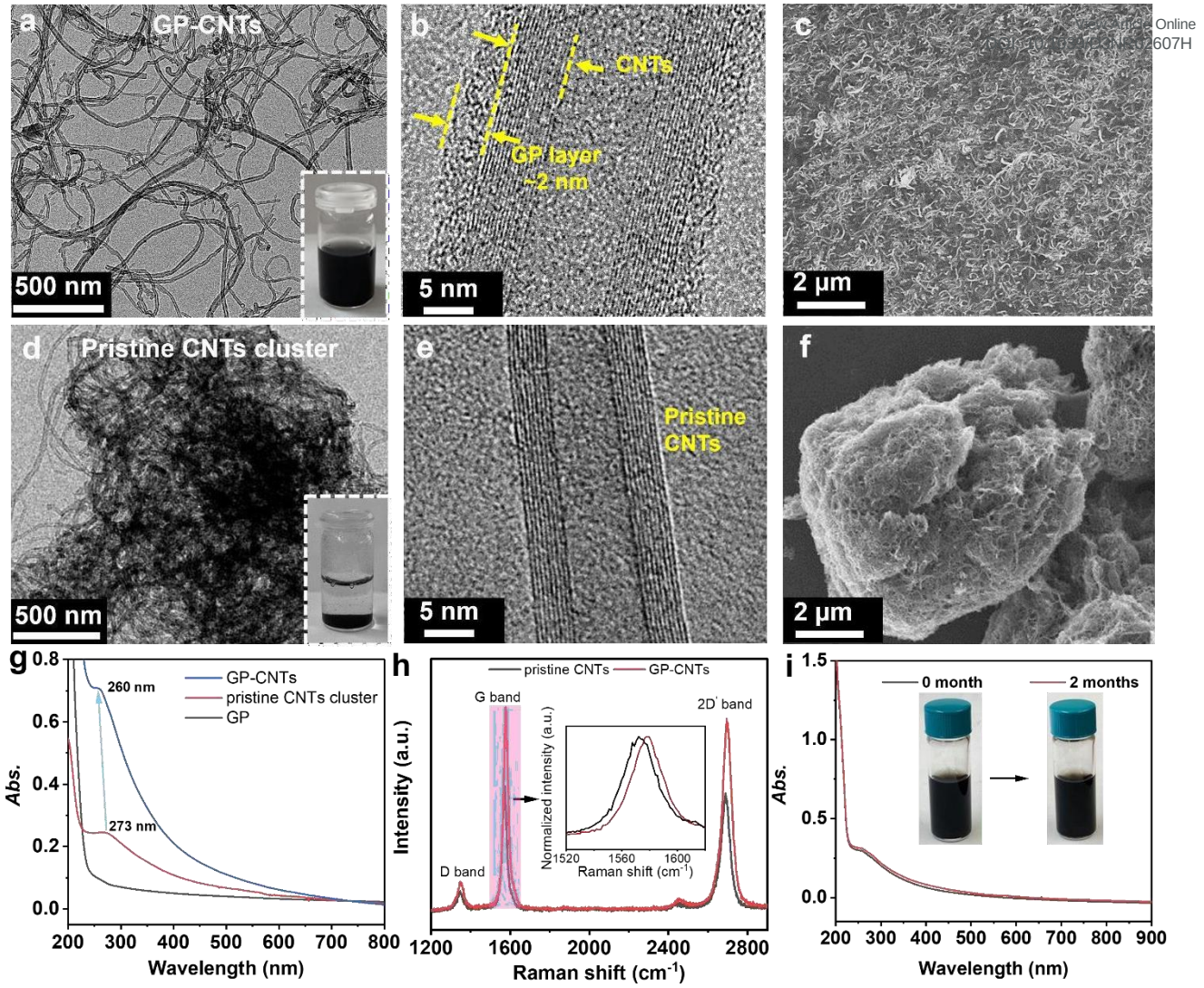

Fig. 1. (a, b) TEM and (c) SEM images of the GP-CNTs dispersion. (d, e) TEM and (f) SEM images of the pristine CNTs cluster dispersion. The insets in (a, d) are corresponding photos of the CNTs dispersions. (g) UV-Vis absorption spectra of the CNTs cluster, GP, and GP-CNTs dispersion. (h) Raman spectroscopy of the CNTs cluster and GP-CNTs powder after freeze-drying. (i) UV-Vis absorption spectra of the GP-CNTs dispersion at 0.01 mg/mL and their corresponding photos (inset) before and after static storage for 2 months.

transmission electron microscopy (HRTEM), as shown in Fig. 1b. The aromatic phenylalanine moieties of GP molecules are expected to attach to the surface of CNTs *via* hydrophobic interactions, while the hydrophilic moieties head to the water phase. The presence of carboxyl groups on the head of hydrophilic moieties gives rise to strong electrostatic repulsions among CNTs, thus leading to a homogenous and stable dispersion of CNTs. As spotted by scanning electron microscopy (SEM), a uniform CNTs layer was also achieved by simply drop- casting the GP-CNTs dispersion on a silicon wafer and followed by drying under ambient conditions, while the pristine CNTs clusters merely showed large aggregates (Fig. 1c, 1f, and S2). Cryogenic TEM (cryo-TEM) was employed to *in situ* monitor the native dispersion state of GP-CNTs. The outcome displayed that, in the presence of GP molecules, the CNTs could be well-dispersed in water without appreciable aggregation, verifying their excellent dispersibility of CNTs enabled by amphiphilic GP molecules (Fig. S3). On the contrary, in the absence of GP molecules, the pristine CNTs sample was found to quickly aggregate and precipitate within a few seconds (Fig. 1d and e). In addition to MWCNTs, single-wall CNTs (SWCNTs) could be also well-dispersed in water with the aid of GP molecules (Fig. S4). It is worth mentioning that MWCNTs are much more affordable and available compared with SWCNTs, we thereby chose MWCNTs as the model material for practical applications in the subsequent parts of this research.

It has been reported that the uniform dispersion of bundled CNTs will lead to a blue shift in resonant absorption peaks due to the weakened electronic coupling effects among the CNTs framework.[6, 9] Accordingly, an appreciable blue shift in maximum from 273 nm for pristine CNTs to 260 nm for GP-CNTs in their UV-Vis absorption spectra further confirmed the

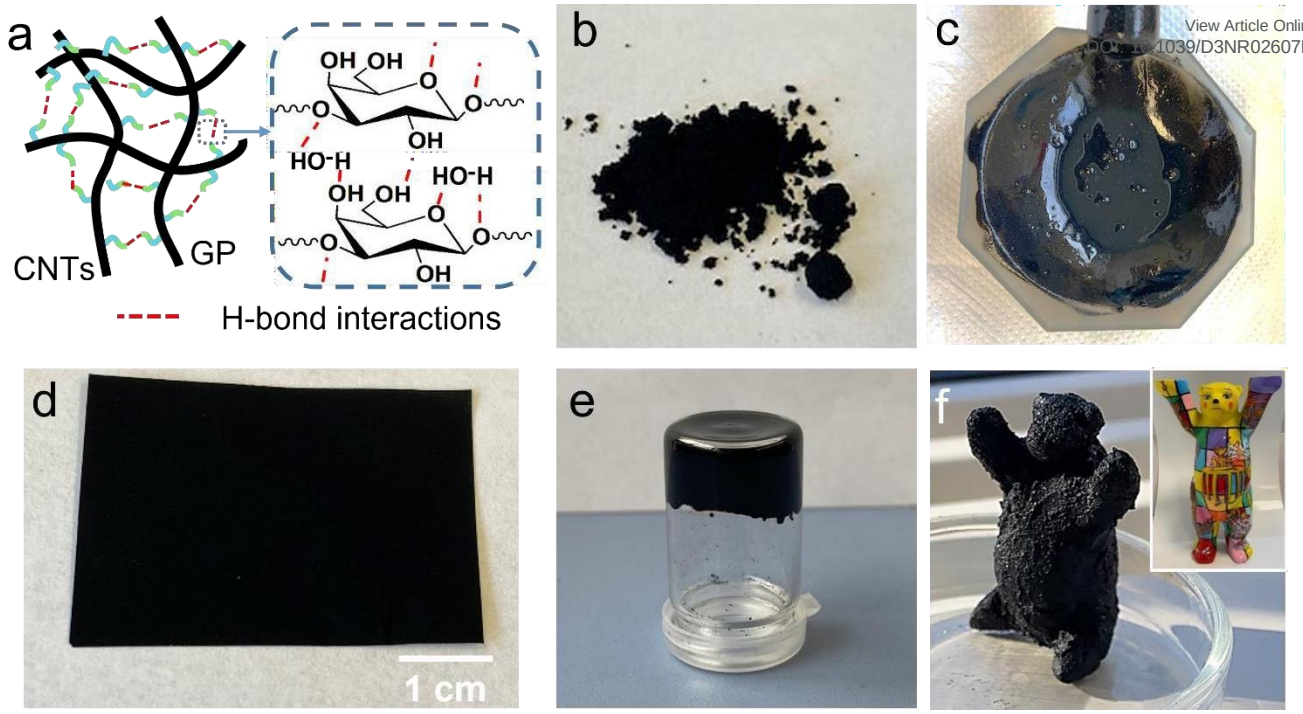

Fig. 2. (a) Scheme of the formation of processable GP-CNTs. Photos of pristine CNTs powder (b) and high concentrated GP-CNTs in various states: (c, d) paste (~5 mg/mL), (e) gel (~70 mg/mL), and (f) playdough (~200 mg/mL) of handmade "United Buddy Bear" model with an inset of its corresponding real landmark.

uniform distribution of CNTs (Fig. 1g). Note that the higher absorption intensity of GP-CNTs compared to the pristine CNTs cluster also revealed the superior dispersibility of GP- functionalized CNTs in water.[27]

To further investigate the electronic interaction between CNTs and GP molecules, both pristine CNTs cluster and GP-CNTs in the solid state were investigated by Raman spectroscopy. As shown in Fig. 1h, three distinct peaks were found in both samples at 1340, 1572, and 2696 cm^{-1}, which respectively refer to D-band, G-band, and 2D band of MWCNTs. The intensity ratio of D-band (I_D) at 1340 cm^{-1} to G-band (I_G) at 1572 cm^{-1} is usually used as an indicator for the evaluation of defect amount in CNTs. In the current study, the I_D/I_G of the pristine CNTs cluster and the GP-CNTs showed a comparable value of 0.18 and 0.16, respectively, confirming that the aromatic-aromatic interaction between GP molecules and CNTs does not introduce defects on the sidewall of CNTs, *i.e.* damage to their surface. This finding confirms that the introduction of GP molecules maintains the structural integrity of CNTs, in contrast to the traditional chemical oxidation strategy.[28, 29] As shown in the normalized Raman spectra (the inset in Fig. 1h), the red shift from 1572 cm^{-1} for the pristine CNTs to 1578 cm^{-1} for the GP-CNTs in the G band verified the occurrence of charge transfer between three aromatic phenylalanine residues of GP molecules and CNTs sidewalls *via* π-π stacking, which will decrease the electron density of CNTs. In addition, the apparent charge transfer observed here could also provide evidence for the attachment of GP molecules to the surface of CNTs.[30, 31] Overall, we conclude that the strong π-π stacking interaction between CNTs and GP leads to the attachment of GP molecules to CNTs and thus enabled the superior dispersion of CNTs in water.

The colloidal stability of the CNTs dispersion is vital for practical applications. Hence, we evaluated the stability of the resulting GP-CNTs dispersion against aggregation by storing them statically for 2 months under ambient conditions. The result showed that 2 months of storage did not cause any obvious bundling behaviors of GP-CNTs (inset in Fig. 1i). Besides, similar UV-Vis absorption profiles shared by the GP-CNTs dispersion before and after storage verified their long-term stability (Fig. 1i). The HRTEM analysis showed that even after 2 months of storage, a distinct thin layer of GP molecules was still found firmly attached to the surface of CNTs (Fig. S5), accounting for the long-term stability of the GP-CNTs dispersion. The good colloidal stability of GP-CNTs could be ascribed from the electrostatically repulsive interaction owing to the deprotonation of carboxyl groups among GP-CNTs. As such, we attempted to manipulate the electrostatically repulsive interaction among GP-CNTs by varying the pH value of the GP- CNTs dispersion. The pH of the GP-CNTs dispersion was modulated from an initial value of *ca.* 6.5 to 5 and 10 by adding hydrochloride acid (HCl) and sodium hydroxide (NaOH), respectively. Isolated CNTs in GP-CNTs dispersion progressively agglomerated overnight at pH of 5, while no obvious change was found for the dispersion at pH of 10 (Fig. S6). Adding HCl in the GP-CNT dispersion is likely to weaken the deprotonation of the carboxyl groups in the GP molecules, thus decreasing the electrostatic repulsion between neighboring GP molecules.[25] Overall, owing to the functionalization with amphiphilic GP

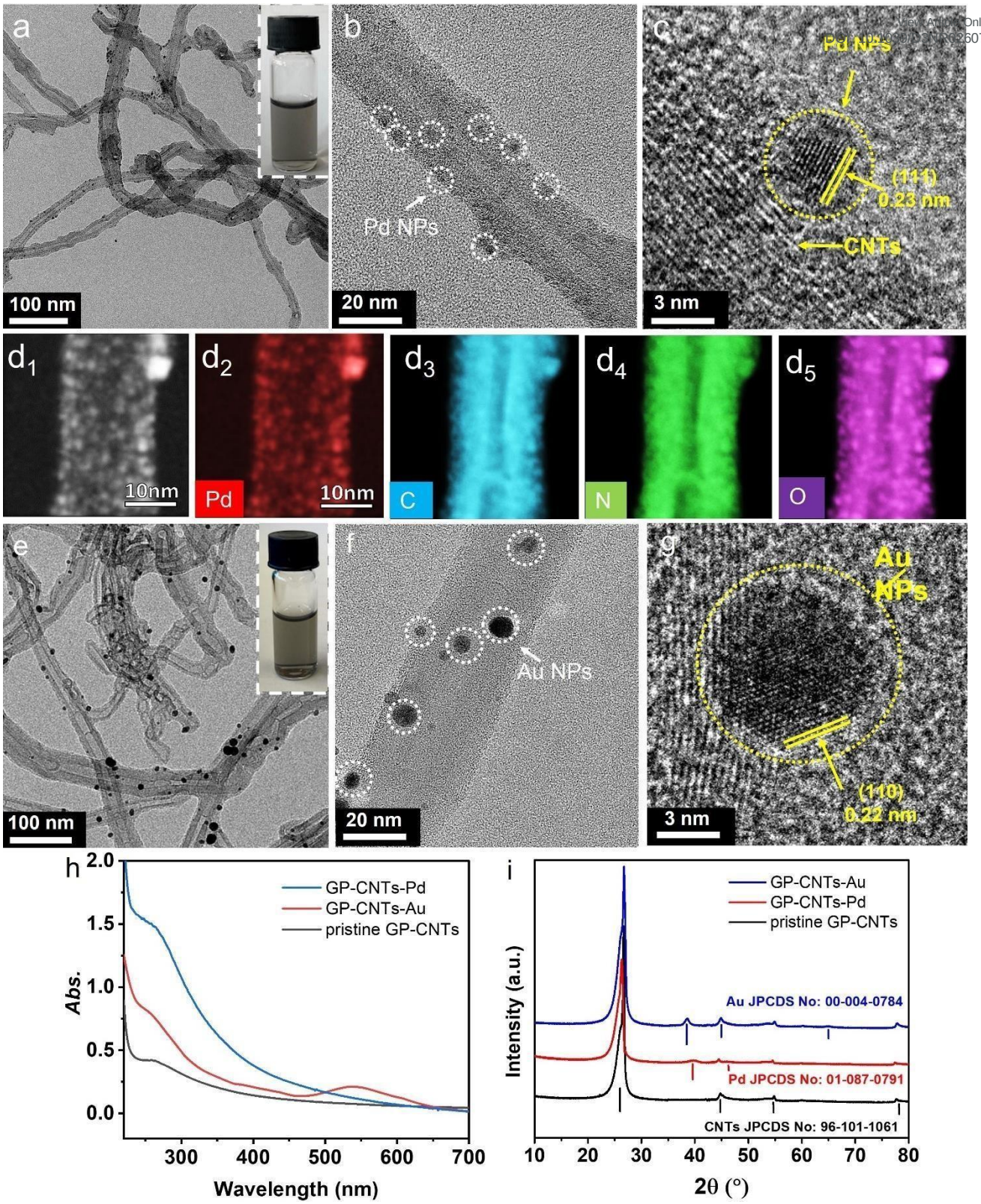

Fig. 3. (a-c) TEM and (d_1) HAADF-STEM images of GP-CNTs-Pd. (d_2-d_5) The corresponding STEM-EELS maps (same scale bar) of various chemical elements in the GP-CNTs-Pd composite. TEM images (e-g) of the GP-CNTs-Au composite. The insets in (a, e) are corresponding photos of the metal/CNTs dispersions. (h) UV-Vis absorption spectra of the pristine GP-CNTs, GP-CNTs-Pd, and GP-CNTs-Au dispersion. (i) XRD patterns of the pristine GP-CNTs, GP-CNTs-Au, and GP-CNTs-Pd powder after freeze-drying.

molecules, CNTs exhibit outstanding colloidal stability in water phase.

At a low concentration of GP-CNTs in water, the electrostatic repulsion among the GP molecules wrapped on the CNTs

surface primarily governs the stable and uniform dispersion of GP-CNTs. However, at high concentrations, another type of non-covalent interaction, namely hydrogen bonding, will begin to replace the role of electrostatic repulsion. This transition occurs because the distance between GP and surrounding CNTs is dramatically decreased when the concentration of GP-CNTs increases, leading to a significant intensification of the inter-CNTs saccharide hydrogen bonds. Besides, it might be conceivable that the available inter-CNTs saccharide hydrogen bonds will confer excellent plasticity upon the GP-CNTs (Fig. 2a). Herein, as a step forward to explore its plasticity, we further increased the GP-CNTs concentration (~5 to 200 mg/mL) in water with simple sonication and/or grinding carefully in a mortar. Interestingly, a paste, gel, and dough state was continuously achieved from powder (Fig. 2b-f). Note that better dispersion of GP-CNTs in various states can be achieved by concentrating the diluted dispersion through centrifugation. When increasing the GP-CNTs concentration up to ~5 mg/mL, a viscous paste was obtained (Fig. 2c), which can be further spread on an aluminum foil to form a uniform thin film (Fig. 2d). The GP-CNTs film could still show a good dispersion state without obvious aggregation (Fig. S7). A drastic increase in GP- CNTs concentration up to ~70 mg/mL led to a self-standing gel (Fig. 2e). Once its concentration was finally elevated up to ~200 mg/mL, a playdough-like CNTs was produced. To demonstrate its superior processing capability, a typical landmark of Berlin (*e.g.* United Buddy Bear here) model was directly crafted by hand (Fig. 2f). The outstanding plasticity and shaping capability of versatile GP-CNTs materials experimentally demonstrated the enhanced processibility of such GP-CNTs, owing to the abundant inter-CNTs saccharide hydrogen bonds. Beyond the conventional approaches that rely on either toxic organic solvents (surfactants) or inevitable surface modifications, the use of eco-friendly and biocompatible GP molecules offers a promising alternative for wide and green applications of pristine CNTs.[6, 7, 32]

GP-enabled *in situ* generation of metal NPs on CNTs

Considering numerous hydroxyl groups in the GP molecules, we subsequently employed the GP-CNTs as a versatile template for the preparation of metal/CNTs composites, where GP molecules could functionalize CNTs with metal NPs (*i.e.* Pd, Ag, and Au) through an *in situ* reducing and stabilizing strategy. Thus, the corresponding metal/GP-CNTs composites (*i.e.* GP- CNTs-Pd, GP-CNTs-Au, GP-CNTs-Pt, and GP-CNTs-Ag) could be simply obtained under mild stirring at room temperature. Taking Pd as an example, $PdCl_2$ was used as the metal precursor and directly added into the GP-CNTs dispersion without any external reducing agents. Positive Pd^{2+} ions were electrostatically captured by the negative carboxyl group in GP. As a result, the Pd NPs were *in situ* reduced by GP and subsequently stably anchored on the surface of CNTs, as revealed in the TEM and SEM images (Fig. 3a-b and S8). As spotted in the photo (inset in Fig. 3a), a uniform GP-CNTs-Pd dispersion was achieved, demonstrating good stability even after functionalization with metal NPs. Moreover, no obvious change was observed in the TEM images of the composites after storing for one month, demonstrating good stability (Fig. S9). The lattice spacing was determined from its corresponding HRTEM image to be 0.23 nm, which matches well with the (111) plane of the Pd crystal (Fig. 3c). The obtained Pd NPs show an ultra-small size of 1.8 ± 0.4 nm (Fig. S10). The tiny Pd particles and their distributions on CNTs were confirmed by high-angle annular dark-field scanning transmission electron microscopy (HAADF-STEM) and corresponding electron energy loss spectroscopy (EELS), as shown in Fig. 3d. The HAADF-STEM image revealed a dense decoration of small Pd NPs on the CNTs surface (Fig. $3d_1$). The presence of Pd was further confirmed through EELS-STEM analysis (Fig. $3d_2$). As the STEM data is a projection through the sample, the seemingly higher density of Pd NPs at the borders of the GP-CNTs are consistent with those located on the surface of GP-CNTs. Additionally, the C, N, and O species exhibited a homogenous distribution in the GP-CNTs-Pd composite (Fig. $3d_{3\text{-}5}$). A distinct hollow core was observed in all the C, N, and O maps, suggesting the successful incorporation of GP molecules and Pd NPs on outer surface of CNTs. X-ray photoelectron spectroscopy (XPS) was used to study the oxidation state of Pd NPs in the GP-CNTs-Pd composite. The raw and fitted Pd 3d spectra demonstrated the presence of a mixture of Pd^0 and Pd^{2+} (Fig. S11). The Pd $3d_{5/2}$ peak at 335.7 eV and Pd $3d_{3/2}$ peak at 340.9 eV correspond to metallic Pd^0. In addition, the shoulder peaks at 337.7 and 342.9 eV are assigned to Pd^{2+}, primarily indicating the presence of oxidized Pd (PdO) on the surface of Pd NPs.[33] The PdO species are mainly resulted from the exposure to air during the sample preparation. Smaller Pd NPs show higher specific surface area, indicating more exposed Pd atoms that are easily to be oxidized.

Compared with Pd NPs, the obtained Au NPs on CNTs were relatively larger, with an average size of 5.6 ± 1.3 nm (Fig. 3e-g, S10). The lattice spacing of 0.22 nm corresponds to the (110) planes of the Au NPs (Fig. 3g).[34] The size of Au NPs on the GP- CNTs has been tuned by varying the GP concentration, $HAuCl_4$ concentration, as well as reaction temperature (Fig. S12). First of all, keeping the Au precursor concentration constant, the particle size of Au NPs slightly increased (~4 to 5 nm) when increasing the GP concentration from 0.02 to 0.05 mg/mL. Further increase of the GP concentration to 0.1 mg/mL would lead to the formation of inhomogeneous Au NPs with various morphologies, as indicated with red circles in Fig. S12a-c. Secondly, when keeping the GP concentration constant, no obvious change in the particle size has been observed by increasing the concentration of Au precursor from 0.05 to 0.15 mM, but the number of the Au NPs deposited on the CNTs surface is significantly increased (Fig. S12b and d). Further increase of the Au precursor concentration to 0.3 mM results in the sharp increase of the particle size from 5 to 23 nm, with irregular shape and broad size distribution, as indicated in Fig. S12e. Finally, elevating the reaction temperature from room temperature to 40 ℃ leads to the formation of irregular morphology and huge aggregates of Au NPs (Fig. S12f). Therefore, we just focused on the sample (Fig. S12b) prepared with 0.05 mg/mL of GP and 0.15 mM of $HAuCl_4$ at room temperature for the following catalysis study.

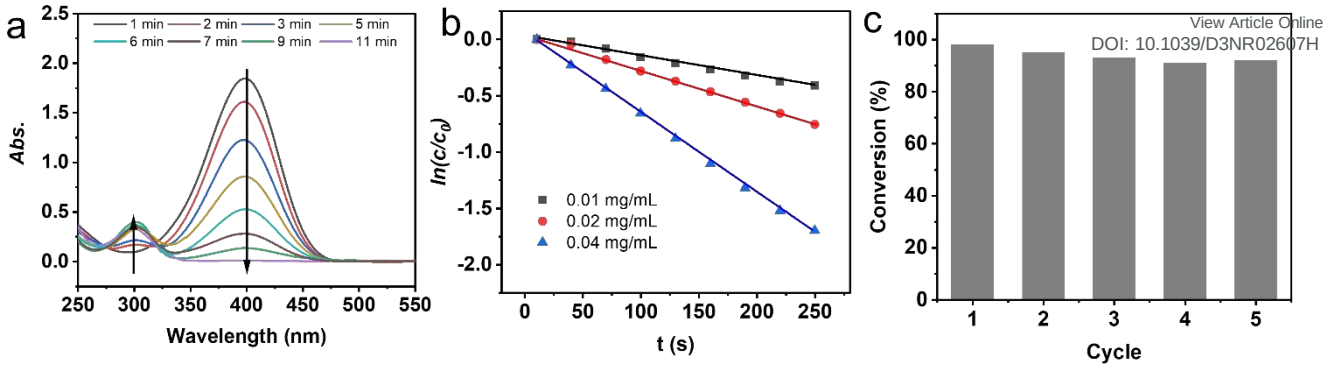

View Article Online
DOI: 10.1039/D3NR02607H

Fig. 4. (a) UV-Vis absorption spectra of the reduction of 4-NP with the concentration of GP-CNTs-Pd at 0.01 mg/mL. (b) Plots of $ln(c/c_0)$ as a function of reaction time of GP-CNTs-Pd at various concentrations. (c) Catalytic cycles of GP-CNTs-Pd with the concentration of GP-CNTs-Pd at 0.01 mg/mL, 4-NP at 0.1 mM, and $NaBH_4$ at 20 mM at room temperature.

The successful incorporation of Au NPs on GP-CNTs was further confirmed by the UV-Vis absorption spectroscopy. A broad peak at *ca.* 530 nm was observed for the GP-CNTs-Au dispersion (Fig. 3h), which results from the surface plasmon resonance of Au NPs. To further confirm the presence of metal NPs, the obtained metal/GP-CNTs composites were characterized by X-ray diffraction (XRD). As shown in Fig. 3i, the distinct peaks located at 25.6, 44.7, 55.1, and 77.6° were observed for all the metal/GP-CNTs composites, which respectively refer to the (002), (100), (004), and (110) plane of the MWCNTs (JPCDS NO.
96-101-1061). Meanwhile, peaks at 38.6, 44.3, and 64.5° were observed in GP-CNTs-Au, which can be indexed to the (110), (200), and (220) plane of the face-centered cubic (*fcc*) phase of metallic Au crystal (JPCDS NO. 00-004-0784), respectively.[35] In the case of GP-CNTs-Pd, two peaks at 40.1 and 46.5° were observed, which respectively stand for the (111) and (200) reflections of the (*fcc*) metallic Pd (JPCDS NO. 05-0681).[36] Apart from Au and Pd NPs, Ag and Pt NPs can be also successfully incorporated into GP-CNTs (Fig. S13). As a proof-of-concept, the proposed method demonstrates our versatile GP-CNTs can be applied for the facile synthesis of various noble metal nanoparticles. The amount of metal loading in the metal/GP- CNTs composites was estimated from the aerobic residual in the thermogravimetric Analysis (TGA) measurement (Fig. S14). The metal loading in GP-CNTs-Au and GP-CNTs-Pd was calculated to be 13.2 and 11.5 wt.%, respectively. As control experiments, the pristine CNTs alone was found to be incapable of reducing metal ions to metallic NPs (*e.g.* Pd, Au, or Ag), as verified in Fig. S15a. By contrast, directly mixing GP molecules with Au precursor (*e.g.* $HAuCl_4$) solution in the absence of the CNTs template led to the formation of stably dispersed Au NPs, as demonstrated in Fig. S15b. These findings confirm that GP molecules indeed function as the reducing agent (and stabilizer) for the generation of metal NPs on CNTs even at room temperature. The noticeable reducibility of GP molecules for the formation of metal NPs is presumably due to their abundant hydroxyl groups in the trisaccharide moieties, which has been reported in our previous work. [37] During the reduction process, the hydroxyl groups of the GP molecules are likely to be oxidized into carboxyls by the $HAuCl_4$.[38] In brief, we demonstrated a straightforward strategy for the green synthesis of water-dispersible metal/CNTs composites enabled by amphiphilic GP molecules. Importantly, the small size of metal NPs *in situ* generated on the CNTs surface indicates a high specific surface area, which could provide sufficient active sites for efficient catalysis.

Catalytic reduction of 4-nitrophenol

Noble metal NPs are crucial catalysts for the catalytic degradation of organic pollutants in water *via* reduction or

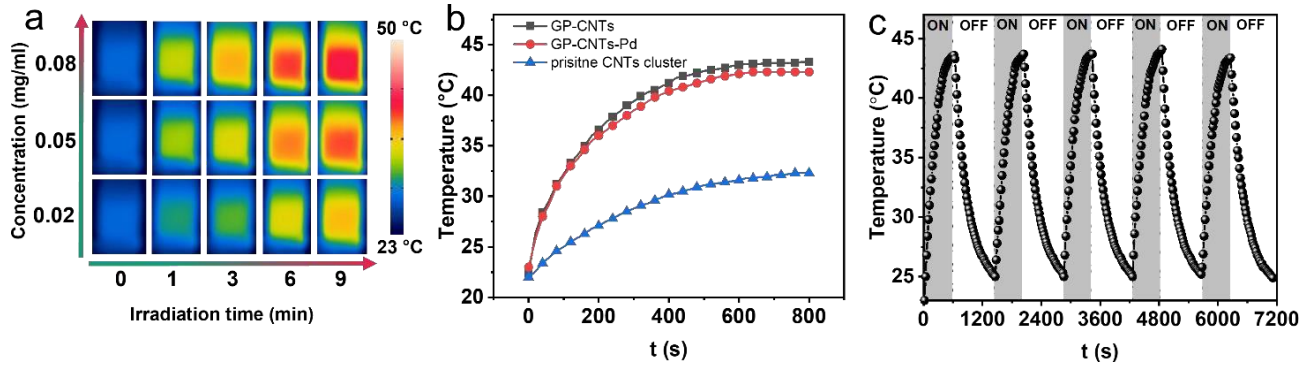

Fig. 5. (a) Time-dependent IR thermal photos of the GP-CNTs-Pd dispersion under 808 nm laser (3 W/cm^2) irradiation at various concentrations (0.02, 0.05, and 0.08 mg/mL). (b) Comparison of the photothermal heating of various dispersions at 0.08 mg/mL. (c) Heating/cooling profiles of the GP-CNTs-Pd dispersion at 0.08 mg/mL under NIR irradiation at 3 W/cm^2.

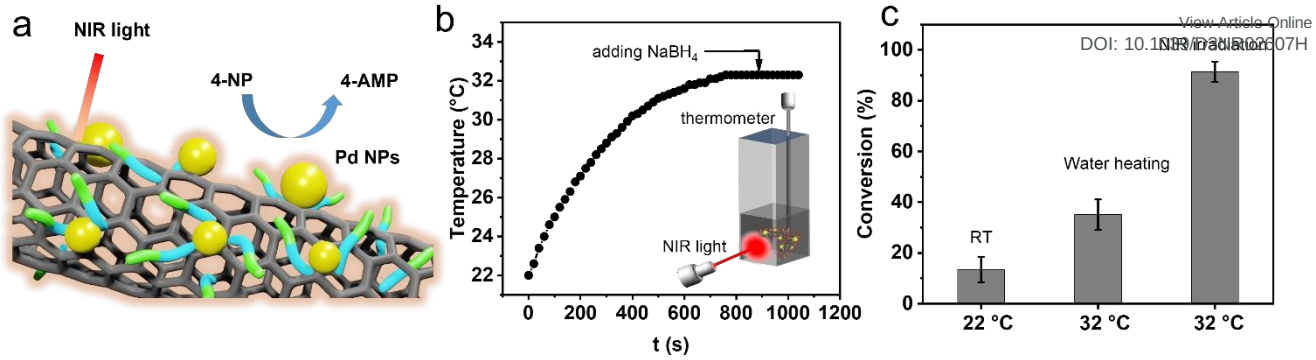

Fig. 6. (a) Scheme of the reduction reaction of 4-NP using GP-CNTs-Pd as the catalyst under NIR irradiation. (b) Temperature profile of the reactant under light irradiation. (c) Conversion comparison of reduction of 4-NP under various heating conditions in 5 min with the concentration of GP-CNTs-Pd at 0.03 mg/mL, 4-NP at 1 mM, and $NaBH_4$ at 0.2 M.

coupling reactions.[39, 40] As a typical temperature-dependent and surface reaction, the reduction of 4-nitrophenol (4-NP) to 4-aminophenol (4-AMP) in aqueous solution has been regarded as a benchmark reaction and was utilized to evaluate the catalytic performance of various catalysts.[41] Thanks to the outstanding photothermal conversion capability under near- infrared (NIR) light irradiation, CNTs have also found numerous applications including cancer therapy, bio-sensing, and photothermal-assisted catalysis.[42, 43] In this study, we used the as-prepared metal/GP-CNTs composites (GP-CNTs-Pd and GP- CNTs-Au) as the catalyst, and $NaBH_4$ as the reducing agent, to investigate their catalytic behavior in the reduction of 4-NP under NIR light irradiation.

As an initial test, catalytic performance of the GP-CNTs-Pd composite in the reduction of 4-NP without NIR light irradiation was assessed in aqueous solution. As the reaction progresses, a characteristic absorption peak at 400 nm gradually faded and disappeared due to the conversion of 4-NP, while a new peak at 290 nm came into being and progressively increased in intensity due to the generation of 4-AMP (Fig. 4a).[44] To compare the catalytic performance of various metal/CNTs composite catalysts, we fixed the same surface area of the catalytic metal (Pd in GP-CNTs-Pd and Au in GP-CNTs-Au) used for the reaction. The apparent rate constant (k_{app}) and surface area-normalized rate constant (k_1) were determined to quantitatively evaluate the reaction rate of these two catalysts (more details in Fig. S16). As a result, GP-CNTs-Pd displays a fast catalytic conversion of 4- NP, giving a much higher k_1 value of 0.062 s^{-1} m^{-2} L compared with that of GP-CNTs-Au (k_1 of 0.0081 s^{-1} m^{-2} L). Note that the as-synthesized GP-CNTs-Pd shows high rate constant among the reported Pd-based catalysts under similar reaction conditions (Table S1), demonstrating their good catalytic performance. The particle dimension and electron structure of catalytic metal particles on the surface have been reported to influence the adsorption/desorption behavior of 4-NP molecules.[45, 46] Hence, the fast conversion of 4-NP could be predominantly explained by the small size of Pd as well as its intrinsically catalytic activity when applied in the reduction of 4-NP. As reference, acid- oxidized CNTs were also used as the template for the preparation of Pd/CNTs composites (denoted as a-CNTs-Pd).[2] When used as catalyst for the reduction of 4-NP with the same concentration as GP-CNTs-Pd at 0.02 mg/mL, the a-CNTs-Pd displays a reaction conversion of 32.3 % after reaction for 10 min, which is much lower than that of the GP-CNTs-Pd (a conversion of 99.2 %) (Fig. S17). Considering that the type and number of the functional groups (hydroxyl or carboxyl groups) on the CNTs surface from strong acid oxidation are not very controllable, this may cause the inhomogeneous distribution and propensity of aggregation of the Pd NPs on CNTs. These factors will lead to the relatively lower catalytic activity of the a- CNTs-Pd. Based on these findings, GP-CNTs-Pd was utilized in the subsequent measurements. It is found that an increase in the concentration of the GP-CNTs-Pd catalyst from 0.01 to 0.04 mg/mL led to the k_{app} elevating from 1.81×10^{-3} to 7.21×10^{-3} s^{-1} (Fig. 4b). Moreover, GP-CNTs-Pd still presented a high conversion above 90 % even after 5 consecutively catalytic cycles, demonstrating their excellent catalytic stability (Fig. 4c). No visible change in the morphology of GP-CNTs-Pd was found after the catalytic cycles, confirming its good structural stability (Fig. S18a). As control experiments, no conversion of 4-NP was observed when only pristine GP-CNTs-Pd or GP molecules were used in the absence of $NaBH_4$, revealing that neither GP molecules nor CNTs alone can reduce 4-NP into 4-AMP (Fig. S18b).

Next, we tested the photothermal conversion of the as-prepared GP-CNTs-Pd dispersion in a quartz cuvette under NIR light irradiation (wavelength of 808 nm, 3 W/cm^2). As visualized by an IR camera, the temperature of the GP-CNTs-Pd dispersion increased with the irradiation time and concentration of the GP-CNTs-Pd dispersion (Fig. 5a). To precisely track the temperature rise of GP-CNTs-Pd under NIR irradiation, the temperature of the dispersion was further measured and confirmed by a digital thermometer. Notably, the temperature of the GP-CNTs-Pd dispersion with the concentration of 0.08 mg/mL increased by *ca.* 23 ℃ after irradiation for 15 min (Fig. S19). By comparison, pure water merely displayed a temperature change of *ca.* 5 ℃ under the same light intensity, indicating the negligible photothermal conversion effect of water alone. In addition, the photothermal performance of GP-CNTs and pristine CNTs cluster was also evaluated under the same conditions (*e.g.* concentration, laser power, and irradiation time). GP-CNTs showed a similar temperature variation with GP-CNTs-Pd, while

the pristine CNTs cluster only showed a mild temperature increase by *ca.* 8 ℃ (Fig. 5b). The photothermal conversion efficiency (η) of the GP-CNTs dispersion was calculated to be 22.3 %, which is higher than that of the pristine CNTs cluster dispersion (4.2 %), as shown in Fig. S20. As mentioned above, the pristine CNTs tend to form big aggregates in water owing to the inherent hydrophobicity. In such scenario, only little surface area can be exposed for the light harvest. The majority of incident light will just pass through the water molecules. As comparison, the NIR light can be efficiently captured by the GP- CNTs owing to a high exposed surface area. In addition, better dispersity of the GP-CNTs improves the water diffusion, thus enhances the heat transport from the surface of CNTs to the surrounding solution. Overall, the GP-modified CNTs show better photothermal conversion performance than that of the pristine CNTs. Also, the loading of the small size of Pd NPs exerts no influence on their photothermal heating activities. Furthermore, GP-CNTs-Pd displayed superior photothermal stability, as revealed by its negligible reduction in its photothermal conversion performance after 5 consecutive ON-OFF laser cycles (Fig. 5c).

To take advantage of the photothermal conversion effect of GP-CNTs-Pd, we further explored its catalytic performance under NIR light irradiation (Fig. 6a). To reach an equilibrium temperature (32 ℃), the GP-CNTs-Pd dispersion was first continuously stirred under NIR light irradiation (3 W/cm^2) for 15 min prior to the reaction, *i.e.* in the absence of $NaBH_4$. The UV-Vis absorption spectrum showed no 4-NP conversion on this occasion (Fig. S21), indicating that the NIR light irradiation alone does not affect the reduction process of 4-NP. Afterwards, a fresh $NaBH_4$ solution was rapidly injected into the reaction mixture to trigger the reduction of 4-NP (Fig. 6b). As expected, the reaction under NIR light illumination showed a high conversion up to ~ 91.2 % in 5 min, which is 6.8-fold to the conversion (~13.5 %) achieved at room temperature without light illumination. Considering that light irradiation leads to a significant increase in the dispersion temperature, the enhanced reaction conversion is thus assigned to the high temperature induced by the photothermal heating of CNTs. To further confirm the role of photoheating effect, the reduction of 4-NP was conducted at the same reaction temperature (32 ℃) in a water bath, in the absence of light illumination. In this case, only ~35.1 % of the conversion was achieved, which is much lower than that obtained under NIR light irradiation (Fig. 6c and S22). As a control experiment, the reduction of 4-NP has been conducted under NIR light irradiation with the light wavelength of 976 nm, as shown in Fig. S23. It is found that the GP-CNTs-Pd shows a conversion of the reduction reaction of ~88.5% after reaction for 5 min (solution temperature at 33 ℃), which is similar to the reduction reaction conducted at the wavelength of 808 nm (91.2%, solution temperature at ~32 ℃). This indicates that the catalytic performance does not show obvious difference when exposed to the light wavelength of 808 and 976 nm. As the reduction of 4-NP is a thermal driven reaction, the catalytic performance is primarily controlled by the reaction temperature under NIR illumination. Therefore, the comparable catalytic performance of the GP-CNTs-Pd composite can be attributed to the similar photothermal conversion under these two wavelengths, which is confirmed by the similar solution temperature under NIR irradiation at 808 nm (~32 ℃) and 976 nm (~34 ℃), respectively. It has been reported that hollow architecture of nanomaterials is capable of facilitating the light harvesting and subsequent localization, resulting in a relatively higher surface temperature compared to the bulk solution.[47, 48] In the present work, we hypothesize that the heat induced by light irradiation is relatively higher on the nanotube surface supporting the catalytic Pd NPs than that in the solution phase. This localized heat predominantly contributes to the substantial enhancement in the fast conversion of 4-NP, as the reduction of 4-NP is a typical temperature-dependent and surface reaction. Overall, the incorporation of catalytic metal particles with photothermal CNTs realized by the multi- functional GP molecules demonstrates great potential in the efficient degradation of organic pollutants. In addition, a more systematic study will be conducted in the future to gain deeper insights into the dependence of catalytic performance of the metal/CNTs composites on the light wavelength. Considering that Au NPs could also show significant photothermal effects, the combination of photothermal Au NPs with CNTs could be promising for enhancing the catalytic performance. Thus, we will continue the optimization of Au NPs synthesis and even investigate Pd-Au nanoalloy particles in our future work.

Conclusions

In summary, we provided a novel strategy for the facile and green synthesis of versatile metal/CNTs composites based on amphiphilic glycopeptide (GP) biomolecules. GP was first employed to disassemble the CNTs cluster in water through non-covalent π-π interaction. Particularly, GP-CNTs exhibit an enhanced processibility, forming a paste, gel, and dough at high concentrations. In contrast to conventional single-functional surfactants, the GP molecules also show strong reducibility towards noble metal ions. This unique property enables the *in situ* generation of various metal NPs including Au, Ag, and Pd NPs on CNTs at room temperature, which was scarcely reported in the literature. To explore their practical applications, GP- CNTs-Pd with ultra-small size of Pd NPs (1-3 nm on average) was applied as the catalyst for the reduction reaction of the typical organic pollutant, 4-NP, with the assistance of NIR light irradiation. Enhanced degradation of 4-NP was realized mainly due to the small size of catalytic Pd NPs as well as the localized photothermal heating of the CNTs template under NIR light irradiation. The proposed approach provides new opportunities for the integrally green synthesis of CNTs-based catalytic platform that are inaccessible for the conventional surfactant strategy.

Experimental Section/Methods

Chemicals

Single-wall carbon nanotubes (SWCNTs, diameter of 1-2 nm, length of 5-30 μm, ≥ 95 %) and multiple-wall carbon nanotubes

(MWCNTs, outer diameter of 10-30 nm, inner diameter of 3-5 nm, length of 10 -50 μm, ≥ 99.9 %) were obtained from Timesnano. Palladium chloride ($PdCl_2$, 99 %), gold chloride trihydrate ($HAuCl_4 3H_2O$, ≥ 99 %), chloroplatinic acid hydrate (H_2PtCl_6), silver nitrate ($AgNO_3$, ≥ 99.99 %), sodium borohydride ($NaBH_4$, 99 %), sodium hydroxide (NaOH, ≥ 97%), hydrochloric acid (HCl, 37%), and 4-nitrophenol (4-NP, ≥ 99 %), dimethyl sulfoxide-*d6* (DMSO-*d6*, ≥ 99 %), and tetramethylsilane (TMS, ≥ 99 %) were purchased from Sigma-Aldrich. Ultrapure water with a resistance of 18.2 MΩ·cm was purified using the Thermo Scientific Barnstead GenPurex CAD Plus system. All chemicals were used without any further purification.

Materials synthesis

Synthesis of glycopeptide

The glycopeptide (GP) molecule was prepared according to the methods reported in our previous study.[25] In short, the GP molecules was synthesized through a coupling reaction between the hydrazide group of triphenylalanine and hydroxyl end of sialyllactose at 50 ℃. The reaction yield is *ca.* 59%. Its NMR spectrum can be found in Fig. S1.

Water-dispersible GP-CNTs in various states

For diluted CNTs dispersion, the as-purchased MWCNTs powders (1 mg) were mixed with GP in water (1 mL) and dispersed by gentle sonication (30 W, 37 kHz, constant parameters thereafter) in an ice bath for 30 min. Following centrifugation at 8000 rpm for 20 min to remove the residual bundle complexes, a diluted GP functionalized CNTs (termed as GP-CNTs) dispersion was obtained. The preparation of SWCNTs dispersion followed the same procedure as described above. The final concentration of the resulting GP-CNTs dispersion was calculated by its solid content in water, which was obtained through freeze-drying overnight. As a control experiment, the pristine MWCNTs powders were directly dispersed in water in the absence of GP molecules. To synthesize the GP-CNTs paste, the diluted GP-CNTs dispersion was concentrated further by centrifugation (8000 rpm, 1 h) to form a highly viscous state. The concentrated paste was subsequently coated on an alumina foil and dried in an oven at 40 ℃, ultimately yielding a uniform thin film. For the preparation of gel and dough, the MWCNTs powder was directly mixed with GP molecules at the same weight ratio (1:1) but the total concentration in water increased from ~70 to 200 mg/mL, or even higher and followed by simple hand-grinding carefully in a mortar for 30 min.

Metal/GP-CNTs composites

Taking Pd as the example, a fresh $PdCl_2$ solution (50 μL, 10 mM) was directly mixed with the as-obtained GP-CNTs dispersion (4 mL, 0.05 mg/mL). The pH value of the GP-CNTs dispersion was adjusted to ~8.5 by adding NaOH. After stirring at 250 rpm at room temperature for 15 min, the Pd NPs coated GP-CNTs (denoted as GP-CNTs-Pd) were obtained by centrifugation at 8000 rpm for 20 min. When it comes to Au, Pt, and Ag, $HAuCl_4$ (60 μL, 10 mM), H_2PtCl_6 (60 μL, 10 mM), and $AgNO_3$ (60 μL, 5 mM) solution was respectively used as the precursor for the synthesis of Au NPs coated GP-CNTs (denoted as GP-CNTs-Au), Pt NPs coated GP-CNTs-Pt (denoted as GP-CNTs-Pt), and Ag NPs coated GP-CNTs (denoted as GP-CNTs-Ag).

Catalytic reduction of 4-nitrophenol

Catalytic reaction of metal/GP-CNTs composites without NIR light irradiation

In a typical run, 1.75 mL of fresh water, 0.25 mL of 4-NP solution (1 mM), and an appropriate amount of metal/GP-CNTs composite dispersion (50-150 μL, 0.1 mg/mL) was successively introduced to a clean quartz cuvette (110-QS Hellma, 10 mm) under stirring at 250 rpm at room temperature. Next, a fresh $NaBH_4$ (0.5 mL, 0.1 M) solution was swiftly injected to start the reduction of 4-NP. The reaction dispersion in the cuvette was *in situ* tracked by UV-Vis spectroscopy. To note, all the dispersions were thoroughly purged with continuous N_2 bubbles for 30 min to remove dissolved O_2 prior to the reduction reaction.

Photothermal conversion performance

The GP-CNTs-Pd dispersions at various concentrations (1 mL, 0.01-0.08 mg/mL) were stirred at 300 rpm in a clean cuvette (110-QS Hellma, 10 mm) under the NIR light irradiation (PhotonTec Berlin, a wavelength of 808 nm) at 3 W/cm^2 for *ca.*10 min. The thermometer was placed in the back corner of cuvette with the distance of 6.5 cm between the laser point and the cuvette. The temperature variation of the dispersion was visualized by an infrared (IR) camera (FLIR-E8 XT) and also recorded by a digital thermometer (P300 Thermometer, Dostmann electronics) at the time interval of 20 s.

Catalytic reaction of GP-CNTs-Pd with NIR light irradiation

0.45 mL of fresh water, 0.5 mL of 4-NP solution (2 mM), and 0.03 mL of GP-CNTs-Pd dispersion (1 mg/mL) was successively added in a clean cuvette (110-QS Hellma, 10 mm) and stirred at 300 rpm. The dispersion was irradiated by NIR light (3 W/cm^2) for ~15 min to reach a constant temperature. A fresh $NaBH_4$ solution (100 μL, 2 M) was rapidly introduced to trigger the reaction. To monitor the reduction progress, 0.1 mL of the reaction dispersion was extracted after 5 min and then diluted with 1.9 mL of fresh water. The diluted dispersion was then subjected to filtration using a syringe filter with a pore size of 0.1 μm. The remaining solution was eventually analyzed using UV-Vis absorption spectroscopy. In comparison to the NIR-assisted reduction, the non-irradiated reaction was conducted in a water bath heated at the same temperature under the same condition as above.

Characterization

X-ray diffraction (XRD) analysis was conducted on a Bruker D8 diffractometer with a monochromatic X-ray beam with Cu K_α radiation at a scan rate of 0.05 °/min. All the samples were collected after freeze-drying overnight and stored in air-tight XRD holders for measurements. The oxidation state of Pd in the GP-CNTs-Pd composite was determined by X-ray photoelectron spectroscopy (XPS) with an ESCA-Lab-220i-XL X-ray photoelectron spectrometer (Thermo Fisher Scientific) with Al

View Article Online
DOI: 10.1039/D3NR02607H

K_α sources ($h\nu$ = 1486.6 eV). Nuclear magnetic resonance (NMR) measurement was performed on AVANCE III HD 400 MHz of Bruker BioSpin International. Dimethyl sulfoxide-*d6* (DMSO-*d6*) was used as a solvent and tetramethylsilane (TMS) was employed as the reference with the peak of chemical shift at 0 ppm.

Conventional transmission electron microscopy (TEM), high-resolution TEM (HRTEM), and cryogenic TEM (cryo-TEM) were performed on a JEOL JEM-2100 instrument operated at an accelerating voltage of 200 kV. For conventional TEM and HRTEM, all the samples were prepared by dropping ~5 µL of the resulting dispersions on continuous carbon-coated copper TEM grids (200 mesh, Science Services). Cryo-TEM specimens were prepared on Lacey carbon-coated copper grids (200 mesh, Science Services) and subsequently plunge-frozen into liquid ethane with an FEI Vitrobot Mark IV at 4 ℃ with a humidity of 95%. Vitrified grids were either directly transferred to the cryogenic transfer holder (Gatan 914, Gatan, Munich, Germany) or stored in a liquid N_2 tank. The imaging process was carried out at *ca.* - 183 ℃ with a defocus of the objective lens ranging from 2.5 to 3 µm. Cryo-TEM images were recorded at various magnifications using a bottom-mounted 4 k×4 k CMOS camera (TemCam-F416, TVIPS, Gauting, Germany). The total electron dose for each image was maintained below 20 $e^-/Å^2$. Scanning transmission electron microscopy (STEM) for electron energy- loss spectroscopy (EELS) analysis was performed on a Nion HERMES microscope (Nion Co., Kirkland, WA, USA) equipped with a Dectris ELA direct electron detector (Dectris AG, Baden- Daettwil, Switzerland). Similar to the sample preparation for cryo-TEM, ~5 µL of the GP-CNTs-Pd dispersion was placed on a lacey carbon-coated copper grid (200 mesh, Electron Microscopy Sciences, Hatfield, PA) and followed by drying under mild conditions. Scanning electron microscopy (SEM) images were recorded using a LEO GEMINI 1530 microscope at 5 kV. Thermogravimetric analysis (TGA) was performed on a Netzch Phoenix F204 instrument with a temperature range of 25-900 ℃ at a heating rate of 10 ℃/min in a synthetic air atmosphere. Raman spectra were recorded using an InVia 2R9X81 Raman spectrometer equipped with a detector of Renishaw Centrus 2MYA08 and a HeNe laser (a wavelength of 532 nm). UV-Vis absorption spectroscopy were recorded at room temperature on a PerkinElmer Lambda 650 spectrometer. All the aqueous solutions or dispersions were contained in a clean quartz cuvette (110-QS Hellma, 10 mm).

Conflicts of interest

There are no conflicts to declare.

Acknowledgements

The authors thank the Deutsche Forschungsgemeinschaft (DFG, project number: 410871749) for financial support. G.C. thanks NSFC/China (Nos. 52125303, 51721002, and 21861132012) for financial support. The authors also appreciate the Joint Lab for Structural Research at the Integrative Research Institute for the Sciences (IRIS Adlershof) for the cryo-TEM and STEM measurements.

References

1. Z. Li, J. Peng and Z. Lin, *Giant*, 2021, **5**, 100048.
2. D. H. Kweon, M. S. Okyay, S.-J. Kim, J.-P. Jeon, H.-J. Noh, N. Park, J. Mahmood and J.-B. Baek, *Nat. Commun.*, 2020, **11**, 1278.
3. K.-I. Kim, S. Yoon, J. Chang, S. Lee, H. H. Cho, S. H. Jeong, K. Jo and J. H. Lee, *Small*, 2020, **16**, 1905821.
4. B. Zhang, T. Li, L. Huang, Y. Ren, D. Sun, H. Pang, J. Yang, L. Xu and Y. Tang, *Nanoscale*, 2021, **13**, 5400-5409.
5. K. Chiou, S. Byun, J. Kim and J. Huang, *Proceedings of the National Academy of Sciences*, 2018, **115**, 5703-5708.
6. S. Wang, Z. Huang, W. Shi, D. Lee, Q. Wang, W. Shang, Y. Stein, Y. Shao-Horn, T. Deng, B. L. Wardle and K. Cui, *ACS App. Mater. Interfaces*, 2021, **13**, 28583-28592.
7. K. Chiou and J. Huang, *Matter*, 2020, **3**, 302-319.
8. T. Premkumar, R. Mezzenga and K. E. Geckeler, *Small*, 2012, **8**, 1299-1313.
9. M. Bystrzejewski, A. Huczko, H. Lange, T. Gemming, B. Büchner and M. H. Rümmeli, *J. Colloid Interface Sci.*, 2010, **345**, 138-142.
10. V. A. Davis, A. N. G. Parra-Vasquez, M. J. Green, P. K. Rai, N. Behabtu, V. Prieto, R. D. Booker, J. Schmidt, E. Kesselman, W. Zhou, H. Fan, W. W. Adams, R. H. Hauge, J. E. Fischer, Y. Cohen, Y. Talmon, R. E. Smalley and M. Pasquali, *Nature Nanotechnology*, 2009, **4**, 830-834.
11. X. Wu, Z. Wang, D. Zhang, Y. Qin, M. Wang, Y. Han, T. Zhan, B. Yang, S. Li, J. Lai and L. Wang, *Nat. Commun.*, 2021, **12**, 4018.
12. Z. Ma, C. Lian, D. Niu, L. Shi, S. Hu, X. Zhang and H. Liu, *ChemSusChem*, 2019, **12**, 1724-1731.
13. A. Benko, J. Duch, M. Gajewska, M. Marzec, A. Bernasik, M. Nocuń, W. Piskorz and A. Kotarba, *Nanoscale*, 2021, **13**, 10152-10166.
14. M. Youssry, M. Al-Ruwaidhi, M. Zakeri and M. Zakeri, *Emergent Materials*, 2020, **3**, 25-32.
15. A. Ezzeddine, Z. Chen, K. S. Schanze and N. M. Khashab, *ACS App. Mater. Interfaces*, 2015, **7**, 12903-12913.
16. A. Star, J. F. Stoddart, D. Steuerman, M. Diehl, A. Boukai, E. W. Wong, X. Yang, S. W. Chung, H. Choi and J. R. Heath, *Angew. Chem.*, 2001, **113**, 1771-1775.
17. L. Vaisman, H. D. Wagner and G. Marom, *Adv. Colloid Interface Sci.*, 2006, **128-130**, 37-46.
18. T. Li, Y. Chen, W. Hu, W. Yuan, Q. Zhao, Y. Yao, B. Zhang, C. Qiu and C. M. Li, *Nanoscale*, 2021, **13**, 4444-4450.
19. J. John, E. Gravel, I. N. N. Namboothiri and E. Doris, *Nanotechnology Reviews*, 2012, **1**, 515-539.
20. S. Chu and A. Majumdar, *Nature*, 2012, **488**, 294-303.
21. Y. Shi, W.-M. Huang, J. Li, Y. Zhou, Z.-Q. Li, Y.-C. Yin and X.-H. Xia, *Nat. Commun.*, 2020, **11**, 4558.
22. Y. Liu, X. Li, Q. Zhang, W. Li, Y. Xie, H. Liu, L. Shang, Z. Liu, Z. Chen, L. Gu, Z. Tang, T. Zhang and S. Lu, *Angew. Chem. Int. Ed.*, 2020, **59**, 1718-1726.
23. D. Wang, Q. Li, C. Han, Q. Lu, Z. Xing and X. Yang, *Nat. Commun.*, 2019, **10**, 3899.
24. F. Morales-Lara, V. K. Abdelkader-Fernández, M. Melguizo, A. Turco, E. Mazzotta, M. Domingo-García, F. J. López-

View Article Online
DOI: 10.1039/D3NR02607H

Garzón and M. Pérez-Mendoza, *J. Mater. Chem. A*, 2019, **7**, 24502-24514.
25. R. Liu, R. Zhang, L. Li, Z. Kochovski, L. Yao, M.-P. Nieh, Y. Lu, T. Shi and G. Chen, *J. Am. Chem. Soc.*, 2021, **143**, 6622-6633.
26. R. Liu, L. Li, S. Chen, Z. Yang, Z. Kochovski, S. Mei, Y. Lu, L. Zhang and G. Chen, *ACS Nano*, 2023, **17**, 2245-2256.
27. S. Attal, R. Thiruvengadathan and O. Regev, *Anal. Chem.*, 2006, **78**, 8098-8104.
28. S. Costa and E. Borowiak-Palen, *Acta Phys. Pol., A*, 2009, **116**, 32-35.
29. B. Shen, W. Zhai, C. Chen, D. Lu, J. Wang and W. Zheng, *ACS App. Mater. Interfaces*, 2011, **3**, 3103-3109.
30. Q. Xu and W. Zhang, *e-Polymers*, 2021, **21**, 166-178.
31. P. Song, Z. Xu, Y. Wu, Q. Cheng, Q. Guo and H. Wang, *Carbon*, 2017, **111**, 807-812.
32. L. Yu, C. Shearer and J. Shapter, *Chem. Rev.*, 2016, **116**, 13413-13453.
33. P. J. Cappillino, J. D. Sugar, M. A. Hekmaty, B. W. Jacobs, V. Stavila, P. G. Kotula, J. M. Chames, N. Y. Yang and D. B. Robinson, *J. Mater. Chem. A*, 2012, **22**, 14013-14022.
34. M. Mohammadnezhad, G. S. Selopal, O. Cavuslar, D. Barba, E. G. Durmusoglu, H. Y. Acar, Z. M. Wang, G. P. Lopinski, B. Stansfield, H. Zhao and F. Rosei, *Chem. Eng. J.*, 2021, **421**, 127756.
35. Q. Yu, J. Li, Y. Zhang, Y. Wang, L. Liu and M. Li, *Sci. Rep.*, 2016, **6**, 26667.
36. X. Shu, Q. Yang, F. Yao, Y. Zhong, W. Ren, F. Chen, J. Sun, Y. Ma, Z. Fu, D. Wang and X. Li, *Chem. Eng. J.*, 2019, **358**, 903-911.
37. L. Su, C. Wang, F. Polzer, Y. Lu, G. Chen and M. Jiang, *ACS Macro Letters*, 2014, **3**, 534-539.
38. E. V. Pronina, Y. A. Vorotnikov, T. N. Pozmogova, A. O. Solovieva, S. M. Miroshnichenko, P. E. Plyusnin, D. P. Pishchur, I. V. Eltsov, M. V. Edeleva, M. A. Shestopalov and O. A. Efremova, *ACS Sustain. Chem. Eng.*, 2020, **8**, 5371-5379.
39. P. Hervés, M. Pérez-Lorenzo, L. M. Liz-Marzán, J. Dzubiella, Y. Lu and M. Ballauff, *Chem. Soc. Rev.*, 2012, **41**, 5577-5587.
40. M. Hartings, *Nature Chemistry*, 2012, **4**, 764-764.
41. S. Mei, Z. Kochovski, R. Roa, S. Gu, X. Xu, H. Yu, J. Dzubiella, M. Ballauff and Y. Lu, *Nano-Micro Lett.*, 2019, **11**, 83.
42. X. Ye, X. Shi, H. Zhong, T. Wang, J. Duo, B. Jin and F. Jin, *Green Chemistry*, 2022, **24**, 813-822.
43. Y. Zhao, T. Zhao, Y. Cao, J. Sun, Q. Zhou, H. Chen, S. Guo, Y. Wang, Y. Zhen, X.-J. Liang and S. Zhang, *ACS Nano*, 2021, **15**, 6517-6529.
44. S. Wunder, Y. Lu, M. Albrecht and M. Ballauff, *ACS Catalysis*, 2011, **1**, 908-916.
45. Y. Chen, X. Ge, Y. Cao, C. Yao, J. Zhang, G. Qian, X. Zhou and X. Duan, *Industrial & Engineering Chemistry Research*, 2022, **61**, 6427-6435.
46. Y. R. Mejá and N. K. Reddy Bogireddy, *RSC Advances*, 2022, **12**, 18661-18675.
47. J. Sun, J. Zhang, M. Zhang, M. Antonietti, X. Fu and X. Wang, *Nat. Commun.*, 2012, **3**, 1139.
48. X. Pan, R. M. Sarhan, Z. Kochovski, G. Chen, A. Taubert, S. Mei and Y. Lu, *Nanoscale*, 2022, **14**, 6888-6901.

Supporting Information

Multi-functionalized carbon nanotubes towards green fabrication of heterogeneous catalyst platforms with enhanced catalytic properties under NIR light irradiation

Xuefeng Pan[a,d†], Rongying Liu[b†], Zhilong Yu[a], Benedikt Haas[c], Zdravko Kochovski[a], Sijia Cao[a,d], Radwan M. Sarhan[a], Guosong Chen[b], and Yan Lu[a,d]**

[a] *Department for Electrochemical Energy Storage, Helmholtz-Zentrum Berlin für Materialien und Energie, Hahn-Meitner-Platz 1, 14109 Berlin, Germany*

[b] *The State Key Laboratory of Molecular Engineering of Polymers and Department of Macromolecular Science, Fudan University, Shanghai 200433, China*

[c] *Department of Physics & IRIS Adlershof, Humboldt-Universität zu Berlin, Newtonstr. 15, 12489 Berlin, Germany*

[d] *Institute of Chemistry, University of Potsdam, Karl-Liebknecht-Str. 24-25, 14476 Potsdam, Germany*

† These two authors contribute equally to this manuscript.

* *Corresponding authors:*

Guosong Chen: guosong@fudan.edu.cn

Yan Lu: yan.lu@helmholtz-berlin.de

Supplementary data

Supplementary Figures

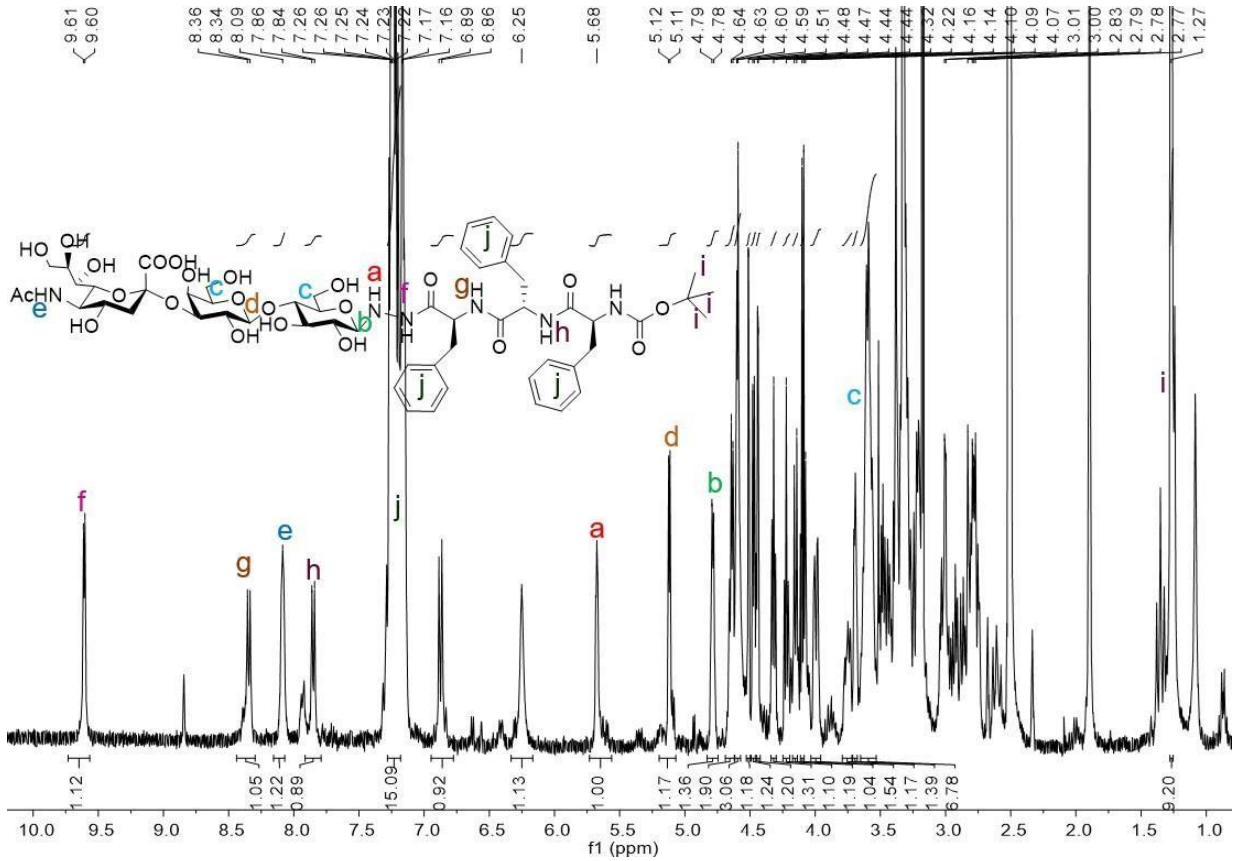

Fig. S1. ^{1}H-NMR spectrum of the GP powder dissolved in DMSO-*d6*.

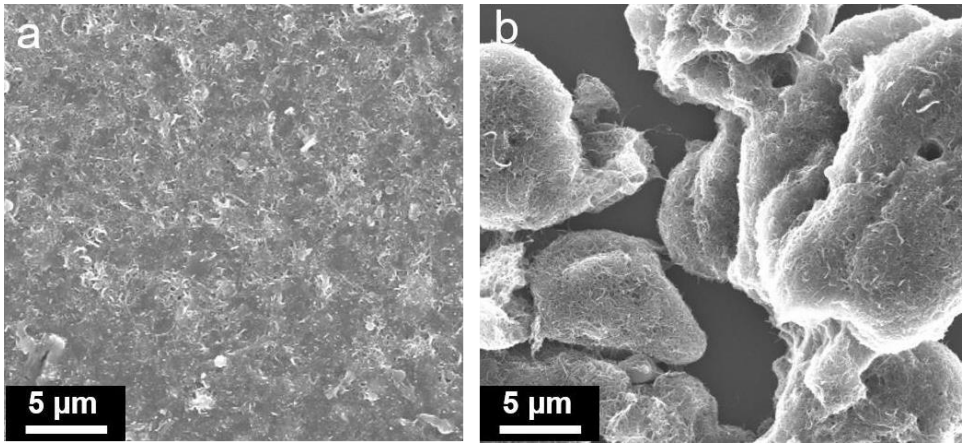

Fig. S2. SEM images of (a) the GP-CNTs dispersion and (b) the pristine CNTs cluster with a scale bar of 5 µm.

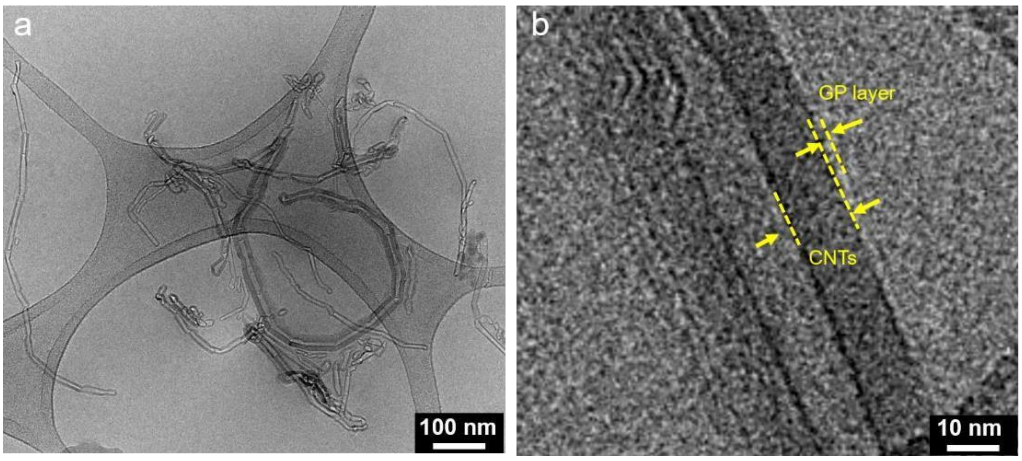

Fig. S3. Cryo-TEM images of the GP-CNTs dispersion at different magnifications**.**

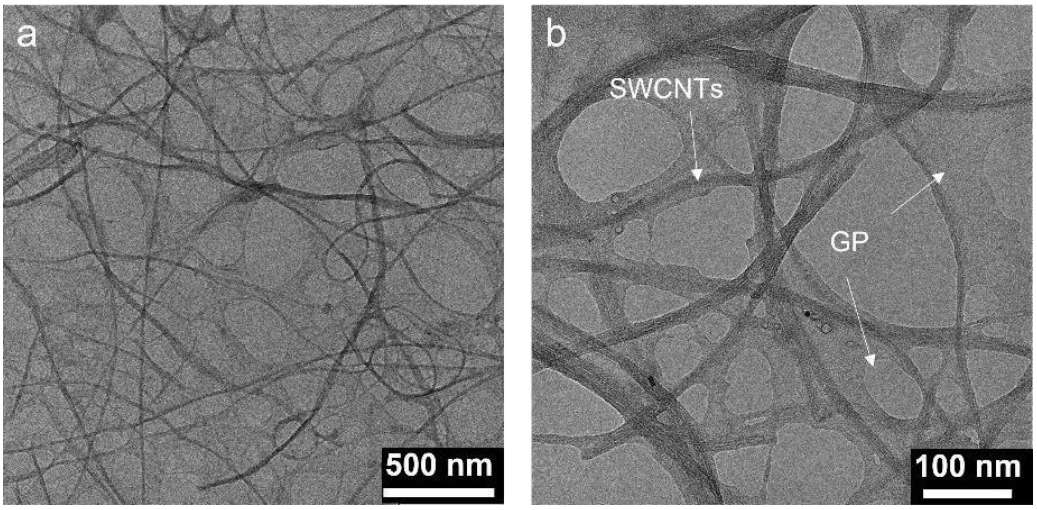

Fig. S4. TEM images of the SWCNTs dispersed with GP (same mass ratio of 1:1) at different magnifications**.**

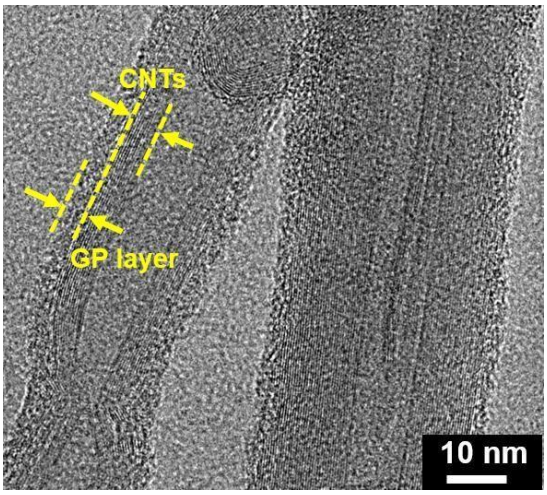

Fig. S5. HRTEM image of the GP-CNTs dispersion after storage for 2 months**.**

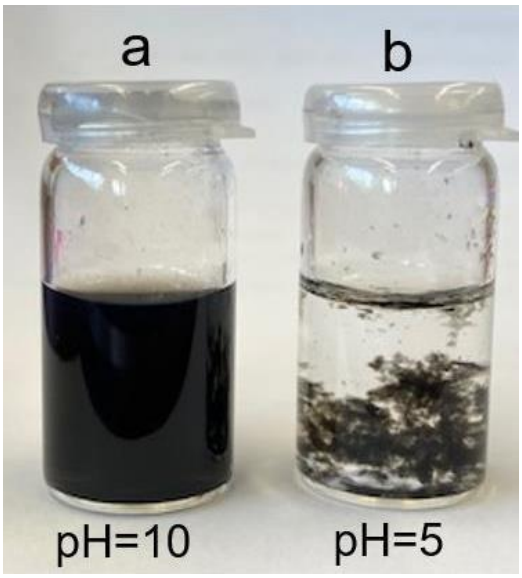

Fig. S6. Photos of the GP-CNTs dispersions at 0.2 mg/mL and the pH of (a) 10 and (b) 5 overnight**.**

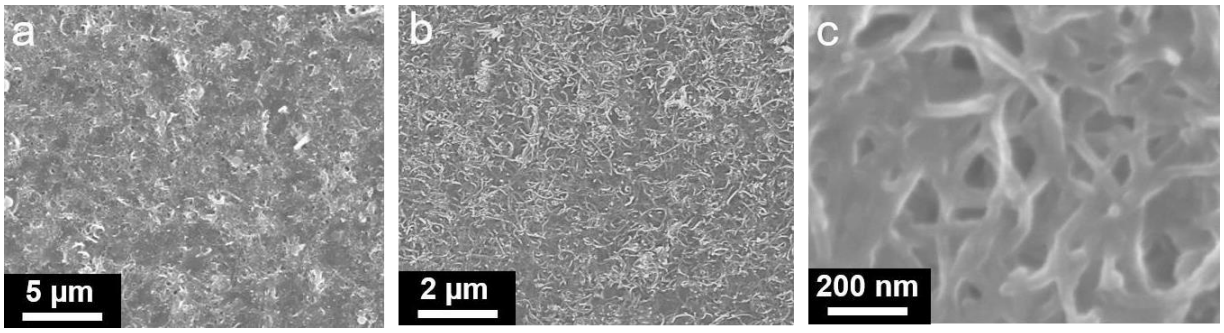

Fig. S7. SEM images of the GP-CNTs film after drying at various magnifications.

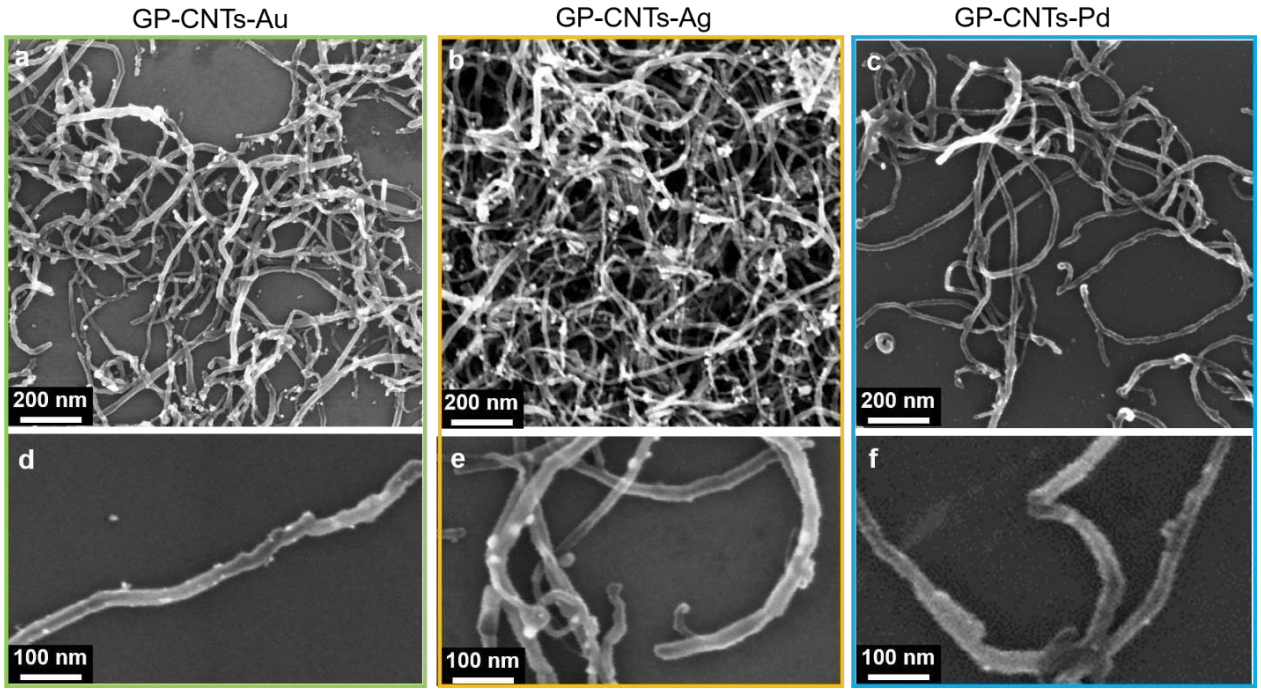

Fig. S8. SEM images of (a) GP-CNTs-Au, (b) GP-CNTs- Ag, and (c) GP-CNTs-Pd.

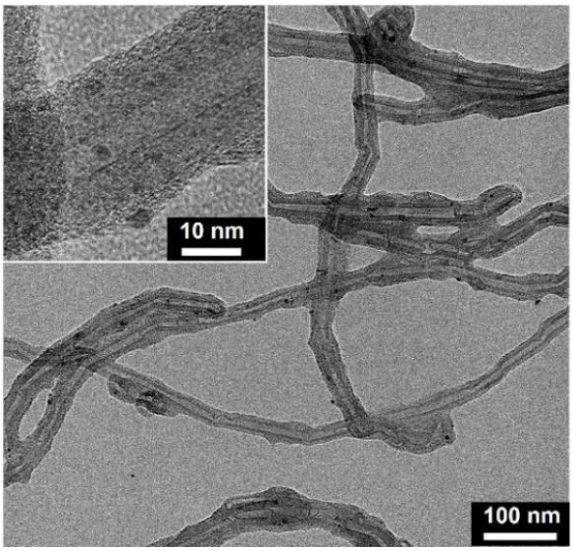

Fig. S9. TEM images of the GP-CNTs-Pd sample after storage for 1 month.

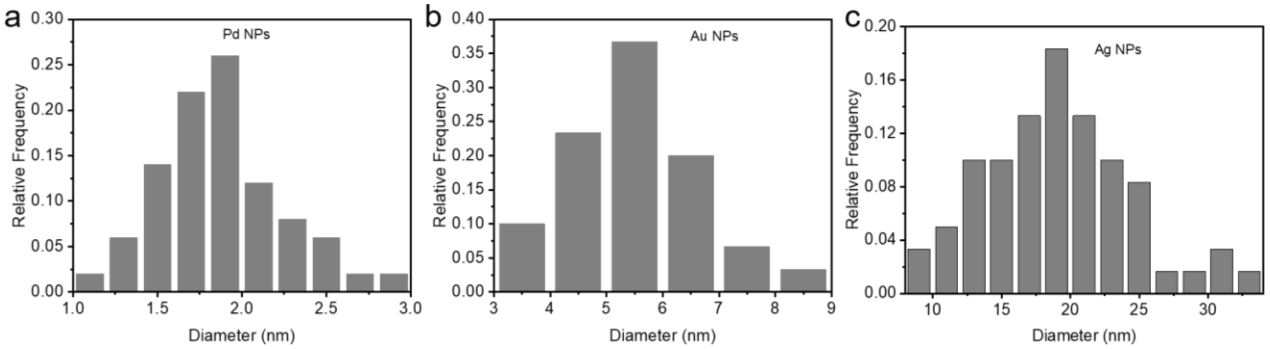

Fig. S10. Histograms of particle size distribution (based on over 50 particles) of (a) Pd NPs in GP-CNTs-Pd, (b) Au NPs in GP-CNTs-Au, and (c) Ag NPs in GP-CNTs-Ag determined from TEM analysis based on more than 50 particles.

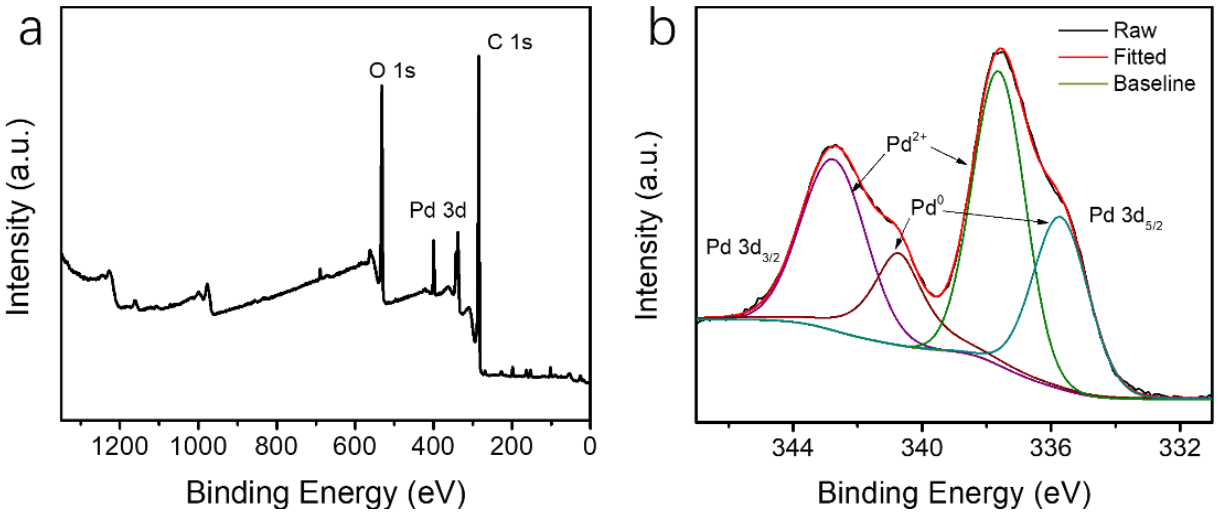

Fig. S11. (a) Full XPS spectrum and (b) high-resolution Pd 3d spectrum of the GP-CNTs-Pd composite.

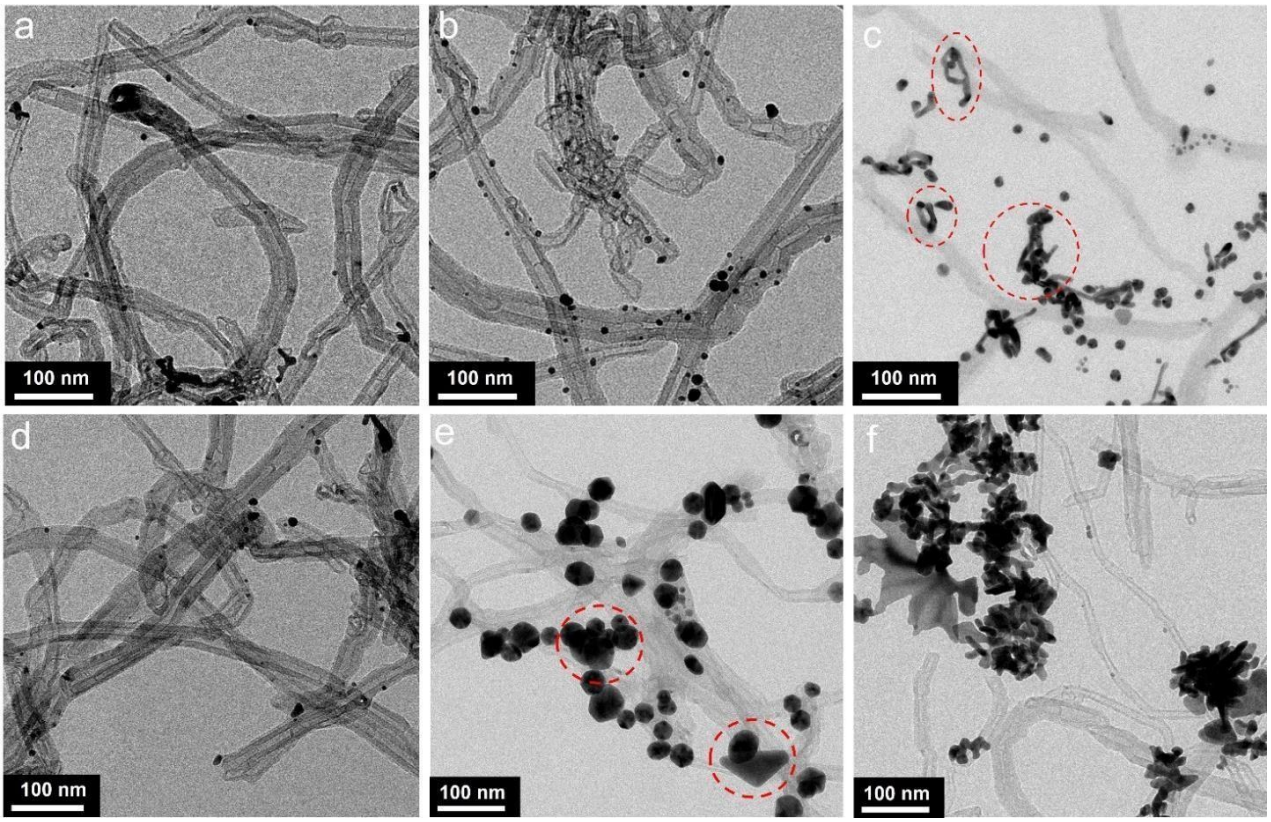

Fig. S12. TEM images of GP-CNTs-Au prepared at (a) 0.02 mg/mL of GP, 0.15 mM of $HAuCl_4$; (b) 0.05 mg/mL of GP, 0.15 mM of $HAuCl_4$; (c) 0.1 mg/mL of GP, 0.15 mM of $HAuCl_4$; (d) 0.05 mg/mL of GP, 0.05 mM of $HAuCl_4$; (e) 0.05 mg/mL of GP, 0.3 mM of $HAuCl_4$; and (f) 0.05 mg/mL of GP, 0.15 mM of $HAuCl_4$ heated at 40 °C. Note that all the samples in (a-e) were prepared at room temperature.

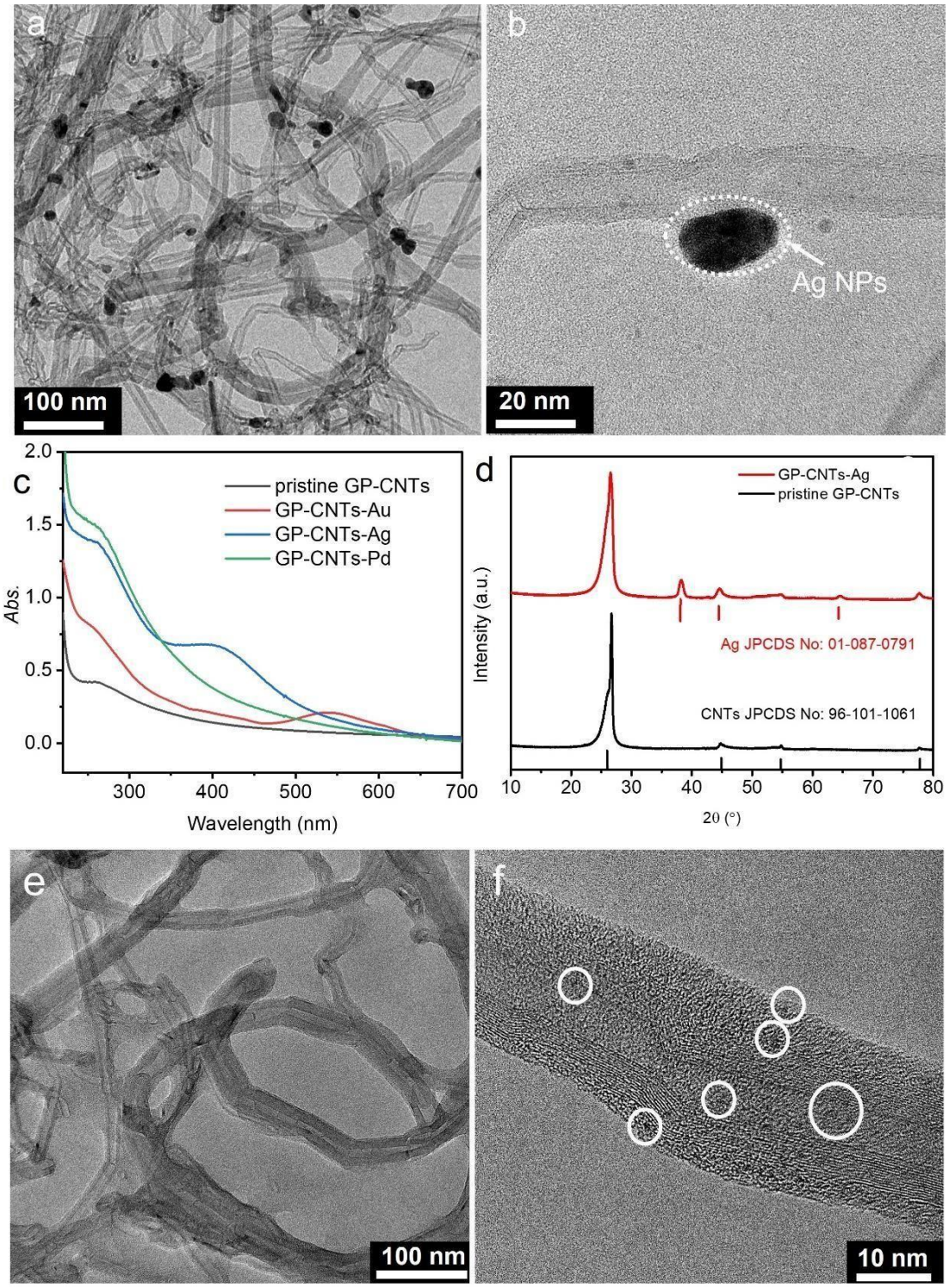

Fig. S13. (a, b) TEM images of GP-CNTs-Ag at different magnifications. (c) UV-Vis absorption spectra of various metal/CNTs composites. (d) XRD patterns of the pristine GP-CNTs and GP-CNTs-Ag powder after freeze-drying. The peaks at 38.2, 44.3, and 64.7° in XRD indicate the (111), (200), and (220) planes of the (*fcc*) metallic Ag (JPCDS NO. 01-087-0719).[1] (e-f) TEM images of the GP-CNTs-Pt prepared by mixing GP-CNTs (0.05 mg/mL) with H_2PtCl_6 (0.15 mM) at room temperature with stirring for 24 h.

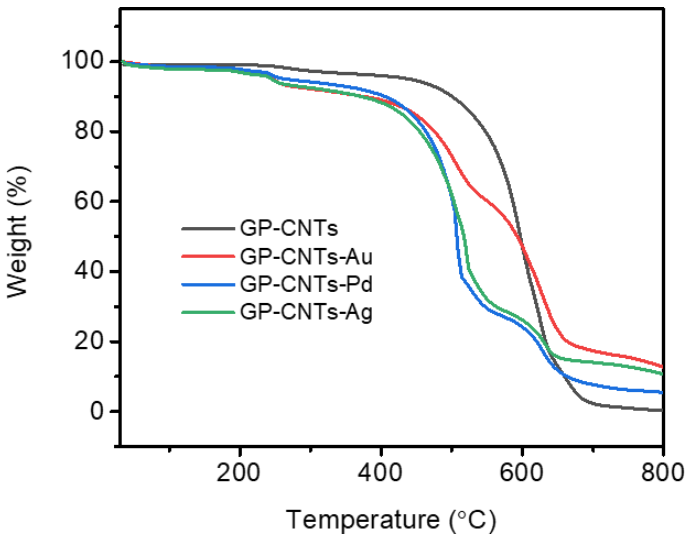

Fig. S14. TGA curves of the GP-CNTs-Au, GP-CNTs-Ag, and GP-CNTs-Pd powder in synthetic air.

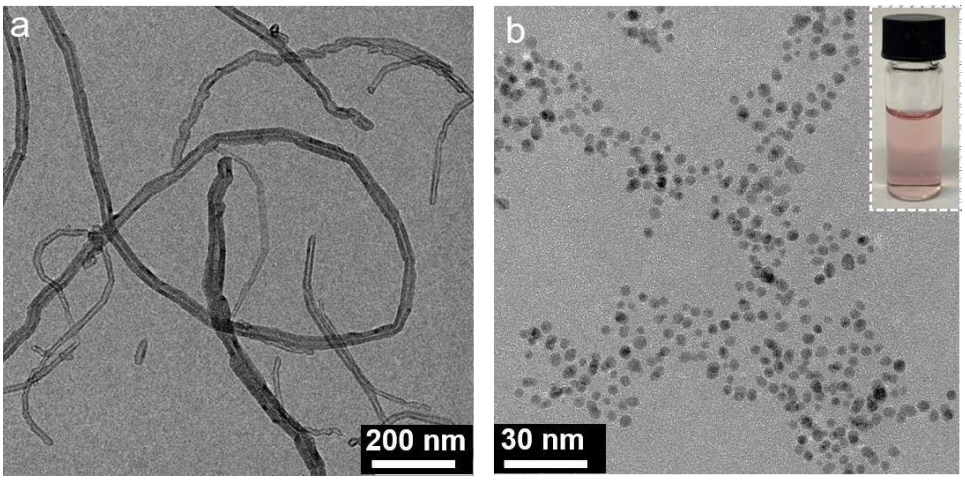

Fig. S15. TEM images of (a) Pristine CNTs cluster mixed with $HAuCl_4$ in the absence of GP molecules. (b) Au NPs generated in the mixture of $HAuCl_4$ (0.01 mM) and GP (0.1 mg/mL) solution. The inset in (b) is the corresponding photo of the obtained Au NPs dispersion.

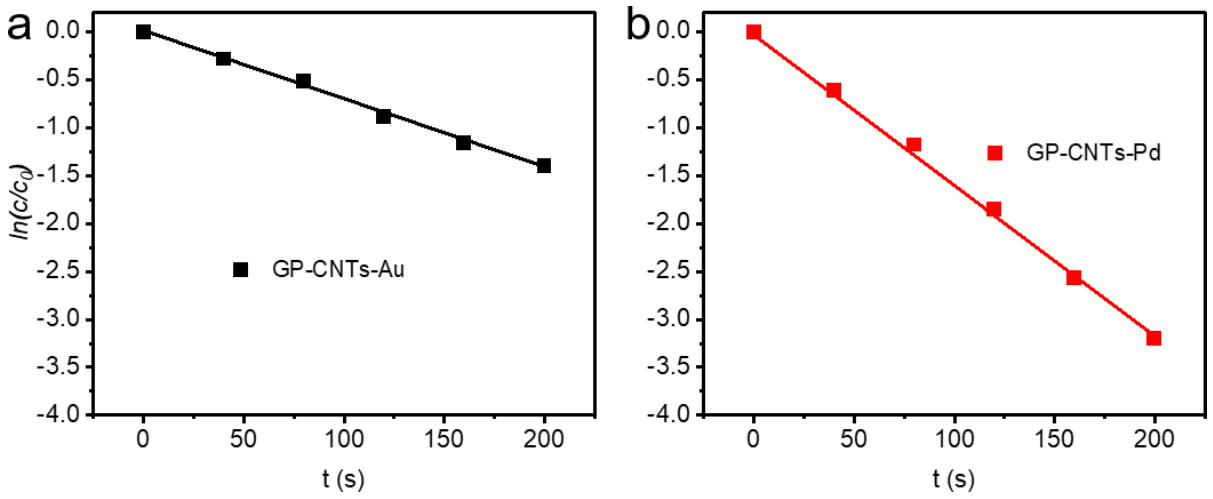

Fig. S16. Reduction of 4-NP with (a) GP-CNTs-Au at 10.5 μg/mL and (b) GP-CNTs-Pd at 1.80 μg/mL. The concentration of 4-NP and $NaBH_4$ was 0.005 mM and 0.1 M, respectively.

When adding an excess amount of $NaBH_4$, the reduction kinetics of 4-NP mainly follow a pseudo-first-order law. Apparent rate constant (k_{app}) of 4-NP can be given by:

$$ln\frac{c}{c_0} = ln\frac{I}{I_0} = -k_{app}\,t = -k_1 S_t t \quad (1)$$

where c and c_0 are the concentration and I and I_0 are the absorption intensity at 400 nm of 4-NP at the given time t and the very beginning of the reaction, respectively.[2] S_t is the total surface of catalytic particle and k_1 is the rate constant normalized to S_t. k_{app} can be obtained from the linear correlation between $ln(I/I_0)$ or $ln(c/c_0)$ and t. As a result, GP-CNTs-Pd displayed a fast catalytic conversion of 4-NP, giving a k_{app} value of 0.016 s^{-1}, while a k_{app} value of 0.0021 s^{-1} has been measured for GP-CNTs-Au (Fig. S16).

Note that the reduction mainly proceeds on the surface of the metal NPs. If we assume both Pd and Au particles are ideally spherical, S_t can be thus calculated by:

$$m_0 = \frac{1}{6}\rho\pi d^3 \quad (2)$$

$$S_0 = \pi d^2 \quad (3)$$

$$n = \frac{m}{m_0} \quad (4)$$

$$S_t = \frac{nS_0}{V} \quad (5)$$

where m_0 S_0, and n are the mass and surface of a single catalyst particle and the total number of metal particles, respectively; m is the total mass of metal catalyst that can be estimated from TGA measurement (13.2 wt.% for GP-CNTs-Pd and 11.5 wt.% for GP-CNTs-Au); ρ is the density of the catalytic particle, assuming it is the same as the density of their bulk material (12.0 g/cm^3 for Pd and 19.3 g/cm^3 for Au); d is the diameter of the particle, which can be obtained from the HRTEM analysis (1.8 nm for Pd and 5.6 nm for Au).[3] V is the reaction volume (2.5 mL here). According to Table S2, the S_t was thereby fixed to be 0.26 m^2/L. The value of GP-CNTs-Pd was calculated to be 0.062 s^{-1} m^{-2} L, which is higher than that of GP-CNTs-Au (0.0081 s^{-1} m^{-2} L), demonstrating the superior catalytic activity of GP-CNTs-Pd.

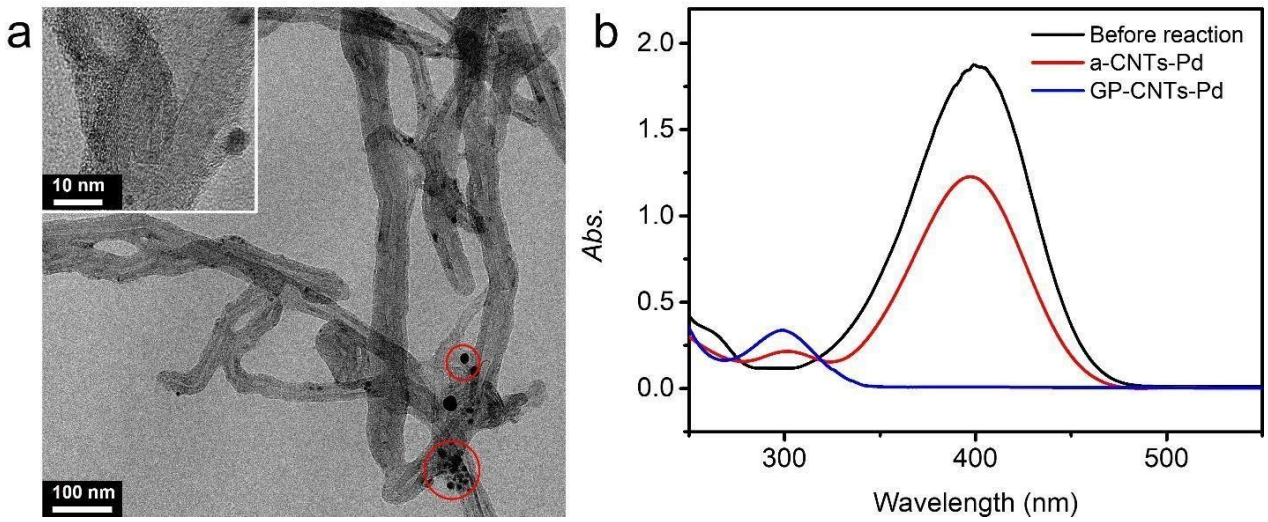

Fig. S17. (a) TEM images of a-CNTs-Pd. (b) Reaction comparison: both a-CNTs-Pd and GP-CNTs-Pd at the concentration of 0.02 mg/mL, 4-NP at 0.1 mM, and $NaBH_4$ at 20 mM at room temperature.

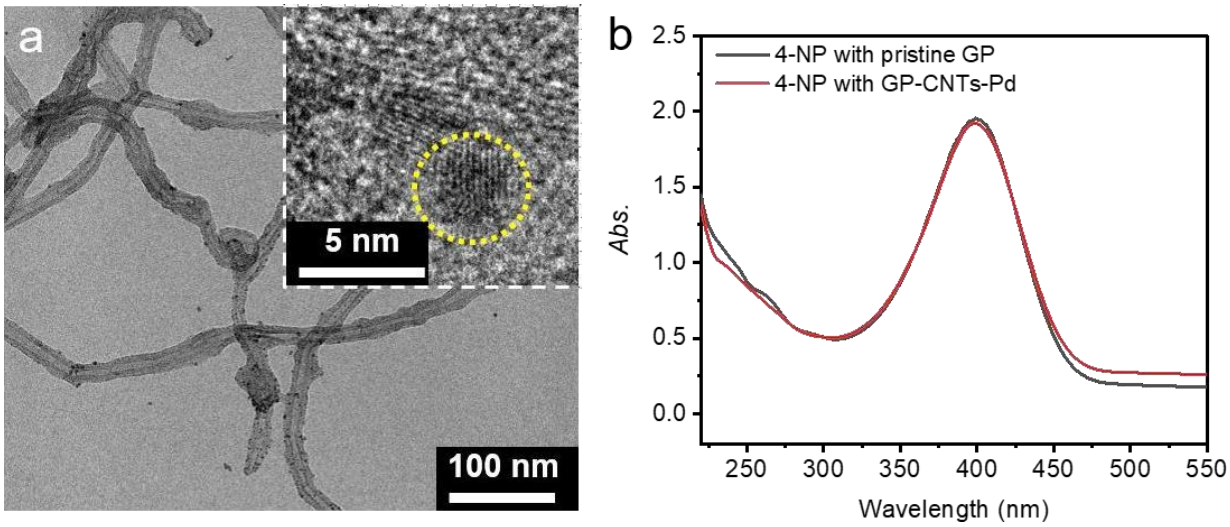

Fig. S18. (a) TEM image of the GP-CNTs-Pd dispersion after catalytic cycles. (b) Reduction reaction of 4-NP with either GP-CNTs-Pd or pristine GP molecules at pH of ~10 without $NaBH_4$ after 15 min.

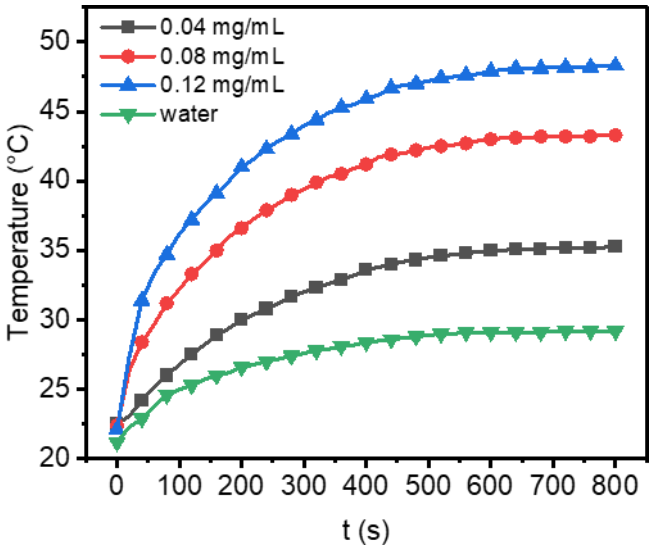

Fig. S19. Temperature variation of the GP-CNTs-Pd dispersion at various concentrations.

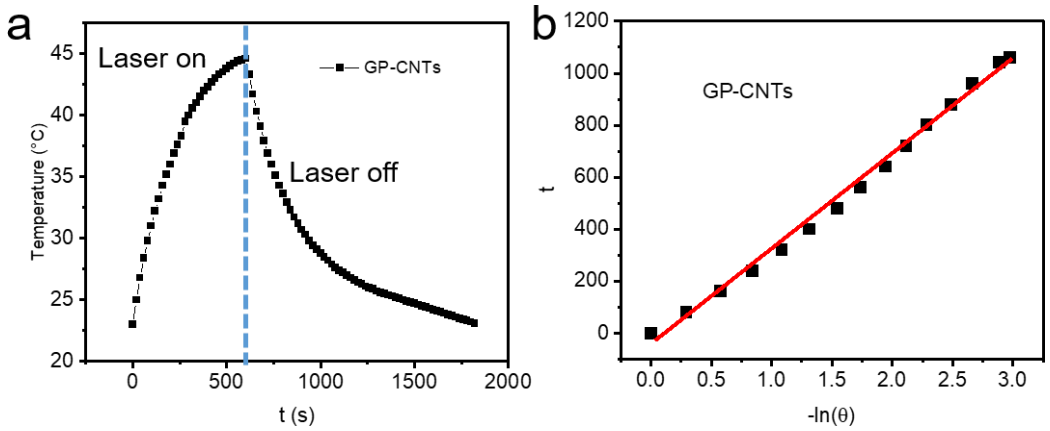

Fig. S20. (a) Temperature variation of the GP-CNTs dispersion under NIR irradiation. (b) *t* versus *–ln(θ)* obtained from the cooling curve.

The photothermal conversion efficiency (η) can be calculated based on the heating-cooling profiles and given by:

$$\eta = \frac{hS(T_{max}-T_{sur})-Q_{Dis}}{I(1-10^{A808})} \quad (2)$$

where *h*, *s*, Q_{Dis}, are the heat transfer coefficient, surface area of the container, heat dissipated from the light absorbed by the quartz sample cell containing with pure water, respectively. *I* and A_{808} are the laser intensity and absorption of dispersion at the wavelength of 808 nm, respectively. where T_{sur}, T_{max} are surrounding temperature and maximum temperature of the GP-CNTs dispersion, respectively.[4, 5]

To calculate *hs*, a dimensionless parameter (θ) needs to be introduced and determined by:

$$hs = \frac{m_D C_D}{\tau_s} \quad (3)$$

where m_D and C_D are the mass of water (1 g) and heat capacity (4.2 J/g·°C), respectively. The time constant (τ_s) can be determined from the slop of cooling curve (**Fig. S16b**) according to the equations below:

$$t = -\tau_s \ln(\theta) \quad (4)$$

$$\theta = \frac{T-T_{sur}}{T_{max}-T_{sur}} \quad (5)$$

where t and T are the time and cooling temperature of the dispersion during cooling stage. Hence, τ_s of the pristine CNTs cluster and GP-CNTs dispersion were determined to be 328.1 and 370.4 s, respectively. Correspondingly, the value η of CNTs cluster and the GP-CNTs dispersion were determined to be 4.2 % and 22.3 %, respectively.

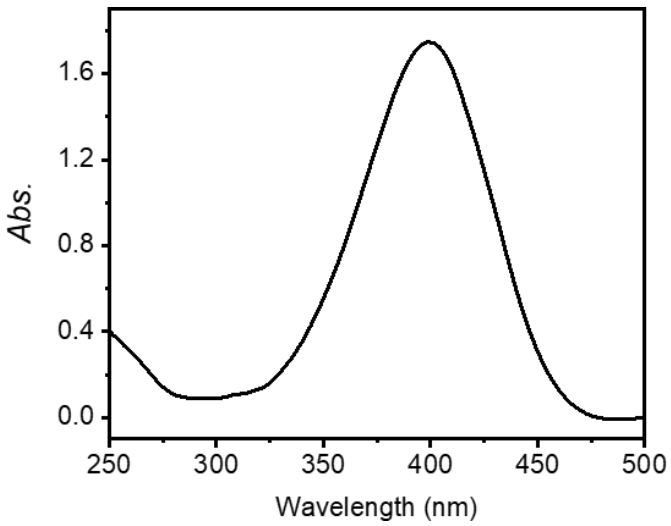

Fig. S21. Reduction reaction of 4-NP after NIR light irradiation for 15 min before introducing $NaBH_4$.

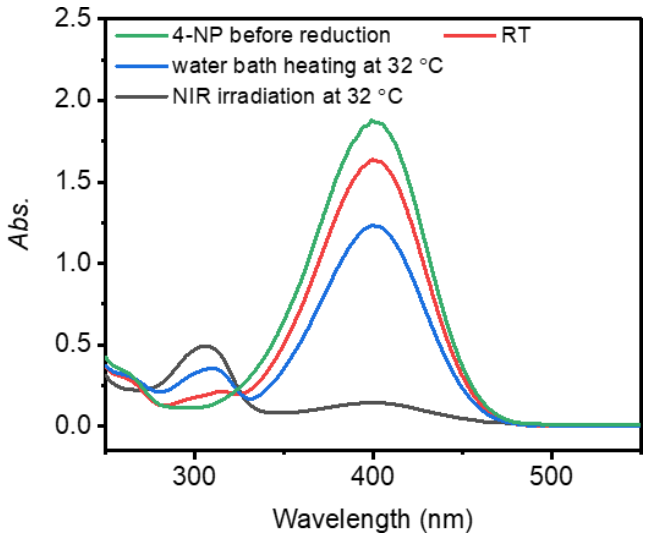

Fig. S22. Reduction reaction of 4-NP under various heating conditions after 5 min.

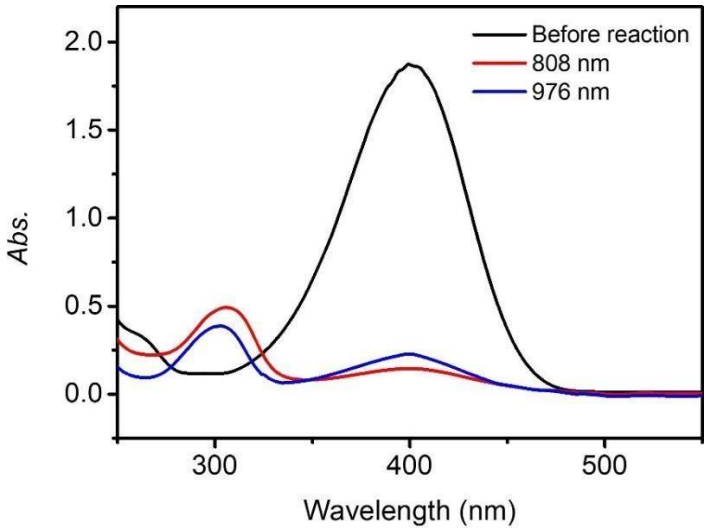

Fig. S23. Reaction comparison of GP-CNTs-Pd under NIR light illumination at 808 and 976 nm (3 W/cm^2) for 5 min with the concentration of GP-CNTs-Pd at 0.03 mg/mL, 4-NP at 1 mM, and $NaBH_4$ at 0.2 M.

Supplementary Tables

Table S1. Comparison of the catalytic activity of the Pd-based catalysts.

Sample	Size (nm)	$C_{cat.}$	C_{NaBH4} (mM)	$C_{4\text{-}NP}$ (mM)	t (min)	T (°C)	$k_m \times 10^{-3}$ s^{-1} mg^{-1}	Ref.
Pd-peptide	2.6	79 μM	10	0.05	10	25	8.73	6
Pd	26.5	5 μg/mL	100	2	20	25	24	7
Pd-Au/PS-PVP	3.1	3.6 μg/mL	20	0.1	10	25	95.6	8
Pd/protein	2.8	0.6 mg/mL	10.5	0.1	10	20	3.33	9
Pt-Pd alloy	~57	5 μg/mL	100	0.1	10	22	226.7	10
Pd-PAMAM	1.8	0.01 mM	10	0.2	15	15	113.3	11
GP-CNTs-Pd	1.8	50 μg/mL	20	0.1	10	25	146.5	This work

Note that C_{cat}, C_{NaBH4}, $C_{4\text{-}NP}$, t, T, and k_m are the catalyst concentration, $NaBH_4$ concentration, 4-NP concentration, reaction time, reaction temperature, and k_{app} normalized with the catalyst mass, respectively.

Table S2. Summary for the calculation of S_t.

Metal	m (μg)	ρ (g/cm^3)	d (nm)	m_0 (g)	n	S_0 (m^2)	S_t (m^2/L)
Pd	0.59	12.0	1.8	3.66×10^{-20}	1.61×10^{13}	4.07×10^{-17}	0.26
Au	3.02	19.3	5.6	1.77×10^{-18}	1.70×10^{12}	3.93×10^{-16}	0.26

References in SI:

1. S.-H. Min, G.-Y. Lee and S.-H. Ahn, *Composites Part B: Engineering*, 2019, **161**, 395-401.
2. S. Wunder, F. Polzer, Y. Lu, Y. Mei and M. Ballauff, *J. Phys. Chem. C*, 2010, **114**, 8814-8820.
3. P. Hervés, M. Pérez -Lorenzo, L. M. Liz-Marzán, J. Dzubiella, Y. Lu and M. Ballauff, *Chem. Soc. Rev.*, 2012, **41**, 5577-5587.
4. X. Liu, B. Li, F. Fu, K. Xu, R. Zou, Q. Wang, B. Zhang, Z. Chen and J. Hu, *Dalton Trans.*, 2014, **43**, 11709-11715.
5. G. M. Neelgund and A. Oki, *Ind. Eng. Chem. Res.*, 2018, **57**, 7826-7833.
6. R. Bhandari and M. R. Knecht, *ACS Catalysis*, 2011, **1**, 89-98.
7. N. K. Reddy Bogireddy, K. K. H. Anand and B. K. Mandal, *Biointerface Res. Appl. Chem.*, 2018, **8**, 3319-3323.
8. S. Mei, J. Cao and Y. Lu, *J. Mater. Chem. A*, 2015, **3**, 3382-3389.
9. S. Behrens, A. Heyman, R. Maul, S. Essig, S. Steigerwald, A. Quintilla, W. Wenzel, J. Bürck, O. Dgany and O. Shoseyov, *Adv. Mater.*, 2009, **21**, 3515-3519.
10. Y. Wang, Q. Li, P. Zhang, D. O'Connor, R. S. Varma, M. Yu and D. Hou, *J. Colloid Interface Sci.*, 2019, **539**, 161-167.
11. K. Esumi, R. Isono and T. Yoshimura, *Langmuir*, 2004, **20**, 237-243.